A TECHNIQUE FOR EVALUATING THE FLUCTUATING AERODYNAMIC FORCES ON A FLEXIBLE STRUCTURE

BY

N. ELLIS B.Sc.

A THESIS PRESENTED FOR THE DEGREE OF DOCTOR OF PHILOSOPHY OF THE UNIVERSITY OF LONDON.

MARCH 1974.

CONTENTS

SUMMARY AND ACKNOWLEDGEMENTS		
CHAPTER I	INTRODUCTION	PAGES 4 TO 15
CHAPTER II	NEW STRUCTURAL TECHNIQUE	16 TO 31
CHAPTER III	EXPERIMENTAL MODEL,	32 TO 57
	APPARATUS DESIGN AND CONSTRUCTION	
	DYNAMIC TESTING.	
CHAPTER IV	AERODYNAMIC RESULTS AND CONCLUSIONS	58 TO 73
	MATHEMATICAL SYMBOLS AND REFERENCES	74 TO 78
APPENDIX I	DATA GATHERING, STATISTICAL CONCEPTS AND COMPUTER PROGRAM STRUCTURE.	79 TO 85
APPENDIX II	RESULTS FROM AND MATRICES USED IN DYNAMICAL MODELS	86 TO 95
APPENDIX III	INDEX TO FIGURES	96 TO 99
	TABLES I AND II FLUCTUATING LIFT AND DRAG FORCE DISTRIBUTIONS	99 TO 101
	GRAPHS AND PHOTOGRAPHS	
	FIGURE 1 TO FIGURE 67	
	ENCLOSED PUBLISHED PAPER "A TECHNIQUE FOR EVALUATING THE FLUCTUATING FORCES ON A FLEXIBLE BUILDING" BY N. ELLIS. PRESENTED AT THE INTERNATIONAL CONFERENCE FOR VIBRATION PROBLEMS IN INDUSTRY, APRIL 1973, KESWICK, ENGLAND.	

SUMMARY

A new computer orientated technique is presented that allows the spatial distribution and cross correlations of the fluctuating aerodynamic lift and drag forces on a flexible building model to be evaluated by experimentally measuring the random response of the model. This inverse approach places no restrictions on the nature or coherence between these forces, thereby allowing the technique to be applied to models of real buildings in complex environments.

The dynamic linearity of the structural model used in wind tunnel tests is experimentally verified by vibrating the model with known random and harmonic forcing functions, and the prediction of these forces with unity coherence and correct phase verifies the structural and computing techniques used in the analysis.

Two approaches to the problem of predicting the input force spectra from the models random response are presented and one of these is shown to be susceptible to small bias errors in the measured response spectra.

Statistically integrating the distribution of fluctuating lift and drag coefficients obtained using the technique gave good agreement with Vickery[2] for these integrated forces.

ACKNOWLEDGEMENTS

The author wishes to acknowledge the Building Research Establishment for sponsoring the research under contract number SE/37/71/C. Thanks also to the research supervisors Dr. P.W. Bearman and Dr. P.F. Kilty of the Department of Aeronautics, Imperial College, for invaluable advice and assistance during the research period.

1.0 INTRODUCTION

DESIGN OF TALL BUILDINGS

When the natural wind flows past a bluff structure it interacts in a manner that leads to the structure experiencing both static and dynamic motion in the in line (drag) and transverse (lift) directions. The effect of this interaction is more pronounced with modern tall structures, which tend to be of lightweight construction and have low structural damping characteristics, both of which can give rise to the structure experiencing large dynamic oscillations, with the accompanying problems of high dynamic stresses, fatigue failure, and serviceability problems. It therefore follows that the stability of such structures in the natural wind is to a greater degree dependent on the structural engineer's knowledge of the unsteady aerodynamic forces acting on the structure in its environment. For example, in tall buildings such as the twin towers of the World Trade Centre, New York, (1400ft. high) the correct dynamic response calculations are essential not only from the stability point of view but also because of the sensitivity of occupants to the motion of the structure, which if serious, could render the structure uninhabitable.

There is no method in the British Code of Practice[41] for wind loading design for calculating the unsteady forces on buildings and it deals mainly with static forces. The Australian Code of Practice[42] however does present a simple method for calculating the fluctuating drag response due to gust loading and is based on Davenport[8] and Vickerys[1] work on the admittance theory. A further inadequacy of the Codes of Practice in general is that there is no information that deals with design for transverse vibrations due to an oscillatory lift force. Thus the present Codes of Practice for wind loading are inadequate in presenting design criteria regarding oscillating lift forces, and are only of limited use in designing for in-line oscillations in modern tall structures.

Hence the object of the research programme outlined within is to try to bridge this gap in knowledge and to devise a new technique that could be used by structural engineers for evaluating the fluctuating aerodynamic forces on tall structures.

1.1 BLUFF BODY AERODYNAMICS

Vortex shedding was studied by Strouhal[28] who noticed that there was a direct linear relationship between flow velocity (U) and the frequency at which vortices are shed from a bluff body, $^{(n)}$ and this frequency non-dimensionalised is called the Strouhal frequency ($^{nD}/U$). The arrangement of these vortices in the wake was further studied by Von Karman[29] who found that they formed a regular vortex street with constant spacing in the wake of the body. Morkovin [31] in an apercu of research on the circular cylinder at sub critical Reynold's number, shows the instantaneous pressure distribution on the surface of the cylinder for short step increments in time during the vortex formation and shedding cycle. Alternate shedding occurs in that as one vortex is shed from one side of the cylinder another is forming on the opposite side and this leads to an oscillating pressure distribution in the lift direction at the Strouhal frequency. These oscillatory lift forces are typical of most bluff body shapes and it is when the frequency of these forces coincide with the transverse natural frequency of the structure that large dynamic amplitudes can arise. The effect of having a sharp edged bluff body such as the square or rectangle is to tend to induce stronger vortex shedding and results in a larger oscillating lift force, because of the fixed flow separation points increasing the correlation length of the vortices.

The Strouhal frequency tends to vary for different sectional shapes, for example S = 0.2 for a circular cylinder at sub critical Reynold's number, whereas for some rectangular sections the Strouhal number varies from 0.06 to 0.16 depending on the section aspect ratio B/D. (See Parkinson[24]). Furthermore, sharp edged bluff bodies tend to have Strouhal numbers that are independent

of Reynolds number because of the fixed flow separation points. However, small front edge curvatures or protrusions were shown to induce Reynold's number dependence (see Davenport[30]).

Vickery[3] studied the fluctuating lift and drag forces on the two dimensional square in smooth and turbulent flow. The results show that the magnitude of the static drag, dynamic drag and fluctuating lift remained mainly independent of Reynold's number. However, the effect of free stream turbulence was shown to have a pronounced effect on these quantities, indicating that the turbulent structure of the oncoming flow had the effect of modifying the aerodynamics of the wake formation and also gives rise to buffetting in the lift and drag directions. For example, in smooth flow the fluctuating lift coefficient $\sqrt{C_{LF}^2}$ was 1.32, compared with 0.68 with large scale turbulence. The importance of sectional shape, especially of the afterbody, on the aerodynamic drag was outlined by Nakaguchi et al[26] when investigating the 2 : 1.25 section ratio rectangular prism. Nakaguchi found that this section had an exceptionally high drag coefficient of nearly 3.0 which is even greater than that obtained from the two dimensional flat plate where $C_D = 2.0$. This phenomenon was further investigated by Bearman and Trueman[6] who found that this high drag was due to the vortices being formed close to the rear face of the model which resulted in a higher rate of air entrainment from this "base" region thereby increasing the static drag force. The high drag associated with this section led to it being called the "critical" section.

1.2 OSCILLATING BLUFF BODIES

As tall bluff structures tend to vibrate in the wind it is questionable whether the fluctuating forces measured on stationary models are applicable to vibrating ones. Feng[37] investigated the effect of oscillating a circular cylinder in smooth flow at sub critical Reynold's numbers. The cylinder moving transverse to the flow resulted in the shedding frequency no longer remaining linear with increase in velocity, and as the shedding frequency increased to

a value close to the natural lift frequency of the cylinder it "locked on" to the structural natural frequency and remained constant for a range of wind speeds around resonance. Furthermore, the fluctuating lift force was found to increase with increasing lift displacement reaching a maximum value of about 1.8, and this was attributed to the oscillating amplitude increasing the strength of vortex shedding thereby increasing the oscillating lift force. For very small displacements there was little change in the oscillating lift force.

The lift oscillations of square prisms were investigated by Parkinson and Smith[33]. A two dimensional square prism was mounted on springs in a wind tunnel and lightly damped, very large lift oscillations were found to occur at wind speeds much higher than those required for vortex shedding to be resonant with the lift natural frequency. This phenomenon was first outlined by Den Hertog[32] when dealing with large dynamic oscillations of overhead electrical conductors and is termed "galloping". These galloping oscillations are due to certain rectangular sections becoming aerodynamically unstable, in that small amplitude vibrations generate aeroelastic forces which further increase the amplitude of oscillation, that is, self excited oscillations. Parkinson developed a "quasi" steady theory that predicted the galloping amplitude, and the magnitude of the lift force was found by rotating the angle of incidence of a stationary square cylinder to the flow, and measuring the static lift force. A maximum value of $C_{FY} = 0.6$ was found at an angle of rotation of 13^{o}. The physical explanation of the galloping phenomenon is that it is due to the separated shear layers moving close to reattaching to the afterbody sides of the prism thereby inducing an oscillating lift force which is in the opposite direction to the motion of the structure and effectively acts as a negative damping force, and the maximum galloping lift force for the square prism corresponds to the shear layer reattaching to the afterbody as discussed by Parkinson[24]. Using the quasi steady theory it can be shown that for the section mounted on springs without

damping it becomes aerodynamically unstable from rest at any wind speed, and so for any particular level of damping there is a certain "critical" wind speed at which the instability is onset (i. e. $U > U_o = \frac{2\beta}{M_n A}$) and this is discussed in chapter 3.0.

The theoretical and experimental results of Parkinson apply only when the reduced velocity of the test is much higher than the reduced velocity required for structural resonance with vortex shedding, and in fact tests by Parkinson and Santosham[34] show that the quasi steady theory does not give an acceptable prediction of the galloping amplitude when the system is resonant with vortex shedding. It was further shown that if the onset velocity is close to the value required for vortex resonance then the wake structure tends to lead to asymmetric quenching of the galloping oscillations, and only when the reduced velocity was three times higher than the resonant value ($U > 3U_{RES}$) did the quasi steady theory predict galloping amplitudes that related to those observed by experiment. When $U < 3U_{RES}$ the experimental amplitudes of vibration were much lower than the values indicated by the quasi steady theory.

In some modern tall structures vortex resonance may occur with one or more of the structures natural frequencies, depending on wind speed, and this may lead to making the structure more aerodynamically stable and hence less prone to galloping oscillations. Thus it would appear from Parkinson and Santosham's results that the combination of high damping and of having a multi degree of freedom structure will lead to better aerodynamic stability as both factors tend to reduce the probability of galloping oscillations occurring, and the structures design will therefore be dominated by the vortex shedding phenomenon.

The effect of turbulence on galloping oscillations was investigated by Novak[9, 10, 11] who found that some rectangular prisms that were stable in smooth flow could become unstable in turbulent flow, and with other prisms the converse was true. This phenomenon was emphasised by aerodynamic tests on the 2 : 1 section with the large

face windward, and the section remained stable for all reduced velocities in smooth flow unless given an initial amplitude displacement. The effect of turbulence gave a quite drastic change in the galloping behaviour in that there was now a strong tendency to gallop, i. e. the section tended to become a soft oscillator, furthermore, tests on the 1 : 2 section, with the small face windward, indicated that this section became a "hard oscillator" in turbulent flow, whereas it is a soft oscillator in smooth flow. Thus Novak showed that the effect of turbulence can either increase or decrease the aerodynamic stability of rectangular prisms to the natural wind.

The non dimensional galloping parameters relating to the present model design (of 2 : 1.25 section) have been evaluated and the experimentally measured oscillating lift amplitudes plotted on Novak's[11] stability diagram as shown on Figures 66 and 67. These oscillating lift amplitudes were always found to be in the stable region of the diagram this indicating that the present model will not exhibit any galloping oscillations. The calculations involved with galloping are outlined in chapter 3.

The effect of having both turbulence and a sheared flow on the galloping behaviour was experimentally investigated by Novak and Davenport[35] for a free ended building model. They found that generally both factors tend to increase the onset velocity and reduce the magnitude of galloping oscillations relative to the two dimensional square results.

Thus it can be concluded that galloping in general is a complicated aerodynamic phenomenon that arises when tall prismatic structures with low damping are exposed to the natural wind, and the aerodynamic forces induced by the motion of the structure create a non linear dynamic problem that is complicated by three dimensionality, shear flow, sectional shape, free stream turbulence and structural damping.

1.3 EFFECTS OF ATMOSPHERIC TURBULENCE

Another main source of vibrations in tall structures arises because of the interaction between turbulence in the earths boundary layer and the structure, which in many instances, produce large in-line or drag oscillations. This effect is further magnified by the tendency to have low natural frequencies which moves the peak dynamic response, especially in the fundamental mode of vibration, into the most energetic part of the turbulent energy spectrum corresponding to eddy length scales of the order 300 to 600 metres. The effect of this lowering of the natural frequency is most pronounced at higher wind speeds since the root mean square drag force increases to a significant power of wind speed. The power in the horizontal $\bar{u}$ component of velocity fluctuation increases with $U^{8/3}$ (as shown in Owen[38]), however as outlined by Bearman[5] in studying the fluctuating drag on square plates in turbulent flow the fluctuating drag force increases at a faster rate than $U^{8/3}$ as the turbulent eddy scale increases, this being due to the increased cross correlation between points on the plate. Thus lowering the natural frequency of a tall structure gives rise to two main effects (i) one is to increase the power centred at the natural frequency corresponding to the large scale eddies, and (ii) these larger eddies cause fluctuating drag forces that are better correlated along the length of the structure. These two combined effects give rise to the structure experiencing high dynamic stresses due to the turbulent interaction of the wind.

The dynamic response of bluff structures is dependent to a large extent on the local prevailing wind conditions. At above 300 to 600 metres the mean velocity of the wind remains unaffected by the general terrain roughness, whereas at heights closer to the ground, especially below 100 metres the ground friction effects tend to reduce the mean wind velocity and increase the fluctuating velocity due to an

energy transfer into the turbulent part of the flow. The earths boundary layer variation in mean velocity with height was defined by Davenport[8] and is expressed as an exponent law

$$U_Z = \bar{U} \left(Z/_{Zo} \right)^{\alpha}$$

where $\bar{U}$ is the mean velocity at 10 metres above ground level (Zo), Z is the height, and α is the power exponent which varies from 0.16 for an open terrain to 0.4 for the centre of a large city. In the case of a city centre the mean velocity close to the ground level is much reduced because of built up obstructions, however, as the mean velocity reduces the turbulent intensity of the wind tends to rapidly increase, especially below 100 metres. Examples where this turbulent intensity is very important are outlined in Davenport and Isymov's[39] work on the stability of the Seattle First National Bank and Whitbread and Scrutons[40] work on the World Trade Centre, New York where turbulent intensities $\sqrt{\overline{u}^2}/U$ of up to and greater than 30% were used. Obviously this parameter is very important when designing thin shell structures such as cooling towers which tend to have large circumferential bending stresses, as is outlined by Davenports[36] tests on a model of the Fort Martin cooling tower. Davenport[8] further defines that the turbulent intensity varies according to

$$I_Z (u) = 2.45 \, K^{\frac{1}{2}} (Z/Zo)^{\alpha}$$

i.e., is dependent on the roughness factor of the local terrain K, velocity exponent α, and height (Z/Zo).

Davenport extended this approach to obtain a technique that allowed an estimate of the fluctuating drag response in a turbulent wind to be obtained using a statistical approach based on meteorological data for the local prevailing wind conditions, and is generally termed the admittance theory.

It is important to note that Davenports admittance function relates the fluctuating drag spectrum to a known static drag coefficient the additional mass parameter C_m, and the power spectrum of the upstream velocity fluctuations due to turbulence in the form:

$$F(C_D)(n) = \frac{4 C_D^2 \; F(u)(n)}{U^2} \left(1 + \frac{C_m^2}{C_D^2} \left(\frac{wD}{U} \right)^2 \right)$$

By examining what is actually meant by this equation it becomes obvious that this approach has several limitations, for example, the fluctuating force spectrum does not include the low frequency drag fluctuations on the rear face of the structure caused by the wake and the fluctuating drag is considered to be totally dependent on the fluctuating upstream velocity. Work by Bearman[5] on the fluctuating drag forces on square plates suggests that the admittance theory underestimates the fluctuating drag force for small turbulent scale parameters $Lx/D < 1.5$, since there is an interaction between the turbulence and the wake that affects the fluctuating drag. Further work outlined in Bearman[4] suggested that with a free ended triangular prism, with the bluff face windward, the admittance theory underestimated the dynamic response at low frequencies $nD/U < 0.03$ and this was thought to be due to either low frequency wake effects or caused perhaps by the free end. Thus it is important to take into account or at least be aware of the three dimensional effects that can considerably modify the aerodynamic forcing function which to some degree may invalidate results obtained from a basically two dimensional approach.

In extending the admittance theory to apply it to a multi-degree of freedom structure using a vertical variation in fluctuating upstream velocity the cross correlation terms required in the dynamic analysis are generally found from the experimental evaluation of the cross correlations between a family of hotwire anemometers. Obviously the truecross correlation should be between the integrated drag

pressure distribution on the front and rear faces of the structure, with this integrated quantity at another station. The analysis should also include the effect of the reverse flow into the near wake associated with the free end which further complicates the nature of the wake pressure fluctuations and overall dynamic response.

1.4 EXISTING METHODS FOR MEASURING THE FLUCTUATING LOADS ON BLUFF BODIES.

Many researchers have used pressure transducers to measure the fluctuating pressure distribution around bluff models. The limitation in their use is that a very large number are required to get an estimate of the integrated fluctuating force around the model, and since these have to be experimentally recorded very large data handling systems are required making calibration and data analysis cumbersome, expensive and impractical. Another approach is to subdivide the rectangular structure into panel elements and elastically mount each element on a strain gauged connector, and relate the fluctuating force on each element to the fluctuating output voltage from the strain gauge. However, it is very difficult to isolate these elements from the supporting structure and give a measurable response while trying to prevent air leakage into the supporting structure. A seal would therefore be required and this would seriously affect the results, as it would affect the damping and stiffness characteristics of each element.

Vickery[2] used a rigid cantilevered two degree of freedom model (one lift, one drag) built on gimbals and used the output from a dynamometer fixed at the bottom of the model to measure the fluctuating aerodynamic shear force on the model. The aerodynamic shear force value represents the integrated shear force due to the effect of all the local fluctuating forces. The work presented by Vickery[2] is the only work known by the author that evaluates the integrated fluctuating lift and drag forces on building models,

although these results are restrictive in that only one fluctuating lift and drag value is found for any particular building shape. It must be emphasised that it is the distribution of the fluctuating forces that is important because of the three dimensional nature of the flow, for example, there is a tip flow region caused by the free end, a middle region and a region near ground level, within which complicated interactions between the wake and the external turbulent flow takes place. The integrated value obtained using Vickerys method represents a 'macro' or overall value of all these effects along the structure, and theoretically this force could act anywhere up the height of the building and consequently it is only of limited use to the designer as its point of application is required, for example, it could be a force at the top, middle or bottom of the building.

The object of the research outlined within is to develop a new technique for evaluating the distribution of fluctuating lift and drag forces, and their cross correlations up the height of a building. A literature survey by the author indicated that there is no technique available that predicts the distribution and cross correlations between forces acting on a building structure.

1.5 STRUCTURAL CONCEPT

The structural concept of the present technique is to invert the standard procedure for predicting the dynamic response of a structure for "given" loads and instead use the dynamic response at various stations on a flexible model with a fixed base, measured from wind tunnel tests, to predict the distribution and cross correlations of the fluctuating aerodynamic forces, as shown on Figure 1.

The validity of the technique used is verified by the prediction of known random and harmonic fluctuating forces applied to the model using mechanical vibrators, and also by extensive dynamic testing and calibration. The model used has therefore to be designed to have measurable acceleration and dynamic strain response for wind tunnel tests in smooth and turbulent flow.

The dynamic linearity of the model was checked by plotting the structural response loci for the first four modes of vibration using the technique of Kennedy and Pancu[15]. The spatial variation in damping for each mode of vibration was also evaluated as it was required in the dynamic analysis. Further dynamic tests were made and these included the comparison between the theoretical and experimental eigenvectors, eigenvalues, and the experimental determination of the frequency response function.

A computing system was designed to handle the large amount of data generated by the technique, and a family of programs written that evaluated the fluctuating aerodynamic forces from the random response and this is discussed in Appendix 1.

It is hoped that now the technique is fully developed it will be used in predicting the fluctuating loads on tall buildings situated in highly complicated aerodynamic environments, for example, where a building is surrounded by other buildings in an urban area.

2.0 NEW TECHNIQUE - MATHEMATICAL MODEL

The object of the technique is to evaluate the distribution of the fluctuating aerodynamic lift and drag forces by experimentally measuring the dynamic accelerations $\ddot{X}(t)$ and strains $\mathcal{E}(t)$ on a flexible model. The mathematical model used was developed from the field and point transfer matrix approach to structural analysis as applied to random vibrations outlined in LIN[18].

Consider the beam elements and lumped masses defined at their nodal points, and the model vibrating due to the random fluctuating pressure field, $\underset{\sim}{P}(Z, t)$, representing the spatial and time variation in the fluctuating aerodynamic pressure across the section of the model. The random pressure field is assumed to vary linearly between the points where the strain gauges are attached to the model i.e. at a position slightly above the nodal points as shown on Diagram A, Appendix II, to ensure that the local bending stresses associated with the models transverse panels do not affect the linearity of the strain gauge output signals. Hence knowing the dynamic bending moment distribution (found by calibrating the strain gauges) and accelerations (found by using accelerometers) two equations of equilibrium can be formed at time instant t_i ; and can be interpreted in the following matrix form:

$$\text{for moments,} \quad \mu M = \alpha P + \beta S - [\gamma m + \eta \lambda + \rho]\ddot{X} \qquad \text{(i)}$$

$$\text{for shear forces} \quad \delta P + \Omega S = [m + \pi_s \lambda + \pi_\rho]\ddot{X} \qquad \text{(ii)}$$

and the above matrices can be interpreted as follows:

- μM - column of differences in dynamic moment across each element.
- αP - column of dynamic moments due to the fluctuating aerodynamic pressure field.
- βS - column of dynamic moments due to the shear forces at the ends of each element.

$\gamma m \ddot{X}$ - column of dynamic moments due to nodal mass acceleration.

$\eta \lambda \ddot{X}$ - " " " due to shell " "

$\rho \ddot{X}$ - " " " due to transverse panel "

SHEAR EQUATION (ii)

δP - column of dynamic shear forces due to random force.

ΩS - " " " across elements

$m \ddot{X}$ - " " " due to nodal mass acceleration.

$\pi_s \lambda \ddot{X}$ - " " " due to shell mass acceleration.

$\pi_\rho \ddot{X}$ - " " " due to transverse panel accel.

The evaluation of these matrices is shown in AppendixII and the construction of the experimental model is discussed in Chapter 3.

The substitution for S from (ii) into (i) gives equation (iii) which defines the distribution of the random load in terms of the instantaneous dynamic moment $M(t_i)$ and nodal acceleration $\ddot{X}(t)$ in the time domain.

$$P(t_i) = [a - \beta \bar{\Omega}^{-1} \delta]^{-1} \{ \mu M(t_i) + [\Gamma - \Lambda] \ddot{X}(t_i) \}$$

where $\Gamma = \gamma m + \eta \lambda + \rho$

and $\Lambda = \beta \bar{\Omega}^{-1} [m + \pi_s \lambda + \pi_\rho]$

equation (iii) can be reinterpreted as

$$P(t_i) = A^* M(t_i) + B^* \ddot{X}(t_i) \qquad \text{(iv)}$$

where $A^* = [a - \beta \bar{\Omega}^{-1} \delta]^{-1} \mu$

$B^* = [a - \beta \bar{\Omega}^{-1} \delta]^{-1} [\Gamma - \Lambda]$

The bending strain $\mathcal{E}(t)$ is measured using strain gauges and the dynamic moment $M(t)$ is related to it in the frequency domain by

$$M(\omega) = G(\omega) \cdot \mathcal{E}(\omega)$$

where $G(\omega)$ is a diagonal complex structural damping matrix with typical terms e.g.

$$G_{11}(w) = \frac{EI}{\ell} \cdot (1 + ig(w))$$

FIG. 17 shows how the non-dimensional damping factor varies for the different modes of vibration of the experimental model, and to take this into account equation (iv) is Fourier Transformed into the frequency domain to give:

$$P(\omega) = A^* G(\omega) \hat{\mathcal{E}}(\omega) + B^* \ddot{X}(\omega) \qquad (v)$$

i.e., to describe the variation in the random pressure field $P(\omega)$ in terms of the complex Fourier coefficients of strain $\hat{\mathcal{E}}(\omega)$ and acceleration $\ddot{X}(\omega)$

The Fourier coefficients of the aerodynamic shear force on each element $P_s(\omega)$ can be found by integrating the fluctuating pressure over the element lengths

$$P_s = \delta P(\omega)$$

thus for any circular frequency ω the j'th element represents the Fourier coefficients of the aerodynamic shear force acting on that element.

The stabilised force spectra matrix associated with $P_s(\omega)$ is found from:

$$S_p(\omega) = \overline{P_s(\omega) P_s^*(\omega)^t}$$

where the j^{th} diagonal element represents the power spectrum of the fluctuating aerodynamic force on the j^{th} element of the model, and hence all the diagonal elements represent the vertical distribution of these forces. Similarly the relationship between each of the elemental forces can be found by consulting the power in the off diagonal elements.

For aerodynamic tests the non-dimensional fluctuating lift and drag spectra are obtained from:

$$\frac{U}{Dw} \cdot S\,(C_{LFi})(n) = \frac{U}{Dw} \cdot \frac{S\,(P_{Li})\,(n)}{(\frac{1}{2}\rho U^2 \cdot A_{Li})^2}$$

and

$$\frac{U}{Dw} \cdot S\,(C_{DFi})\,(n) = \frac{U}{Dw} \cdot \frac{S\,(P_{Di})\,(n)}{(\frac{1}{2}\rho U^2 \cdot A_{Di})^2}$$

Thus the distribution of fluctuating root mean square (rms) lift and drag forces can be found from:

$$\sqrt{\overline{C_{LFi}^2}} = \sqrt{\Delta n \cdot \sum_{i=1}^{N} S\ (C_{LFi})\ (n)}$$

and $$\sqrt{\overline{C_{DFi}^2}} = \sqrt{\Delta n \cdot \sum_{i=1}^{N} S\ (C_{DFi})\ (n)}$$

i.e., by integrating the individual elements power spectrum.

Having mathematically described the distribution of the fluctuating forces on the structure it is also important to describe the statistical relationship between the forcesin terms of how well correlated or coherent they are spatially. The cross correlation between the elemental forces become very important when trying to obtain a correct estimate for the dynamic response and hence stress level within a structure, i.e. the higher the cross correlation between the aerodynamic forces the higher will be the dynamic stress level. Thus an underestimation of the magnitude of the cross correlation coefficient can lead to severe overstressing, while an overestimation will lead to overdesigning of the structure.

2.1 CROSS CORRELATIONS, COHERENCE AND PHASE

The matrix of cross correlations between the fluctuating aerodynamic forces at time lag τ is given by:

$$R_p(\tau) = E\left[P(t)\ P^t(t+\tau) \right]$$

which applies to the time domain prediction of $P(t)$. In the frequency domain solution the coherence and phase are defined by Bendat and Piersol[19] giving

$$\text{coherence}\quad C_{pipj}(w) = \frac{S_{pipj}(w)^2 + Q_{pipj}(w)^2}{S_{Pi(w)} \cdot S_{Pj}(w)}$$

$$\text{and phase}\quad \Theta_{pipj}(w) = \tan^{-1}\left(\frac{Q_{pipj}(w)}{S_{pipj}(w)} \right)$$

where $S_{pi}(w)$ and $S_{pj}(w)$ are the diagonal power spectra terms and $S_{pipj}(w)$ and $Q_{pipj}(w)$ are the cross and quadrature spectra respectively.

The cross correlation at time lag $\tau = 0$ is related to the cross spectrum by

$$R_{pipj}(0) = \int_{-\infty}^{\infty} S_{pipj}(w)\, d\omega$$

or in terms of the cross correlation coefficient

$$C_{pipj}(0) = \frac{\sum_{r=1}^{N} S_{pipj}(w_r)}{\sqrt{\sum_{r=1}^{N} S_{pi}(w_r) \cdot \sum_{r=1}^{N} S_{pj}(w_r)}}$$

2.2 HIGHER ORDER INTERPRETATION OF THE FLUCTUATING FORCES

Returning to equation (iv) which describes the fluctuating force in terms of $\ddot{X}(t)$ and $\mathcal{E}(t)$ it is obvious that the fluctuating aerodynamic forces need not necessarily vary linearly between elements and in fact a matrix of 5th order polynomial interpolation functions W can be used to relate the global distribution $P(z)$ to the element nodal forces P by

$$P(z) = W\,P$$

where $P_1(Z) = a_1 Z^5 + a_2 Z^4 + a_3 Z^3 + a_4 Z^2 + a_5 Z + a_6$

and by applying the boundary conditions for each element.

$$P(0) = P_6 \qquad Z = 0$$

$$P(\ell_5) = P_5 \qquad Z = \ell_5$$

etc.

gives

$$\begin{bmatrix} P_6 \\ P_5 \\ P_4 \\ P_3 \\ P_2 \\ P_1 \end{bmatrix} = \begin{bmatrix} 1 & 0 & 0 & 0 & 0 & 0 \\ 1 & \ell_5 & \ell_5^2 & \ell_5^3 & \ell_5^4 & \ell_5^5 \\ 1 & \ell_4 & \ell_4^2 & \ell_4^3 & \ell_4^4 & \ell_4^5 \\ 1 & \ell_3 & \ell_3^2 & \ell_3^3 & \ell_3^4 & \ell_3^5 \\ 1 & \ell_2 & \ell_2^2 & \ell_2^3 & \ell_2^4 & \ell_2^5 \\ 1 & \ell_1 & \ell_1^2 & \ell_1^3 & \ell_1^4 & \ell_1^5 \end{bmatrix} \begin{bmatrix} a_6 \\ a_5 \\ a_4 \\ a_3 \\ a_2 \\ a_1 \end{bmatrix}$$

or $\mathbf{P} = \mathbf{L}\,\mathbf{A}$

giving coefficients $\mathbf{A} = \mathbf{L}^{-1}\mathbf{P}$

Calculation of δ_1 and a_1 for 5th order polynomial.

This gives

$$P(Z) = A^t\, Z\, P \qquad \text{(i)}$$

where $Z = \lceil 1Z \quad Z^2 \quad Z^3 \quad Z^4 \quad Z^5 \rfloor$

SHEAR FORCE δ_1

$$P_{e5} = \int_{0}^{\ell_5} P_5\,(Z)\cdot dZ$$

$$P_{e4} = \int_{\ell_5}^{\ell_4} P_4\,(Z)\cdot dZ$$

where P_{ei} represents the aerodynamic shear force on element i

$$P_{ei} = A_i^t \cdot \int_i Z\, dZ \cdot P$$

i.e. for i'th row of (1)

i.e. integrate each row of Z with different boundary conditions

this gives

$$P_e = \delta_1\, P$$

MOMENT

A similar analysis can be performed for the dynamic moments.

$$M_{ei} = \int_{\ell_i}^{\ell_{i-1}} P_i\,(Z)\cdot(Z - \ell_i)\, dZ$$

and integrating as above gives

$$M_{ei} = A_i^t \int_{\ell_i}^{\ell_{i-1}} Z\,(Z - \ell_i)\, dZ$$

giving

$$M_e = a_1\, P$$

The values of a , a_1 , and δ , δ_1 , are shown for comparison in Appendix II. The solution for the fluctuating elemental forces was carried out using equation (v) to compare the results for both the linear and 5th order cases. FIG. 54 (top graph), for reduced velocity $U/n_1 D = 48.4$, smooth flow, shows this comparison for the lift force spectrum and the difference between

the predicted fluctuating force using a linear and 5th order approximation appears to be minimal. Thus the linear interpretation of the aerodynamic force has been used for the wind tunnel analysis.

2.3 CONDITIONING OF MATRICES $\mathbf{A}^*$ $\mathbf{B}^*$

The errors associated with the experimental measurement of $\mathcal{E}(t)$ and $\ddot{X}(t)$ affect the accuracy of the predicted force to a degree depending on the distribution of elements in matrices $\mathbf{A}^*$ and $\mathbf{B}^*$.

The best conditioned problem is when the applied loads are point loads, and act at the nodal masses, and the dynamic strains are measured at these nodal points. This condition is not possible in the practical model because of the following reasons:

(i) in vibration random load tests in the laboratory the loads would be applied on top, or very close to, the semi-conductor strain gauges, and this would affect their performance.

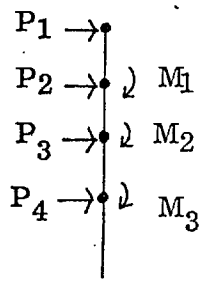
(ii) the strain gauges would have to be placed with their $\mathcal{E}$'s on the $\mathcal{E}$ of the transverse stiffeners, and local stress concentrations might affect the performance of the gauges in measuring pure beam bending strains.

(iii) the fluctuating aerodynamic load is in fact distributed over each element.

Considering equation (v)

$$\mathbf{P} = \mathbf{A}^* \mathbf{G} \mathbf{M} + \mathbf{B}^* \ddot{X}$$

then for the ideal case where the loads are point loads applied at the nodal masses,



$$P = \frac{1}{\ell} \begin{bmatrix} 1 & & & \\ -1 & 1 & & \\ & -1 & 1 & \\ & & -1 & 1 \\ & & & -1 \end{bmatrix} \cdot \mu M + \begin{bmatrix} m_{11} & & & & \\ & m_{22} & & & \\ & & m_{33} & & \\ & & & m_{44} & \\ & & & & m_{55} \end{bmatrix} \cdot \ddot{X}$$

As is seen from this equation localised errors associated with the top elements do not seriously affect the prediction of the force at the lower stations.

For example, in predicting force P4,

$$P_4 = \frac{1}{\ell} (- \Delta M_3 + \Delta M_4) + m_{44} \ddot{X}_4$$

i.e. is dependent on the accuracy of measuring dynamic strains and accelerations close to point 4 only.

where ΔM_i is the difference in moment acrossthe i^{th} element.

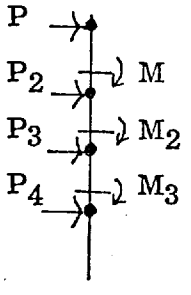
POINT RANDOM LOADS - ACTUAL MODEL

Due to the construction of the model the following practical considerations change the conditioning of the problem, these are:

(i) strain gauges are applied approximately $\frac{3}{8}$" above the mass node points.

(ii) the mass of the shell is kinematically lumped giving small off diagonal terms to the mass matrix, resulting in the following equation:

$$\mathbf{P} = \begin{bmatrix} .35 & 0. & 0. & 0. & 0. \\ -.40 & .36 & 0. & 0. & 0. \\ .05 & -.41 & .35 & 0. & 0. \\ -.01 & .05 & -.39 & .36 & 0. \\ 0. & -.01 & .04 & .42 & .36 \end{bmatrix} \mu\mathbf{M} + \mathbf{B}^* \ddot{\mathbf{X}} \quad \text{(ii)}$$

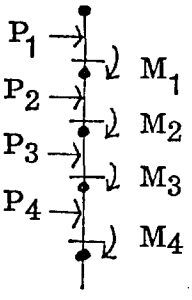


Thus it is seen how the actual conditioning varies from the ideal condition where the point loads are applied at the nodes, giving some small off diagonal elements.

To investigate this further, consider the random point load applied at the midpoint of the elements, i.e. at the intermediate transverse panels.

This gives:

$$P=\begin{bmatrix} .78 & 0 & 0 & 0 & 0 \\ -1.92 & .78 & 0 & 0 & 0 \\ +2.79 & -1.92 & 0.78 & 0 & 0 \\ -4.06 & 2.79 & -1.92 & .78 & 0 \\ 5.90 & -4.06 & 2.79 & -1.92 & .78 \end{bmatrix} \cdot \mu M + B^{*}\ddot{X} \quad \text{(iii)}$$



where B^{*} has similar conditioning as A^{*}

Therefore tests where the random load is applied at close to the midpoint and lower points on each element are highly ill conditioned and will give a large build up in error, the maximum errors being associated with the prediction in the fluctuating force at lower stations i.e., P4, P5.

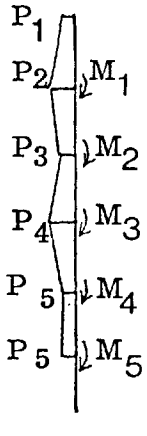
For example $P_4 = -4.06\Delta M_1 + 2.79\Delta M_2 - 1.92\Delta M_3 + 0.78\Delta M_4$ indicating that errors in ΔM_1, ΔM_2, ΔM_3 will lead to much larger errors in the evaluation of P_4.

Since in fact for wind tunnel tests the aerodynamic forces will be distributed along the structure another conditioning problem applies to the representation of the aerodynamic forces.

LINEAR DISTRIBUTION OF THE FLUCTUATING FORCES

This assumes that the fluctuating aerodynamic lift and drag force distribution varies linearly along each element between strain gauges. This approach gives the following equation evaluated using the matrices evaluated in Appendix II.

$$P = \begin{bmatrix} 0.35 & -0.11 & 0.03 & -0.01 & 0 \\ -0.23 & 0.22 & -0.06 & 0.02 & 0 \\ 0.06 & -0.22 & 0.22 & -0.01 & .01 \\ -0.02 & 0.06 & -0.22 & 0.21 & -.03 \\ 0 & -0.01 & 0.04 & -0.16 & 0.13 \end{bmatrix} \cdot \mu M + B^{*}\ddot{X}$$



Thus the linear distribution approximation to the fluctuating aerodynamic force does not give rise to any large off diagonal elements and hence there does not appear to be any serious ill conditioning associated with representing the distribution of aerodynamic forces in this way. Hence the accuracy obtained in the evaluation of the fluctuating lift and drag forces depends mainly on the errors associated with measuring the dynamic strains $\hat{\mathcal{E}}(t)$ and accelerations $\ddot{X}(t)$ with the correct calibration factors and preservation of their phase characteristics.

Another important factor involved with the accuracy of prediction is that the terms in the matrix μM represent the change in moment across each element. Therefore, when predicting the forces on the elements close to the bottom of the model these changes in moment are largely due to the inertia and applied forces higher up, and so the contribution to the change in moment from the aerodynamic force on the element may be small thereby limiting the accuracy of its prediction. The results of the dynamics laboratory tests, relating to the prediction of known random and harmonic forces, as outlined in Chapter 3., indicated that the top five strain gauge signals and five accelerometer signals should be recorded and that these gave a high accuracy when predicting the fluctuating forces on the top four elements.

Inherent in the concept of the technique is that to evaluate the fluctuating force on one element two quantities have to be experimentally measured, one dynamic strain and one dynamic acceleration, thus for the prediction of ' n ' fluctuating forces '2n' quantities have to be recorded. An alternative approach was investigated and rejected by the author (Ellis[7]) as it was shown to be sensitive to perturbations which arise from small experimental errors. This alternative approach required only one dynamic acceleration signal per element to predict the fluctuating aerodynamic force and is based on the solution of the equation:

$$S_X(w) = H(w) \cdot S_p(w) \cdot H^t_*(w)$$

giving $$S_p(w) = H^{-1}(w) \cdot S_X(w) \cdot H^{-t}_*(w) \qquad (1)$$

*complex conjugate

which describes the solution for the nodal force spectra $S_p(w)$ in terms of the nodal displacement spectra $S_X(w)$ and the multi degree of freedom frequency response function $H(w)$.

It is interesting to investigate the prediction $S_p(w)$ from equation (1) which requires the full experimental frequency response function to be inverted for every frequency considered.

The cross correlation function of the generalised displacement can be defined in matrix terms as:

$$R_q(\tau) = E\left[q(t) \; q^t \; (t+\tau) \right]$$

and using the eigenvector transformation:

$$q = \Phi^{-1} X$$

this can be rewritten as:

$$R_q(\tau) = E\left[\Phi^{-1} X X^t \Phi^{-t} \right]$$

$$= \Phi^{-1} R_X(\tau) \Phi^{-t}$$

Since the response spectra is the Fourier Transformation of the cross correlations:

$$S_q(w) = \Phi^{-1} S_X(w) \Phi^{-t} \qquad (i)$$

where $S_X(w)$ is found from the acceleration spectra:

$$S_X(w) = \frac{1}{w^4} S_a(w)$$

In terms of the generalised force spectrum:

$$Q = \Phi^t P$$

and $$R_Q(\tau) = E\left[Q(t) \cdot Q^t \; (t+\tau) \right]$$

$$= \Phi^t \cdot R_p(\tau) \cdot \Phi$$

hence $$S_Q(w) = \Phi^t \cdot S_p(w) \cdot \Phi \qquad (ii)$$

in terms of generalised co-ordinates:

$$S_Q(w) = h^{-1}_q(w) \; S_q(w) \; h^{-t}_{q*}(w) \qquad (iii)$$

where $h_q(w)$ is the generalised frequency response function, which is complex and diagonal.

Substituting (i) and (ii) into (iii) gives

$$S_p(w) = \Phi^{-t}\ h_q^{-1}(w)\ \Phi^{-1}\ S_x(w)\ \Phi^{-t}\ h_{*q}^{-t}(w)\ \Phi^{-1} \qquad \text{(iv)}$$

hence $H^{-1}(w) = \Phi^{-t}\ h_q^{-1}(w)\ \Phi^{-1}$

and since $h_q(w)$ is diagonal no complex inversion of $H(w)$ is necessary, and hence this relationship will obviously save computing time when evaluating $S_p(w)$

The experimental formation of $h_q(w)$ is discussed in section 3.4, and the evaluation of the experimental eigenvectors and damping coefficients in 3.3.

Having completed the experimental determination of the frequency response function, computer programs were written to solve equation (iv) for the fluctuating forces for wind tunnel and random vibration tests, using the experimentally measured accelerations, Fourier Transformed to form the displacement spectra $S_x(w)$

A typical feature of the predicted force spectra obtained using this apparent alternative approach was the high amount of low frequency power obtained in the predicted spectrum, this being orders higher than expected. For example, see the comparison between the approximately expected and predicted spectrum plotted on Figure 18. This phenomenon was further clouded by the apparent convergence between the predicted and expected spectrum at higher frequencies. To try to explain this phenomenon of large errors being incurred at low frequencies a perturbation analysis was conducted.

2.4 PERTURBATION ANALYSIS

To try to discover the mechanism of the perturbation two sources of error were investigated:

(i) errors associated with the experimental frequency response function $\mathbf{H}(w)$.

and

(ii) the effect of random or bias errors associated with the formation of the displacement response spectra matrix $\mathbf{S}_p(\bar{w})$.

The approach used was to form the mathematical response spectra $\mathbf{S}_X(w)$ from an assumed force spectra $\mathbf{S}_p(w)$ and then by introducing separate errors in $\mathbf{H}(w)$ and $\mathbf{S}_X(w)$ observe their effect on the prediction of the known force spectra matrix $\mathbf{S}_p(w)$.

A flow chart for the computer program used to do this is shown on FIG. 19., and the program tested by checking the prediction of $\mathbf{S}_p(w)$ for an unperturbed case, that is, that the input force and output force were the same for all frequencies. The effect introducing small errors in $\mathbf{H}(w)$ gave minimal errors in the prediction of the known force spectra $\mathbf{S}_p(w)$, however, a 1% error introduced into the displacement spectrum at one station $S_{x_{11}}(w)$ (this being synonomous with a small experimental error) gave a predicted force spectrum $S_{p33}(w)$ that was orders higher than the actual $S_{p33}(w)$, for low frequencies as shown on FIG. 20.

This result shows a similar trend to that previously described for wind tunnel tests as shown on FIG. 18., giving the maximum error associated with the low frequency part of the power spectrum, with convergence at higher frequencies, generally greater than 100 HZ.

MATHEMATICAL EXPLANATION OF PERTURBATION

Mathematically the random displacement pattern can be defined as a combination of the eigenvectors, and for a 6 degree of freedom system

$$X = \sum_{i=1}^{6} a_i \Phi_i = \Phi \, a_X$$

where a_i are constants of proportionality and Φ_i the $i^{'th}$ eigenvector.

Consider the solution of the undamped equation of motion

$$[K - \omega^2 m] X' = P$$

Considering X' the displacement to contain some error vector Δ with associated force error δP then at low frequencies when

$$K \{ X + \Delta \} = P + \delta P$$

therefore the error eigenvalue problem becomes

$$K \Delta = \delta P$$

and for the error $\Delta = \Phi \, a_e$

and from the definition of the eigenvalue problem where $\Phi^t m \Phi = I$

$$K\Phi = \Phi \lambda$$

then

$$\delta P = \Phi \lambda a_e$$

and $$\delta P_i = \phi_{1i} \lambda_1 a_{e1} + \phi_{2i} \lambda_2 a_{e2} + \cdots \phi_{6i} \lambda_6 a_{e6}$$

now ϕ_{ij} is of $0(1.0)$

$$\delta P_i \simeq \lambda_1 a_{ei} + \lambda_2 a_{e2} + \cdots \lambda_6 a_{e6}$$

The ratio of a_{ei}'s depend on the frequency content of the error but the ratio of the highest to lowest eigenvalue $\lambda_6/\lambda_1 \simeq 1000$ and so since the noise level for the experimental results is at best 2% the equation for the error is dominated by the term λ_6

Consider the following simple example, for the exact unperturbed solution

$$P_i = \lambda_1 a_1 + \lambda_2 a_2 + \cdots \lambda_6 a_6$$

now for vibration in, for example, the 1st mode or at a low frequency P_i is of $0(\lambda_1 a_1)$ as $\lambda_i a_i \rightarrow 0$ as $i \longrightarrow 6$

for the error analysis δP_i is $0(\lambda_6 a_{e6})$ therefore the ratio of the error associated with the predicted force to the actual force is:

$$\frac{\delta P_i}{P_i} = \frac{0(\lambda_6 a_{e6})}{0(\lambda_1 a_1)} = \frac{\lambda_6}{\lambda_1} \, 0\left(\frac{a_{e6}}{a_1}\right)$$

now if it assumed that the 6th mode contribution is

$0(0.01 a_i)$ i.e. 1% then

$$\frac{\delta P_i}{P_i} \simeq 0.01 \cdot \frac{\lambda_6}{\lambda_1} \simeq 0(10)$$

or $$\delta P_i \simeq 0(10 P_i)$$

hence this very rough estimate indicates that the predicted force from an experimental model evaluated using equation (iv) is dependent on the ratio of the sixth to first eigenvalue, and gives serious errors for the prediction of this force. Obviously as the frequency of the forcing function w tends to w_6 i.e., $w \rightarrow w_6$ then equation (iv) will hold for force predictions, thus the reason for convergence at higher frequencies.

The main conclusion reached from this perturbation approach is that for the prediction of $S_{p(w)}$ from $S_x(w)$ using the frequency response function $H(w)$ to be valid the structure must have a small spread of eigenvalues λ. It is also important

to note that the experimental model will vibrate with more than six degrees of freedom and so by describing it by a 6 x 6 frequency response function has obvious limitations, and this further justifying the conclusion that using:

$$S_p(w) = H^{-1}(w)\ S_x(w) H_*^{-t}(w)$$

to predict the nodal force spectra is impractical and gives results that are sensitive to perturbation errors which invalidate it as an alternative approach to predicting the fluctuating aerodynamic forces.

3.0 EXPERIMENTAL MODEL AND APPARATUS DESIGN

As already outlined in Chapter 2, the prediction of the fluctuating aerodynamic forces on a flexible model is found from the solution of the equation:

$$P(w) = A^* G(w) \mathcal{E}(w) + B^* \ddot{X}(w) \qquad (1)$$

therefore, to find the fluctuating forces $P(w)$ experimentally the model must be designed to have measurable dynamic response when tested in the wind tunnel. A mathematical dynamic analysis was performed to estimate the response of the model using assumed aerodynamic forcing functions. This required the knowledge of the models natural frequencies (eigenvalues) and mode shapes (eigenvectors) which were compared with results from dynamics testing in the laboratory. To check the validity and accuracy of equation (1) above, pseudo random forces were applied to the model using vibrators, and the predicted power spectrum of these forces compared with the actual spectrum measured by a force transducer.

Extensive computer programming was necessary when designing the technique, and consisted of mainly data gathering and data reduction programs. Four computer programs were written and combined in the form of an OVERLAY structure, these analysing the large amount of data generated by the dynamic model to form the force spectra matrix together with the r.m.s values of the fluctuating forces, with their corresponding cross correlations, coherence and phase plots. This computing system is described in detail in Appendix I, and is illustrated pictorially on the computer, flow charts on Figures 22, 23 and 24.

Thus the final system consists of an experimental model together with a computing system and when these are combined together the total system can be thought of as a multi-degree of freedom system that allows the fluctuating force distribution to be evaluated from the random response.

3.1 FLEXIBLE MODEL DESIGN

A matrix finite element analysis of the model was applied using simple beam elements, and the resulting eigenvalue problem for the assembled structure solved to obtain the models natural frequencies and mode shapes for bending oscillations in two directions, lift and drag, and also for torsion. By varying the mass and stiffness distribution as shown on the flow chart Figure 11, the corresponding wind speeds required to excite the lift modes by vortex shedding can be found by assuming a Strouhal number of 0.1 obtained from Parkinson[24]. This information was used in conjunction with assumed harmonic aerodynamic forces from Vickery[2] to estimate the nodal accelerations for wind tunnel tests as shown in Section 3.2.

The chosen mass and stiffness distribution allowed the first and second lift modes to be in resonance with vortex shedding for wind speeds of about 15 and 90 ft/sec., thereby allowing a large range of comparisons between the fluctuating force distributions for "resonant" and "off resonant" vibrations with vortex shedding. Figures 34, 39 and 36, 40 show the actual r.m.s. lift acceleration response of the model for the 31mm and 50mm sides windward in smooth and turbulent flow, while Figures 38 and 41 show the correponding drag responses. These graphs shall be discussed in more detail in the aerodynamic results of Chapter 4.

The main problem associated with designing such a model was to obtain low structural resonant frequencies, with a fixed base model that would be excited by vortex shedding and turbulent flow forces, and still have a model that is representative of a building structure. A main requirement of the design was that dynamic displacements should be kept to a minimum in order to reduce the interaction between the model and the aerodynamic flow.

A rectangular section of 50mm x 31mm was chosen rather than a square as it appeared to have certain advantages in that it allowed the effect of both section and aspect ratios on the aerodynamic forces to be investigated. This shape also has the advantage of keeping the lift and drag resonant frequencies separate thereby minimising lift/drag coupled oscillations.

3.2 MATHEMATICAL DESIGN OF THE EXPERIMENTAL MODEL

The object of creating a mathematical model was to design the experimental model to have the required natural frequencies and to check that rotary inertias and torsional oscillations do not affect the response of the model when dynamically tested in the wind tunnel. Furthermore, it was important to obtain a measure of the dynamic accelerations involved for various mass, stiffness and damping parameters, and to use this to check that suitable accelerometers could be found to measure the acceleration response. The stiffness distribution was varied by increasing the height of the model and by varying the properties of the structural section (Youngs modulus and shell thickness). An initial conclusion from the mathematical model was that aluminium was an unsuitable material for the shell as even in its thinnest obtainable form combined with a lead mass distribution it did not give low enough eigenvalues. This lead to the model design orientating toward the combination of thin perspex and lead as the structural form.

The mathematical model used is a simple idealisation in that the model is subdivided into six beam elements each element having four degrees of freedom.

The equation of motion for an 'n' degree of freedom system subject to harmonic input forces is

$$m\ddot{X} + (1 + ig) K_a X = P e^{i\omega t}$$

where m is the assembled mass matrix

K_a is the assembled stiffness matrix

$ig K_a$ is the complex stiffness matrix representing structural damping

Consider the model to consist of six simple beam elements each having a stiffness matrix:

$$K_\epsilon = \frac{EI}{\ell^3} \begin{bmatrix} 12 & -12 & -6\ell & -6\ell \\ -12 & 12 & 6\ell & 6\ell \\ -6\ell & 6\ell & 4\ell^2 & 2\ell^2 \\ -6\ell & 6\ell & 2\ell^2 & 4\ell^2 \end{bmatrix}$$

Argyris[14] shows how these elements can be assembled giving:

$$K_a = \sum_{i=1}^{6} A_i^t K_\epsilon A_i$$

where A_i is a Boolean selection matrix.

Also partitioning:

$$\begin{Bmatrix} P \\ M \end{Bmatrix} = \begin{bmatrix} K_{11} & K_{12} \\ K_{21} & K_{22} \end{bmatrix} \begin{Bmatrix} X \\ \Theta \end{Bmatrix}$$

Consider the rotary inertias to have negligible effect on the resonant frequencies, the stiffness matrix K_a can be reduced to

$$K_\beta = K_{11} - K_{12} K_{22}^{-1} K_{21}$$

In designing the model the mass is physically lumped at the nodal points, the idea being to try to create a discrete mass distribution. This has been achieved except for the distributed mass of the perspex shell, which has to be kinematically lumped at the nodal points. Hence the total mass matrix consists of two parts:

$$m^* = \underbrace{m}_{\text{NODAL}} + \underbrace{\pi_s + \pi_\rho}_{\text{SHELL}\quad\text{FLOORS}}$$

The matrices π_S and π_P are shown in Appendix II, and have been evaluated using a linear variation in acceleration between the nodal points. This approximation is sufficient as the mass of the shell is only about 10% of the total mass. A higher order approximation is given in detail in Argyris[13].

For the design calculations relating to the model this shell mass was lumped at the nodes so as to keep m diagonal. The solution of the homogeneous equation of motion:

$$m\ddot{X} + K_{\beta}X = O$$

defines the 6 x 6 eigenvalue problem

$$(\lambda I - D)X = O$$

where $D = m^{-1}K$ and the solution of which yields λ, the eigenvalues, and Φ the eigenvectors respectively, typical elements of which are:

λ_i the $i^{'th}$ eigenvalue (w_i^2)

and ϕ_i the $i^{'th}$ eigenvector.

The eigenvalue problem was solved to obtain the models natural frequencies and mode shapes, using a computer iterative technique, as shown on the computer flow chart FIG. 11.

Knowing the theoretical eigenvalues and eigenvectors it is possible to decouple the 'n' degree of freedom equation of motion to 'n' single degree of freedom systems using the transformation $X=\phi q$ that is

$$m\ddot{X} + (1+ig)KX = P e^{i\omega t}$$

becomes $m_q\ddot{q} + (1+ig)\, k q = Q e^{i\omega t}$

where m_q is the diagonal generalised mass matrix $\phi^t m \phi$

k is the diagonal generalised stiffness matrix $\phi^t K \phi$

Q is the generalised force $\phi^t P$

this giving the generalised solution

$$q = h(w)\, Q$$

Thus to check that the model does in fact give measurable response at the top and close to the bottom of the building for wind tunnel tests fluctuating lift and drag coefficients obtained from Vickery[2] were used in this equation. It should be noted that this approach gives only a rough estimate of the response of the model because of

the lack of knowledge about the input forcing functions. Pursuing this analysis for varying structural stiffness, mass and damping gave bounds for the probable acceleration response of the model thereby allowing the type of accelerometer required for the model to be chosen.

The following sections will attempt to outline some of the problems the author investigated, both theoretically and experimentally, when designing the test model.

3.3 THE EFFECT OF ROTARY INERTIAS

Having neglected the effect of rotary inertias in the solution for the fluctuating forces, there effect on the dynamical model has to be shown to be negligible, that is, to show that they do not affect the models design or performance. This is done by solving the 12 x 12 eigenvalue problem where m_a includes the rotary inertias, that is solve $(\lambda I - m_a^{-1} K) X = 0$ for a 12 x 12 system.

The following table compares the first six resonant frequencies for (I) the rotary inertia neglected

(II) the rotary inertia included

(III) the resonant frequencies obtained experimentally by dynamic testing.

HZ	I	II	III
n1	13.99	13.99	15.6
n2	88.92	88.51	85.0
n3	251.50	248.80	229.0
n4	493.40	484.70	346.0
n5	790.60	775.8	437.0
n6	1055.5	1047.4	505.0

This table shows that the effect of the rotary inertias on the lower eigenvalues is not significant and validates neglecting these freedoms in the mathematical model used for finding the fluctuating forces. Note that, as expected, the additional rotary freedoms reduce the eigenvalues. The experimental results shown on column III show reasonable agreement with the theoretical results for the first three eigenvalues, but deviate for the higher eigenvalues. This is because the actual model is a thin shell structure (1mm thick) and cannot be approximated to a beam when evaluating the higher eigenvalues, and so only the lower eigenvalues are relevant because of this mathematical idealisation. Since the frequency band of interest is less than 200 HZ the neglecting of rotary freedoms is validated.

TORSIONAL EFFECTS/COUPLED OSCILLATIONS/PANEL VIBRATIONS

The first torsional natural frequency was found to be at 275 HZ and therefore does not affect the bending dynamic model in the frequency band of interest. The section ratio of the model is 2: 1·25 giving a ratio between the lift and drag resonant frequencies of 1·37: 1 this having the effect of eliminating the possibility of lift/drag coupled oscillations occurring.

Since the end conditions of the individual panels are not exactly known a first resonant panel mode of 386 HZ was found for a simply supported boundary condition, this gives a lower bound for the natural frequency which is higher than the vibration frequency of useful data, hence panel vibrations will not affect the dynamical model.

VERIFICATION OF LINEARITY

As the dynamic response of the model is used to predict the fluctuating random forces, it is important that extensive dynamic testing is carried out to establish that the model has linear dynamic characteristics and also has a sufficient degree of structural damping so as to limit excessive deflections at resonance.

The verification of linearity for the models dynamic response is verified by the application of Kennedy and Pancu's [15] technique for experimentally measuring eigenvectors, as applied to 'n' degree of freedom systems and by plotting the real and imaginary parts of the response to a constant amplitude sinusoidal input force applied using mechanical vibrators.

The dynamic test set up for this, and also for the determination of the experimental frequency response function is shown on Figure 12. A Solartron Transfer Function Analyser (T.F.A.) is used to supply a constant current to the mechanical vibrator, this being amplified through a power amplifier. The frequency and magnitude of the output signal of the T.F.A. can be varied and therefore by scanning through the frequency bands of interest, that is, around resonant frequencies, the experimental eigenvectors can be found by plotting the complex transfer function between the input vibrator force and the acceleration response. This process is repeated for all the six node points for all the various resonant frequencies using a node position selector.

The 'n' degree of freedom damped equation of motion can be orthogonalised using the undamped eigenvectors Φ , when damping is assumed proportional to stiffness.

i.e. using the transformation to a generalised system $X = \phi q$

$$M\ddot{X} + (1 + ig)KX = P e^{iwt}$$

becomes 'n' single degree of freedom systems

$$m_{11}\ddot{q}_1 + (1 + ig_1)\, k_{11} q_1 = Q_1 e^{iwt}$$

$$\vdots$$

$$m_{nn}\ddot{q}_n + (1 + ig_n)\, k_{nn} q_n = Q_n e^{iwt}$$

or in matrix terms

$$m_q \ddot{q} + k_{qc}\, q = Q e^{iwt}$$

where m_q k_{qc} Q are the generalised mass, complex stiffness, and generalised force matrices respectively.

At close to the i 'th resonance the transformation

$$X = \Phi q$$
$$= \Phi_i q_i + B_i$$

where B_i is a column of constants due to the effect of the higher modes

choosing the k'th nodal response

$$X_{ik} = \phi_{ik}\, q_{ik} + B_{ik}$$

$X_{ik} - B_i = X'_k = \phi_{ik} q_{ik}$ and ϕ_{ik} is constant around resonance giving X^1_{ik} the response of the model proportional to q_{ik} at the i'th resonance.

For a single degree of freedom system

$$m_{11}\ddot{q}_1 + (1 + ig_1)\, k_{11} q_1 = Q_1 e^{iwt}$$

the solutionfor the displacements is

$$q_1 = \frac{Q_1}{K_{11}} \left(\frac{1 - \beta^2}{(1 - \beta^2)^2 + g_1^2} + \frac{i \cdot - g_1}{(1 - \beta^2)^2 + g_1^2} \right)$$

$$= R + i\, I \qquad \text{where} \qquad \beta = \frac{w}{w_i}$$

and since $X_1 \alpha q_1$, plotting thereal and imaginary parts of the response around resonance forms a response locus for the individual node point concerned. The point of resonance on the nodal loci is defined where a line joins the centre of the circle to the point where

$$\frac{d\left(\frac{q_1}{Q}\right)}{d(\beta^2)} \text{ is a minimum, or where } \frac{d(S)}{d(\beta^2)} \text{ is a maximum}$$

S being the arc length between increments in frequency.

The ratios of the diameters of the circles are the experimental eigenvectors Φ_{e_i} for resonance in the i^{th} mode. This process can be repeated by plotting the response loci for the modes of interest thereby obtaining the complete experimental eigenvector matrix Φ_e .

Using the T.F.A. as outlined earlier in this section, these experimental eigenvectors were plotted for the 1st six modes and the 1st four modes are shown on FIGS. 13 to 16. Each family of plots have a tabulated comparison between the experimental and theoretical eigenvectors (derived in section 3.2), furthermore, the damping variation between node points indicates how the damping changes heightwise. With reference to LAZAN[17] the non-dimensional damping coefficient or loss factor g for perspex is quoted as being 0(0.08) this being related to critical damping by $g = 2C = \left(\frac{\Delta w_i}{w_i}\right)_{3\ dB}$ that is the change in frequency between the 3dB or $\frac{1}{2}$ power points in the i^{th} mode of vibration. From the results plotted on Figures 13 to 16 the damping coefficient in the bending modes is found to be much lower than this value. Figure 17 shows how the non-dimensionalised damping coefficient varies from mode to mode and it appears that the damping is greatest in the second mode of vibration when $g = 0.045$ compared with approximately 0.025 for higher modes.

Small non-linearities in a structure can cause distortion of the response loci plots, while large non-linearities cause jumps, and the frequency at which these jumps occur varies depending on whether the frequency is increasing or decreasing. Since the response loci for all stations, and for all these modes of vibration as shown on Figures 13 to 16 show no traces of these effects the model is considered to have linear dynamic characteristics within the frequency band width of interest.

It should be noted that generally structural or hysteretic damping is not necessarily totally proportional to stiffness and can in fact be proportional to a combination of both the mass and stiffness matrices. However, the representation of the structural damping in simple beam like structures can be expressed in the form:

$$M_i(w) = \frac{EI}{y} (1 + ig(w)) \hat{\mathcal{E}}_i(w)$$

that is, in the simple form used in the equation for evaluating the fluctuating forces. The effect of the presence of higher modes is to some degree of greater importance than obtaining a more exact definition of the mechanism of damping, although the definition as expressed in the equation above is in a generally accepted form.

HIGHER MODES AND DAMPING

When considering the problem of the models structural damping characteristics the presence of the higher modes of vibration can be shown to be important. This effect is discussed by Hitchings[21], and as already outlined the response around the $k^{'th}$ resonant frequency at the $i^{'th}$ nodal point is given by:

$$x_{ik} = \phi_{ik} q_{ik} + B_{ik}$$

The effect of the higher modes is represented by the presence of the B_{ik} term, and this term effectively shifts the focal point of the response circle from the origin to some other position depending on the degree of their effect. Figure 14 shows the six response circles for the second mode of vibration, the dotted circle represents the position of the circle as measured for station 1. This shift can vary from station to station for any natural mode. The effect of higher modes is generally less pronounced at lower frequencies, for example, the first mode of vibration remains to a greater degree unaffected by the presence of the higher modes.

This phenomenon has important implications when trying to predict a force whose frequency is coincident with a resonant frequency, in that the fluctuating force is not only doing work against the damping term but also against the real part of the response due to the higher modes, and this in general tends to help the accuracy of predicting a resonant fluctuating force.

ORTHOGONALITY OF THE EXPERIMENTAL EIGENVECTORS

Having determined the experimental eignevectors Φ_e it is interesting to check if they possess the orthogonality property of $\Phi_e^t \Phi_e \propto I$. The $\Phi_e^t \Phi_e$ matrix is shown in Appendix II, and indicates that the experimental eigenvectors are close to being an orthogonal set as the first five columns have off diagonal terms of magnitude 0 (10% of diagonal value), where most elements are generally less.

3.4 FORMATION OF THE EXPERIMENTAL FREQUENCY RESPONSE FUNCTION $H(\omega)$

The experimental technique previously discussed in Section 3.3 can be extended to find the experimental frequency response function $h_q(w)$.

Considering the generalised system defined by the transformation

$$X = \Phi q$$

the generalised frequency response function is defined in terms of the generalised mass m_q , stiffness k_q , and damping matrix $g \cdot k_q$. Section 3.3 outlined how to find the experimental eigenvectors Φ_e.

If the generalised mass matrix can be found, k_q follows from:-

$$k_{qii} = w_i^2 \, m_{qii}$$

and $$K = \Phi^{-t} \cdot k_q \cdot \Phi_e^{-1}$$

and $$m_e = \Phi^{-t} \cdot m_q \cdot \Phi_e^{-1}$$

and since damping is assumed proportion to stiffness the experimental frequency response function $h_q(w)$ can be found.

To find the experimental generalised mass matrix nodal masses are added and the variation in resonant frequency observed.

$$w_i^2 = \frac{k_{qii}}{m_{qii}} = \lambda_i$$

$$w_i'^2 = \frac{k_{qii}}{m'_{qii}} = \lambda'_i$$

$$m'_q = \phi^t \, m' \, \phi$$

$$\lambda_i - \lambda'_i = k_{qii}\left(\frac{1}{m_{qii}} - \frac{1}{m'_{qii}}\right)$$

and using $k_{qii} = \lambda' m'_{qii}$ substituted into (1) gives

$$\left(\frac{\lambda_i}{\lambda'_i} - 1\right) = \frac{\Delta m_{qii}}{m_{qii}} = \frac{\phi_{ei}^t \, \Delta m \, \phi_{ei}}{\phi_i^t \, m \, \phi_i}$$

where Δm is the added mass matrix, hence knowing λ_i, λ'_i for this added mass m_{qii} can be found from

$$m_{qii} = \frac{\phi_{ei}^t \, m \, \phi_{ei}}{\left(\frac{\lambda_i}{\lambda'_i} - 1\right)} \qquad \text{for each mode}$$

The following table shows a comparison between the theoretical and experimentally determined generalised mass matrices.

MODE No.	$\phi_t^t m \phi_t$	$\phi_e^t m \phi_e$	m_{eq} experimental
1	·00159	·00161	·00164
2	·00253	·00277	·00273
3	·00233	·00282	·00252
4	·00285	·00240	-
5	·00229	·00276	-
6	·00298	·00208	-

The third column gives the values obtained using the theory above, for the higher modes 4, 5, 6 it was experimentally impossible to obtain a large enough change of frequency to estimate the higher mode terms, but for the 1st three modes the mathematical and experimental modes are in good agreement. Thus knowing the experimental eigenvalues λ_e, eigenvectors ϕ_e and generalised mass m_{eq}, the complete frequency response function $H_e(w)$ can be found.

3.5 GALLOPING OSCILLATIONS

To ensure that the model does not experience galloping oscillations during wind tunnel tests the models lift displacement response is checked against Novaks stability criteria. These calculations are made to verify that the lift displacement response remains in the stable regime for all windspeeds, that is, to preclude galloping response from the analysis. Novaks[11] stability diagrams for the 2:1 and 1:2 section aspect ratios for smooth and turbulent flow are shown plotted in terms of the universal galloping amplitude $\bar{a} = \frac{m_n a}{\beta}$ and universal galloping velocity $\bar{U} = \frac{m_n}{\beta} U'$ in Figures 66 and 67.

Where Mn, β, a, U^1 represent the non-dimensional mass, damping, displacement and reducedvelocity, respectively.

These plots were plotted from the results of the application of Parkinson's quasi steady theory by Novak to these rectangular sections and their validity verified by experiment.

The non-dimensional parameter involved are:

$$m_n = \frac{\rho D^2 \ell}{4m}$$

$$= 0.67 \times 10^{-3}$$

β (damping ratio) $= \frac{0.033}{2} = 0.0165$ (1st mode)

this gives the universal parameters for the present model as

$$\overline{U} = 0.0039\ U \qquad (U \text{ in ft/sec})$$

and $\overline{a} = 0.041 \frac{Y}{D}$ where Y is the peak lift displacement response.

These being for the 1:2 model i.e., the small face windword. The bands of values for $\overline{a}$ v $\overline{U}$ for the present wind tunnel tests are shown superimposed on Novaks stability diagrams for comparable aspect ratios, for both sections in smooth and turbulent flow. For the 1:2 sections as shown on Figure 66, the section is always stable in turbulent flow, and in smooth flow it would require to oscillate with an amplitude greater than 40 times the actual amplitude it experiences in the present wind tunnel tests, for there to be any tendency towards galloping. Similar results are shown on Figure 67 for the 2:1 section and it remains aerodynamically stable for all reduced velocities. Thus the model is stable and does not exhibit any tendency to gallop in wind tunnel tests.

AERODYNAMIC DAMPING

Closely related to the phenomenon of aeroelastic instability is the degree of aerodynamic damping created by the bodies motion in the wind. Since the section does not gallop in the lift direction the effect of aerodynamic damping for this direction is presumed to be small compared with the structural damping.

The aerodynamic damping force for the model vibrating in the drag direction can be found from the total aerodynamic force

$$A_D(t) = \tfrac{1}{2} \rho C_D \ (U - \dot{X}_i)^2 + \underbrace{Cm\ \rho\ D^2\ (-\ddot{X})}_{\text{Virtual Mass Term}}$$

giving the velocity dependent aerodynamic damping term

$$A_{D\dot{x}_i}(t) = \rho C_D \; D \; U \; \dot{X}_i$$

which gives the logarithmic decrement of aerodynamic damping of

$$\delta_a = \frac{\rho C_D \; D \; U}{M \; 2 \; w_i}$$

where M is the mass /unit length $\frac{0.26}{3.142} \cdot \frac{12}{32.2}$ lbm/ft

ρ air density (0.00238 slugs/ft^3)

C_d drag coefficient ($\doteq$ 1.0)

ω_i circular natural frequency (2π x 15.6)

D wind ward dimension (ft) $^{2.0}/_{12.0}$

U wind speed (ft/sec) (100 ft/sec)

$$\delta_a = 0.00656$$

$$\therefore g_a = 0.0021 << \; g \text{ structural}$$

Thus the aerodynamic damping term is negligible compared with the minimum structural non-dimensional damping factor of 0.025.

3.6 CONSTRUCTION DETAILS

The following description together with the engineering drawings and photographs in Appendix III give the complete details relating to the actual construction of the wind tunnel model.

The construction of the shell is shown on Figure 2. The shell is continuous with transverse stiffeners to maintain its rectangular section of 50mm x 31mm. Built into the shell are six lead masses 80mm apart weighing approximately 135 grams each as shown on Detail 2, Figure 3. The shell is made of 1mm thick perspex while the transverse panels are 2mm thick. Each floor containing a mass has two in-built accelerometers and these have been positioned so as to decouple the X (translational) and θ (rotational) motions: one of these accelerometers measures lift accelerations and the other drag accelerations, as shown on the plan Detail 1 on Figure 3.

Intermediate transverse panels are used to reduce the effect of panel oscillations. The base of the 1mm thin shell is reinforced with 2mm thick perspex to stop cracking around the holes at the bottom of the model when the clamp plates (Detail 5, FIG. 4) are tightened. The core block, shown on Detail 4, FIG. 5, is accurately fitted to inside of the bottom of the shell, so that when the clamp plates are tightened no severe bending occurs.

With such a thin shell a "jig" was required to ensure panel alignment and fixing during the model assembly and glueing stages. The model is shown fixed in the jig on photograph FIG.9.

Semi conductor strain gauges were glued to both the inside and outside of the model. The internal wiring required was fixed at each floor level, the wires running to the bottom of the model where they leave through a central hole.

The model sits on a rigid mounting consisting of a circular pipe with end plates as shown on Figure 5 and the general arrangement of the complete assembly used for all wind tunnel tests is shown on Figure 6. The model and mounting are attached to a rotary table on a 1-Ton seismic mass isolated from floor vibrations by springs, this giving a natural frequency of the complete assembly of less than 2 HZ.

A photograph of the 30mm side of the model during its construction stage showing the 1mm thick shell together with the 2mm transverse panels supporting the lead spheres and some internal wiring is shown on Figure 7. The details of the lead sphere and accelerometer connections for a typical floor are shown on the photograph Figure 8.

To obtain the accurate dimensions of the model it was set in a jig as shown on Figure 9 during assembly.

The model was tested in the Department of Aeronautics 5 ft. x 4ft. working section wind tunnel and a photograph of the model protruding through the floor of the tunnel is shown on Figure 10. The dimensions of the model were chosen to keep the length scale of the grid induced turbulence greater than D, a typical width of the model. The longitudinal length scale of turbulence was L_x = 78mm, and the transverse scale L_y = 38mm these being obtained from the cross correlation coefficients obtained from two hot wire probes in the far wake, generated by a 6 inch square grid at the beginning of the working section.

Therefore the following turbulent scale parameters apply to all tests:

(i) for the 31mm side windward, $L_x/D = 2.4$ and $L_y/D_1 = 0.75$ this having an aspect ratio of 15.6 and section ratio 1 : 2.

(ii) for the 50mm side windward, $L_x/D_D = 1.5$ and $L_y/D_1 = 1.24$ this having ar aspect ratio of 9.8 and section ratio of 2 : 1

From the power spectrum of the 'u' component of velocity fluctuations the turbulent intensity $\frac{\sqrt{\overline{u}^2}}{U}$ was found to be 0.065.

Using perspex as the shell material has three other important advantages, these are:-

(i) its bending damping ratio is relatively high at approximately 2% critical, this reducing any effect aerodynamic or acoustic damping may have.

(ii) The high damping also reduces the tendency for the section to gallop, as already discussed, making it aerodynamically more stable. The research outlined in Scruton[12] and Novak[9, 10, 11] emphasise the importance of structural damping in stability calculations.

(iii) The high damping spreads the power in the response spectrum about the resonant peaks thereby improving the prediction of the force spectrum at frequencies between resonant frequencies.

3.7 STRAIN GAUGE ARRANGEMENT

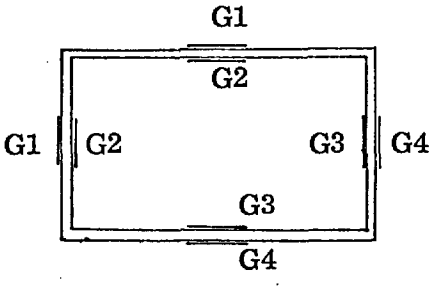
A full 4-strain gauge bridge was used in the configuration as shown in Diagram A below. The semi conductor strain gauges have $^{3}/_{8}$" long silicon filaments with a strain gauge factor of 110 and resistance 350 Ω . When adhesing these gauges to both the inside and outside of the shell to measure bending strains, the final length and therefore resistance varies randomly with a possible out of balance resistance across the bridge of ± 10%. The bridges were balanced using 5 - external potentiometers, 5 - SE Laboratories strain gauge amplifiers type SE 905.

The absolute sensitivity factor is relatively unimportant as the bridge is calibrated by applying known bending moments.

i.e., $K = \frac{M}{\Delta V}$ for all 10 sets of gauges,

and for each gain setting on the amplifiers.

The full bridge with gauges and wiring on both inside and outside of the shell (as shown below) minimises the effect of small panel bending strains.



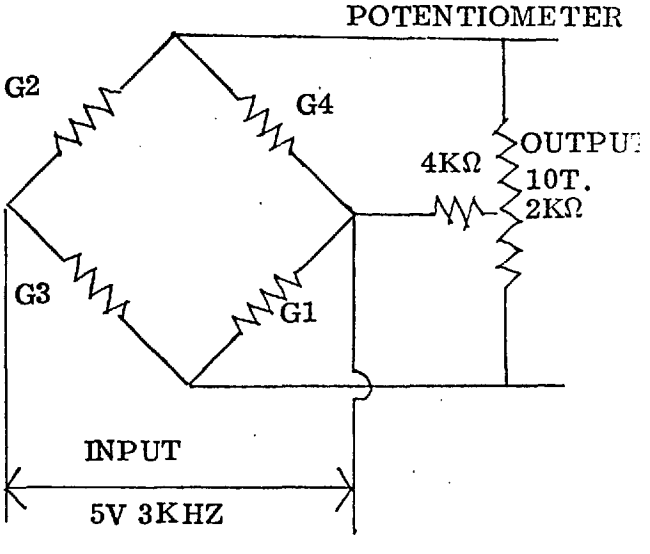
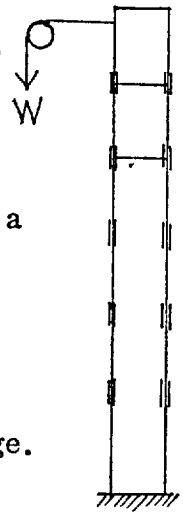


DIAGRAM A.

STRAIN GAUGE CALIBRATION

The strain gauge calibration required is in the form $M_i = k_i \Delta V_i$, where k_i relates the change in output voltage in terms of the applied moment. A fine steel wire was attached to the weight W, and using a high quality low coefficient of friction pulley, applied to the model using a knife edge connection. The change in voltage ΔV_i was recorded on a D.V.M., and this was repeated 10 times and the values of ΔV_i averaged. In most cases the drift was 0(1%), and consistent results were obtained for each sample. This calibration was repeated for each strain gauge bridge.



VERIFICATION OF E.T.B.

To check that as the load W is applied closer to the strain gauges the output remains linear, a plot of $\frac{M_i}{\Delta V_i}$ v Z was made; Z being the height in inches above the gauge to the load applied. FIG. 33 indicates that the output voltage is linear with Z.

THE IMPORTANCE OF RELATING PHASE

There are two basic electronic instruments used:

1. S.E. Laboratories strain gauge amplifiers type SE 905.
2. Birchals charge amplifiers.

The dynamic strain signals are time shifted approximately 500μ secs. relative to the acceleration, by the constant time delay filter in built onto the output of the strain gauge amplifier. This phase error has to be compensated for as the relative phase between the dynamic strain and acceleration signals is important. There are two possible ways of achieving this depending on whether the solution for the dynamic force **P** is in the time or frequency domain. If the 5-acceleration signals are digitised simultaneously at 2 Ks/sec, then by shifting the strains by 1-digit, relative to the acceleration, this will be equivalent to a constant time shift of 500μS . Since an effective Nyquist frequency of 0(300 HZ) is required, this entailed

using only about $\frac{1}{3}$rd of the useful data. This is inefficient and increases computing time considerably since each 12 BIT word has to be unpacked into CDC 6400 60 BIT words. An alternative approach is to sample at 600 s/sec (giving n_q = 300 HZ), and applying a vector rotation on the strain complex Fourier coefficients.

$$\mathcal{E}'(w) = T\,\mathcal{E}(w)$$

where

$$T = \begin{bmatrix} \cos\phi & \sin\phi \\ -\sin\phi & \cos\phi \end{bmatrix}$$

where ϕ is the phase shift due to the strain gauge amplifiers filters. Obviously this approach is only valid for a frequency domain solution.

3.8 ACCELERATION CALIBRATION

This calibration checks the accuracy of the Birchal charge amplifiers in measuring absolute g's for various gain settings. The test rig is used by the Department of Mechanical Engineering to calibrate accelerometer/charge amplifier systems. The test rig used is outlined in diagram B. It uses a heavy duty vibrator which moves vertically upon which the accelerometer is rigidly bolted down. The accelerometer mounting has lines etched at 2, 5, 10, x 10^{-3} inches. The vibrator is driven by an oscillator and power amplifier, the frequency being checked by a counter. A telescope is used to observe the stroboscopic super-position of the etched lines, at the chosen amplitude.

The acceleration is then $\ddot{X}_o = w^2 x_o$. A calibrated accelerometer of known sensitivity was used.

The r.m.s. output of each channel was then compared with the absolute acceleration for all 5 channels used. A typical result is shown on Table C for 1g, 3g, 10g, 30g, and 100g gain settings. The 1g, 10g, 100g settings are correct but the 3g, 30g, settings are about 7% in error, indicating that these outputs are closer to $\sqrt{10}$ and $\sqrt{1000}$. This compensation was allowed for in all test results.

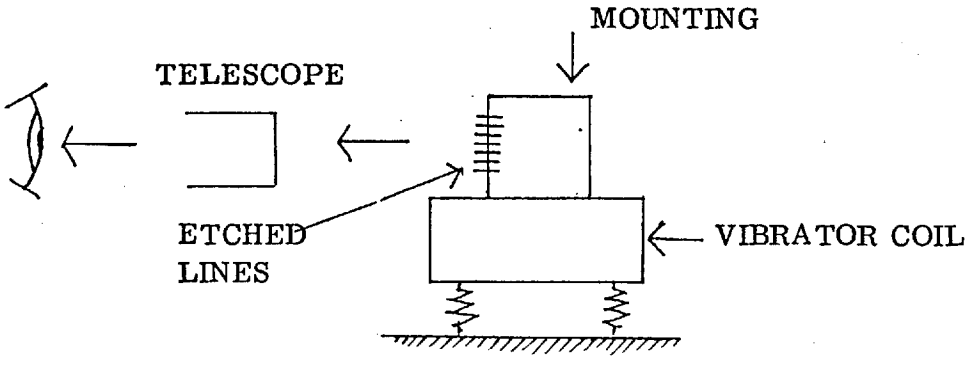


DIAGRAM B

CH. NO.	ERROR $\ddot{X}_o / \ddot{X}_m$				
1	1g	3g	10g	30g	100g
	1.004	1.074	1.007	1.074	1.00

TABLE C

3.9 STATIC TESTS

To check the accuracy of the strain gauge calibration, and model geometry static tests were carried out i.e. $\ddot{X}(ti) = O$

Consider equation (iv) section 2.0,

$$P(ti) = A^* M(ti) + B^* \ddot{X}(ti)$$

giving $P = A^* M$ (i)

then by applying a known static load at a known point, and by measuring the change in voltage outputs at all 5-stations with the corresponding calibration factors, an estimate of the applied load distribution can be found (See Table D).

	ACTUAL LOAD DISBN	PREDICTED FROM i	ERROR %	ΔV_i
P1	.8987	0.9014	0.3	0.383
P2	0.0	- 0.0114	1.27	0.500
P3	0.0	0.0137	1.52	0.666
P4	0.0	0.0170	1.89	1.021
P5	0.0	0.0068	0.76	1.126

TABLE D

The above values were computed by putting $\ddot{X} = 0$ into the program outlined in flow chart FIG. 21 used for the dynamic testing of equation above. This shows how the known bending moment distribution can be used to find the load distribution accurately. The static load was applied at the top nodal mass giving A^* conditioning similar to equation (ii) section 2.3. This approach can be extended further to include the inertia terms $B^*\ddot{X}$ and this is done by using the T.F.A. to measure the Fourier Coefficients for individual frequencies for $\ddot{X}(w)$, $\mathcal{E}(w)$ and solving for the input force $P(w)$. The next section deals with this analysis.

TRANSFER FUNCTION ANALYSER/DISCRETE FREQUENCY TESTS

The solution of equation (v) section 2.0 has four main sources of error.

$$P(w) = A^* G(w) \mathcal{E}(w) + B^* \ddot{X}(w) \qquad (v)$$

(i) errors associated with the calibration of $M(w)$, $\ddot{X}(w)$

(ii) the effect of these errors (i) on $P(w)$ due to the conditioning of A^*, B^*

(iii) phase errors between $\mathcal{E}(t)$ and $\ddot{X}(t)$

(iv) errors due to the magnitude of the difference between the inertia and stiffness contributions. e.g., at resonance the difference is much smaller than off resonance.

To investigate how well the technique predicts the distribution of fluctuating forces a point sinusoidal force was applied at the top mass using a vibrator. The Transfer Function Analyser excites the vibrator and the complex Fourier coefficients of $\mathcal{E}(t)$, $\ddot{X}(t)$ found relative to the phase of the input force. The output from the force transducer is calibrated with respect to the output from the T.F.A. to get the actual input force P_{input} with the correct phase. The Fourier coefficients of $\mathcal{E}(t)$ and $\ddot{X}(t)$ were calibrated and used to predict the magnitude and distribution of P for various discrete frequencies including resonance, using the computer program as outlined in the flow chart FIG. 21.

To investigate the relative contributions from strain and acceleration in the predicted force equation (v) is re-written as

$$P_{PRED} = P_{\ddot{\varepsilon}} + P_{\ddot{X}}$$

Table 1 in Appendix II shows the P input measured together with $P_{PRED} = P_{\ddot{\varepsilon}} + P_{\ddot{X}}$ for various frequencies.

OFF RESONANT RESULTS

The average percentage error between the actual and predicted forces for the top 4 stations is 0 (6%) and if the top 5 stations are considered o(10%), although generally the error in force 5 is higher than the other errors. (see Table 1 Appendix II).

RESONANT RESULTS

Here there is reasonable agreement for the top 3 stations but lower down the model larger errors occur than in the off resonant case. The main reason for this is that at resonance both inertia and stiffness contributions are much larger for an equivalent force off resonant, and consequently the effect of errors is larger. Furthermore, the inertia and stiffness terms tend to cancel out each other, this being typical of resonant systems.

The technique is tested further by making the input forcing function a random force and using the computer programs discussed in Appendix I, to predict the input force spectra.

3.10 PREDICTION OF KNOWN RANDOM AND HARMONIC INPUTS

To prove that the technique works for random loads, the model was dynamically vibrated with known random loads applied using vibrators as shown in Diagram D. The superposition of the predicted and actual force spectrum allows a direct comparison between them.

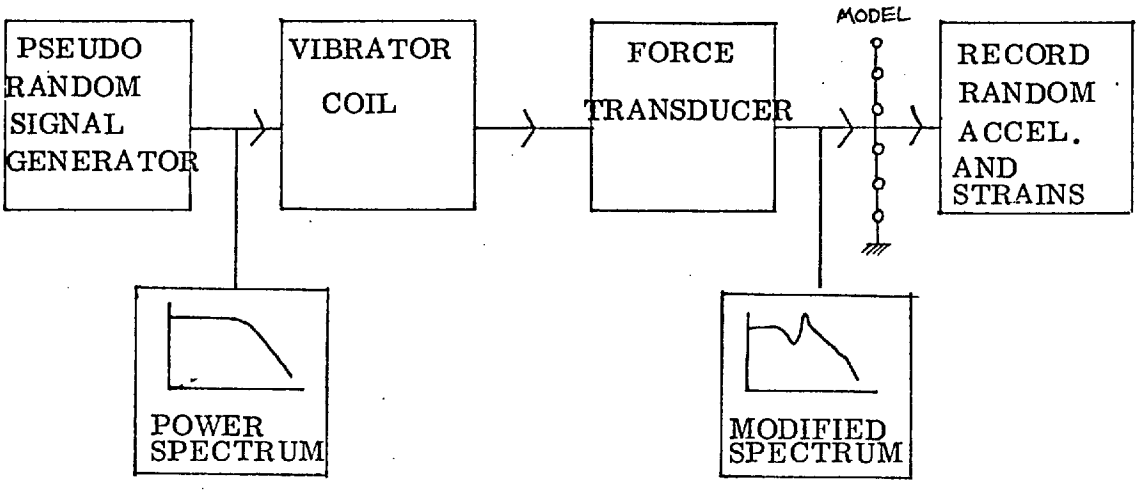


DIAGRAM D - DYNAMIC TEST SET UP

The photograph FIG. 25 shows how the vibrator with attached force transducer is mounted rigidly to the model via small perspex pads located at the transverse panels. The Solartron Pseudo Random Signal Generator signal output has a flat power spectrum. This output is amplified and drives the vibrator which is attached to the model via a KISLER force transducer. The output from the force transducer together with the 5 acceleration and 5 strain signals were recorded on an Ampex FR 1300 analogue tape recorder (see FIG. 22). This data is then analysed using the same computer program that predicts wind tunnel test fluctuating loads, to give a comparison between the actual and predicted force power spectrum. The computer analyses is outlined in Appendix I and the corresponding flow charts on FIG. 23 and FIG. 24 which deal with the data gathering and computing techniques.

The mass of the vibrator coil and attachments introduces a random inertia force that can considerably modify the flat power spectrum, depending on the displacement of the model at the point where the force transducer is connected. The effect of this added inertia force is shown in the difference between FIG. 26 and FIG. 27. FIG. 26 shows close agreement between the actual and predicted force power spectrum at Station 1. FIG. 27 and FIG. 28 show a different modified input force spectrum at Station 1, together with the coherence and phase between the actual and predicted spectra.

Ideally the coherence should be unity and phase zero in the band width of interest. There is a degree of incoherence near the resonant frequency and slight change in phase (see FIG. 28). For a sinusoidal force at Station 1, resonant with the 1st lift structural frequency giving results on FIG. 29 and FIG. 30, there is good agreement between the actual and predicted force spectra.

The random force test was repeated at a position between Stations 2 and 3, that is on the second top element, and again good agreement was obtained between the results as shown on FIG. 31 and FIG. 32.

SUMMARY OF DYNAMIC FORCE PREDICTION RESULTS

The results for the prediction of the distribution of forces as shown on Table 1 Appendix II indicate that the technique allows the accurate prediction of the fluctuating forces on the top four elements of the structure.

The prediction of the distribution of the fluctuating forces is better at frequencies away from resonant frequencies as shown in Section 3.9.

The technique can predict the power spectra of fluctuating random forces giving good agreement with the measured power spectrum.

The magnitude of the errors in the predicted force is associated with errors in the experimental measurement of response and also on the conditioning of the $\mathbf{A}^*$, $\mathbf{B}^*$ matrices.

The prediction of the random load spectra using the wind tunnel computer programs validates their use for wind tunnel data.

4.0 AERODYNAMIC RESULTS

A total of eleven sets of wind tunnel recordings were analysed to obtain the distribution of fluctuating lift and drag forces and their cross correlation coefficients together with the corresponding nodal displacements.

The data gathering and computing techniques used to evaluated these quantities are discussed in detail in Appendix I.

The results have been subdivided into two sections, one section in table 1 Appendix III dealing with seven sets of results, where five of these relate to the fluctuating lift forces when the vortex shedding frequency is away from structural resonance, the remaining two sets dealing with fluctuating drag forces in turbulent flow. The second section in Table 2, Appendix III deals with the special cases where the fluctuating lift force frequency is resonant with the 1st and 2nd natural frequencies, and contains four sets of results.

Tables I and II also show the r. m. s. nodal displacements ($\sqrt{\overline{x_i^2}}$) and the values of $\sqrt{\overline{C_{LF}^2}}$ and $\sqrt{\overline{C_{DF}^2}}$ which represent the integrated lift and drag shear force coefficients obtained from the distribution of forces, together with the corresponding integrated value obtained from Vickery[2]. The tables further cross reference the figure numbers for the plots of the force spectra and corresponding cross correlation coefficients.

The following table shows the six flow conditions for which the fluctuating forces can be found

	LIFT		DRAG
ASPECT RATIO 9.8	SMOOTH	TURBULENT	TURBULENT
ASPECT RATIO 15.6	SMOOTH	TURBULENT	TURBULENT

Thus Table I Appendix III shows the results for these permutations for 'non resonant conditions', and table 2 for 'resonant' conditions, and for both cases the fluctuating drag coefficient in smooth flow was found to be negligible.

4.1 COMPARISON OF RESULTS WITH VICKERY

There is no published work known by the author that presents the distribution and cross correlation coefficients of the fluctuating aerodynamic forces up a flexible structure. The only quantitative values for the fluctuating lift and drag force coefficients found by a literature survey are in Vickery[2] which deals with turbulent flow only. There is no published work on the fluctuating forces for three dimensional building structures in smooth flow. Vickery[2] suspended building models of various sizes with different section and aspect ratios in a water tunnel and used a dynamometer at the bottom of the building to measure the integrated aerodynamic lift and drag shear forces.

To compare the results obtained for the distribution of forces from the present test with the integrated force representing them for comparison with Vickery, a statistical addition has to be made.

Consider the distribution of forces to be on 'n' elements then the total force is given by :

$$P_{FT}(t_i) = P_{F1}(t_i) + P_{F2}(t_i) \cdots\cdots P_{FN}(t_i)$$

then the mean square value is given by the time averaged square that is

$$P_{FT}^2 = \overline{(P_{F1} + P_{F2} + \cdots P_{FN})^2}$$

As already outlined in a previous section the matrix of cross correlation coefficients is given by :

$$R(o) = \overline{P\ P^t}$$

where $P = \{ P_{F1} \quad P_{F2} \cdots\cdots P_{FN} \}$

then the mean square is given by

$$\overline{P_{FT}^2} = \sum_{i=1}^{N} \sum_{j=1}^{N} R_{ij}(o)$$

hence the magnitude of the integrated fluctuating shear force is dependent on the cross correlation coefficients and distribution

of the elemental fluctuating forces.

In terms of the non dimensional aerodynamic force coefficients,

$$\overline{C_{FT}^2} = \frac{\overline{P_{FT}^2}}{(\frac{1}{2}\rho U^2 A_T)^2} = \frac{\sum_{i=1}^{N}\sum_{j=1}^{N} R_{ij}(o)}{(\frac{1}{2}\rho U^2 NA_e)^2}$$

where Ae is the area of an element and A_T is the total area equal to N. Ae.

This equation can be reinterpreted as

$$\overline{C_{FT}^2} = \frac{1}{N^2}\sum_{i=1}^{N}\sum_{j=1}^{N} C_{ij}(o) \qquad (1)$$

where $C_{ij}(o)$ represents the non dimensional elemental shear force coefficient.

Now consider, for example, the two extremes of zero cross correlation and unity cross correlations with all the elemental forces equal, then

$$\sqrt{\overline{C_{FT}^2}} = \frac{1}{\sqrt{N}} \cdot \sqrt{\overline{C_{Fe}^2}}$$ for zero correlation between the aerodynamic forces

and $$\sqrt{\overline{C_{FT}^2}} = \sqrt{\overline{C_{Fe}^2}}$$ for unity correlation between the aerodynamic forces

Thus for zero correlation between four elements

$$\sqrt{\overline{C_{FT}^2}} = \frac{1}{2}\sqrt{\overline{C_{Fe}^2}}$$

i.e the integrated force coefficient is half the elemental one.

This explains why the fluctuating force coefficient obtained from Vickery's tests for the integrated shear force coefficient is generally lower the individual elemental force coefficients obtained from present tests, the difference being dependent on the cross correlation between the elemental forces.

To obtain a comparison between the distribution of forces obtained from present tests and Vickery's integrated results, the distribution and cross correlation coefficients were used in equation (1) above to obtain the integrated aerodynamic force coefficients. These are tabulated together with Vickery's values on Table I Appendix III. In this table Vickery's values have been redimensionalised with respect to the lift area.

It should be noted that the integrated forces presented for the present tests relate to the top four elements of the model, and ideally the correct comparison with Vickery should be for the top six elements, that is, over the total length of the structure, however, it was found by the author that introducing these forces had little effect on the integrated value for the force coefficient, for example, for turbulent flow forces at reduced velocity $U/n_1D=14.0$ gave $\sqrt{\overline{C_{LF}^2}} = 0.42$ for the top five elements compared with $\sqrt{\overline{C_{LF}^2}} = 0.41$ for the top four elements. This calculation is shown in Appendix II, where the cross correlation matrix is shown.

Vickery presented the variation of the integrated fluctuating lift and drag coefficients $\sqrt{\overline{C_{LF}^2}}$ and $\sqrt{\overline{C_{DF}^2}}$ with aspect ratio, for fixed section ratios. These have been reinterpreted and replotted as a variation with section ratio for the two fixed aspect ratios of 9.8 and 15.6 and are shown on Figures 42 and 43. The values obtained from equation (1) above for the present tests have also been plotted for comparison.

For both aspect ratios there is very good agreement for the corresponding integrated lift and drag coefficients $\sqrt{\overline{C_{LF}^2}}$ and $\sqrt{\overline{C_{DF}^2}}$ with Vickery. These results are discussed in greater detail in the following results.

4.2 AERODYNAMIC RESPONSE : ASPECT RATIO 15.6

Figure 34 shows the variation in the lift acceleration response and Strouhal number with wind speed (U) for smooth and turbulent flow. It shows how the models 1st and 2nd resonant modes, can be excited by the vortex shedding lift force as indicated by the two marked peaks at 18ft./s and 98ft/s. The acceleration response varies with wind speed depending on the node point chosen, for example node point 4, marked 0, has a small acceleration response at the firstmode wind speed, while conversely, it becomes the largest acceleration response at the second mode wind speed. Node point 2 however, has a large acceleration at the 1st mode but has a small response relative to the other nodes at the second mode. Thus it is seen how for various wind speeds the acceleration response consists of a combination of the models eigenvectors. Figure 35 shows a typical lift displacement spectrum for station 1 (top of model) for the reduced velocity $U/n1D = 35$ where $n1$ is the first lift natural frequency, and as expected most of the displacement comes from the fundamental mode of vibration, this being typical of most wind tunnel tests. At around the Strouhal frequency $nD/U = 0.1$ the lift displacement spectrum shows the interesting feature of two vortex shedding frequencies one at $\frac{nD}{U} = 0.1$ and the other at $\frac{nD}{U} = 0.08$. This phenomenon reflects itself in the corresponding predicted force spectra and shall be discussed in section 4.3

Four sets of data were recorded at wind speeds corresponding to the arrowed positions (↑) on the U axis as shown on Figure 34. i.e for $U/n1D = 11.25,\ 35.0,\ 48.4,\ 60.6$, and these analysed to predict the fluctuating aerodynamic forces and their cross correlations. Two of these sets of recordings correspond to the vortex shedding frequency coincident with the first and second natural frequencies.

The effect of free stream turbulence in this case is to induce shedding over a broad band of frequencies, and consequently the sharp peak at resonance as exhibited in Figure 34 for smooth flow is evened out as is shown on Figure 36 for turbulent flow.

Base pressure measurements taken on the rear face of the model gave an increase from $C_{PB} = -0.73$ to $C_{PB} = -0.64$ at the top of the model and from $C_{PB} = -0.85$ to $C_{PB} = -0.53$ at close to the bottom station in turbulent flow. This increase in base pressure is similar to the effect first observed by Vickery[3] for tests on a two dimensional square section in that less static drag was found when there was turbulence present in the free stream. The effect of turbulence on the fluctuating lift displacement spectrum is shown on Figure 37, and most of the displacement still comes from the fundamental mode of vibration with small contributions from the higher modes as shown by the peaks at higher frequencies. The spectrum of the response is, however, wider as the first four modes of vibration have been excited, as well as the first natural torsional mode. Hence for this turbulent case the vortex shedding is not as strong at the Strouhal frequency as in the smooth flow.

Two sets of data were recorded and analysed for the reduced velocities $U/n1D = 8.8$ and $U/n1D = 15.0$ for turbulent flow. The corresponding drag response for the turbulent flow condition is shown on Figure 38. Since there are no peaks in the drag acceleration response for the wind speed range obtained in wind tunnel tests, the fluctuating drag force appears to be random in nature with little or no harmonic components from vortex shedding. The dotted line on Figure 38 corresponds to a slope of 2 and shows how the forcing function increases approximately with U^2 as the response line has a slope of 2.

One set of data was recorded for the turbulent drag fluctuations at the reduced velocity $U/n1D = 38$, and these were analysed to find the fluctuating drag forces.

AERODYNAMIC RESPONSE : ASPECT RATIO 9.8

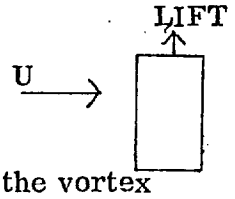
Considering the model with its bluff face windward, in smooth flow there does not appear to be continuous periodic vortex shedding and the models response occurs in bursts as is shown from the acceleration trace on Figure 39. This is accompanied with very small r. m. s.

values of lift acceleration, although during a burst they become instantaneously large. The base pressure at the top station of the model $C_{PB} = -0.62$ and at the bottom station $C_{PB} = -0.9$ indicating that there is less drag at the top than at the bottom of the model. One set of data was recorded for the reduced velocity $U/_{n1D} = 22.4$ and analysed to find the fluctuating lift force distribution for smooth flow.

In turbulent flow the family of acceleration response plots, Figure 40 is very interesting in that the lift acceleration has a marked peak where the shedding frequency coincided with the lift structural frequency, and this response is much larger than the corresponding smooth flow response as described in Figure 39. Thus it appears that turbulence has the effect of enhancing periodic vortex shedding for this section and aspect ratio, and makes the fluctuating lift forces more coherent up the building. This effect is accompanied by a decrease in base pressure to a uniform value of $C_{PB} = -1.0$, indicating a large increase in static drag for turbulent flow. Hence, it can be said that turbulence in this case has the complete opposite effect that it had for an aspect ratio of 15.6 where turbulence increased the base pressure. The corresponding effect of this on the fluctuating lift forces is significant and is discussed in more detail in section 4.3. Two sets of recordings were taken for reduced velocities of $U/_{n1D} = 8.8$ and 15.0 and analysed to find the fluctuating lift forces in turbulent flow.

The corresponding drag response is shown on Figure 41 for turbulent flow. As in Figure 38 the drag acceleration response varies with U^2 and no peaks were found in the drag response. One set of data was recorded for this case at the reduced velocity $U/_{n1D} = 13.9$ and analysed to find the fluctuating drag forces in turbulent flow.

4.3 AERODYNAMIC FORCE RESULTS : ASPECT RATIO 9.8



For this section as a three dimensional building shape in smooth flow the influence of the tip flow seems to control the vortex formation in that vortices are generated in "bursts" and not in a continuous manner as shown by the acceleration trace on Figure 39 and comparing this with Figure 40 for turbulent flow the effect of oncoming turbulence is to "wash out" the tip effect and allow

coherent vortex formation as is indicated by the increase in lift response. Since the strength of vortex formation is closely related to the magnitude of the base pressure, two pressure tappings were placed on the rear face to measure the base pressure C_{PB} at close to the top and bottom of the building. The values obtained for smooth flow gave the base pressure as $C_{PB} = -0.62$ at the top and $C_{PB} = -0.9$ at the bottom, compared with $C_{PB} = -1.0$ found for both positions in turbulent flow. Thus a more two dimensional wake is formed together with presumably a greater rate of entrainment of air from the base region, this indicating that there is stronger more coherent vortex shedding in a turbulent flow for this aspect and section ratio.

This phenomenon further reflects itself clearly when examining the family of fluctuating lift force spectra and cross correlations found for a smooth flow analysis as shown on Figures 44 and 45 and comparing them with the corresponding turbulent flow values on Figures 46 and 47. In smooth flow the r. m. s. fluctuating lift coefficients varies from the very small values of $\sqrt{\overline{C_{LFi}^2}} = 0.028$ to 0.068, while the turbulent flow values are at least an order higher varying from 0.372 to 0.725. The smooth flow lift force spectra as shown on Figure 44 have much less power than the turbulent flow values on Figure 46 at the Strouhal frequency of around 0.12. This justifies the postulate that for this 2 : 1 section and aspect ratio the effect of turbulence is to increase the strength of the vortices shed from the body thereby greatly increasing the magnitude of the fluctuating lift force, and correspondingly tending to two dimensionalise the wake. This phenomenon is further verified by the comparison between the family of lift force cross correlation coefficients for smooth and turbulent flow as shown on Figures 45 and 47. In smooth flow the cross correlation coefficients drop off very rapidly along the structure, as shown on Figure 45, and show little indication of the existence of a symmetrical pattern of oscillating lift forces, however, the turbulent flow lift forces are very well correlated up the building and the family of cross correlation coefficients have a nearly symmetrical

distribution as shown on Figure 47.

As already discussed Vickery[2] designed a test rig to measure the integrated aerodynamic shear force acting on various building models in a water tunnel in turbulent flow. Vickery did not present details relating to the calibration of the dynamic system used, however, assuming it to be properly calibrated with linear dynamic characteristics an approximate comparison can be made for the integrated aerodynamic force coefficients. For aspect ratio 9.8 and section ration 2 : 1.25 which is similar to present tests Vickery's value for the integrated fluctuating lift force is $\sqrt{\overline{C_{LF}^2}} = 0.41$ which compares favourably with $\sqrt{\overline{C_{LF}^2}} = 0.39$ for present tests, this being obtained using the predicted lift force distribution from table 1, and the cross correlation coefficients on Figure 47. It should be borne in mind that the two approaches used to find the integrated force coefficients are fundamentally different and it is surprising that there is such a good comparison between Vickery's results and the present test results. Other differences exist, in that the turbulent scale parameters Lx/D, Ly/D, and the turbulent intensity $\sqrt{\overline{u^2}}/U$ are not exactly similar. Vickery's spectrum for the fluctuating lift for aspect ratio 4.4 and section ratio $B/D = 2 \cdot 3$ is shown superimposed on Figure 46, as there is no spectrum presented in Vickery for the present model shape. This is plotted to give a qualitative comparison only, since for a true quantitative comparison the distributed force spectra would have to be statistically added to obtain the total shear force spectrum, however,there is a reasonable qualitative agreement between the spectra.

AERODYNAMIC DRAG FORCE RESULTS : ASPECT RATIO 9.8

The corresponding distribution of fluctuating drag coefficients for this aspect ratio and section ration 2 : 1.25 varies from $\sqrt{\overline{C_{LF1}^2}} = 0.15$ to $\sqrt{\overline{C_{LF4}^2}} = 0.225$, which are smaller than the fluctuating lift force values. As shown on Figure 48 the force spectrum for each of the top four elements approximate closely to being flat, as would be expected for drag fluctuations in turbulent flow. The corresponding cross correlation coefficient distribution as shown on Figure 49 indicate

that the fluctuating drag forces are less well correlated than the fluctuating lift forces as they drop off very rapidly along the model. This result is physically correct, as the fluctuating lift spectrum is dominated by vortex shedding over a small frequency band which tends to give better cross correlation than the random drag force. This family of cross correlation coefficients is also close to having a symmetrical distribution and this is in agreement with the phenomenon that the wake flow is more two dimensional in turbulent flow. Vickery's[2] fluctuating drag spectrum is plotted on Figure 48 for comparison and relates to a model of dimensions 29mm. x 12.2mm. x 125mm. high, which gives both a different aspect and section ratio compared with the present test model, nevertheless, there is a reasonable comparison except at the low frequency end of the spectrum. Vickery's spectrum does not extend below $nD/U = 0.06$ and this low frequency cut off is difficult to understand as the corresponding turbulent scale parameter $Lx/D = 3.0$ is much higher than for present tests, indicating that Vickery's spectrum should contain more power at low frequencies. On the same plot on Figure 48 the resulting fluctuating drag spectrum obtained from Bearman's[5] more fundamental research into the fluctuating drag forces on square plates is plotted and the comparison shows that the present tests give slightly more low frequency power for the corresponding square plate, and it is thought that this extra power is due to low frequency fluctuations on the rear face caused by the afterbody shape altering the wake structure, and also possibly by the free end.

The integrated fluctuating drag coefficient was found to be $\sqrt{\overline{C_{DF}^2}} = 0.102$ compared with Vickery's value of $\sqrt{\overline{C_{DF}^2}} = 0.105$ as is shown on the plot on Figure 42, for the same section and aspect ratio as in present tests.

In concluding this section on aspect ratio 9.8 tests there appear to be certain disadvantages relating to this bluff 2 : 1.25 section in a turbulent flow. These are, high static drag C_D, high fluctuating drag $\sqrt{\overline{C_{DF}^2}}$, and a high fluctuating lift force $\sqrt{\overline{C_{LF}^2}}$ whose distribution is well correlated up the building.

AERODYNAMIC DRAG FORCE RESULTS : ASPECT RATIO 15. 6

The fluctuating drag spectra for the less bluff 1. 25 : 2 section are shown on Figure 50. The distribution of r. m. s. fluctuating drag $\sqrt{\overline{C_{DFi}^2}}$, varies from 0. 116 to 0. 140 for the top three stations in turbulent flow, and these are smaller than the values obtained for the 2 : 1. 25 bluffer section of the model. This would be as expected since the more streamlined the section becomes the smaller will be the drag force. Again, the fluctuating drag cross correlation coefficients fall off much faster than the corresponding fluctuating lift force as shown on Figure 51.

The drag spectrum for position 4 appears to be in error as it contains two extraneous peaks corresponding to the first lift and first drag natural frequencies, and this is reflected in the very low cross correlation between the neighbouring stations 3 and 4, i. e. $C_{43}(0)$ is very small indeed.

Vickery's spectrum for B/D = 0. 42 and turbulent scale parameter of L_x/D = 6. 25, which is much higher than for present tests, has been superimposed on Figure 50, and as expected, because of the large difference between the corresponding L_x/D parameters, Vickery's spectrum has a greater amount of power at low frequencies, and a higher fluctuating drag coefficient $\sqrt{\overline{C_{DF}^2}} = 0.15$. Vickery's integrated fluctuating drag coefficient for aspect ratio 15. 6 and section ratio 1. 25 : 2 was found to be $\sqrt{\overline{C_{DF}^2}} = 0.09$ from Figure 43, and this compares favourably with the present test values of $\sqrt{\overline{C_{DF}^2}} = 0.093$ obtained from the distribution of fluctuating drag coefficients and corresponding cross correlation coefficients on Figure 51.

AERODYNAMIC LIFT FORCES : ASPECT RATIO 15. 6

For the short face windward two sets of data were analysed for the reduced velocities U/n_1D = 35. 0 and U/n_1D = 48. 4 these giving vortex shedding frequencies that lie between the first and second natural frequencies in smooth flow. Both sets of data gave very similar results for the fluctuating lift force distribution and their corresponding cross correlation coefficients, for example, Figure 52 shows the force spectra for U/n_1D = 35. 0 and gives a variation in the

fluctuating lift $\sqrt{\overline{C_{LFi}^2}}$ between 0.22 and 0.29, with an equivalent integrated r. m. s. value of $\sqrt{\overline{C_{LF}^2}}$ =0.198, which compare favourably with the values obtained for the set of data at $U/_{n1D}$ = 48.4 as shown on Figure 54, which gave the distribution of the fluctuating lift coefficient $\sqrt{\overline{C_{LFi}^2}}$ varying from 0.24 to 0.27 with an integrated value of $\sqrt{\overline{C_{LF}^2}}$ =0.194. In both cases the distribution of the fluctuating forces was found to be nearly unform indicating a regular vortex formation with little change in vortex strength up the building. However, a very interesting feature about the force spectra obtained from both sets of results is the existence of two regular shedding frequencies in the lift force,one at the strouhal frequency nD/U = 0.087 related to the top of the building and the other at nD/U = 0.097 at the lower stations. Thus it appears that the low shedding frequency is associated with the free end of the structure, while a higher frequency is associated with the lower region of the structure. However, the magnitude of the fluctuating forces remain nearly uniform in both regions. The corresponding cross correlation coefficient distribution shown on Figures 53 and 55 indicate the the cross correlation in any zone of constant shedding frequency is very high while the cross correlation between zones is very small, for example $R_{12}(0)$ = 0.75 while $R_{14}(0)$ = 0.13 for cross correlations relative to the top of the building where nD/U = 0.087, while R_{43} = 0.89 and R_{41} = 0.13, for nD/U = 0.097 for the lower region. Thus both zones have vortex formation which is uncorrelated between zones.

This phenomenon of varying shedding frequency is generally more typical of a body in a sheared flow where there is a variation in the mean wind velocity with height. Research by Maull and Young[25] on the vortex shedding characteristics of a stationary bluff body with a free end gave zones of varying shedding frequencies found from the spectral analysis of velocity fluctuations measured on a hot wire anemometer probe in a smooth flow, and these were thought to be affected by the free end condition, and also by horizontal streamwise vortices which were thought to exist at the boundary between zones.

The effect of turbulence on the fluctuating lift force distribution for the turbulent scale parameter $Lx/D = 2.4$ is shown on Figure 56. The lift force spectra now indicate a broad band range of shedding frequencies centred on a Strouhal frequency of $nD/U = 0.115$. The fluctuating lift coefficient drops slightly at the top of the building to a value of $\sqrt{\overline{C_{LF1}^2}} = 0.28$ compared with 0.375 for lower down the building, these having an integrated value of $\sqrt{\overline{C_{LF}^2}} = 0.277$ compared with $\sqrt{\overline{C_{LF}^2}} = 0.194$ obtained for smooth flow conditions, this indicating that the fluctuating lift forces in turbulent flow for this aspect and section ratio, are much higher than in smooth flow. The broad band vortex shedding is caused by the turbulence in the external flow region interacting with the vortex formation. It is important to note that in this case the fluctuating lift force is highly correlated up the building, and in fact the cross correlation is higher in turbulent flow than it is in smooth flow as is shown on Figure 57, for example examining this plot shows that the cross correlation within the two zones are very similar to the smooth flow values, however, the cross correlation between zones is much higher in turbulent flow, this difference being due to the varying shedding frequencies that exist in smooth flow.

Superimposed on station 1 force spectrum on Figure 56 is Vickery's spectrum for a model of section ratio B/D = 0.42 which is bluffer than the present model. One major difference is that Vickery's peak is centred at a very low Strouhal frequency Sn = 0.04 compared with Sn = 0.115 obtained for present tests. This difference is though to be due to the different section ratios, since Vickery's value for the present section ratio B/D = 0.67 is Sn = 0.08. Vickery's corresponding integrated fluctuating lift coefficient for section ratio B/D = 0.67 is $\sqrt{\overline{C_{LF}^2}} = 0.26$ which is in close agreement with the present value of $\sqrt{\overline{C_{LF}^2}} = 0.277$, as shown on Table I, Appendix III

4.4 AERODYNAMIC FORCE RESULTS FOR STRUCTURAL RESONANCE WITH VORTEX SHEDDING

Seven sets of wind tunnel results for the distribution and cross correlation of the fluctuating lift and drag forces have been analysed and discussed for the case where the vortex shedding frequency is not coincident with any of the structures natural frequencies, in smooth flow, and also for the more random forces associated with turbulent flow, and these results have been compared with those obtained from Vickery[2] for the integrated forces. These results also deal with all the combinations of varying aspect and section ratios for smooth and turbulent flow. As already outlined in sections 3.9 and 3.10 which dealt with the prediction of single frequency and random forces, the technique is least accurate when trying to predict a distribution of sinusoidal forces whose frequency is coincident with any of the structures natural frequencies, this being due to the small difference between the stiffness and inertia force distribution at resonance. It is obvious by comparing the various r. m. s. displacements forthe different flow conditions as shown on Table I and Table II that the models displacements for the special case when the vortex shedding frequency is coincident with the lift natural frequency are approximately twice the "non resonant" values. The maximum and minimum displacements were 0.0085 inches and 0.00083 inches respectively or about 0.004D to 0.0004D, these depending on the magnitude of the aerodynamic forcing function. To keep these displacements very small compared with the size of the model was a primary design feature which has been successful, the object of this being to minimise aeroelastic interactions that might occur in wind tunnel tests. Research by Protos Goldschmit and Toebes [27] on the hydro elastic forces on cantilevered bluff triangular cylinders in a two dimensional flow gave an increase in the integrated fluctuating lift coefficient $\sqrt{C_{LF}^2}$ of 20% for lift amplitudes of about 0.04D which is an order higher than the maximum amplitude

obtained in present tests. Thus for the present building model it should be expected that the dynamic displacements do not have any serious effect on the magnitude of the fluctuating lift. However, it is clear from the results obtained in the special case of vortex resonance in smooth flow as shown on Table 2 and Figure 60, that the fluctuating lift appears to increase considerably, especially at the lower stations of the model. Little is known about the change in magnitude and distribution of the fluctuating forces when the forcing frequency is coincident with a natural frequency of the structure, but clearly if this increase in the fluctuating force is actually present it can only be due to some complicated aeroelastic interaction that is not necessarily displacement dependent. The corresponding cross correlation coefficients for both the first and second modes in resonance with the vortex shedding frequency as shown on Figures 59 and 61, become negative along the structure indicating that large phase changes take place between the forces on each element.

These resonant results cannot be explained by the author but it is thought that they may be due to a combination of a complex change in the vortex formation combined with the resonant properties of the dynamic model. Furthermore, this phenomenon appears to be typical of smooth flow only, since when the flow is turbulent, and there is a broad band of shedding frequencies at a natural frequency, the magnitude of the fluctuating lift coefficients are much closer to their corresponding "non-resonant" values, for example, the distribution of fluctuating lift coefficients vary from $\sqrt{\overline{C_{LFi}^2}} = 0.261$ to 0.447 for the "resonant" case with an integrated value of $\sqrt{\overline{C_{LF}^2}} = 0.288$, all of which compare favourably with the "non resonant" values of $\sqrt{\overline{C_{LFi}^2}}$ varying from 0.283 to 0.375 with an integrated value of 0.277 as shown on Tables I and 2 and on the lift force spectra plots of Figures 56 and 62.

4.5 CONCLUSIONS

The new technique described within allows both the distribution and cross correlation coefficients of the fluctuating aerodynamic lift and drag forces on a flexible building to be evaluated by measuring response, and is the only technique known by the author that allows the prediction of these quantities for building shapes.

The dynamic analysis and computing systems used to find these fluctuating forces have been extensively tested in the dynamics laboratory by predicting the magnitude of distribution of known harmonic and random forcing functions.

The technique requires only two dynamic quantities to be experimentally measured per element to allow the TOTAL aerodynamic force on that element to be found.

Good quantitative comparisons have been found with Vickery's[2] results for the integrated fluctuating lift and drag coefficients for both aspect and section ratios of the building model.

FUTURE RESEARCH

Interesting future research using this technique would include comparisons with the aerodynamic forces found from full scale buildings and also the application of the technique to measure the full scale fluctuating forces on an actual structure.

Further experiments are also required for the special case where the vortex shedding frequency is coincident with a natural frequency of the structure, including the effects of aerodynamic damping.

Other interesting applications could be made by placing the model between or surrounded by other buildings and observing the change in the distribution of the fluctuating aerodynamic forces for this complicated aerodynamic environment.

In concluding it is hoped that the technique would be applied to find the fluctuating aerodynamic forces on other building shapes such as the circular cylinder, and extended into other fields of research such as for the fluctuating forces on bridge decks.

MATHEMATICAL SYMBOLS

A	Aspect ratio (height / windward breadth)
$\mathbf{A_i}$	Boolean selection matrix
A_{oi}	element drag area
A_{Li}	element lift area
AT	total side area
Ae	element area
Aw	windward area
$A_D(t)$	aerodynamic drag force (total)
$\beta = \frac{\omega}{\omega_i}$	frequency ratio
$B \equiv D_w$	windward dimension
B/D	section aspect ratio with B windward/frequency
$C_{Pi\ Pj(\omega)}$	coherence between forces at
$C_{Pi\ Pj(o)}$	cross correlation coefficient
$\sqrt{C^2_{LFi}}$	r. m. s. element lift force
$\sqrt{C^2_{DFi}}$	r. m. s. element drag force
$\sqrt{C^2_{LF}}$	r. m. s. integrated lift force
$\sqrt{C^2_{DF}}$	r. m. s. integrated drag force
$D_W \equiv B$	windward width
D_{Li}	lift width
$\mathbf{G}_{(\omega)}$	damping matrix
$g(\omega)$	non dimensional damping
$\mathbf{H}(\omega)$	' ' degree of freedom frequency response function
$\mathbf{h}(\omega)$	' n ' degree of freedom frequency response function (generalised)
$\mathbf{K}_a$	assembled stiffness matrix
$\mathbf{K}_\beta$	reduced stiffness matrix
$\mathbf{K}_\epsilon$	element stiffness matrix
$\mathbf{k_q}$	generalised stiffness matrix
$\mathbf{igK}$	complex stiffness matrix
L_x	longitudinal length scale of turbulence
L_y	transverse length scale of turbulence
$\mathbf{M}(t)$	dynamic moment matrix
$\mathbf{M}(\omega)$	dynamic moment matrix (Fourier Coefficients)
$\mathbf{m}$	mass matrix
$\mathbf{m_q}$	generalised mass matrix
n_i	i'th natural frequency in HZ
n	frequency in HZ

$\mathbf{P}(t)$	column of dynamic forces (distribution)
$\mathbf{P}_{(\omega)}$	column of dynamic forces (Distribution) Fourier Coefficients
$\mathbf{P}_{S(\omega)}$	total element dynamic forces (Fourier Coefficients)
$P(Z)$	special distribution of forces
$\delta \mathbf{P}$	error associated with $\mathbf{P}$
$\mathbf{Q}$	generalised force
$\mathbf{q}$	generalised displacement
$\mathbf{R}(t)$	matrix of cross correlations at time
$\mathbf{S}$	non dimensional lift force spectra
$\mathbf{S}$	non dimensional drag force spectra
$\mathbf{S}$	force spectra
$\mathbf{T}$	vector rotation
$U^1 = \frac{U}{nD}$	reduced velocity
$\bar{U} = \frac{Mn}{\rho} \cdot U^1$	universal reduced velocity
U	windward velocity (ft/sec)
ω	circular frequency
ω_i	natural circular frequency
$W(\tau)$	Hanning Function
$\mathbf{X}(t)$	dynamic displacements
$\ddot{\mathbf{X}}(t)$	dynamic accelerations
$X(\omega)$	dynamic displacements (Fourier Coefficients)
$\ddot{X}(\omega)$	dynamic acceleration (Fourier Coefficients)
Z	distance vertically
λ_i	i'th eigenvalue (ω_i^2)
λ	eigenvalue
Φ	eigenvectors
$\mathcal{E}(t)$	dynamic strain
$\mathcal{E}(\omega)$	dynamic strain (Fourier Coefficients)
$\theta_{Pi\ Pj(\omega)}$	phase between cross spectra components

1	VICKERY B.J.	On the flow behind a coarse grid and its use as a model of atmospheric turbulence in studies related to wind loads on buildings. NPL. Aero Report 11431965.
2	VICKERY B.J.	Load fluctuations in turbulent flow. Proc. A.S.C.E. Journal Eng. Mech. Div. P. 31. Feb. 1968.
3	VICKERY B.J.	Fluctuating lift and drag on a long cylinder of square cross section in smooth and turbulent flow. J.F.M. Vol. 25. Part 3 1966.
4	BEARMAN P.W.	Turbulence induced vibrations of bluff bodies. Paper H1 Symposium on Flow-induced Vibrations, Karlsruhe, Germany, August 1972.
5	BEARMAN P.W.	An investigation of the forces on flat plates normal to a turbulent flow. J.F.M. 46, 1971.
6	BEARMAN P.W. and TRUEMAN	An investigation of the flow around rectangular cylinders. I.C. Aero Report 71-15, June 1971.
7	ELLIS N.	A technique for evaluating the fluctuating aerodynamic forces on a flexible building. International Symposium for Vibration Problems in Industry. Paper 312, Keswick, England, April 1973.
8	DAVENPORT A.G.	The application of statistical concepts to wind loading on structures. Proc. Inst. Civ. Eng. Vol. 19, Paper 6480, 1961.
9	NOVAK M.	Galloping and vortex oscillations of structures. Proc. Wind Effects on Buildings and Structures, P. 799, Tokyo 1971.
10	NOVAK M.	Aeroelastic galloping of prismatic bodies. Trans. A.S.C.E. Journal Eng. Mech. Div. P. 115, Feb.1969.
11	NOVAK M.	Galloping oscillations of prismatic structures. Trans. A.S.C.E. Journal Eng. Mech. Div. P. 27, Feb. 1972, Vol. 98.
12	SCRUTON C.	On wind excited oscillations of stocks, towers and masts. Inter. Conf. NPL Teddington, June 1963.
13	ARGYRIS J.H.	Continua and Discontinua. Inter. Conf. Finite Elements Air Force Conference. Patterson Air Base, Oct. 26-28 1965.
14	ARGYRIS J.H. and KELSEY S.	Energy Theorems and Structural Analysis. Butterworths Press. 1971.

15	KENNEDY C.C. and PANCU D.P.	Use of vectors in vibration measurement and analysis Jrn. Aero. Science. Nov. 1947.
16	HURTY and RUBENSTEIN	Dynamics of structures, Prentice Hall 1970
17	LAZAN	Structural damping. Pergamon, 1968.
18	LIN Y.K.	Probabilistic Theory of structural dynamics. McGraw Hill 1967.
19	BENDAT and PIERSOL	Measurement and Analysis of random data. J. Wiley 1966. Republished 1971.
20	ROBSON	An introduction to random vibrations. Edinburgh Univ. Press.
21	HITCHINGS D.	M.Sc. Thesis Dept. Aeronautics. Univ. of London, 1966
22	BLACKMAN and TUKEY	The measurement of power spectra. Dover Publication, New York 1958.
23	COOLEY J.W., LEWIS P.A.W., WELCH P.D.	The fast Fourier Transform Algorithm and its Application. IBM Research 1967. RC 1743.
24	PARKINSON G.V.	Wind induced instability of structures. P 395. Phil. Trans. of Royal Society. Vol. 269, 1971.
25	MAULL and YOUNG	Vortex shedding from a bluff body in shear flow Paper H2. Symposium on Flow-induced Vibrations, Karlsruhe, Germany, August 1972.
26	NAKAGUCHI H. HASHIMOTO K. and MUTO S.	Proc. of symposium on low speed wind tunnels. Tokyo University, April 1967.
27	PROTOS, GOLDSCHMIDT and TOEBES.	Hydroelastic forces on bluff cylinders. Journal Bas. Eng. Trans. A.S.M.E. Series D. Vol 90 1968, P. 378 to 386.
28	STROUHAL V.	Uber Eine Besondere Art der Tunerregung Annatender Physik Und Chemie, Vol. 15, 1878. P. 216.
29	VON KARMAN	Uber den Mechanisms des Widersttandes den ein be Wegter Korper in einer Flussigkeit, Erfarht Gottinger Narchrichten, Math/Phys. K1 1911. P. 547.
30	DAVENPORT A.G.	The response of building shapes to the wind. Phil. Trans. Royal Society, London, Vol 269. P. 385/394, 1971.

31	MORKOVIN	Flow around a circular cylinder. Symposium on Fully separated flows. A.S.M.E.
32	DEN HERTOG	Trans. Amer. Inst. of Elect. Eng. Vol. 49, 1930, P444.
33	PARKINSON G.V. and SMITH	The square prism as a non-linear oscillator Quart. Journal Mech. Applied Math. Vol. 17, 1964.
34	PARKINSON G.V. and SANTOSHAM	Cylinders of rectangular section as aeroelastic non-linear oscillators. A.S.M.E. Vibrations Conf. Boston, Mass. March 1967.
35	NOVAK M. DAVENPORT A.G.	Aeroelastic instability of prisms in turbulent flow. Proc. Amerc. Soc. of Civ. Eng. Journ. Eng. Vol.96. February, 1970.
36	DAVENPORT A.G.	The dynamic and static action of wind on hyperbolic cooling towers. University of Western Ontario, London, Canada. BLWT-1-66.
37	FENG C.C.	The measurement of vortex induced effects in flow past stationary and oscillating circular and D section cylinders. Mech. Eng. Dept., Univ. of British Columbia.
38	OWEN P.R.	Buildings in the wind. Quarterly Journ. of the Royal Meteorological Society, Vol. 97, No. 414, Oct. 1971.
39	DAVENPORT A.G. ISYMOV.	Wind tunnel study of a proposed 53 storey building for the Seattle First National Bank, Univ. of Western Ontario, London, Canada. Report BLWT-1-67.
40	WHITBREAD SCRUTON C.	An investigation of the aerodynamic stability of a model of the proposed tower blocks for the Wind Trade Centre, New York, NPL. Aero Report 1156 July 1965.
41	BRITISH CODE OF PRACTICE, CP3, Chapter V, Part II - Wind loading 1972.	
42	STANDARDS ASSOCIATION OF AUSTRALIA. SAA Loading Code Part II- Wind Forces. Aust. Standard CA 34, Part II, 1971.	

APPENDIX I

DATA GATHERING, STATISTICAL CONCEPTS AND COMPUTER PROGRAM STRUCTURE

DATA GATHERING AND REDUCTION

There are two basic stages involved in statistically analysing the data generated by the technique

(i) DATA GATHERING

(ii) DATA REDUCTION

(i) DATA GATHERING

A simple flow chart for the gathering of information is shown on Diagram A of Figure 23. During wind tunnel tests the outputs of 5 accelerations and 5 strain signals are calibrated to give a r. m. s. voltage of 350mV, this value giving the optimum signal/noise ratio for the analogue recorder. These signals are recorded simultaneously on an Ampex FR1300 14 track analogue recorder to ensure the preservation of phase between accelerations and strains. Eleven sets of wind tunnel data were recorded for various flow conditions, aspect ratio, and wind tunnel speeds. The analogue data obtained from wind tunnel tests was digitised using the Department of Aeronautics multi-channel data logging system to generate a digital magnetic tape compatible with the CDC 6400 computer. The data logging system uses a PDP/8 L computer together with an interfaced analogue to digital convertor (ADC) capable of digitising at 25K samples/sec, the discrete values being written to a digital magnetic tape. The A. D. C. has a sample and hold which allows all ten channels to be sampled at the same instant in time again preserving the strain/acceleration phase relationship, this being of prime importance. The generated digital tape has the strain and acceleration values stored consecutively in variable records, which always contain a multiple of ten useful data points.

The digital tape may contain several files for different flow conditions, each file separated by an end of file marker which ensures the correct positioning of the tape drive for each set of data.

(ii) DATA REDUCTION

The data reduction is done using the Imperial College Computer Centre's CDC 6400 computer. As outlined on Diagrm B, Fig. 23, the digital magnetic tape input is read to obtain corresponding arrays $\mathcal{E}(t_i)$ and $\ddot{X}(t_i)$, arranged in 1024 data blocks suitable for Fast Fourier Transforming.

FAST FOURIER TRANSFORM AND HANNING FUNCTION

The Finite Fourier Transform is outlined in Bendat and Piersol[19].

Considering a finite time interval (0, T) the Fourier Transform of acceleration and strain become

$$\ddot{X}(n, T) = \int_0^T \ddot{x}(t) e^{-i2\pi nt} dt$$

and

$$\mathcal{E}(n, T) = \int_0^T \mathcal{E}(t) e^{-i2\pi nt} dt$$

for a discretised signal of equal time intervals (Δt) $t_h = h \Delta t$ considering $\ddot{x}(t)$

$$\ddot{x}(t) = \ddot{x}_h = \ddot{x}(h \Delta t)$$

giving

$$\ddot{X}(n, T) = \Delta t \sum_{h=0}^{N-1} x_h e^{-i2\pi n h \Delta t}$$

at frequency $n_k = kn = \frac{k}{T} = \frac{k}{N \Delta t}$

then the Fourier Coefficients are defined by

$$\ddot{X}_k = \frac{\ddot{X}(n, T)}{\Delta t} = \sum_{h=0}^{N-1} \ddot{x}_h \; e^{\frac{-i\,2\,\pi\,kh}{N}}$$

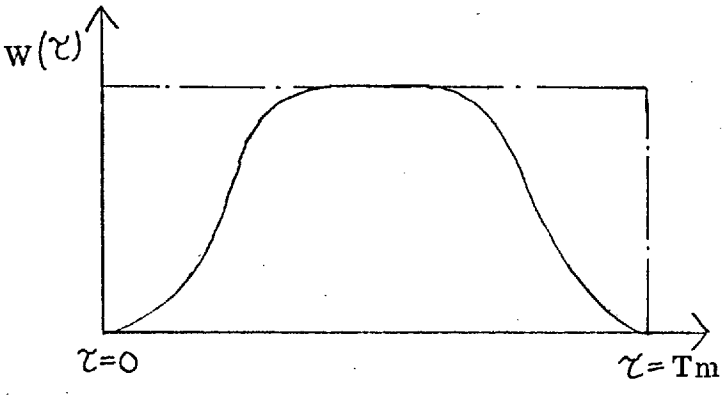
and similarly for $\ddot{\mathcal{E}}_k$.

This is the Finite Fourier Transform.

The Fast (finite) Fourier Transform algorithm used is based on Cooley Lewis and Welch's[23] program, the basic concept being that if N is a power of 2 the series can be split into $\log_2 N$ subseries, and the doubling algorithm can be applied to compute the Finite Fourier Transform in LOG_2 N doublings i. e. the number of operations become N LOG_2 N instead of the conventional N^2 thereby giving a very large saving in computer time.

HANNING WINDOW

To smooth the "apparent" power spectrum to obtain a better estimate of the "true" power spectrum the conventional one sided Hanning function is used



For a one sided spectrum

$$W(\tau) = \tfrac{1}{2}\left(1 - \cos\frac{2\,\pi\,\tau}{Tm}\right)$$

now by Hanning the Fourier Coefficients (ref [19, 22])

$$\ddot{X}_0 = \tfrac{1}{2}\ddot{x}_0 + \tfrac{1}{2}\ddot{x}_1$$

$$\ddot{x}_r = -\tfrac{1}{4}\ddot{x}_{r-1} + \tfrac{1}{2}\ddot{x}_r - \tfrac{1}{4}\ddot{x}_{r+1}$$

$$\ddot{x}_N = \tfrac{1}{2}\ddot{x}_{N-1} - \tfrac{1}{2}\ddot{x}_N$$

for $2 \leq r \leq 1023$, and similarly for $\ddot{\mathcal{E}}_r$

The final power is consequently lower by the ratio of areas of the Hanning to Rectangular window and this can be shown to be $^3/_8$. The one sided spectrum has twice the power of the two sided spectrum therefore a further factor of 2 has to be included giving

$$S_p(\omega) = P(\omega)\ \overset{*}{P}(\omega)\cdot\frac{16}{3}$$

where $P(\omega)$ are the hanned Fourier Coefficients.

STATISTICAL PROPERTIES OF RANDOM DATA

Number of channels digitised	P = 10
Sampling Rate/Channel	SR = 666.6 s/sec
Nyquist Frequency	Nq = 333.3 HZ
Band width	B = 0.65 HZ

Degress of Freedom N' = 2N = 76

Number of 1024 data blocks = 38/channel

Total number of data points = 390 K

Sample time T = 1.54 secs.

ERRORS ASSOCIATED WITH POWER SPECTRA

From Bendat and Piersol the normalised standard error for a two sided spectrum

$$\epsilon^2 = \frac{1}{BT}$$

and for 1 block of data BT = 1, therefore for N blocks data

$$\epsilon = \frac{1}{\sqrt{N'}}$$

and for a one sided spectrum $N^1 = 76$

Therefore $N^1 = 76$ gives $\epsilon = 0.114$

Thus the error in the individual components are of 0 (10%) for a Gaussian Distribution, applicable to Bandwidth Limited white noise. For smooth flow vortex shedding, where there is a modulated sinusoidal response, the standard error is probably less. Improvement of the standard error could be achieved by either of :

(i) increasing the number of data blocks

(ii) frequency averaging.

Neither of these were thought to be necessary as in (i) it would make the data handling and computing time involved unrealistic with consequent delay in analysis time, and (ii) would tend to smooth out the peaks in the force spectra with consequent clouding of the physical interpretation of the results, e.g. Fig. 52 and 54 where there are two vortex shedding frequencies close to each other.

GENERAL STRUCTURE OF COMPUTER PROGRAM

The execution of the overlay structure for the program is shown in Diagram A below. The use of Overlay structures optimises the use of Central Processor Time and core capacity requirements for large amounts of data undergoing different operations.

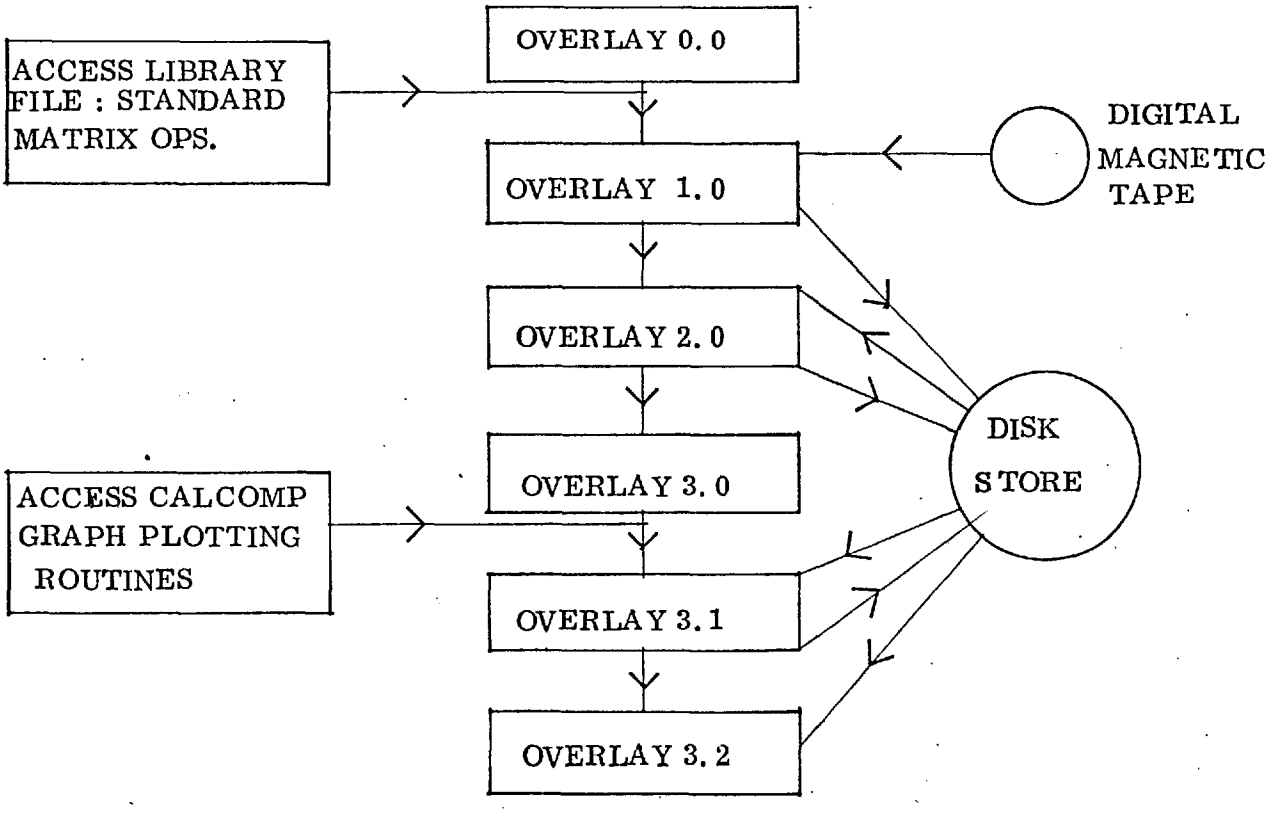


DIAGRAM A - OVERLAY STRUCTURE

The data generated after each overlay program execution is written to disk storage making it easily and quickly accessible to the next overlay program. The program is designed so that it operates for both dynamic random force tests, and wind tunnel response data, and predicts the force spectra in both cases.

The following sections present a short synopsis of the general computer operations involved in each overlay, and should be read in conjunction with the flow chart, Fig. 24.

OVERLAY 1.0 - PROGRAM DEMULT

The input digital tape has 1535 12 BIT word records, and the total number of useful words is variable depending on the sampling rate. Overlay 1.0 searches for the end of useful information in each record and counts the number of useful data. These 12 BIT words are then unpacked into corresponding CDC 6400 - 60 BIT words. Reading from the digital tape continues until a two dimensional array of size A (10,1024) is filled, the 1024 size array being in the correct form for Fast Fourier Transforming. A(10,1024) is written to disk storage and A overwritten with the next set of incoming data. This is repeated 38 times, with the sampled data running consecutively in time : all the discrete data points are now stored on disk allowing fast access. There are filemarks interspersed with the data to check the flow of data when reading.

OVERLAY 2.0 - PROGRAM TRANSFORM

The data is read in consecutive 1024 word records, Fast Fourier Transformed and the Fourier Coefficients Hanned. The r.m.s. displacements are found by integrating the displacement spectra formed from $x(\omega) = \ddot{x}(\omega) / \omega^2$ allowing for a low frequency cut off below $3H_Z$. The data is stored in 10 x 1024 blocks of Fourier Coefficients, the first five being strain, and the second five runs being acceleration. Each column then corresponds to a particular frequency component. These columns are then used to obtain the individual Fourier Coefficients of the random force $\mathbf{P}(\omega)$, including variable damping. $\mathbf{P}(\omega)$ overwrites the column of data used in its calculation, thereby optimising core space. When one block is completed the Fourier Coefficients of $\mathbf{P}(\omega)$ are stored on disk, and the process repeated for the next block of data (repeated 38 times)

OVERLAY 3.0 PROGRAM SPECTRA 1

This overlay is used to access the Calcomp graph plotting routines used in OVERLAYS 3.1 and 3.2. Accessing the graph plotting routines here saves core space in the lower overlays 0.0, 1.0, 2.0, where graph plotting is not required.

OVERLAY 3.1 PROGRAM SPECTRA 2

This program forms the individual estimates of the force power spectra matrix $S_p(\omega)$ from the 38 blocks of Fourier Coefficients, and stabilises each term in the spectra matrix. i.e., the diagonal power spectra terms, and off diagonal cross and quadrature terms. If the incoming data is from wind tunnel tests it then uses the graph plotting routines to plot non-dimensional force power spectra-$V-^{nD}/_{U}$ non-dimensional frequency. This is described in section 3.0.

For wind tunnel data it forms the cross coefficient matrix, i.e. cross correlates all forces with each other, by integrating the cross power spectra terms, for time lag $\tau = 0$. For random force tests it writes the predicted force spectra matrix to disk store together with the actual input force spectrum and calls OVERLAY 3.2.

OVERLAY 3.2 PROGRAM COHR

This reads the data of the force spectra matrix and forms the coherence and phase between the forces for all frequencies and graph plots these. For random force tests it forms the coherence and phase between the actual and predicted force spectrum.

TESTING OF THE PROGRAM

The program is tested by using the response to a random force on the model as outlined in section 3.10. This testing has two important results

(i) It checks that the technique works practically by the comparison between the actual and predicted force spectra.

(ii) As this program is used for wind tunnel tests also, it checks that there are no arithmetic or logical errors associated with the wind tunnel results.

APPENDIX II

1. TABLE I SHOWING COMPARISON OF ACTUAL AND PREDICTED FORCE DISTRIBUTION.

2. EVALUATION OF MATRICES USED IN THE TECHNIQUE.

3. CALCULATION FOR THE COMPARISON OF THE STATISTICALLY INTEGRATED FLUCTUATING FORCE OVER FOUR AND FIVE ELEMENTS.

1. OFF RESONANT RESULTS :

STATION	P_{INPUT}	P_{PRED}	= $P_{\dot{\varepsilon}}$	+ $P_{\ddot{x}}$	% error	FREQUENCY
	R	R	R	R		
P1	38.1	37.40	9.0	28.4	-1.84%	
P2	0.	-0.18	-22.82	+22.64	+.47%	
P3	0.	-0.40	-17.50	+17.10	1.05%	25 HZ
P4	0.	+2.8	-8.1	+10.90	7.4%	
P5	0.	+14.8	+9.1	+ 5.70	38.6%	
P1	56.4	52.7	18.3	34.4	-7 %	
P2	0.	+4.7	-25.0	29.7	8.3%	
P3	0.	-1.4	-23.9	22.5	2.48%	30 HZ
P4	0.	3.3	-11.6	14.9	5.87%	
P5	0	-14.0	-6.2	-7.8	24.8%	
P1	70.0	64.72	30.09	34.63	-7.5%	
P2	0.	4.39	-27.77	32.16	6.27%	
P3	0.	-2.18	-28.41	26.22	3.11%	40 HZ
P4	0.	9.79	- 9.43	19.23	14.00%	
P5	0.	1.44	- 8.79	10.23	2.06%	
P1	77.0	+67.5	62.73	4.2	-15%	
P2	0.	3.9	-28.95	32.87	5%	
P3	0.	3.9	-44.74	48.7	5%	70 HZ
P4	0.	5.2	-44.60	49.8	6.75%	
P5	0.	4.6	-28.60	33.2	6%	

TABLE 1 : Comparison between predicted and actual distribution of forces.

RESONANT RESULTS

STATION	P_{INPUT}	$P_{PRED} = P_{\ddot{\varepsilon}} + P_{\ddot{x}}$			% error	FREQUENCY
	R	R	R	R		
P1	15.9	17.6	-10.5	+28.1	+11.7%	
P2	0.	-1.7	-24.4	+22.62	11.7%	
P3	0.	-2.9	-19.3	-16.29	18.2%	1st Mode
P4	0.	+7.6	-2.1	+ 9.7	48.0%	
P5	0.	-26.5	-21.9	- 4.6	167.0%	
P1	24.2	26.9	-15.40	+42.3	+11.2%	
P2	0.	-0.18	-10.60	+10.42	0.75%	
P3	0.	-3.61	+13.76	-17.37	14.85%	2nd Mode
P4	0.	-8.16	+24.57	-32.73	33.6%	
P5	0.	4.29	+34.12	-29.81	17.8%	

TABLE 1 - contd.

2. EVALUATION OF MATRICES FOR FORCE PREDICTION DIMENSIONS AND MASS DISTRIBUTION.

LEAD POINT MASSES	SHELL	TRANSVERSE PANELS
		.006
.2877	.0314	
		.006
.2861	.0277	
		.006
.2874	.0277	
		.006
.2866	.0277	
		.006
.2863	.0277	
		.006

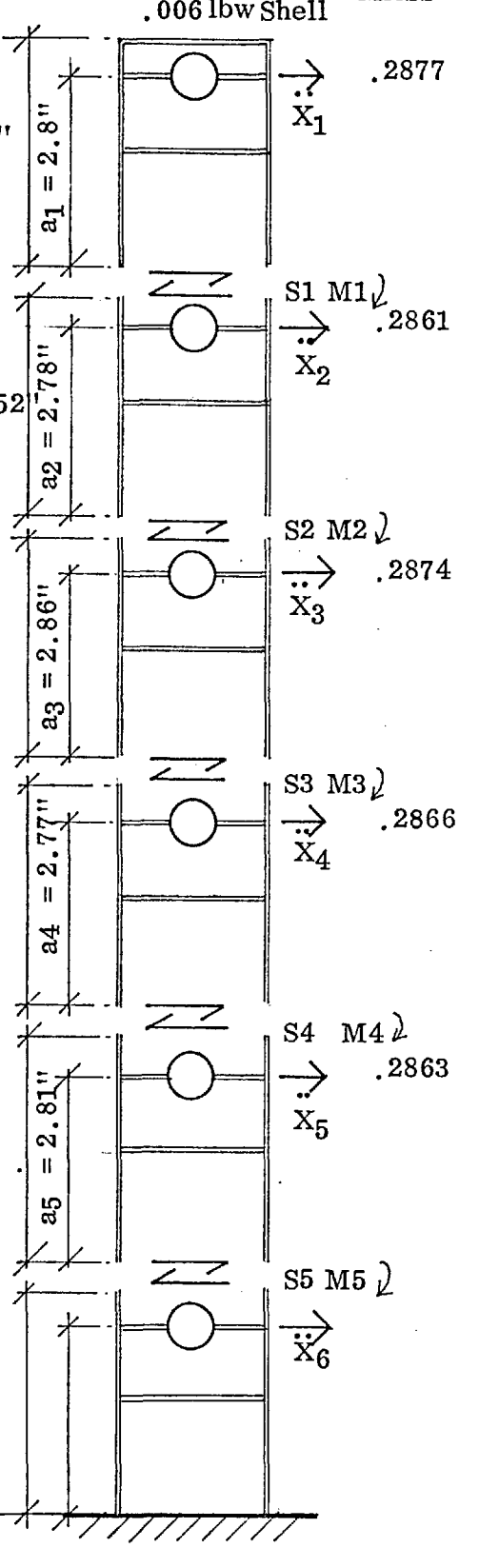


DIAGRAM A

LINEAR DISTRIBUTED LOAD:

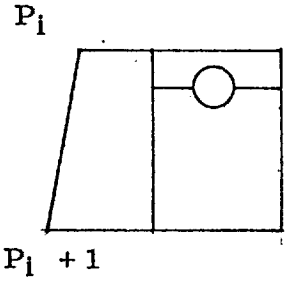
$$\mu = \begin{bmatrix} 1 & & & & \\ -1 & 1 & & & \\ 0 & -1 & 1 & & \\ 0 & 0 & -1 & 1 & \\ 0 & 0 & 0 & -1 & 1 \end{bmatrix}$$

Forms difference in moment across each element.

a EVALUATION:

Consider a typical element then

$$M_i + 1 = \frac{1}{6} \left(2\ell_i^2 P_i + \ell_i^2 P_i + 1 \right)$$



equivalent to the change in moment in the i'th element due to aerodynamic force, hence:

$$a = \frac{1}{6} \begin{bmatrix} 2\ell_1^2 & \ell_1^2 & 0 & 0 & 0 \\ 0 & 2\ell_2^2 & \ell_2^2 & 0 & 0 \\ 0 & 0 & 2\ell_3^2 & \ell_3^2 & 0 \\ 0 & 0 & 0 & 2\ell_4^2 & \ell_4^2 \\ 0 & 0 & 0 & 0 & 3\ell_5^2 \end{bmatrix}$$

$$= \begin{bmatrix} 4.2245 & 2.1123 & 0. & 0. & 0. \\ 0. & 3.3117 & 1.6559 & 0. & 0. \\ 0. & 0. & 3.4776 & 1.7388 & 0. \\ 0. & 0. & 0. & 3.1416 & 1.5708 \\ 0. & 0. & 0. & 0. & 5.2165 \end{bmatrix}$$

β MATRIX

$$\beta = \begin{bmatrix} 0 & 0 & 0 & 0 & 0 \\ \ell_2 & 0 & 0 & 0 & 0 \\ 0 & \ell_3 & 0 & 0 & 0 \\ 0 & 0 & \ell_4 & 0 & 0 \\ 0 & 0 & 0 & \ell_5 & 0 \end{bmatrix} = \begin{bmatrix} 0 & 0 & 0 & 0 & 0 \\ 3.152 & 0 & 0 & 0 & 0 \\ 0 & 3.23 & 0 & 0 & 0 \\ 0 & 0 & 3.070 & 0 & 0 \\ 0 & 0 & 0 & 3.23 & 0 \end{bmatrix}$$

$$\gamma = \begin{bmatrix} a1 & 0 & 0 & 0 & a \\ 0 & a2 & 0 & 0 & 0 \\ 0 & 0 & a3 & 0 & 0 \\ 0 & 0 & 0 & a4 & 0 \\ 0 & 0 & 0 & 0 & a5 \end{bmatrix} = \begin{bmatrix} 2.8 & 0 & 0 & 0 & 0 \\ 0 & 2.78 & 0 & 0 & 0 \\ 0 & 0 & 2.86 & 0 & 0 \\ 0 & 0 & 0 & 2.77 & 0 \\ 0 & 0 & 0 & 0 & 2.81 \end{bmatrix}$$

$\eta\lambda$ kinematically equivalent moment due to shell

η EVALUATION

for a typical element of shell mass M_{si}

$$M_{si+1} = \frac{M_{si}}{6} \ell_i \left(2\ddot{\xi}_i + \ddot{\xi}_{i+1} \right)$$

$$= \frac{M_{si}}{6} \ell_i \begin{pmatrix} 2 & 1 \end{pmatrix} \begin{Bmatrix} \ddot{\xi}_i \\ \ddot{\xi}_{i+1} \end{Bmatrix}$$

λ EVALUATION

$$\lambda = \begin{bmatrix} 1.239 & -.239 & 0 & 0 & 0 & 0 \\ & 1.089 & -.089 & 0 & 0 & 0 \\ 0 & 0 & 1.089 & -.089 & 0 & 0 \\ 0 & 0 & 0 & 1.089 & -.089 & 0 \\ 0 & 0 & 0 & & 1.089 & -.089 \end{bmatrix}$$

relates nodal accelerations to accelerations at strain gauge positions i.e.

$$\eta = \begin{bmatrix} .0456 & .0228 & & & & \\ & .0356 & .0178 & & & \\ & & .0356 & .0178 & & \\ & & & .0356 & .0178 & \\ & & & & .0356 & .0178 \end{bmatrix}$$

ρ Inertia effects of transverse stiffeners

$$M_{st_i} = M_{st}\, 1.2 \left(\frac{X_i + X_{i+1}}{2} \right)$$

$$= .0036 \left(X_i + X_{i+1} \right)$$

$$\rho = \begin{bmatrix} .0036 & .0036 & & & & \\ & .0036 & .0036 & & 0 & \\ & & .0036 & .0036 & & \\ & & & .0036 & .0036 & \\ & 0 & & & .0036 & .0036 \end{bmatrix}$$

m Nodal mass matrix

$$= \begin{bmatrix} .2877 & .2861 & .2874 & .2866 & .2863 \end{bmatrix}$$

π_s, λ Kinematically equivalent shell-shear

$$V_i = \frac{M_{si}}{2} \left(\ddot{\xi}_i + \ddot{\xi}_{i+1} \right)$$

$$\therefore \quad \pi_s = \begin{bmatrix} .0157 & .0157 & & & & \\ & .0139 & .0139 & & & \\ & & .0139 & .0139 & & \\ & & & .0139 & .0139 & \\ & & & & .0139 & .0139 \end{bmatrix}$$

π_ρ Shear force associated with stiffeners

$$V_{STi} = \frac{M_{ST}}{2} \left(\ddot{X}_i + \ddot{X}_{i+1} \right)$$

top element has two stiffeners.

$$\pi_\rho = \begin{bmatrix} .0074 & -.0014 & & & & \\ & .003 & .003 & & & \\ & & .003 & .003 & & \\ & & & .003 & .003 & \\ & & & & .003 & .003 \end{bmatrix}$$

5 x 6

δ Shear force associated with P

$$V_{Pi} = \frac{\ell_i}{2} \left(P_i + P_{i+1} \right)$$

$$\delta = \begin{bmatrix} 1.78 & 1.78 & 0 & 0 & 0 \\ & 1.576 & 1.576 & 0 & 0 \\ & & 1.615 & 1.615 & 0 \\ & & & 1.535 & 1.535 \\ & & & & 3.23 \end{bmatrix}$$

Ω Forms difference in shear force across each element

$$\Omega = \begin{bmatrix} -1 & 0 & 0 & 0 & 0 \\ 1 & -1 & 0 & 0 & 0 \\ 0 & 1 & -1 & 0 & 0 \\ 0 & 0 & 1 & -1 & 0 \\ 0 & 0 & 0 & 1 & -1 \end{bmatrix}$$

ORTHOGONALITY OF EXPERIMENTAL EIGENVECTORS

$$\Phi^t \Phi = \begin{bmatrix} 0.153 & & & & & \\ 0.010 & 0.252 & & & & \\ 0.000 & -0.021 & 0.257 & & \text{SYMMETRICAL} & \\ 0.004 & -0.002 & 0.024 & 0.2180 & & \\ 0.012 & 0.000 & -0.018 & 0.013 & 0.251 & \\ 0.000 & 0.017 & -0.002 & -0.011 & 0.078 & 0.189 \end{bmatrix}$$

5th Order Polynomial gives δ_1 and α_1 below

$$\delta_1 = \begin{bmatrix} 1.139 & 3.831 & -2.47 & 1.56 & -0.49 \\ -.04 & 1.364 & 2.257 & -0.58 & 0.15 \\ .019 & -.200 & 1.785 & 1.828 & -.20 \\ -.0169 & .143 & -.500 & 2.136 & 1.307 \\ .05 & -.363 & -1.059 & -1.840 & 4.327 \end{bmatrix}$$

and

$$\alpha_1 = \begin{bmatrix} 3.03 & 6.03 & -4.83 & 3.12 & -1.01 \\ -.08 & 3.01 & 2.71 & -.923 & +.26 \\ +.03 & -.35 & 3.81 & 2.02 & -.3 \\ -.025 & .21 & -.77 & 4.09 & 1.2 \\ .066 & -.51 & 1.51 & -2.7 & 6.85 \end{bmatrix}$$

COMPARISON OF THE STATISTICALLY INTEGRATED AERODYNAMIC ELEMENTS OVER FOUR AND FIVE ELEMENTS

$$\sqrt{\overline{C_{LF}^2}} = \frac{\sqrt{\sum_{i=1}^{N}\sum_{j=1}^{N} R_{ij}(o)}}{\frac{1}{2}\rho U^2 N A_e}$$

for the case $U/n\,D = 14.0$, turbulent flow lift forces with the large face windward. The cross correlation matrix is:

$$R_{ij}(o) = \begin{bmatrix} 0.120 & -0.100 & 0.069 & 0.016 & 0.038 \\ & 0.148 & 0.148 & 0.102 & 0.160 \\ & & 0.221 & 0.196 & 0.256 \\ \text{SYMMETRICAL} & & & 0.330 & 0.500 \\ & & & & 0.896 \end{bmatrix}$$

$N = 4, \sqrt{\overline{C_{LF}^2}} = 0.410$

$N = 5, \sqrt{\overline{C_{LF}^2}} = 0.420$

APPENDIX III

INDEX TO FIGURES

TABLES I and TABLE 2

FIGURES 1 to 67

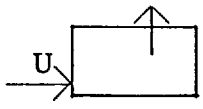
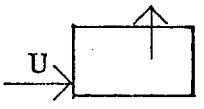
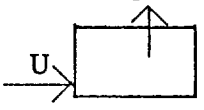
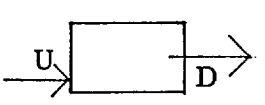
INDEX TO FIGURES

TABLES I AND II OF AERODYNAMIC RESULTS

FIG. 1 CONCEPT OF TECHNIQUE
2 BUILDING MODEL CONSTRUCTION
3 DETAIL DRAWINGS OF MODEL
4 DETAIL DRAWINGS OF MODEL
5 MODEL MOUNTING
6 GENERAL ARRANGEMENT FOR WIND TUNNEL TESTS
7 PHOTOGRAPH OF 30mm SECTION OF MODEL
8 PHOTOGRAPH SHOWING IN-BUILT ACCELEROMETERS
9 PHOTOGRAPH OF MODEL IN ALIGNING JIG DURING CONSTRUCTION
10 PHOTOGRAPH OF MODEL UNDER TEST IN WIND TUNNEL
11 COMPUTER FLOW CHART - MODEL DESIGN
12 DYNAMIC TEST SET UP FOR MEASURING EXPERIMENT FREQUENCY REPONSE FUNCTION
13 1ST EIGENVECTOR RESPONSE LOCI
14 2ND EIGENVECTOR RESPONSE LOCI
15 3RD EIGENVECTOR RESPONSE LOCI
16 4TH EIGENVECTOR RESPONSE LOCI
17 VARIATION ON NON-DIMENSIONAL DAMPING WITH FREQUENCY
18 PREDICTED FORCE SPECTRUM (ALTERNATIVE APPROACH)
19 PERTURBATION PHENOMENON INVESTIGATION FLOW CHART
20 MATHEMATICAL PERTURBATION OF ALTERNATIVE TECHNIQUE
21 FLOW CHART - T.F.A. STATIC AND DYNAMIC TESTS
22 FLOW CHART - DATA GATHERING OF RANDOM SIGNALS
23 FLOW CHART - RANDOM FORCE DATA REDUCTION
24 FLOW CHART FOR MAIN COMPUTER PROGRAM WITH OVERLAY STRUCTURE
25 PHOTOGRAPH OF VIBRATOR + FORCE TRANSDUCER ATTACHED TO MODEL
26 COMPARISON OF ACTUAL AND PREDICTED FORCE POWER SPECTRA
27 COMPARISON OF ACTUAL AND PREDICTED FORCE POWER SPECTRA
28 COHERENCE + PHASE BETWEEN ACTUAL AND PREDICTED RANDOM FORCE:
29/ SINUSOIDAL FORCE AT RESONANCE/COHERENCE AND PHASE
30
31/ PREDICTION OF RANDOM FORCE SPECTRUM/
32 COHERENCE AND PHASE
33 MOMENT - VOLT RELATIONSHIP

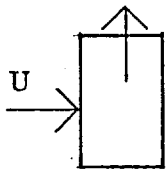
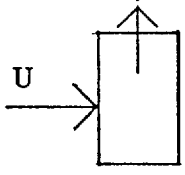
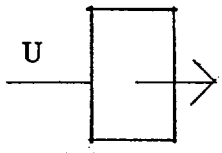
INDEX TO FIGURES CONT'D

FIG.			
	34	SMOOTH FLOW LIFT ACCEL. v U	A = 15.6
	35	SMOOTH FLOW LIFT DISP. SPECTRUM v^{nD}/U	A = 15.6
	36	TURBULENT FLOW LIFT ACCEL. v U	A = 15.6
	37	TURBULENT FLOW LIFT DISP. SPECTRUM v^{nD}/U	A = 15.6
	38	TURBULENT FLOW DRAG ACCEL. v U	A = 15.6
	39	SMOOTH FLOW LIFT ACCEL. v U	A = 9.8
	40	TURBULENT FLOW LIFT ACCEL. v U	A = 9.8
	41	TURBULENT FLOW DRAG ACCEL. v U	A = 9.8
	42	COMPARISON WITH VICKERYS RESULTS	A = 9.8
	43	COMPARISON WITH VICKERYS RESULTS	A = 15.6
	44	SMOOTH FLOW LIFT FORCE SPECTRA $U/n_1D = 22.4$	A = 9.8
	45	SMOOTH FLOW LIFT CROSS CORRLN. COEFFT. "	A = 9.8
	46	TURBULENT FLOW LIFT FORCE SPECTRA $U/n_1D = 14.0$	A = 9.8
	47	TURBULENT FLOW CROSS CORRLN. COEFFT. "	A = 9.8
	48	TURBULENT FLOW DRAG FORCE SPECTRA $U/n_1D = 50$	A = 9.8
	49	TURBULENT FLOW DRAG CROSS CORRLN. COEFFT. "	A = 9.8
	50	TURBULENT FLOW DRAG FORCE SPECTRA $U/n_1D = 36.0$	A = 15.6
	51	TURBULENT FLOW LIFT CROSS CORRLN. COEFFT. "	A = 15.6
	52	SMOOTH FLOW LIFT FORCE SPECTRA $U/n_1D = 35.0$	A = 15.6
	53	SMOOTH FLOW LIFT CROSS CORRLN. COEFFT. U "	A = 15.6
	54	SMOOTH FLOW LIFT FORCE SPECTRA $U/n_1D = 48.4$	A = 15.6
	55	SMOOTH FLOW LIFT CROSS CORRLN. COEFFT. "	A = 15.6
	56	TURBULENT FLOW LIFT FORCE SPECTRA $Un_1D = 31.1$	A = 15.6
	57	TURBULENT FLOW LIFT CROSS CORRLN. COEFFT. "	A = 15.6
	58	SMOOTH FLOW LIFT FORCE SPECTRA $U/n_1D = 60.6$	A = 15.6
	59	SMOOTH FLOW LIFT CROSS CORRLN. COEFFT. "	A = 15.6
	60	SMOOTH FLOW LIFT FORCE SPECTRA $U/n_1D = 11.25$	A = 15.6
	61	SMOOTH FLOW LIFT CROSS CORRLN. COEFFT. "	A = 15.6
	62	TURBULENT FLOW LIFT FORCE SPECTRA $U/n_1D = 14.0$	A = 15.6
	63	TURBULENT FLOW LIFT CROSS CORRLN. COEFFT. "	A = 15.6
	64	TURBULENT FLOW LIFT FORCE SPECTRA $U/n_1D = 8.8$	A = 9.8
	65	TURBULENT FLOW LIFT CROSS CORRLN. COEFFT. "	A = 9.8
	66	GALLOPING STABILITY PLOT FOR THE 1 : 2 SECTION	
	67	GALLOPING STABILITY PLOT FOR THE 2 : 1 SECTION	

FLOW	SMOOTH FLOW LIFT 		SMOOTH FLOW LIFT 		TURBULENT FLOW LIFT 		TURBULENT FLOW 	
FIG. NOS.	52 and 53		54 and 55		56 and 57		50 and 51	
U	57.0 ft/s		78.6 ft/s		50.0 ft/s		58.0 ft/s	
$U/n_1 D$	35.0		48.4		31.1		36.0	
STROUHAL NO.	0.087 and 0.097		0.086 and 0.097		0.081		-	
	$\sqrt{C_{LFi}^2}$	$\sqrt{x_i^2}$	$\sqrt{C_{LFi}^2}$	$\sqrt{x_i^2}$	$\sqrt{C_{LFi}^2}$	$\sqrt{x_i^2}$	$\sqrt{C_{DFi}^2}$	$\sqrt{x_i^2}$
1	0.224	.0028	0.273	.0043	0.283	.0068	0.129	.0022
2	0.247	.0022	0.241	.0032	0.343	.0054	0.116	.0021
3	0.289	.0015	0.245	.0023	0.375	.0037	0.140	.0013
4	0.265	.0010	0.241	.0018	0.342	.0023	0.289	.0011
	$\sqrt{C_{LF}^2}$		$\sqrt{C_{LF}^2}$		$\sqrt{C_{LF}^2}$		$\sqrt{C_{DF}^2}$	
PRESENT TESTS	0.198		0.194		0.277		0.093	
VICKERY[2]	-		-		0.260		0.090	

ASPECT RATIO 15.6 B/D = 0.625

TABLE 1 DISTRIBUTION OF FLUCTUATING FORCE COEFFICIENTS DISPLACEMENTS AND COMPARISON WITH VICKERYS RESULTS.

FLOW	SMOOTH FLOW LIFT 		TURBULENT FLOW LIFT 		TURBULENT FLOW DRAG 	
FIG. NOS.	44 and 45		46 and 47		48 and 49	
U	80.5		50.0		50.0	
$U/n_1 D$	22.4		14.0		14.0	
STROUHAL NO.	0.115		0.121		-	
	$\sqrt{C_{LFi}^2}$	$\sqrt{x_i^2}$	$\sqrt{C_{LFi}^2}$	$\sqrt{x_i^2}$	$\sqrt{C_{DFi}^2}$	$\sqrt{x_i^2}$
1	0.028	.00083	0.372	.0034	0.165	.0043
2	0.041	.00076	0.465	.0027	0.150	.0034
3	0.049	.00055	0.554	.0018	0.225	.0024
4	0.068	.00056	0.725	.0013	0.176	.0015
	$\sqrt{C_{LF}^2}$		$\sqrt{C_{LF}^2}$		$\sqrt{C_{DF}^2}$	
PRESENT TESTS	0.026		0.392		0.102	
VICKERY[2]	-		0.410		0.105	

ASPECT RATIO 9.8 $B/D = 1.6$

TABLE 1 DISTRIBUTION OF FLUCTUATING FORCE COEFFICIENTS, DISPLACEMENTS AND COMPARISON WITH VICKERYS RESULTS.

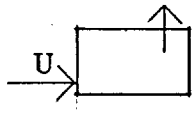
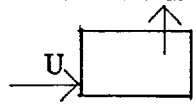
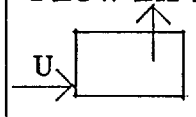
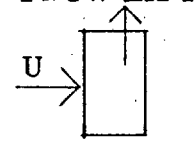
FLOW	SMOOTH FLOW LIFT  1st MODE RESONANCE		SMOOTH FLOW LIFT  2nd MODE RESONANCE		TURBULENT FLOW LIFT  1st MODE RESONANCE		TURBULENT FLOW LIFT  1st MODE RESONANCE	
FIG. NOS.	60 and 61		58 and 59		62 and 63		64 and 65	
U	18.3		98.5		22.7		32.2	
$U/n_1 D$	11.25		60.6		14.0		8.80	
STROUHAL NO.	0.089		0.086 and 0.097		0.081 WIDE BAND		0.115	
	$\sqrt{C_{LFi}^2}$	$\sqrt{x_i^2}$	$\sqrt{C_{LFi}^2}$	$\sqrt{x_i^2}$	$\sqrt{C_{LFi}^2}$	$\sqrt{x_i^2}$	$\sqrt{C_{LFi}^2}$	$\sqrt{x_i^2}$
1	0.208	.0046	0.686	.0085	0.261	.0048	0.407	0.007
2	0.335	.0037	0.885	.0052	0.447	.0037	0.594	0.0050
3	0.613	.0026	0.453	.0058	0.413	.0026	0.976	0.0035
4	0.558	.0015	0.631	.0007	0.424	.0016	1.160	0.0023
	$\sqrt{C_{LF}^2}$		$\sqrt{C_{LF}^2}$		$\sqrt{C_{LF}^2}$		$\sqrt{C_{LF}^2}$	
PRESENT TESTS	0.226		0.222		0.288		0.569	
VICKERY[2]	-		-		0.260		0.410	

TABLE 2 DISTRIBUTION OF FLUCTUATING LIFT COEFFICIENTS, DISPLACEMENTS AND COMPARISON WITH VICKERYS RESULTS, WHEN THE SHEDDING FREQUENCY IS COINCIDENT WITH LIFT RESONANCES.

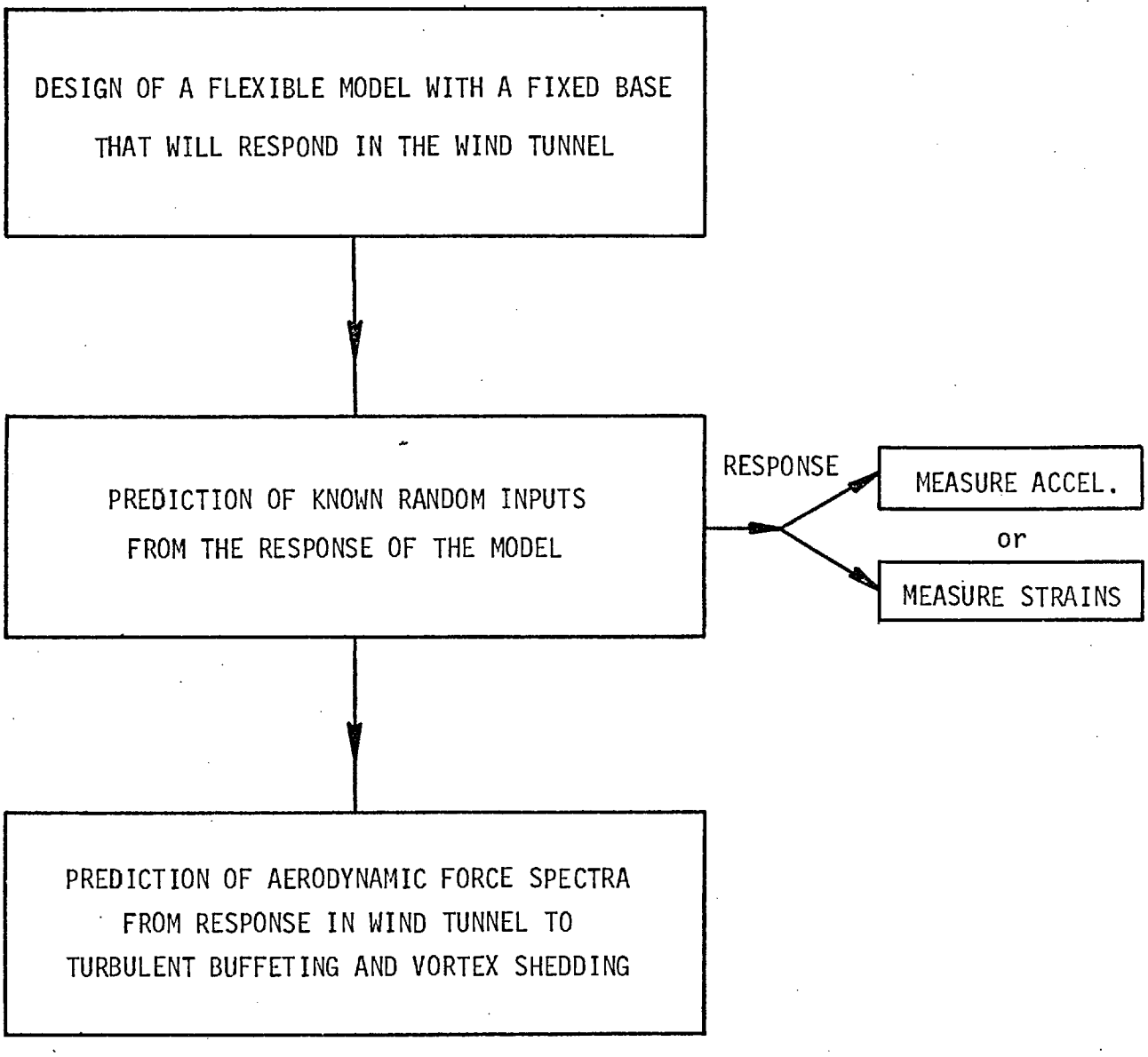
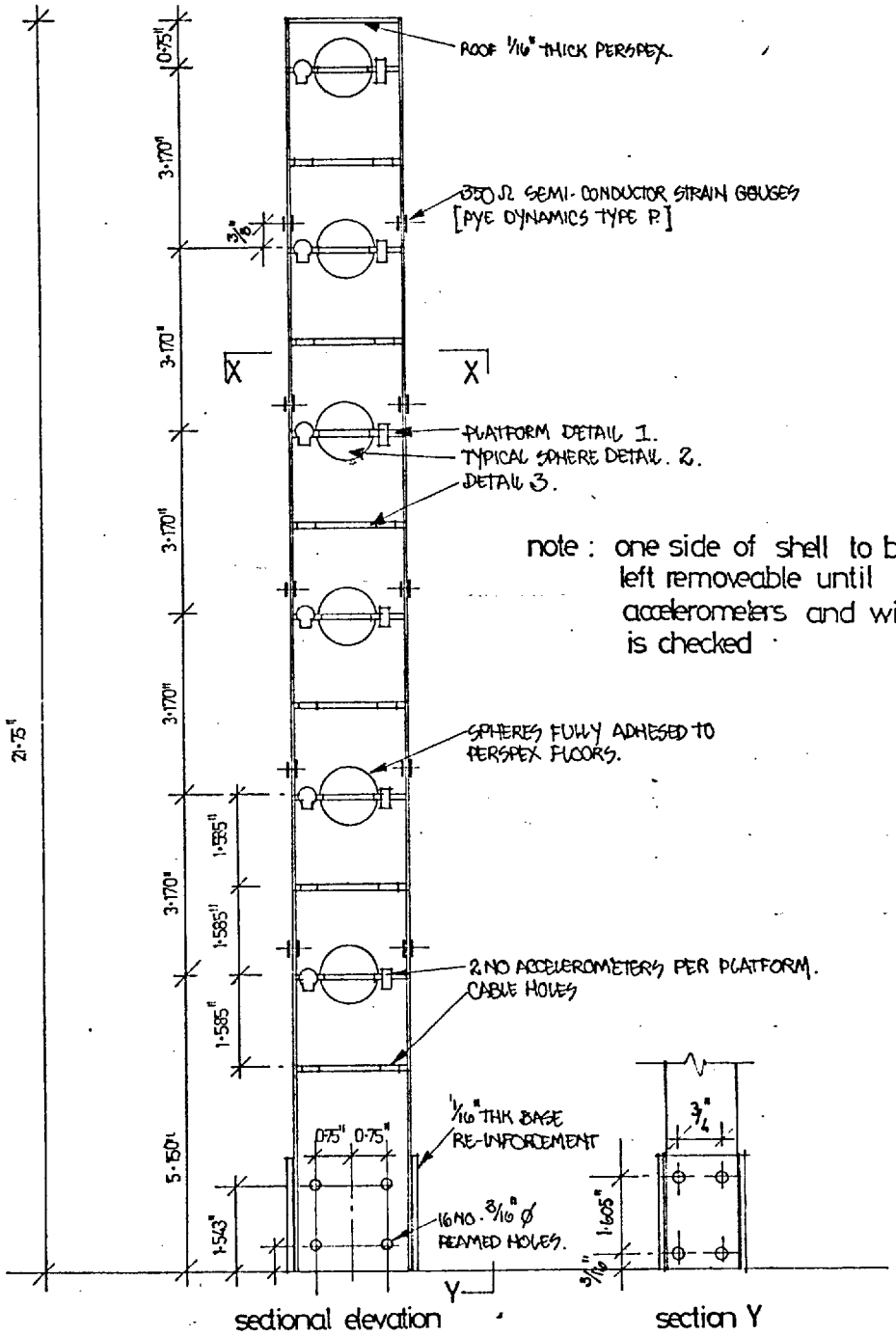
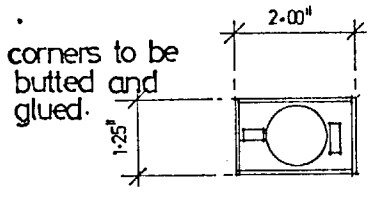


FIG. 1 . CONCEPT OF THE TECHNIQUE.





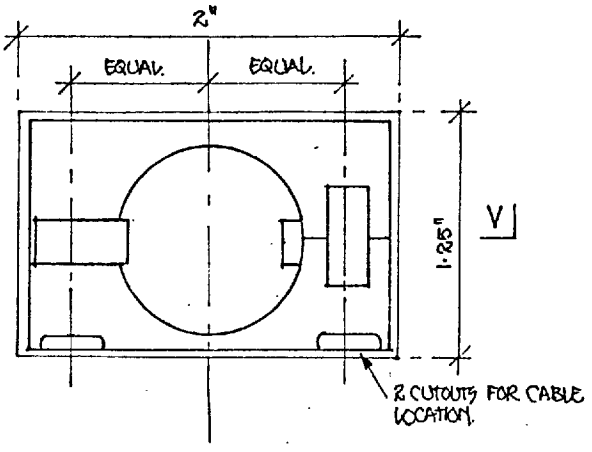
corners to be butted and glued.

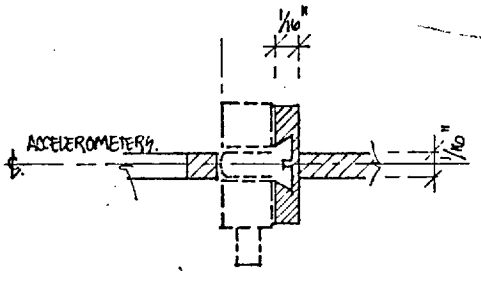
all corners ground sharp

section X

FIG 2

PERSPEX BUILDING MODEL DETAIL : material - I.C.I. Perspex
perspex properties =
$E = 4.5 \times 10^5$ lbs/ ins^2

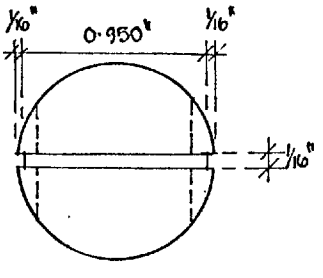




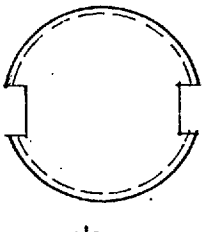
section V

DETAIL 1: PLATFORM DETAIL

weight = 0·260 lb

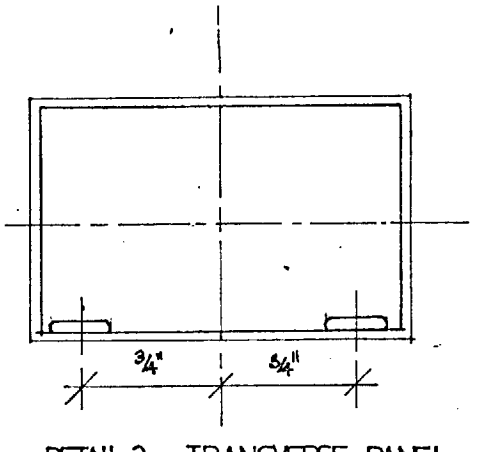


elevation



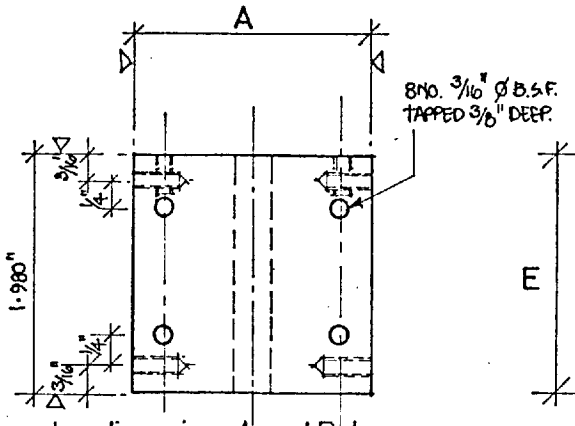
plan

DETAIL 2 : NODAL MASS
material = lead

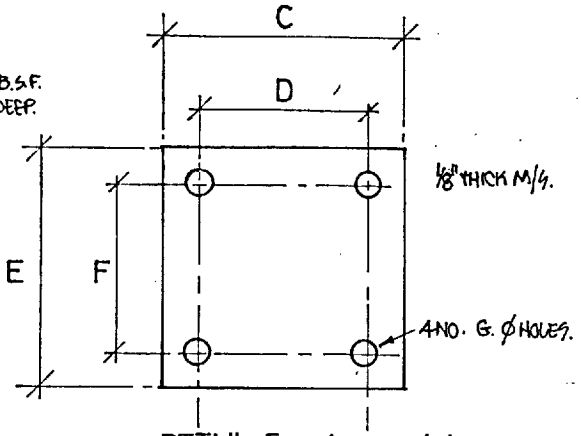


DETAIL 3 TRANSVERSE PANEL

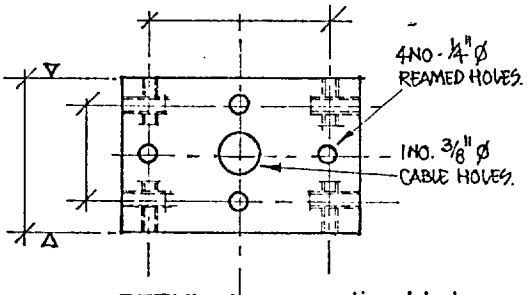
FIG 3



note dimensions A and B to suit inside sizes of perspex



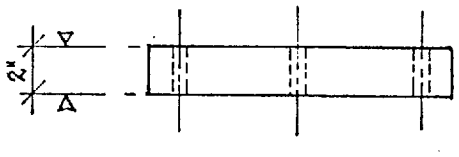
DETAIL 5 clamp plates

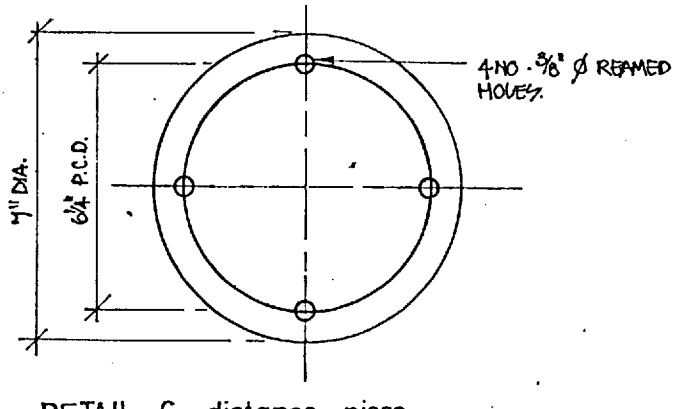


DETAIL 4 mounting block

C	D	E	F	G	No Off

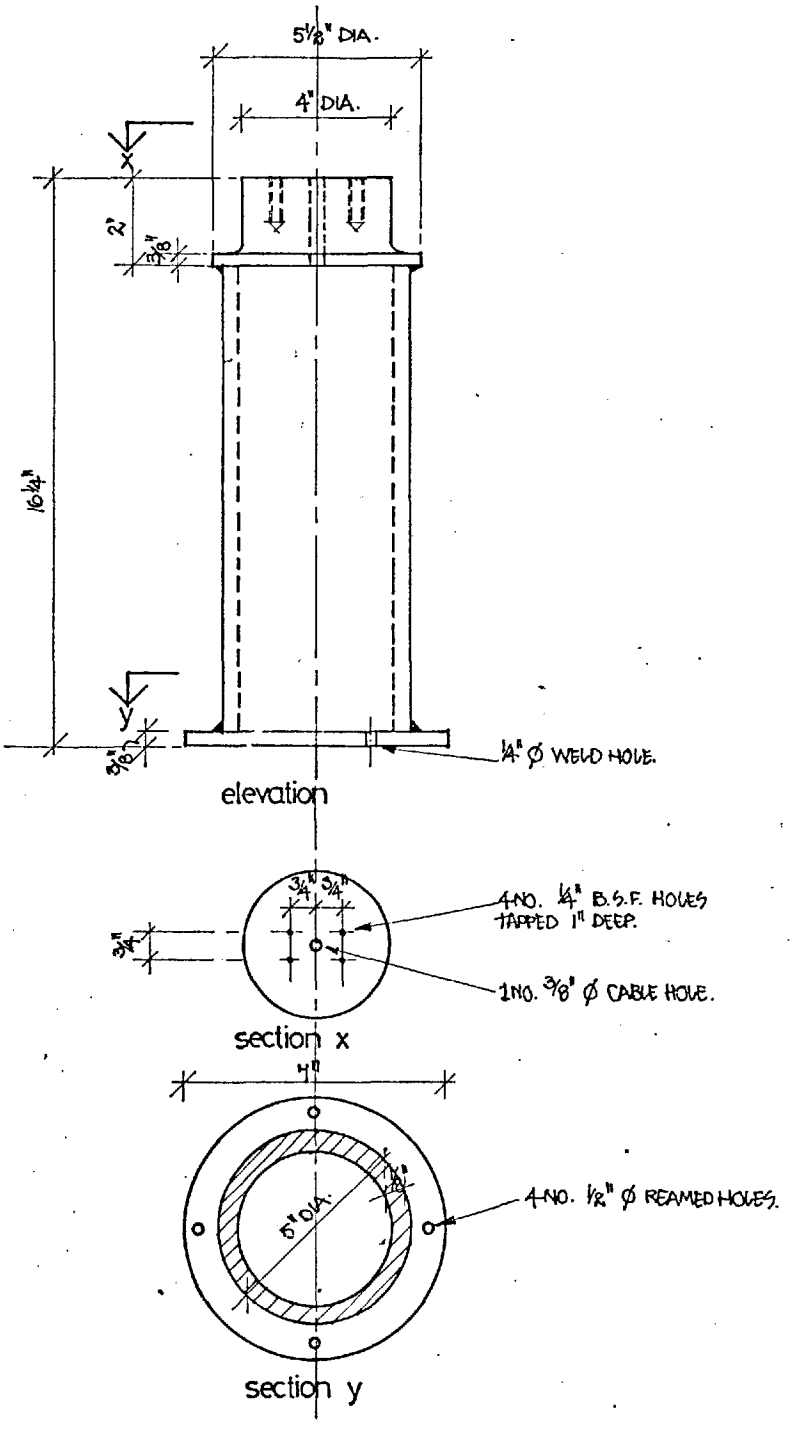
THICKNESS TO SUIT FINAL ASSEMBLY APPROX 2".





DETAIL 6 distance piece
material : mild steel

FIG 4



DETAIL 7 : MODEL MOUNTING
material : mild steel fab.

FIG 5

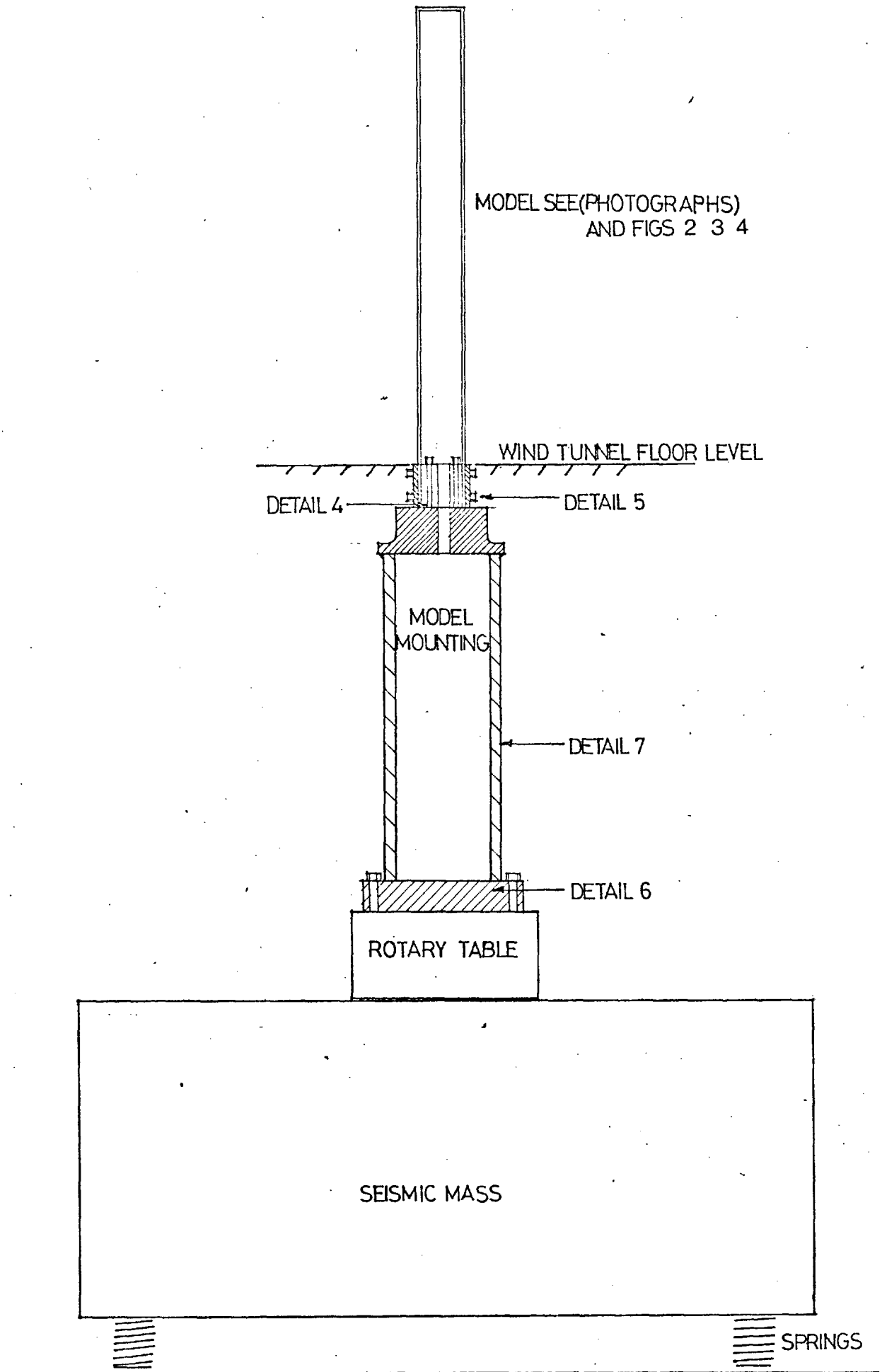

MODEL SEE(PHOTOGRAPHS)
AND FIGS 2 3 4
WIND TUNNEL FLOOR LEVEL
DETAIL 4
DETAIL 5
MODEL
MOUNTING
DETAIL 7
DETAIL 6
ROTARY TABLE
SEISMIC MASS
SPRINGS

FIG 6



FIG 7 SECTION OF MODEL

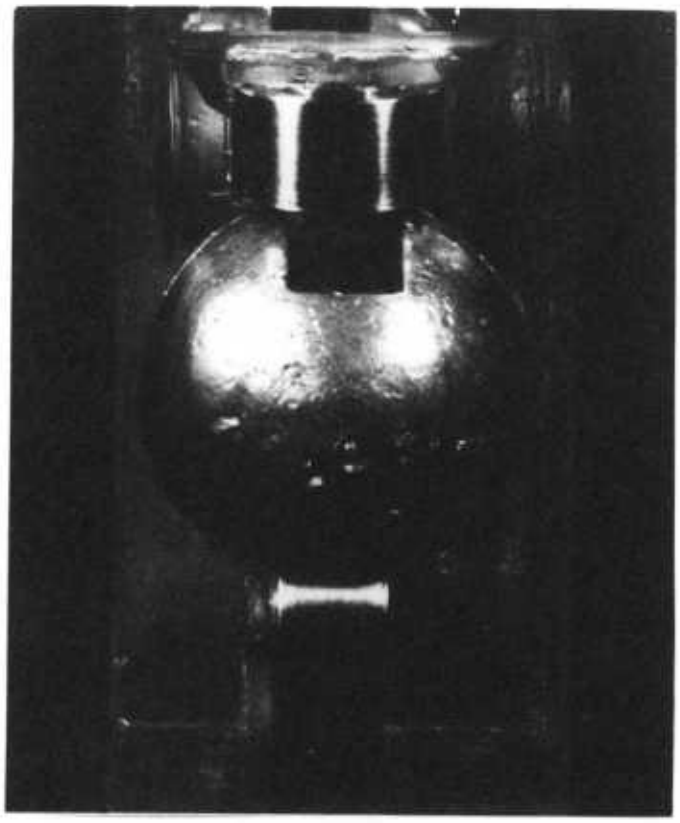


FIG.8 PLAN SECTION SHOWING INBUILT ACCELEROMETERS.

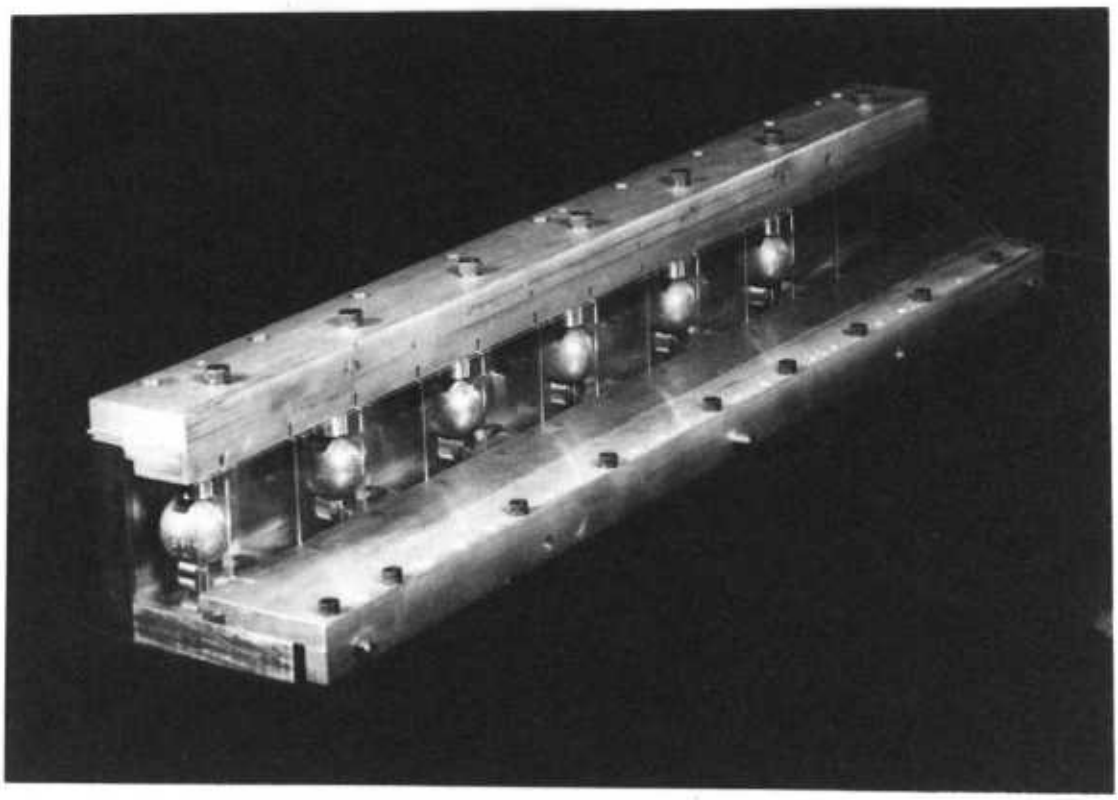


FIG.9 MODEL DURING CONSTRUCTION IN PANEL ALIGNING JIG.

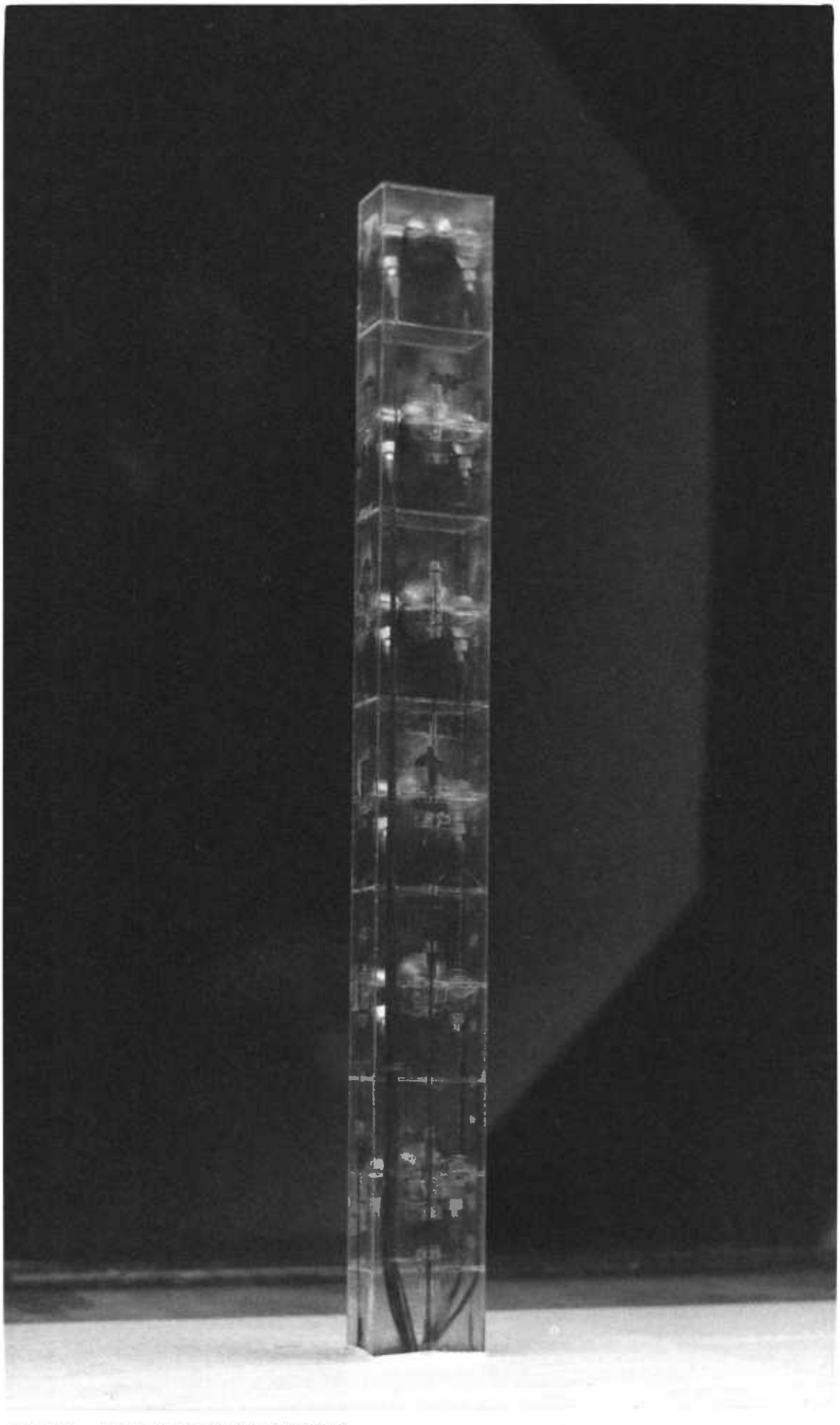
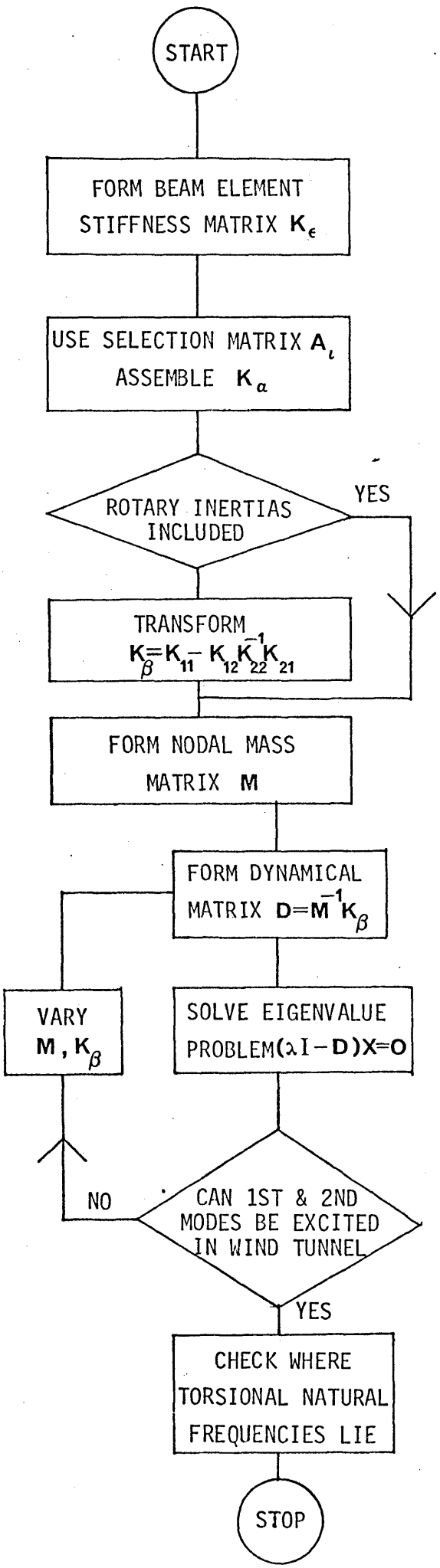


FIG 10 MODEL IN WIND TUNNEL



ESTIMATION OF RESONANT FREQUENCIES MODES, AND RESPONSE

FIG 11 COMPUTER FLOW CHART - MODEL DESIGN

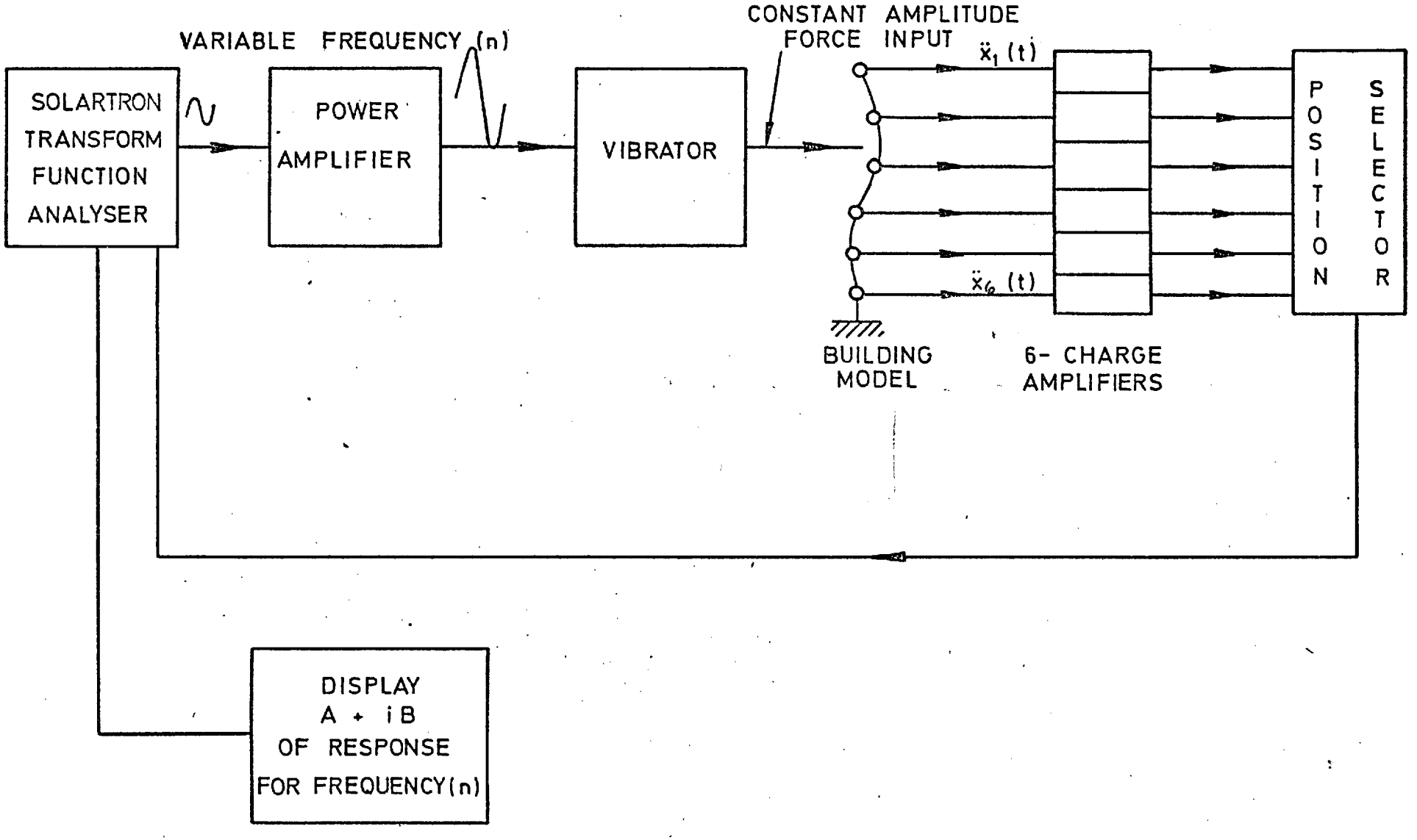
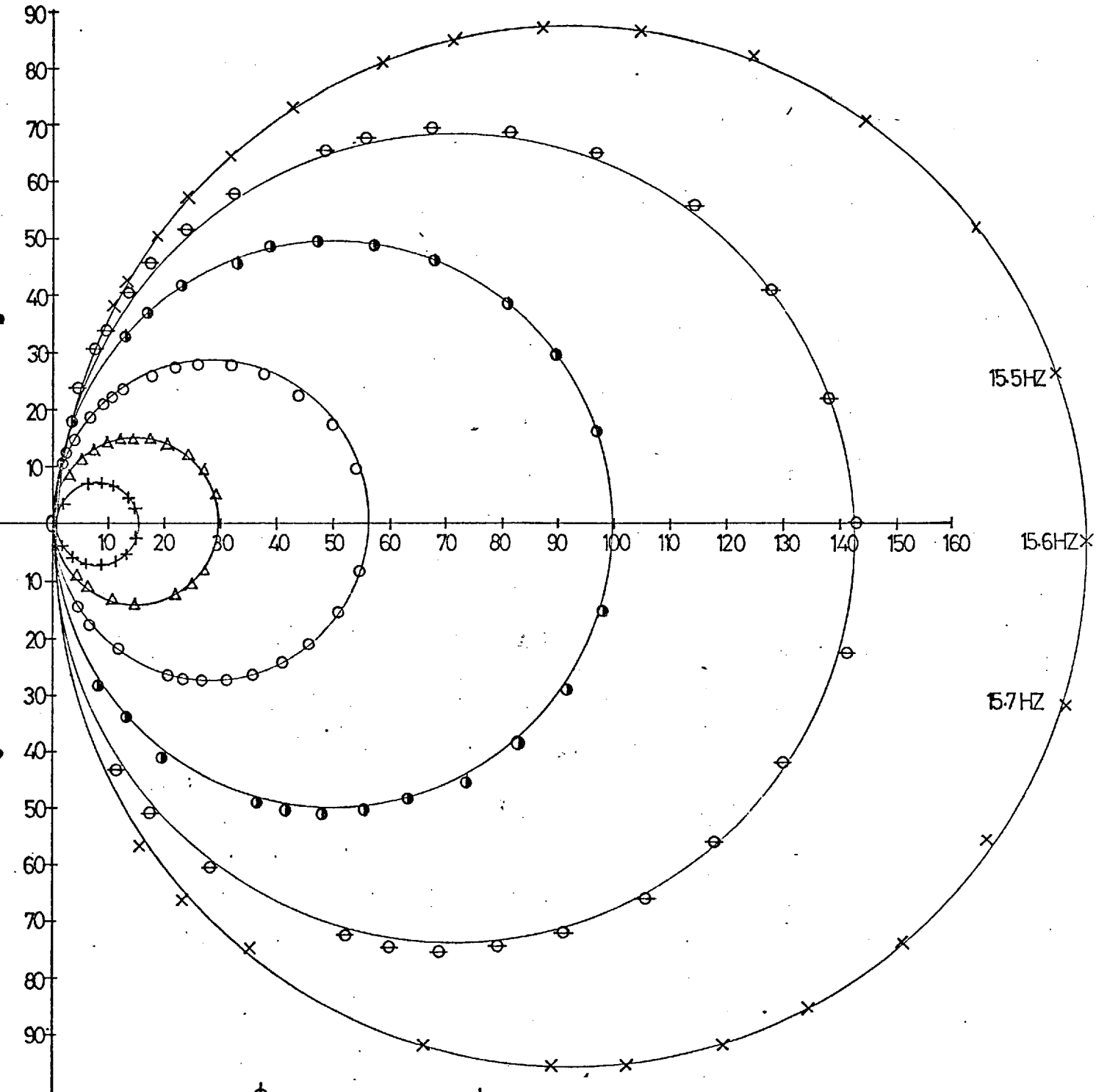
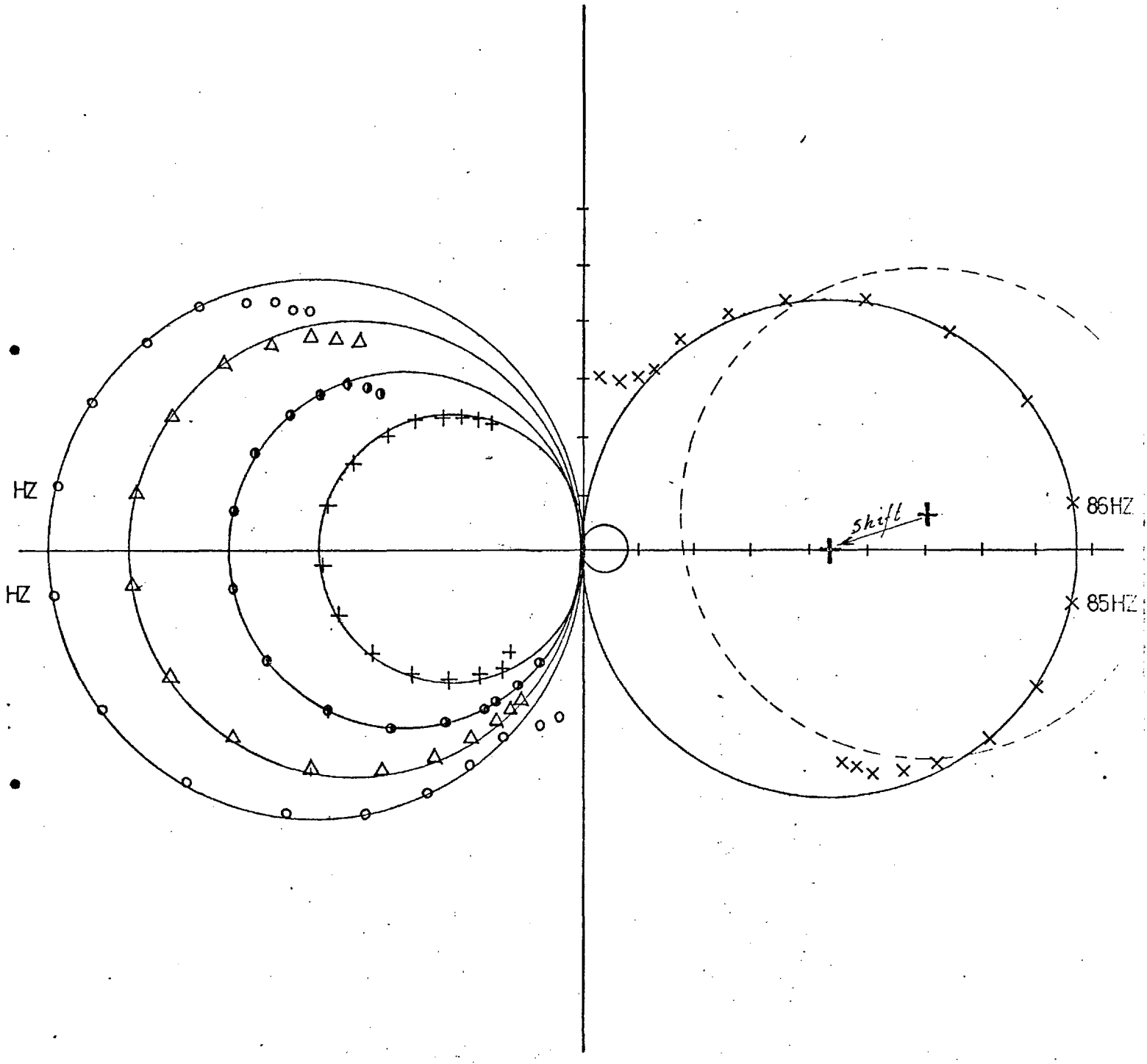


FIG.12 DYNAMIC SET UP FOR MEASURING THE EXPERIMENTAL FREQUENCY RESPONSE FUNCTION H(w).



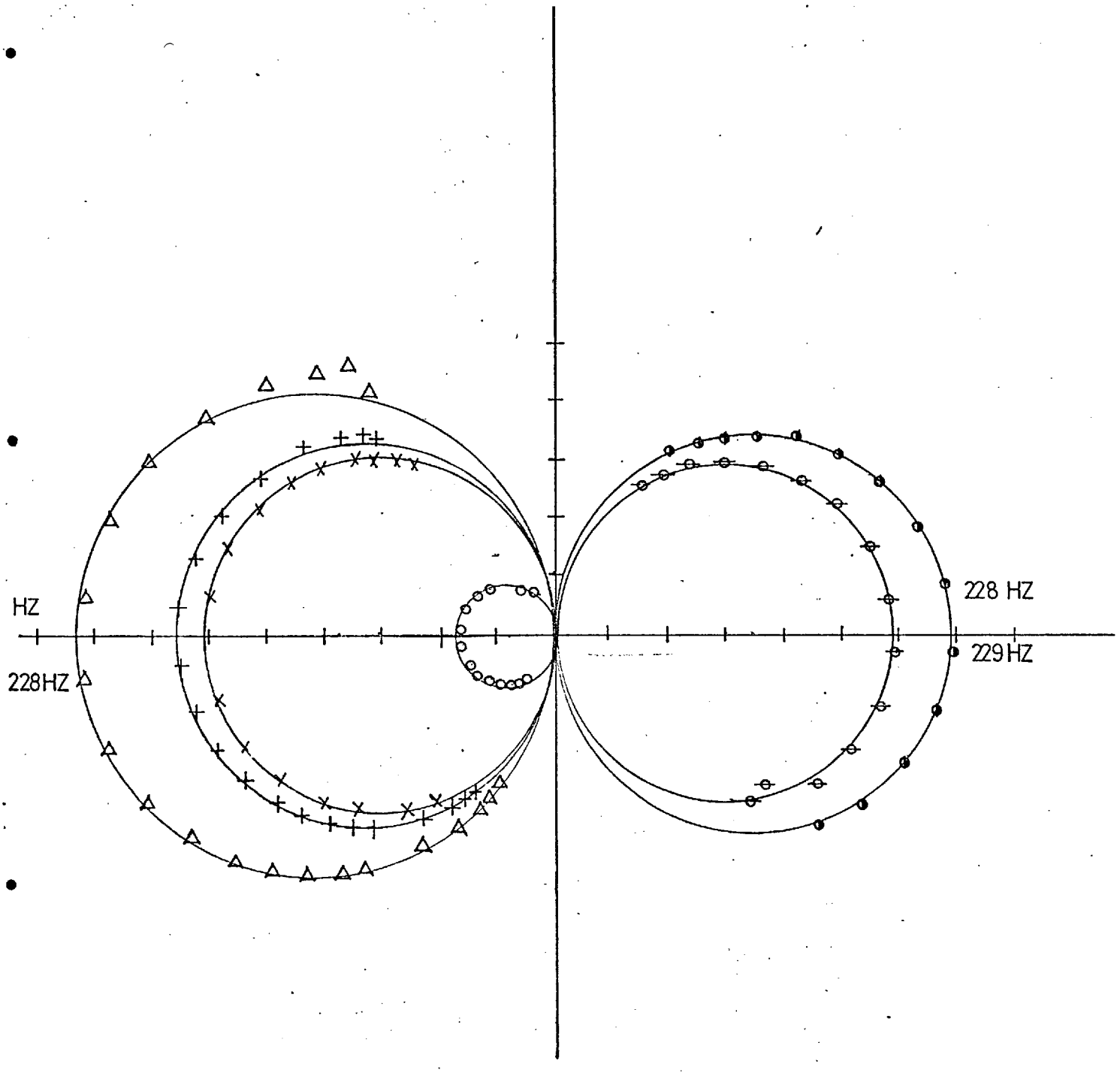
ϕ_{e1} EXPERIMENTAL EIGENVECTOR	ϕ_1 THEORETICAL EIGENVECTOR	g_1 DAMPING $\frac{\Delta\omega}{\omega}$	n_1 RESONANT FREQUENCY
1.000	1.000	0.033	15.6 HZ
0.790	0.765	0.033	15.6
0.567	0.538	0.033	15.6
0.302	0.332	0.033	15.6
0.159	0.160	0.033	15.6
0.070	0.044	0.033	15.6

FIG 13
STRUCTURAL RESPONSE LOCII (FIRST MODE)



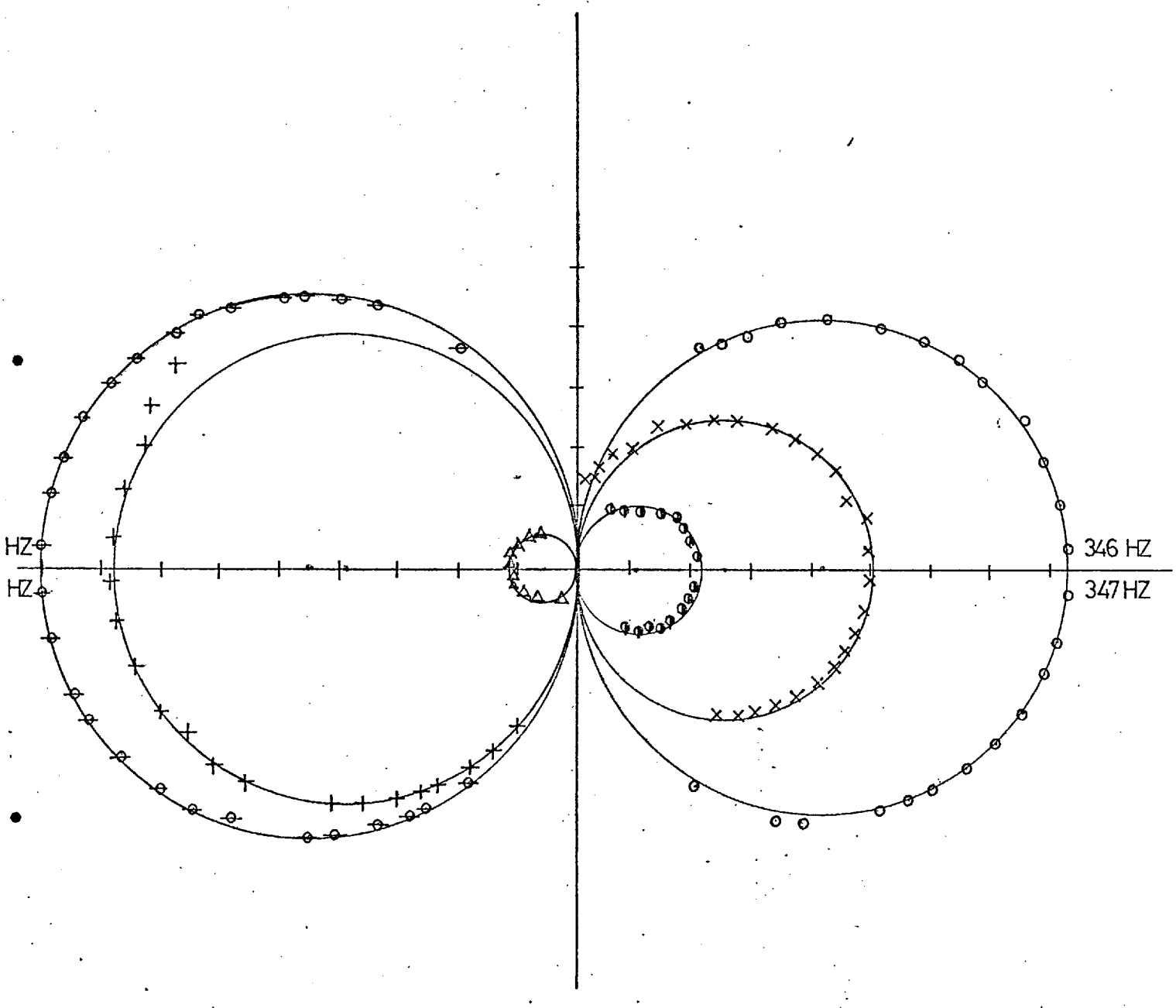
ϕ_{e2} EXPERIMENTAL EIGENVECTOR	ϕ_2 THEORETICAL EIGENVECTOR	g_2 DAMPING $\frac{\Delta\omega}{\omega}$	n_2 RESONANT FREQUENCY
0.952	0.912	.045	85.0 HZ
0.032	- 0.051	.046	85.0
- 0.671	- 0.758	.044	85.0
- 1.000	- 1.000	.044	85.0
- 0.863	- 0.759	.045	85.0
- 0.505	- 0.278	.046	85.0

FIG 14
STRUCTURAL RESPONSE LOCII (SECOND MODE)



ϕ_{e3} EXPERIMENTAL EIGENVECTOR	ϕ_3 THEORETICAL EIGENVECTOR	g_3 DAMPING $\frac{\Delta\omega}{\omega}$	n_3 RESONANT FREQUENCY
- 0.727	- 0.633	0.023	229 HZ
0.710	0.652	0.022	229
0.836	0.752	0.022	229
- 0.247	- 0.253	0.022	229
- 1.000	- 1.000	0.022	229
- 0.796	- 0.601	0.022	229

FIG 15
STRUCTURAL RESPONSE LOCII (THIRD MODE)



Φ_{e4} EXPERIMENTAL EIGENVECTOR	Φ_4 THEORETICAL EIGENVECTOR	g_4 DAMPING $\frac{\Delta\omega}{\omega}$	n_4 RESONANT FREQUENCY
0.536	0.468	.026	346 HZ
- 1.000	- 0.997	.027	346
0.224	0.158	-	346
0.896	1.000	.025	346
0.124	- 0.485	-	346
- 0.865	- 0.989	.025	346

STRUCTURAL RESPONSE LOCII (FOURTH MODE) FIG 16

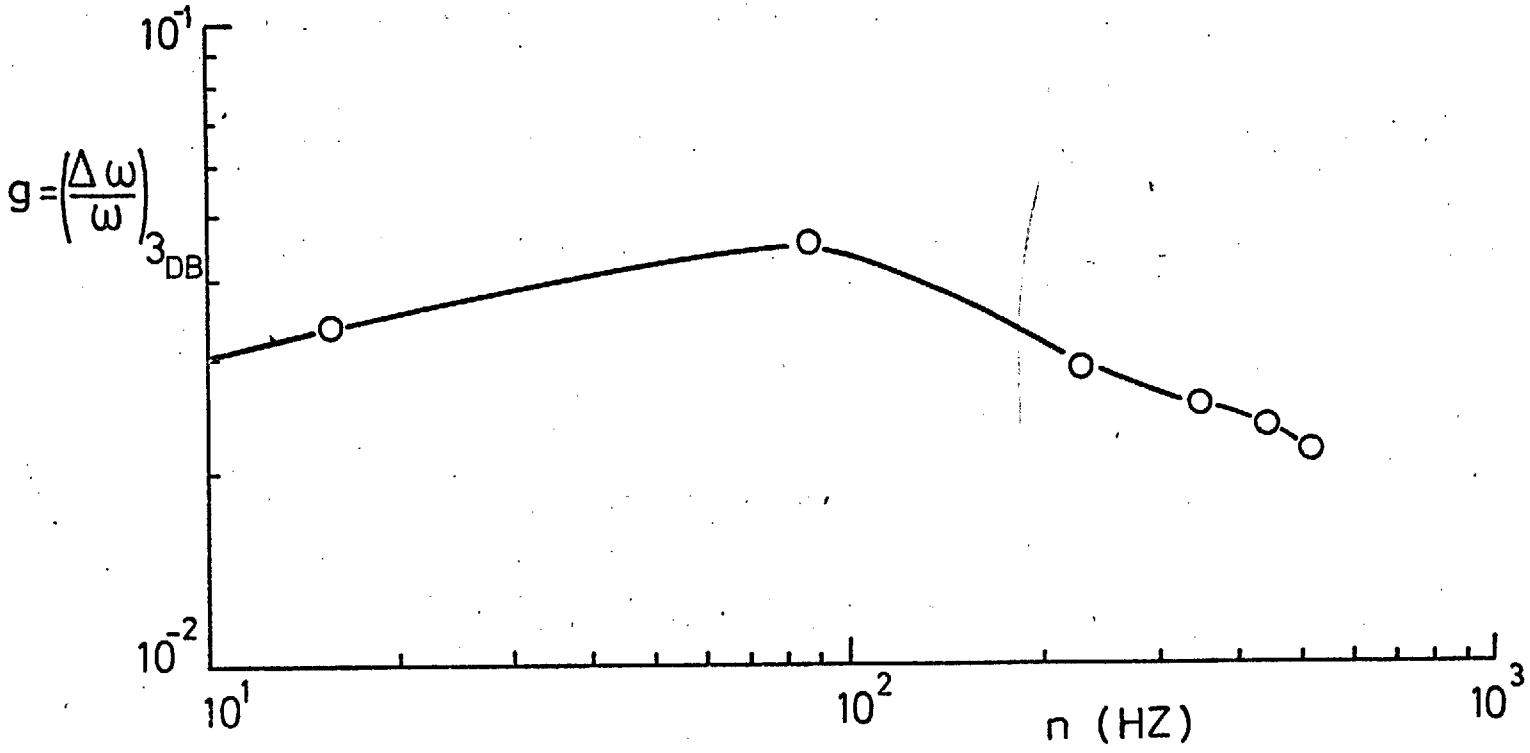


FIG.17 CURVE OF NON DIMENSIONAL DAMPING (g) vs. n (HZ).

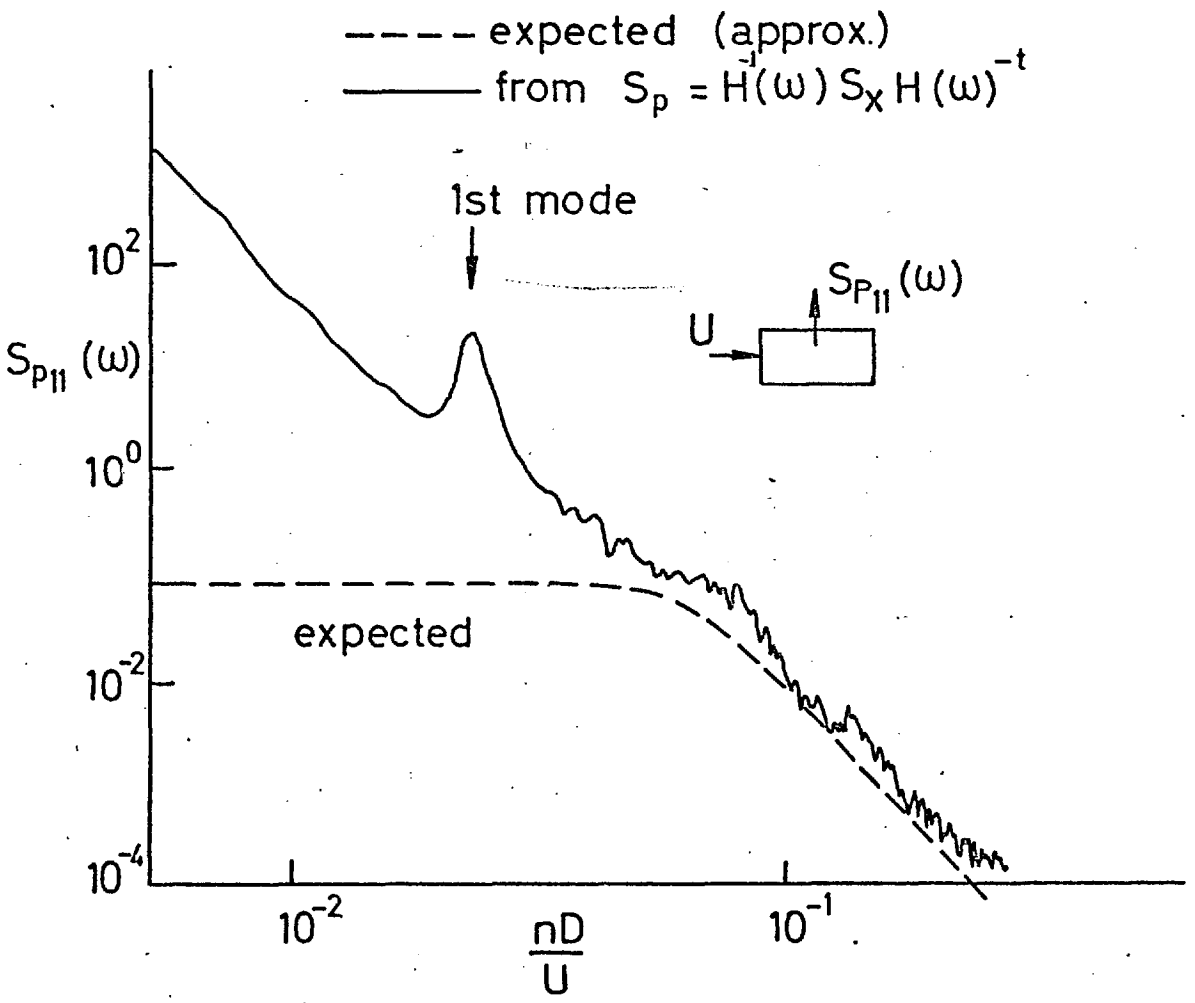


FIG.18 TURBULENT FLOW LIFT FORCE POWER SPECTRA

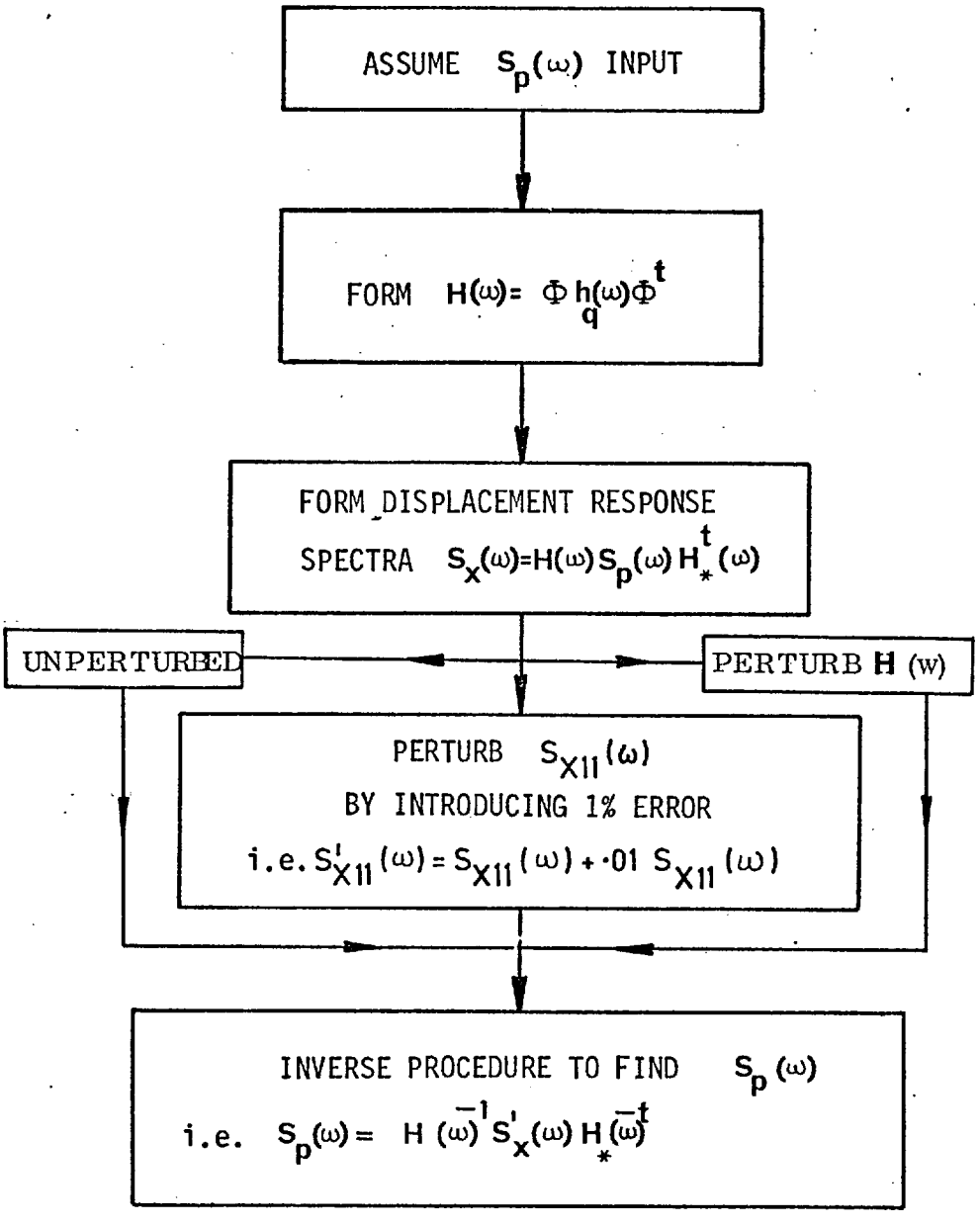


FIG. 19 PERTURBATION PHENOMENON. INVESTIGATION.

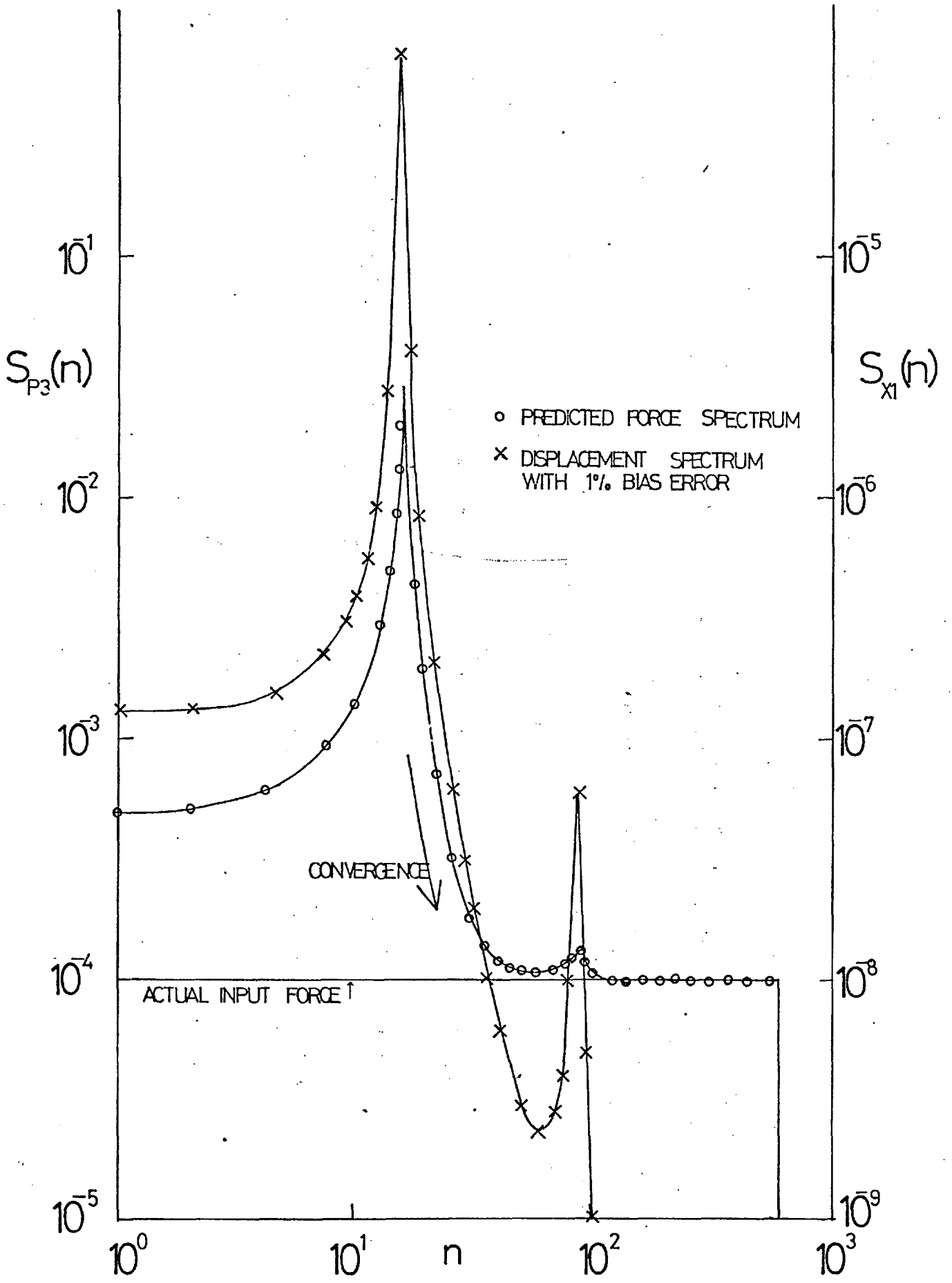


FIG 20 MATHEMATICAL PERTURBATION OF ORIGINAL SYSTEM

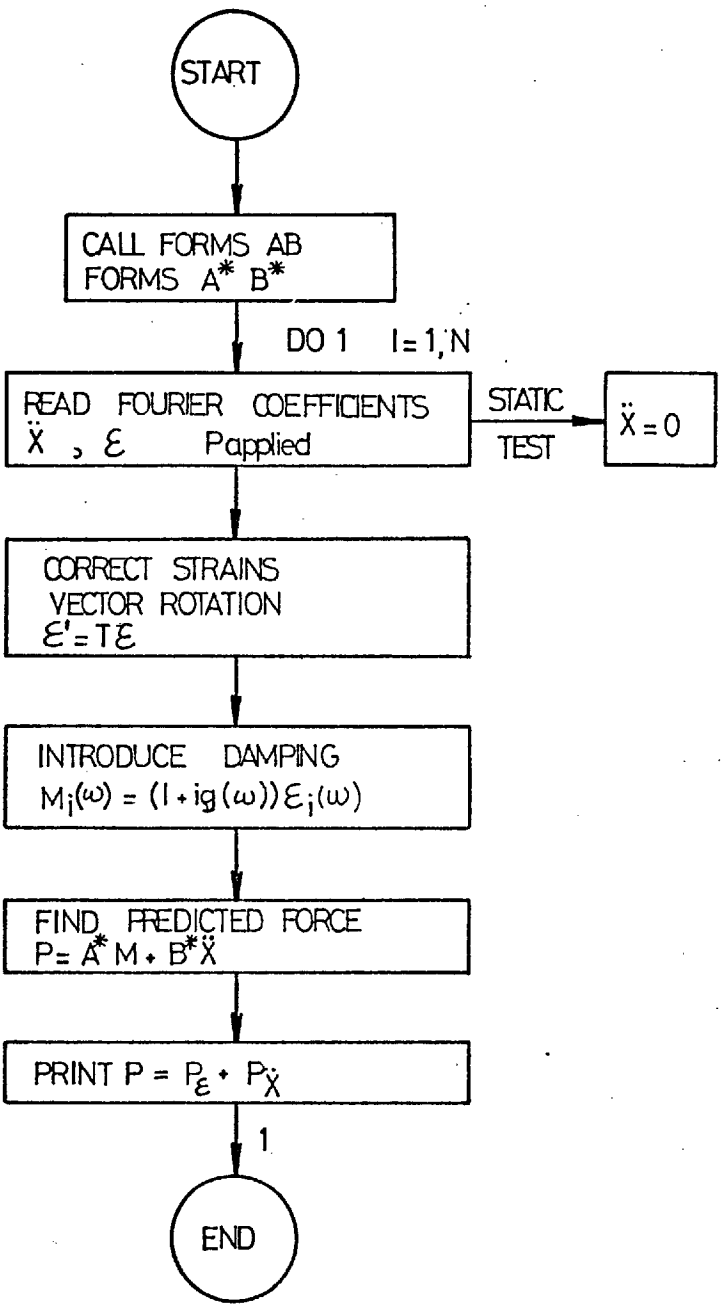
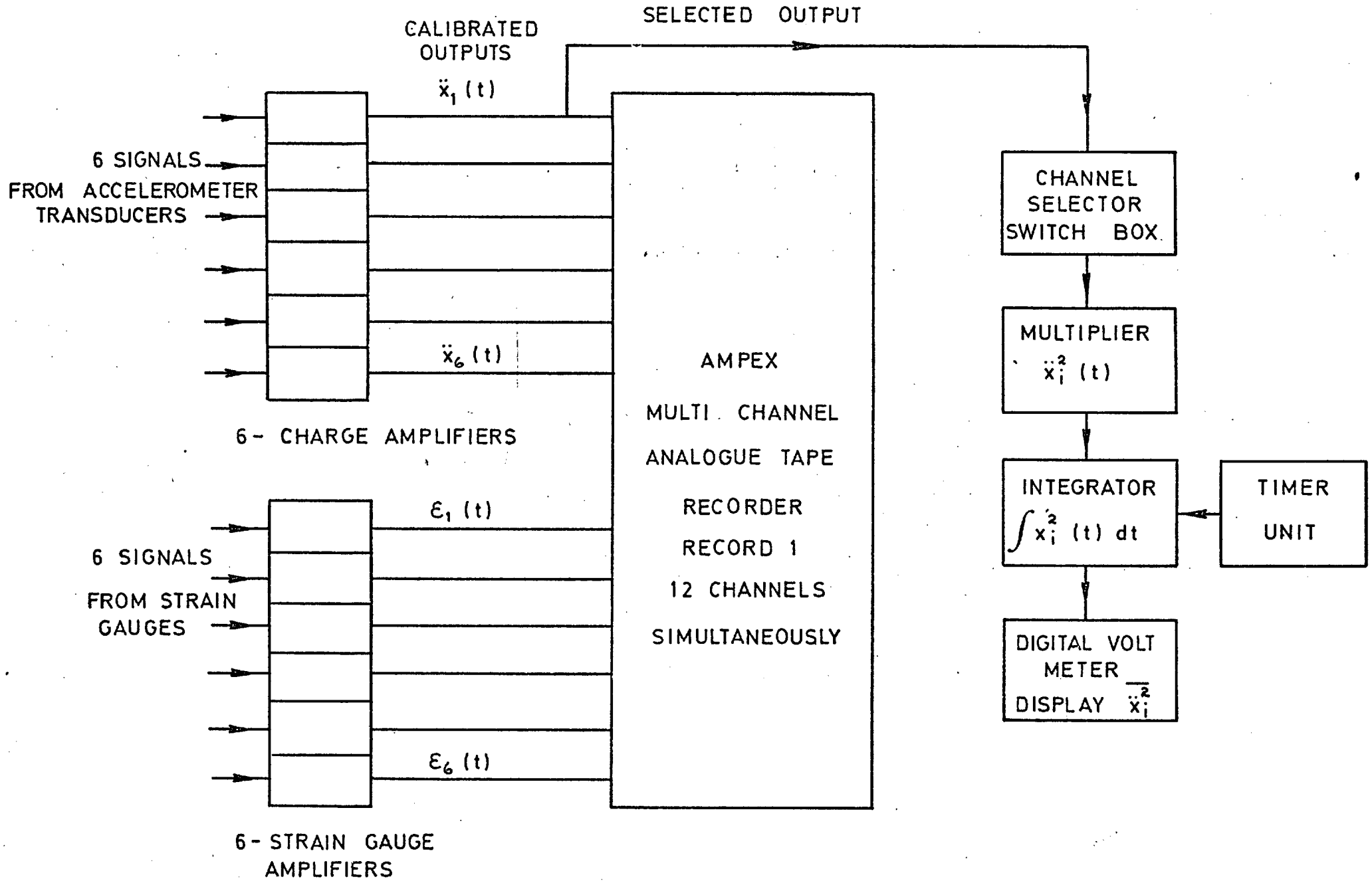


FIG. 21 STATIC & DYNAMIC TESTS
T.F.A. TEST PROGRAM.


CALIBRATED OUTPUTS
SELECTED OUTPUT
$\ddot{x}_1(t)$
6 SIGNALS FROM ACCELEROMETER TRANSDUCERS
$\ddot{x}_6(t)$
6 - CHARGE AMPLIFIERS
AMPEX
MULTI CHANNEL
ANALOGUE TAPE
RECORDER
RECORD 1
12 CHANNELS
SIMULTANEOUSLY
CHANNEL SELECTOR SWITCH BOX
MULTIPLIER
$\ddot{x}_i^2(t)$
INTEGRATOR
$\int \ddot{x}_i^2(t)\,dt$
TIMER UNIT
DIGITAL VOLT METER
DISPLAY $\overline{\ddot{x}_i^2}$
$\varepsilon_1(t)$
6 SIGNALS FROM STRAIN GAUGES
$\varepsilon_6(t)$
6 - STRAIN GAUGE AMPLIFIERS

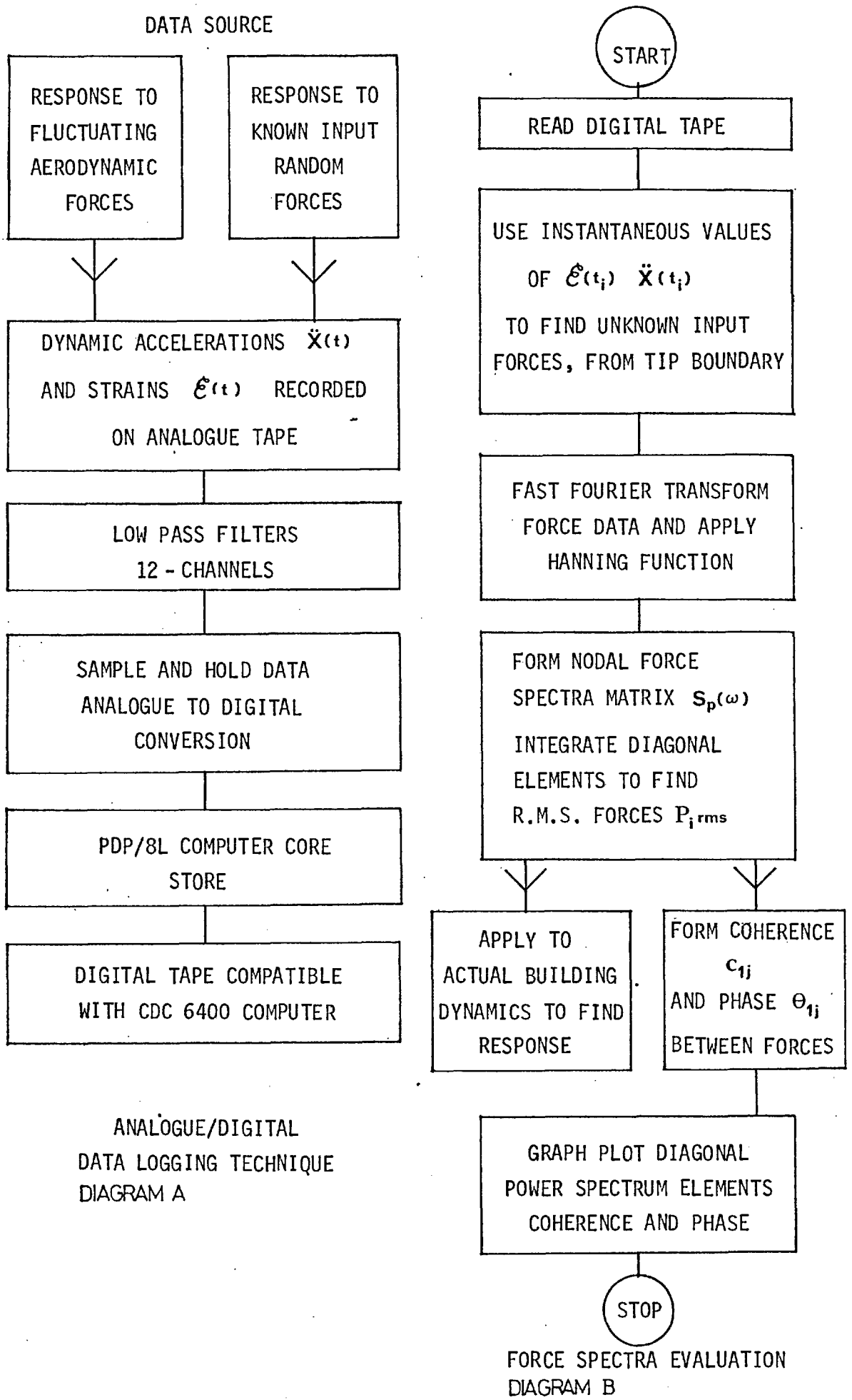


FIG. 23 COMPUTER FLOW CHART- FORCE PREDICTION

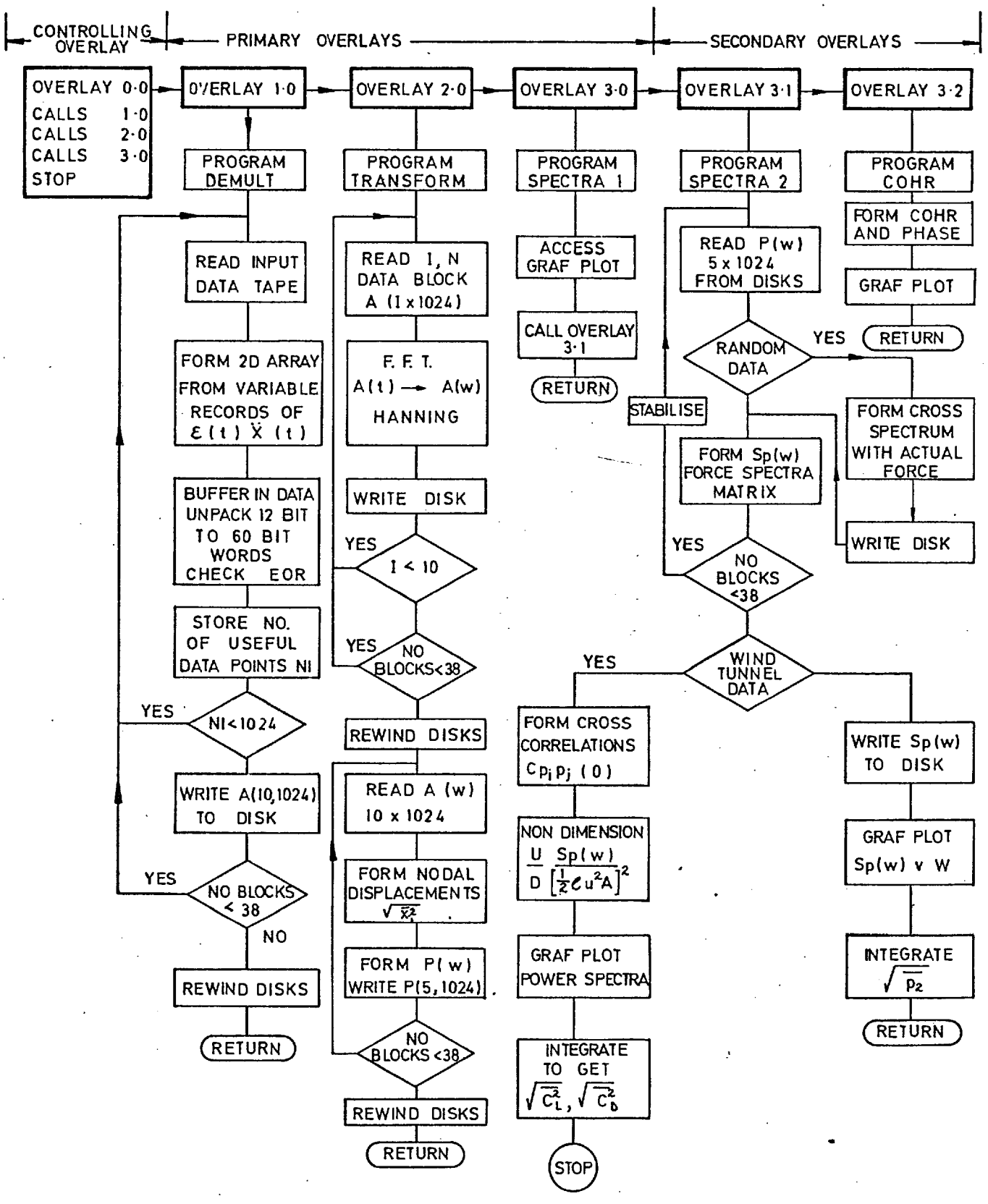


FIG. 24 FLOW CHART FOR RANDOM FORCE / CROSS CORRELATION / COHERENCE PROGRAM.

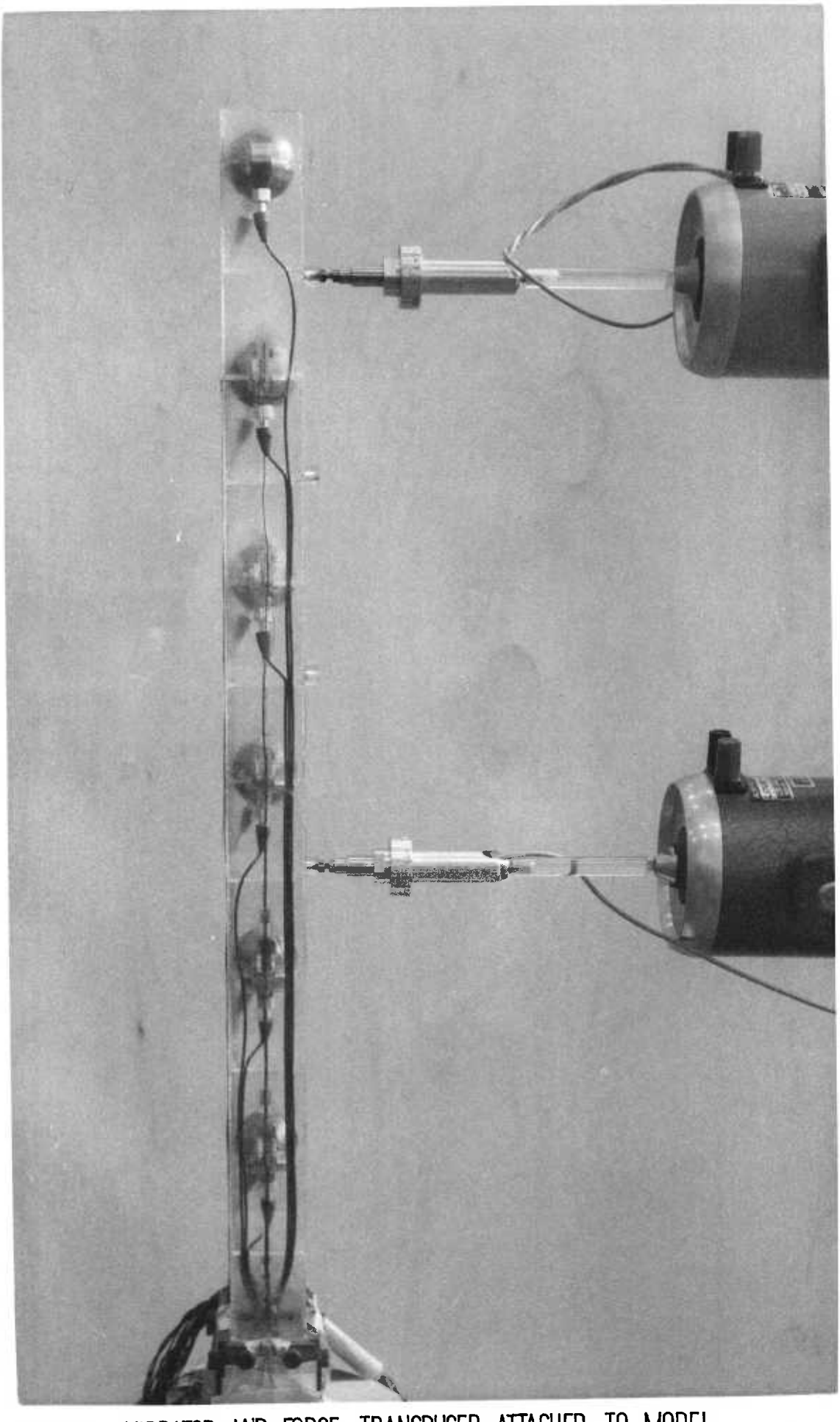


FIG 25 VIBRATOR AND FORCE TRANSDUCER ATTACHED TO MODEL

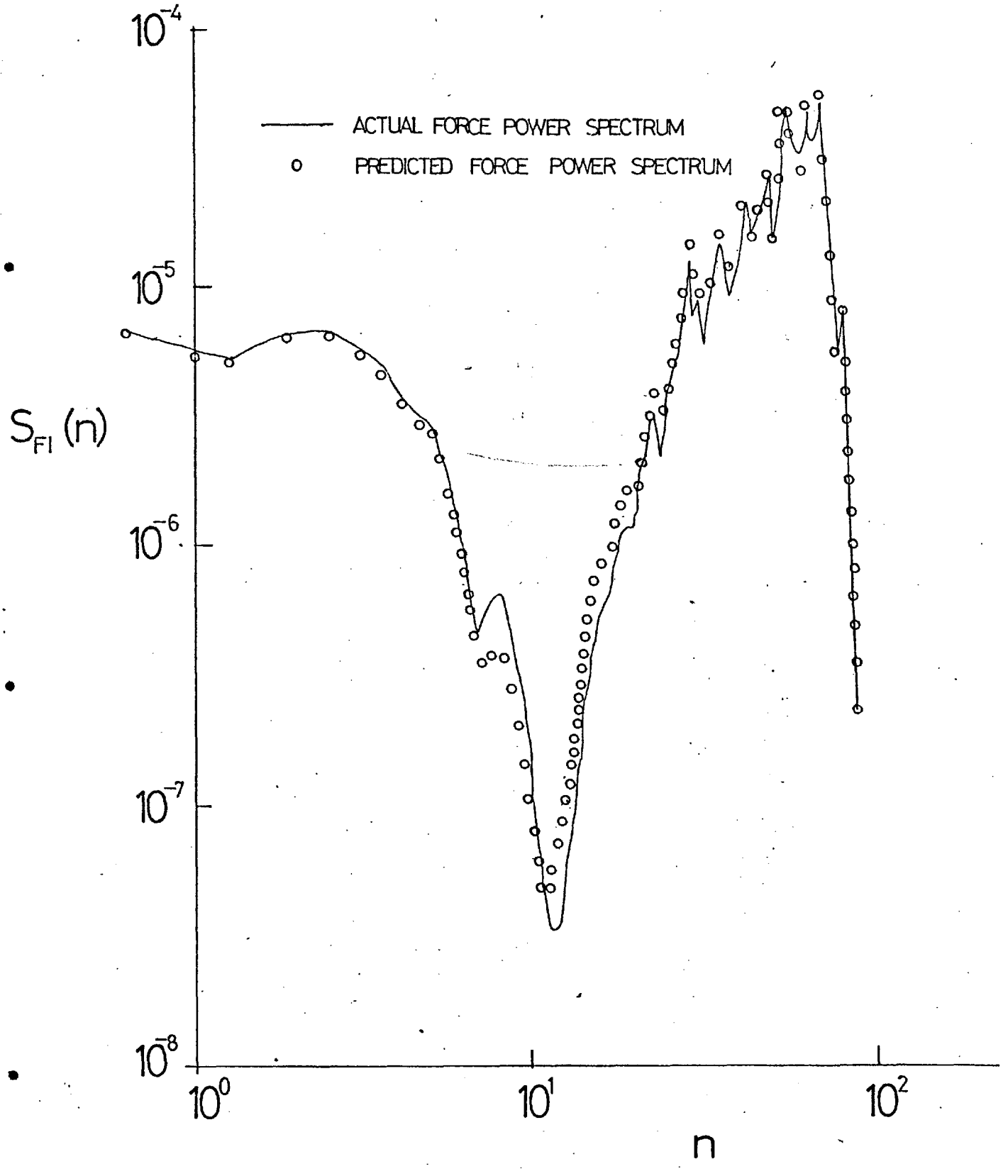


FIG 26 COMPARISON OF ACTUAL AND PREDICTED FORCE POWER SPECTRA

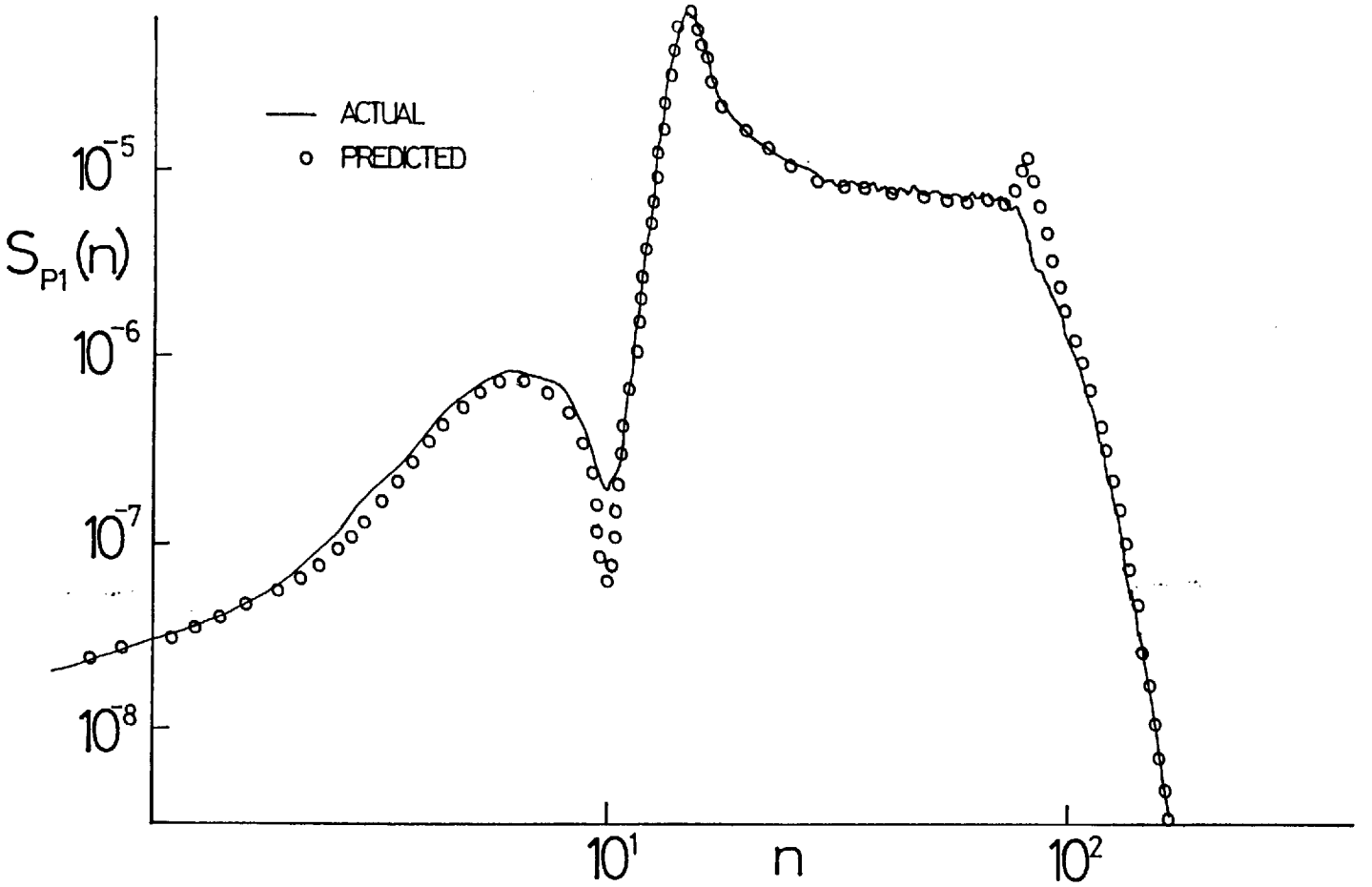


FIG 27. COMPARISON OF ACTUAL AND PREDICTED FORCE POWER SPECTRA

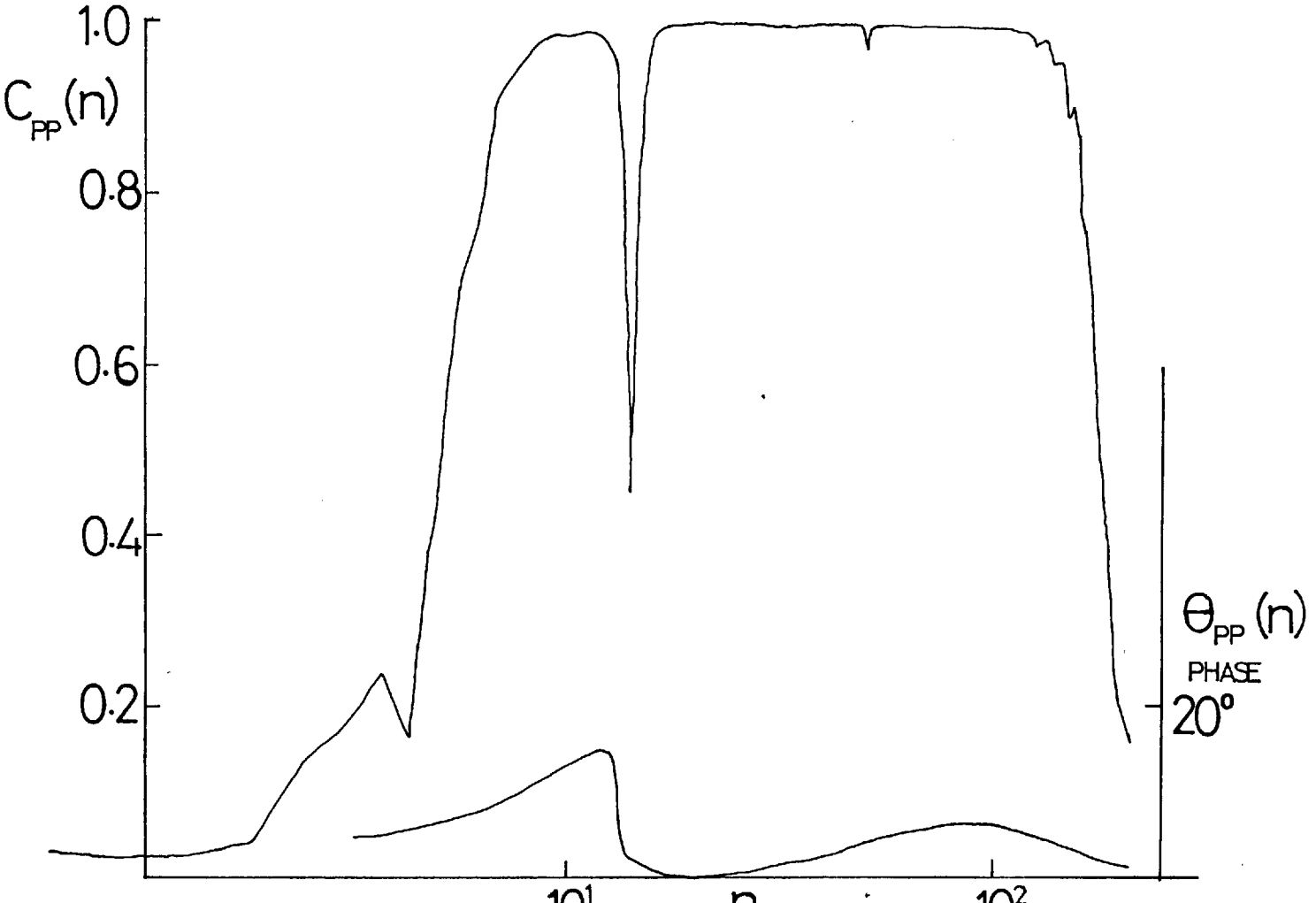


FIG 28 COHERENCE AND PHASE BETWEEN ACTUAL AND PREDICTED RANDOM FORCE

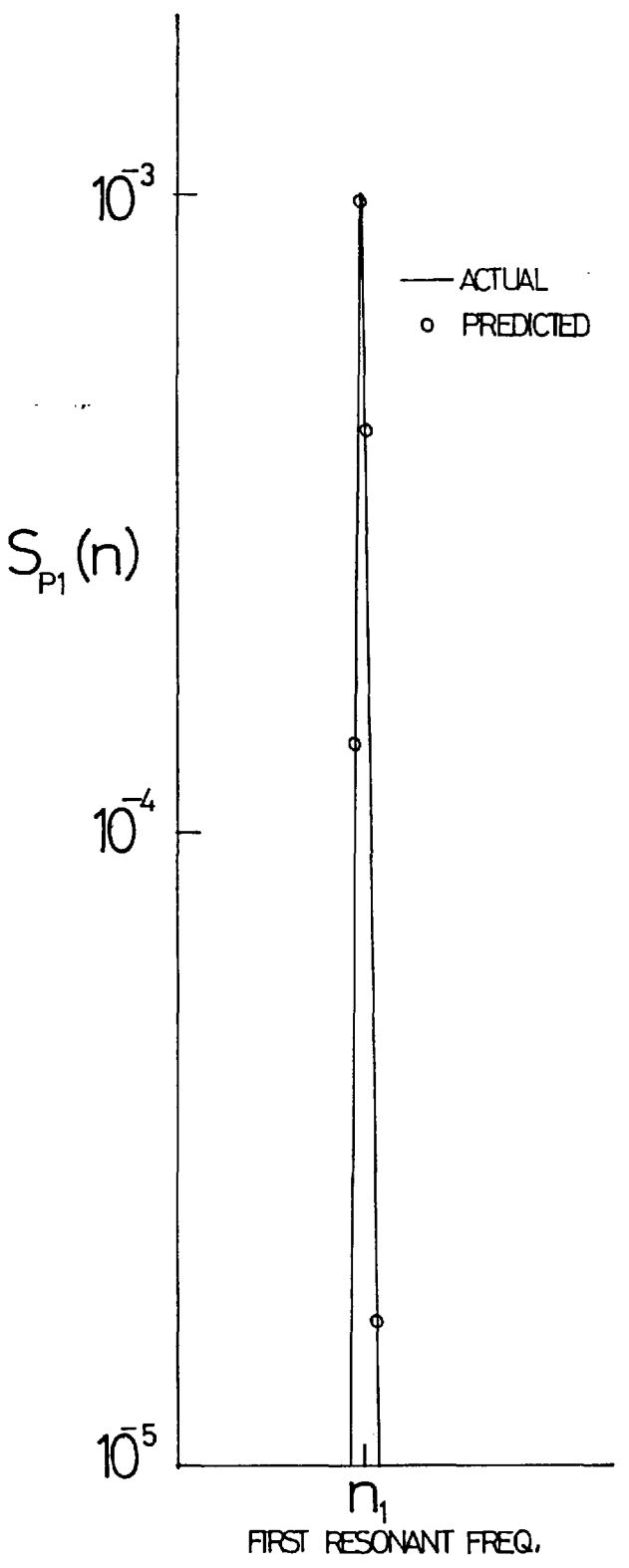


FIG 29 POWER SPECTRUM

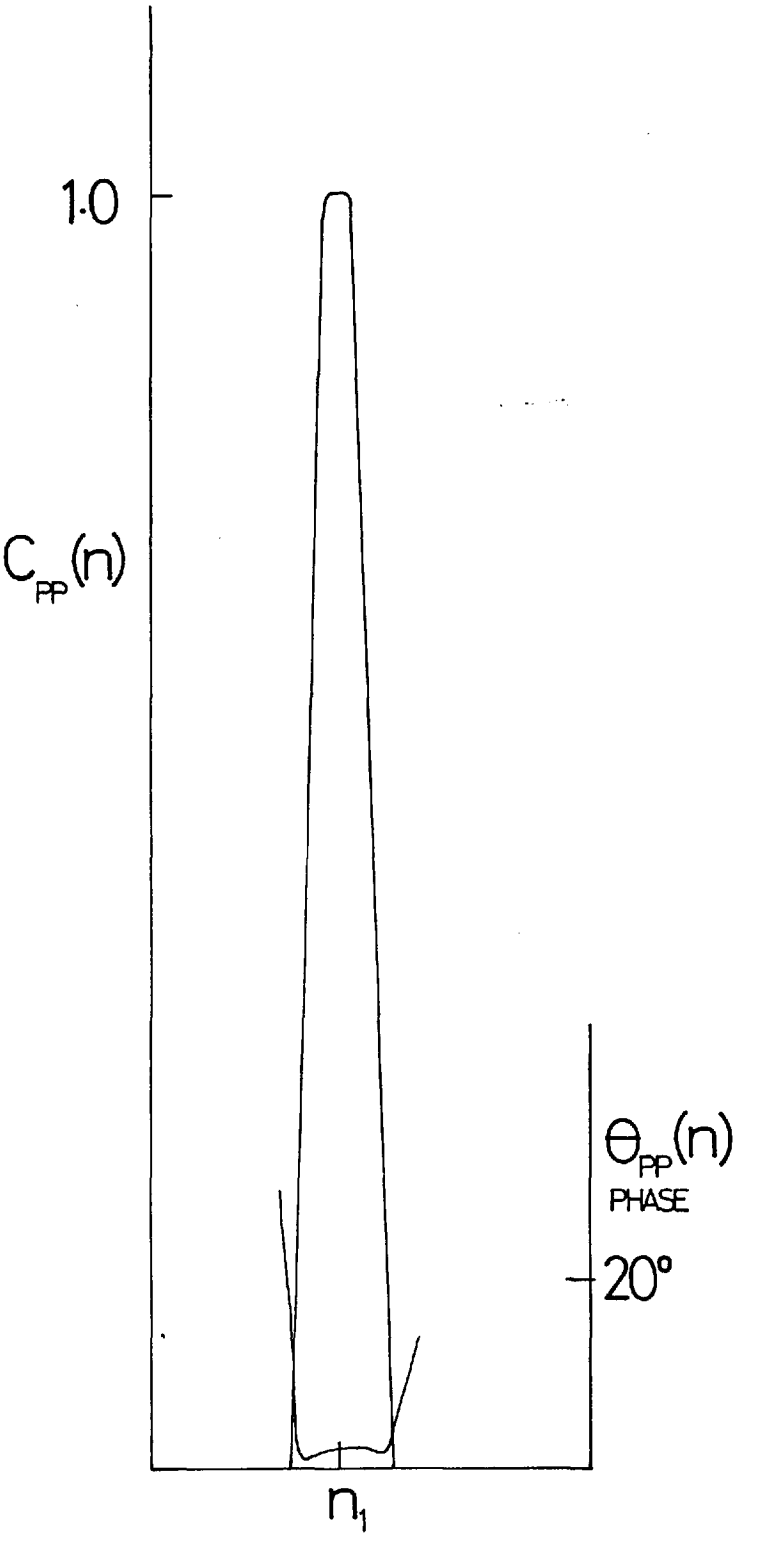


FIG 30 COHERENCE AND PHASE

SINUSOIDAL FORCE AT RESONANCE

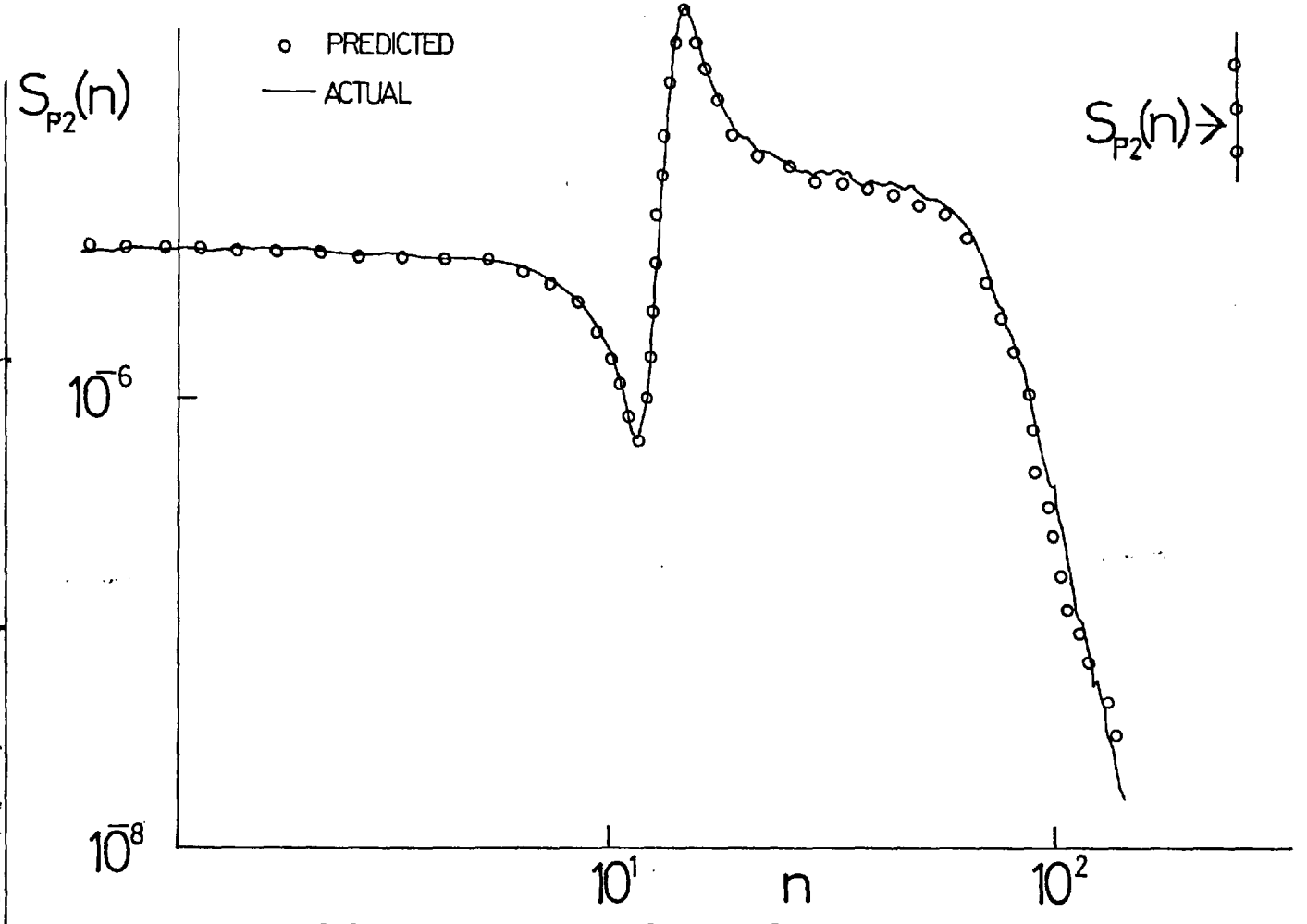


FIG 31 COMPARISON OF ACTUAL AND PREDICTED FORCE POWER SPECTRA

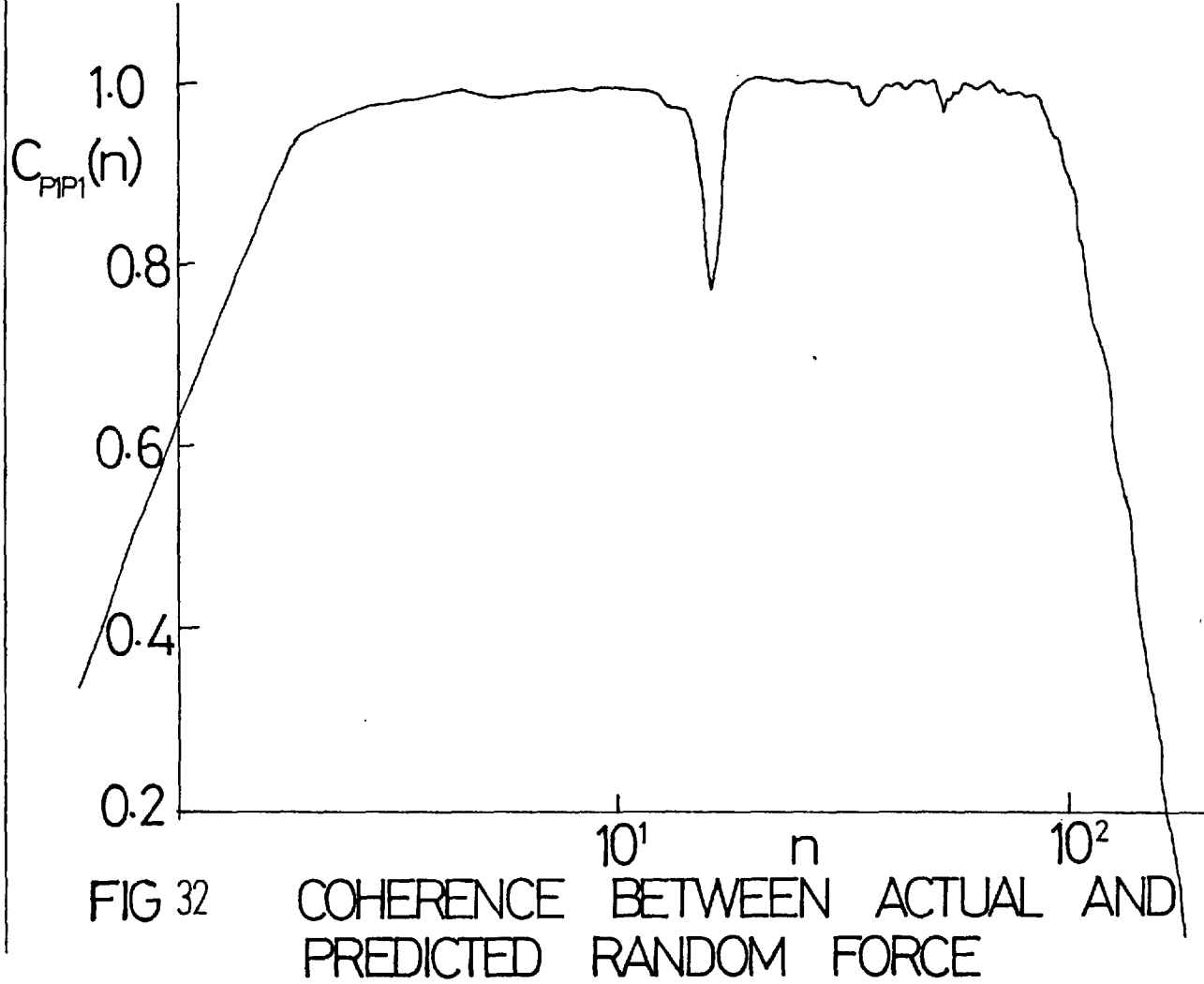


FIG 32 COHERENCE BETWEEN ACTUAL AND PREDICTED RANDOM FORCE

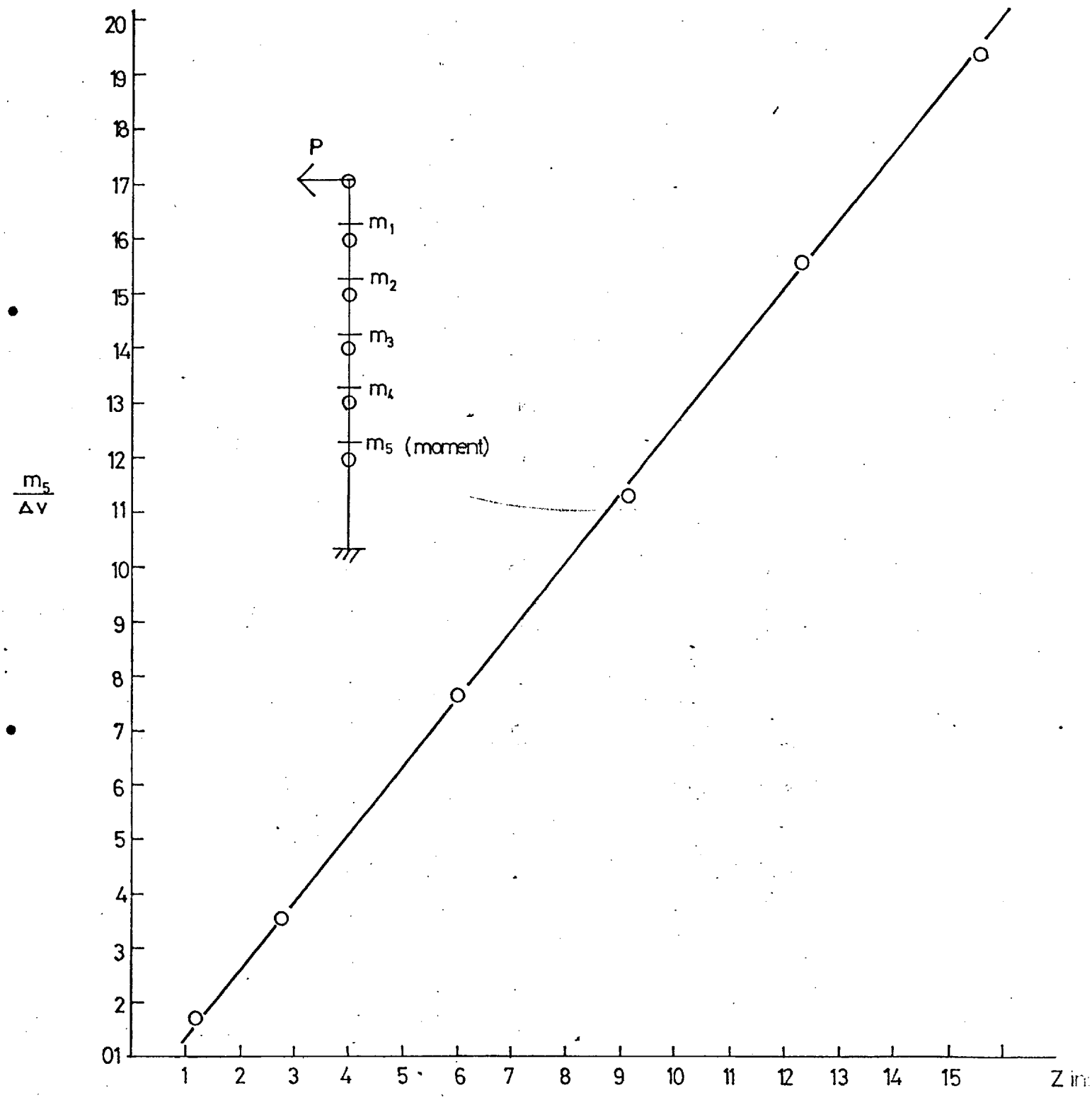


FIG 33 GRAPH PLOT $\frac{m_5}{\Delta V}$ FOR DECREASING Z

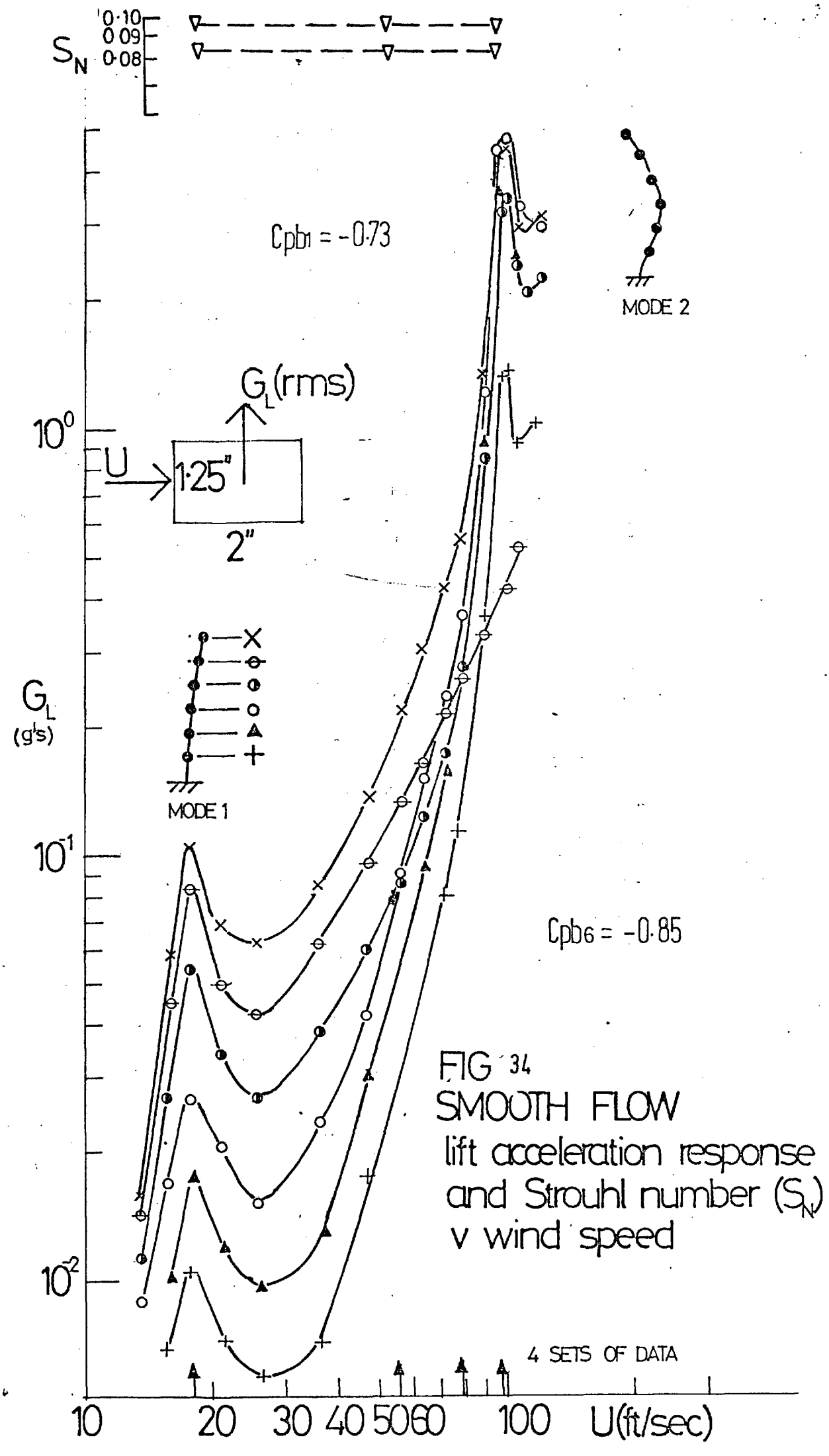


FIG 34
SMOOTH FLOW
lift acceleration response and Strouhl number (S_N) v wind speed

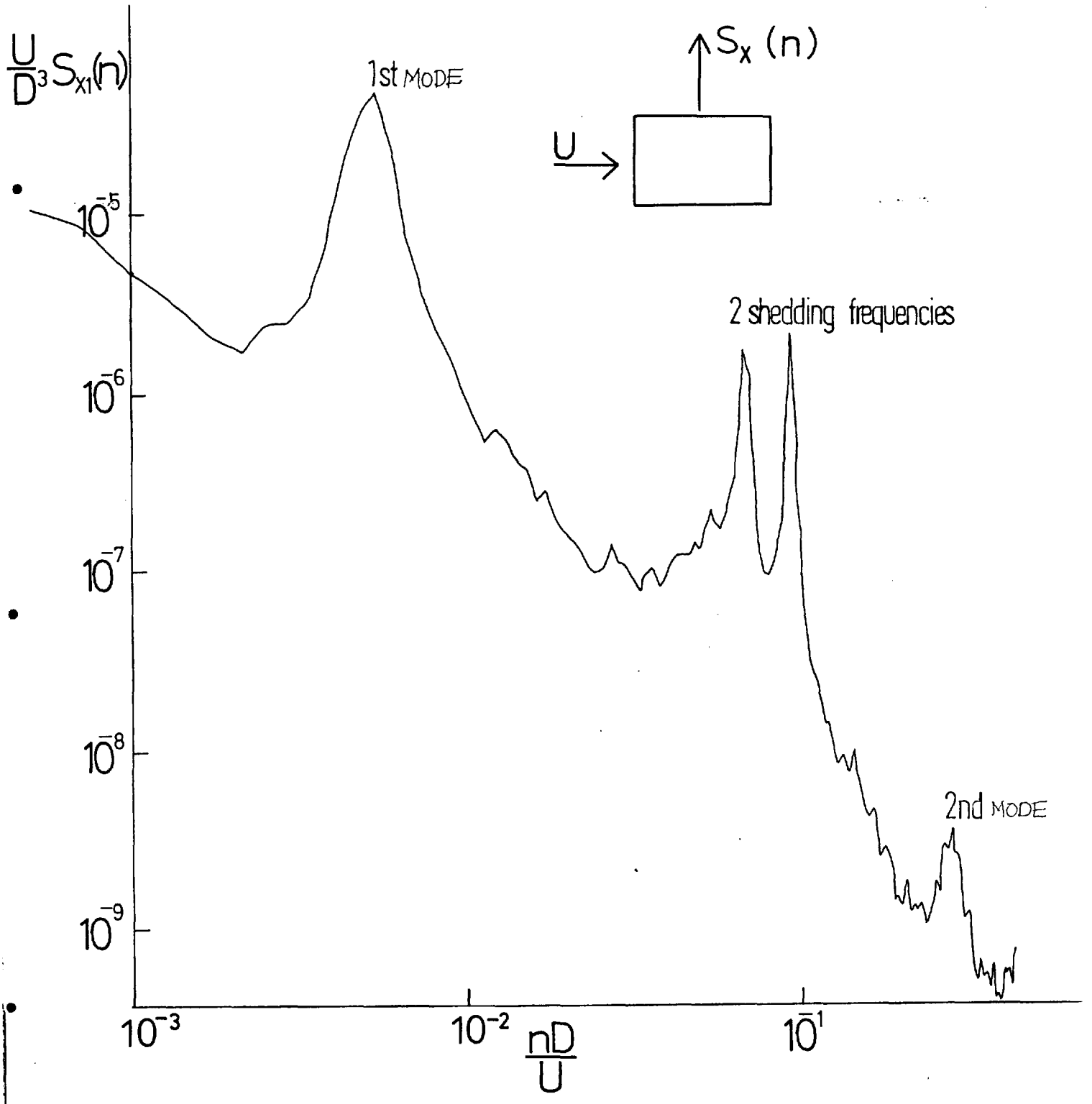


FIG 35 SMOOTH FLOW LIFT DISPLACEMENT POWER SPECTRUM V $\frac{nD}{U}$ $Re = 3.7 \times 10^4$ ($U = 56$ft/sec)

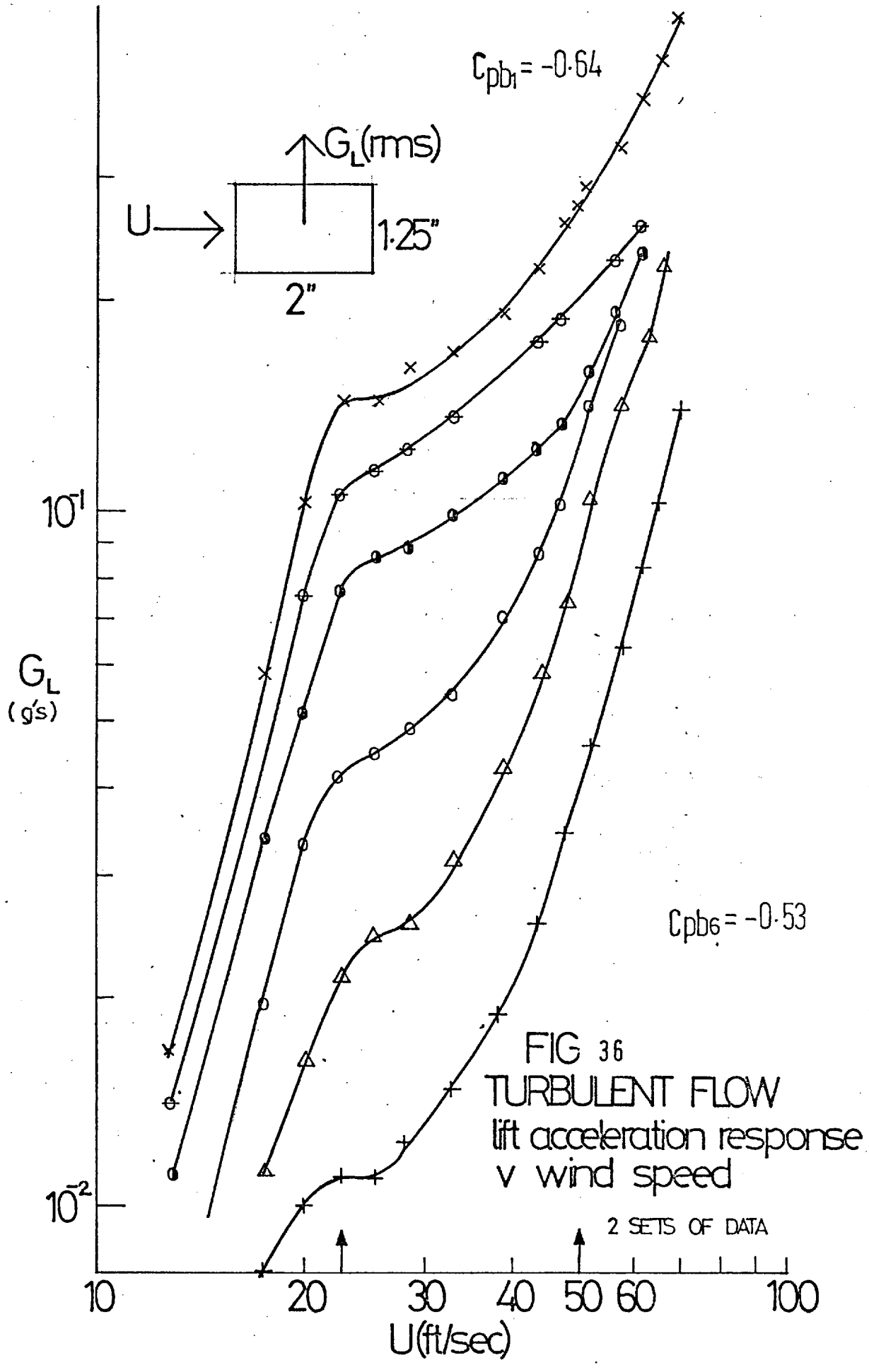


FIG 36
TURBULENT FLOW
lift acceleration response
v wind speed

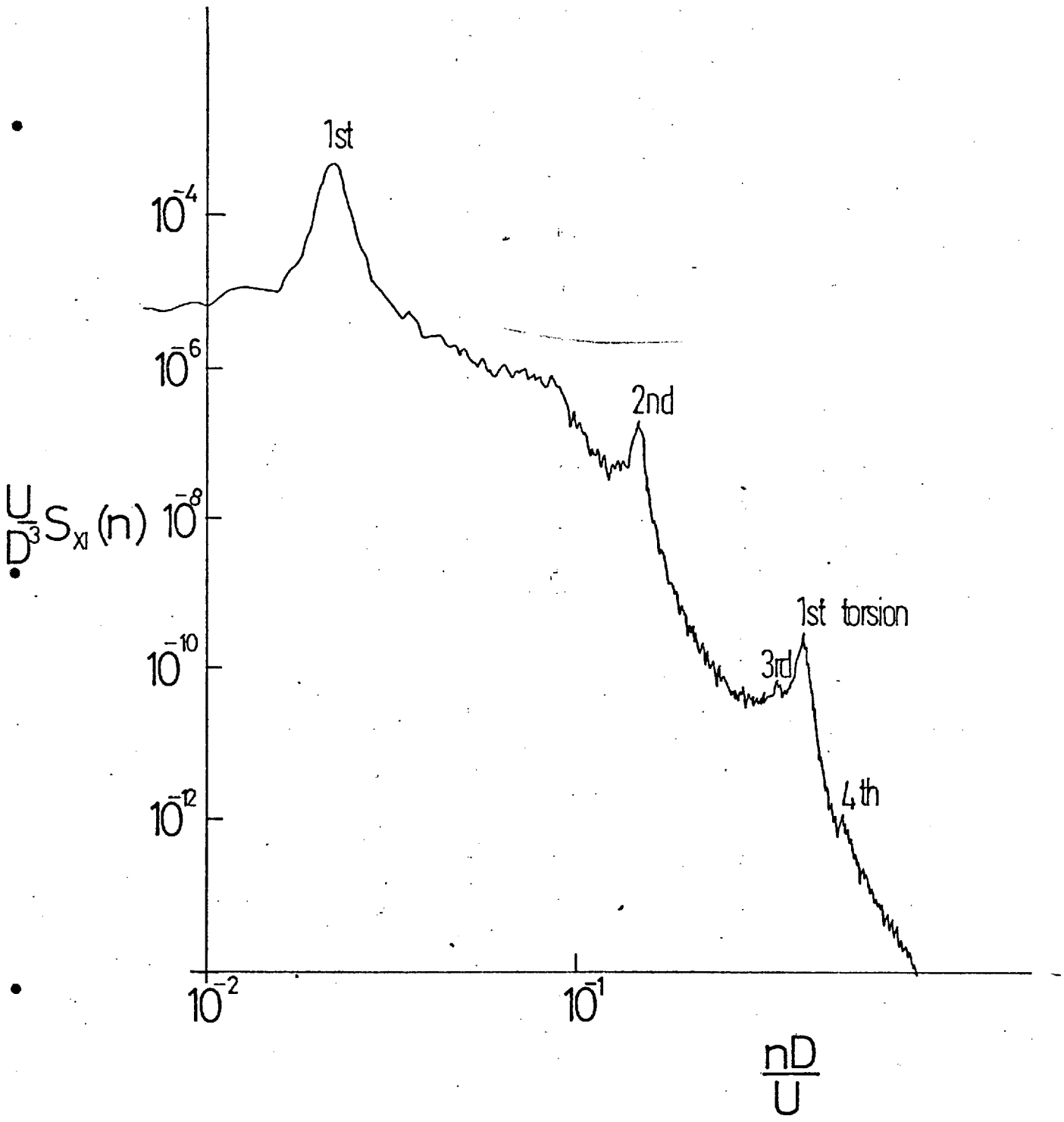


FIG 37 TURBULENT FLOW LIFT DISPLACEMENT POWER SPECTRUM V $\frac{nD}{U}$ $R_e = 5 \times 10^4$ (U = 70ft/sec)

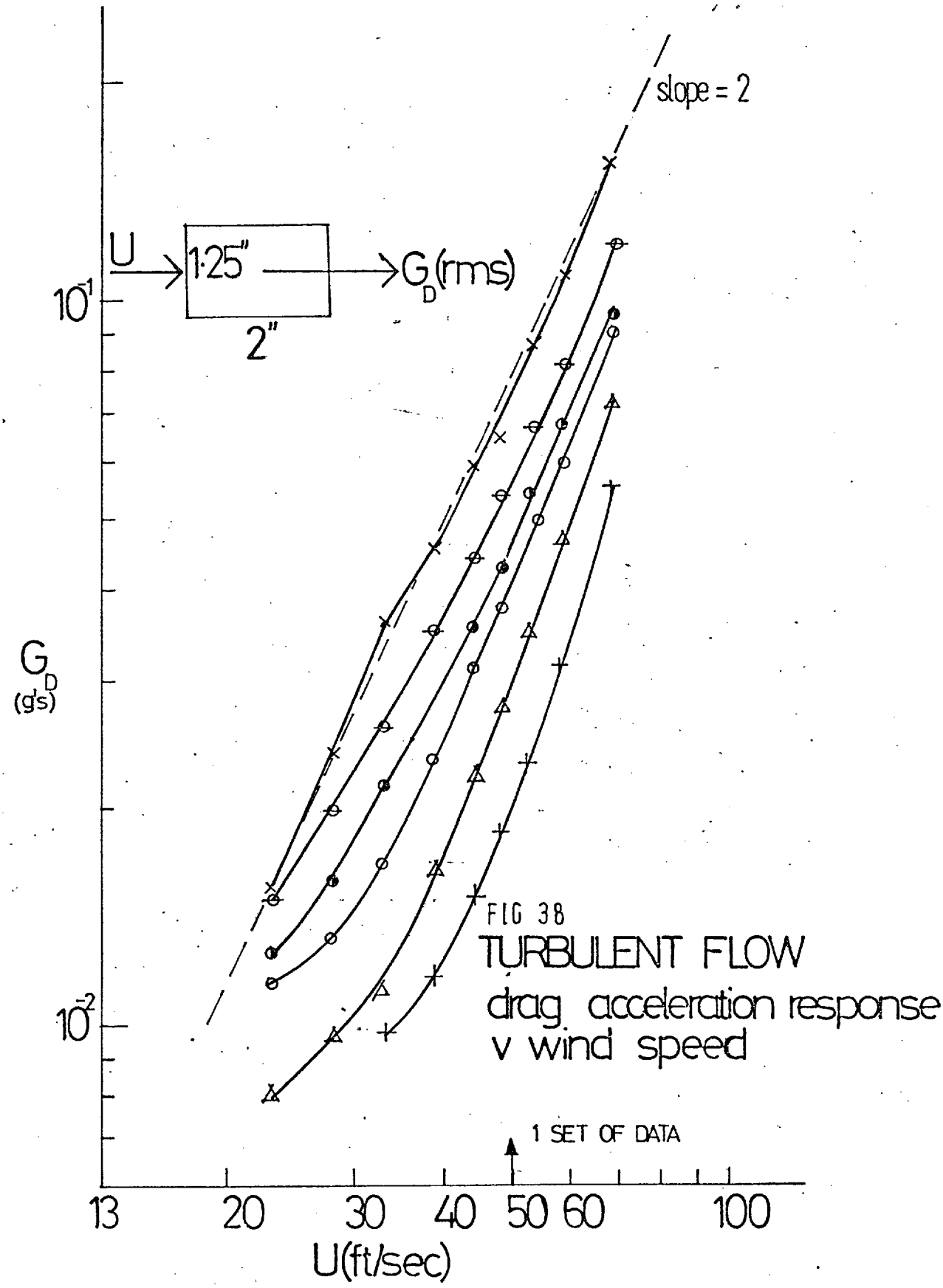
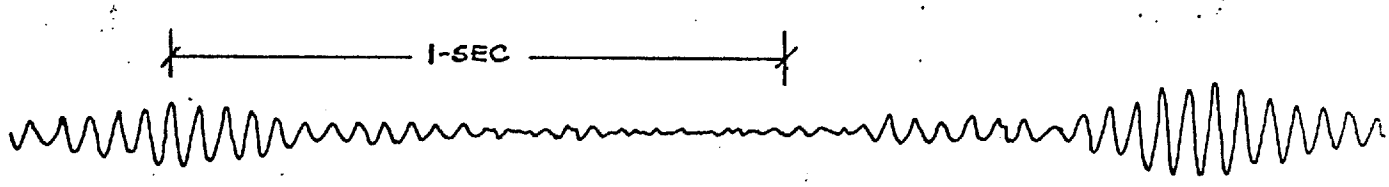


FIG 38

TURBULENT FLOW

drag acceleration response v wind speed



TYPICAL TRACE

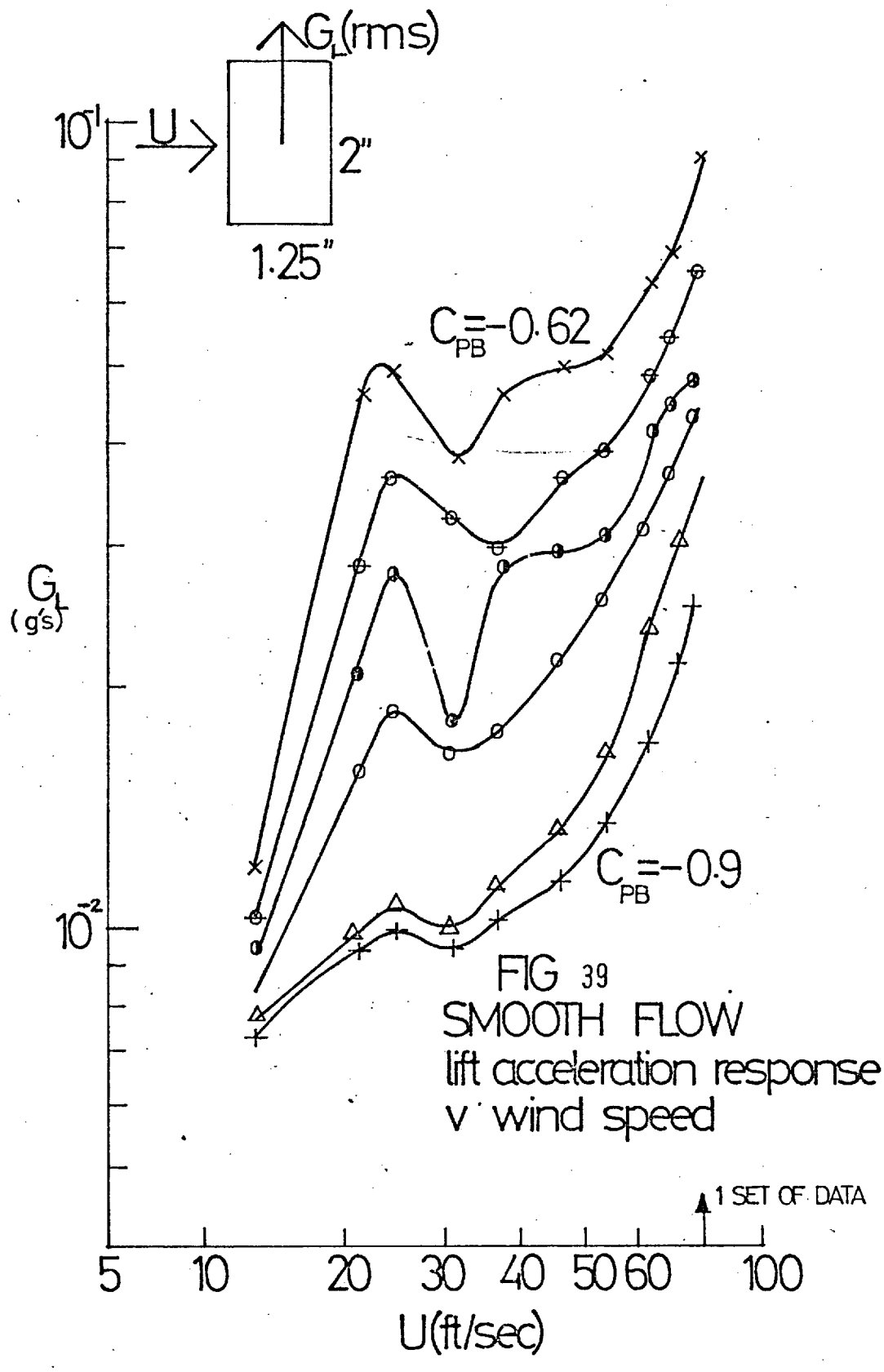


FIG 39
SMOOTH FLOW
lift acceleration response
v wind speed

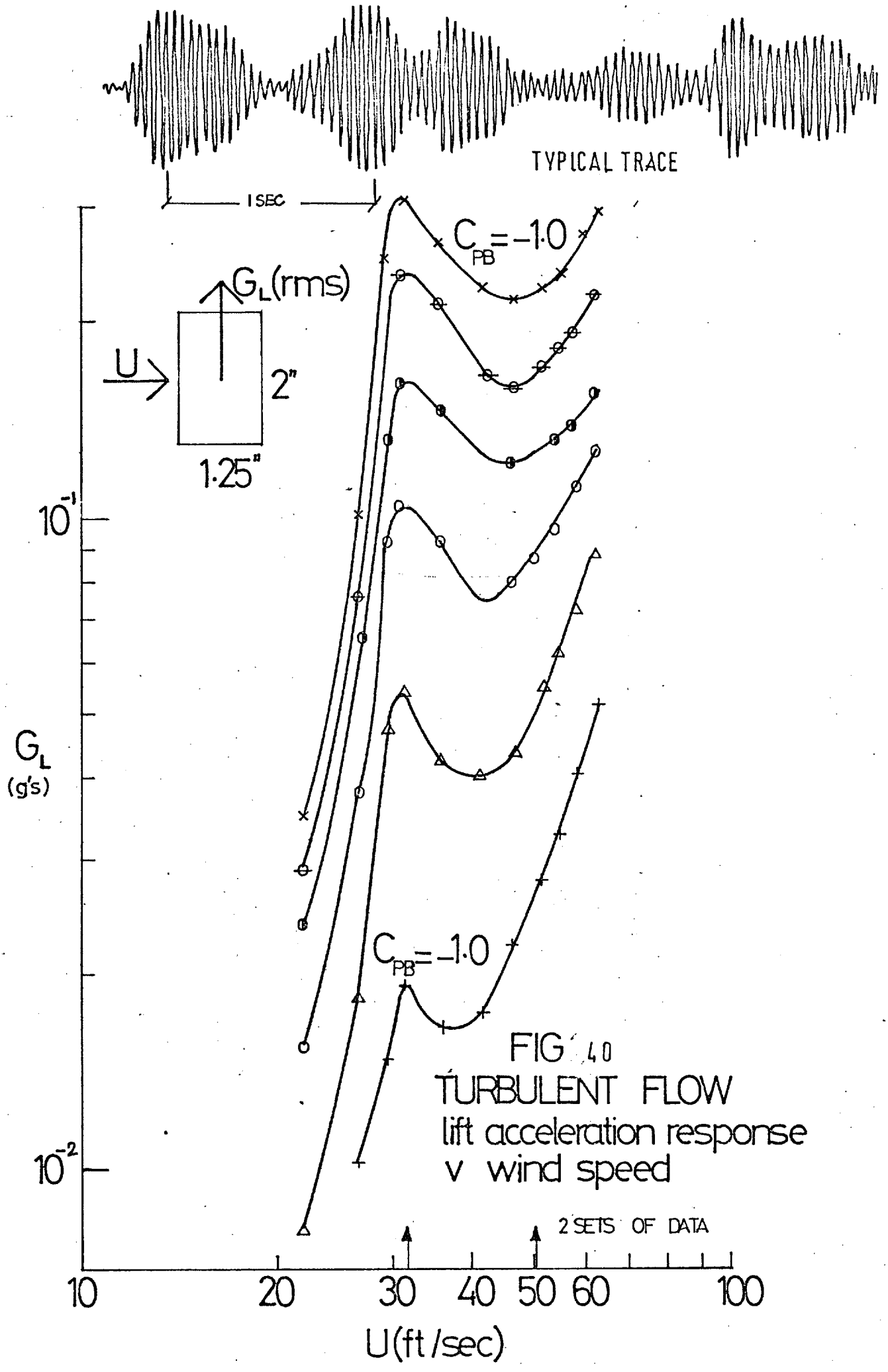


FIG 4.0
TURBULENT FLOW
lift acceleration response
v wind speed

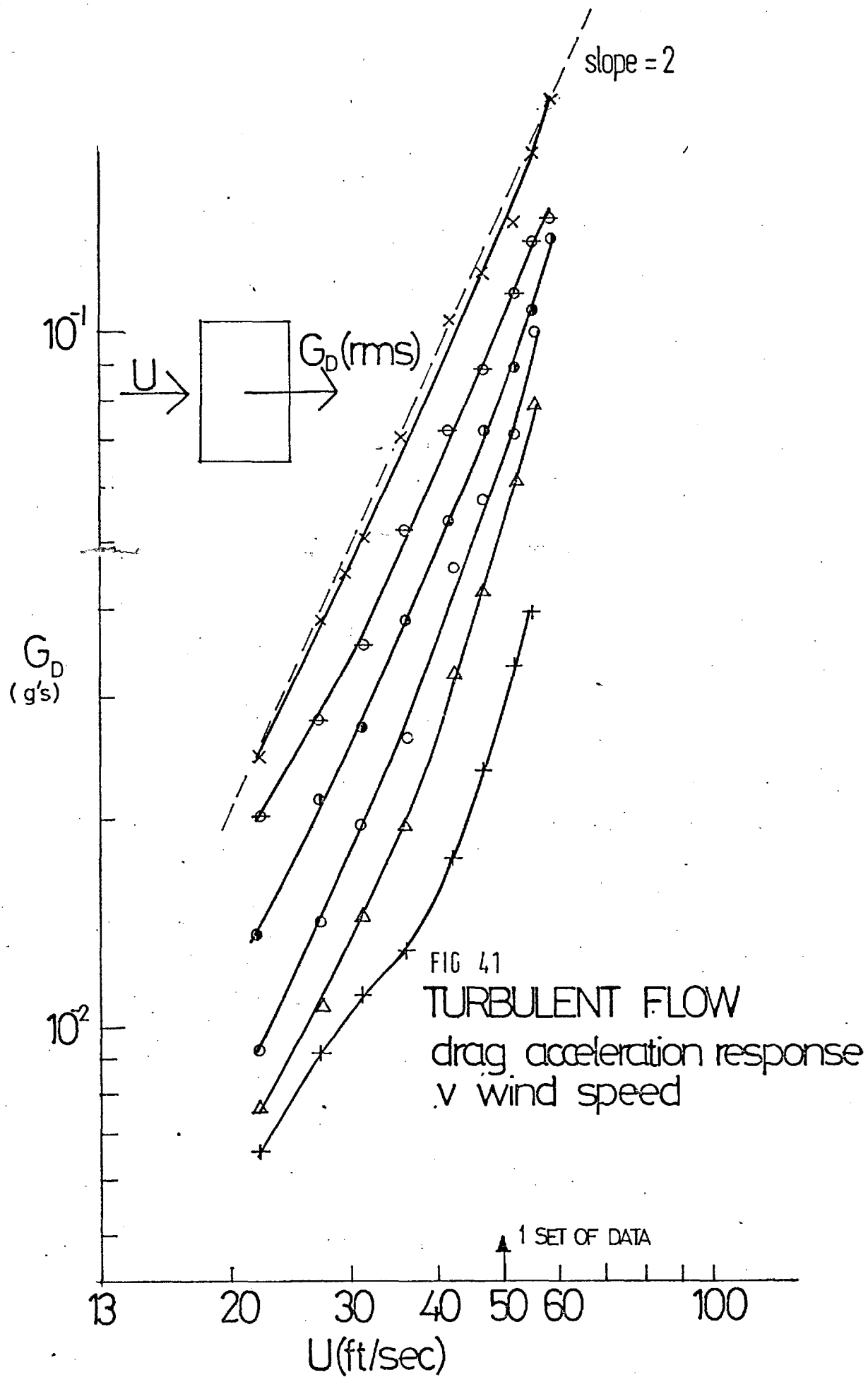


FIG 41

TURBULENT FLOW

drag acceleration response v wind speed

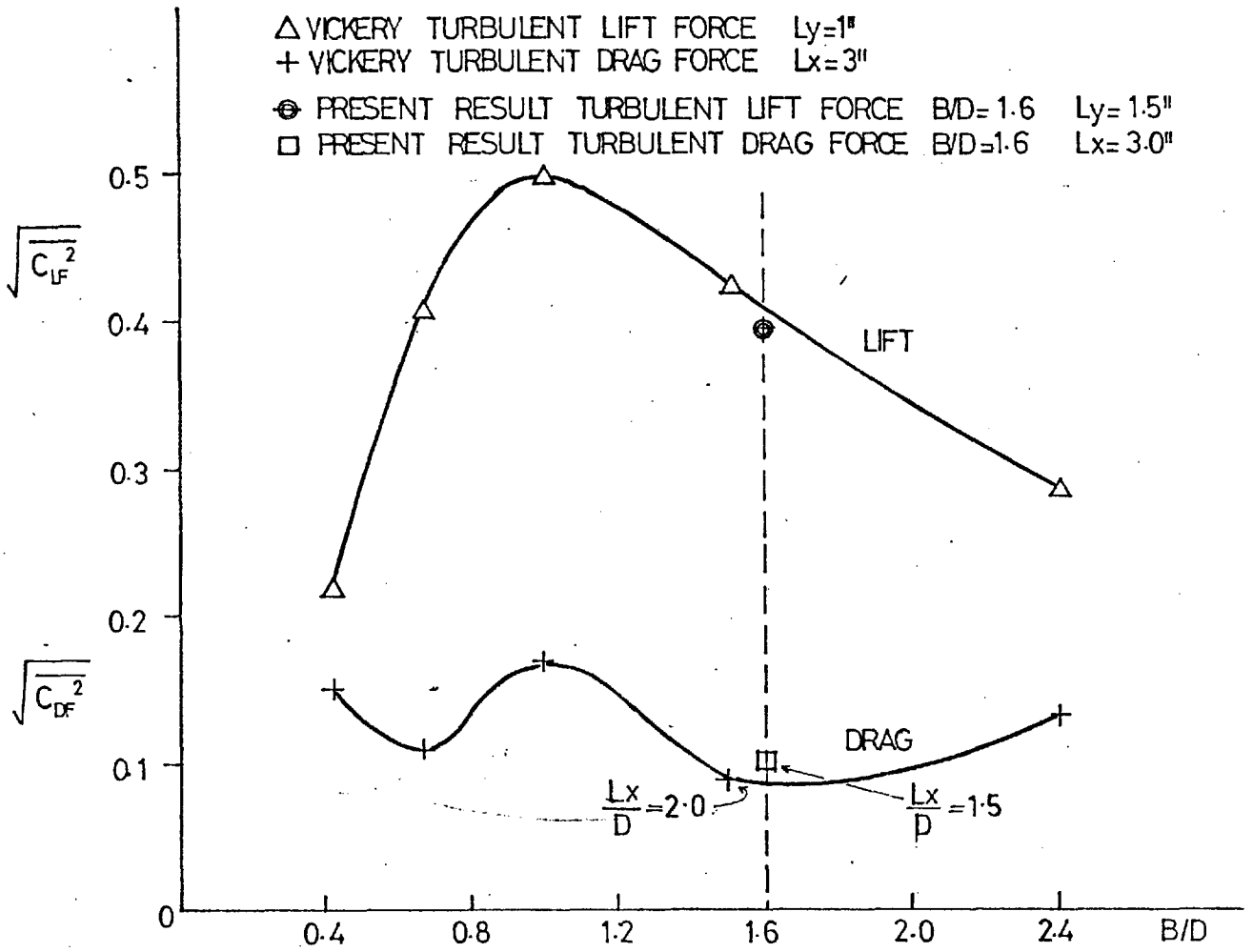


FIG. 4.2 COMPARISON WITH VICKERY'S RESULTS ASPECT RATIO = 9·8

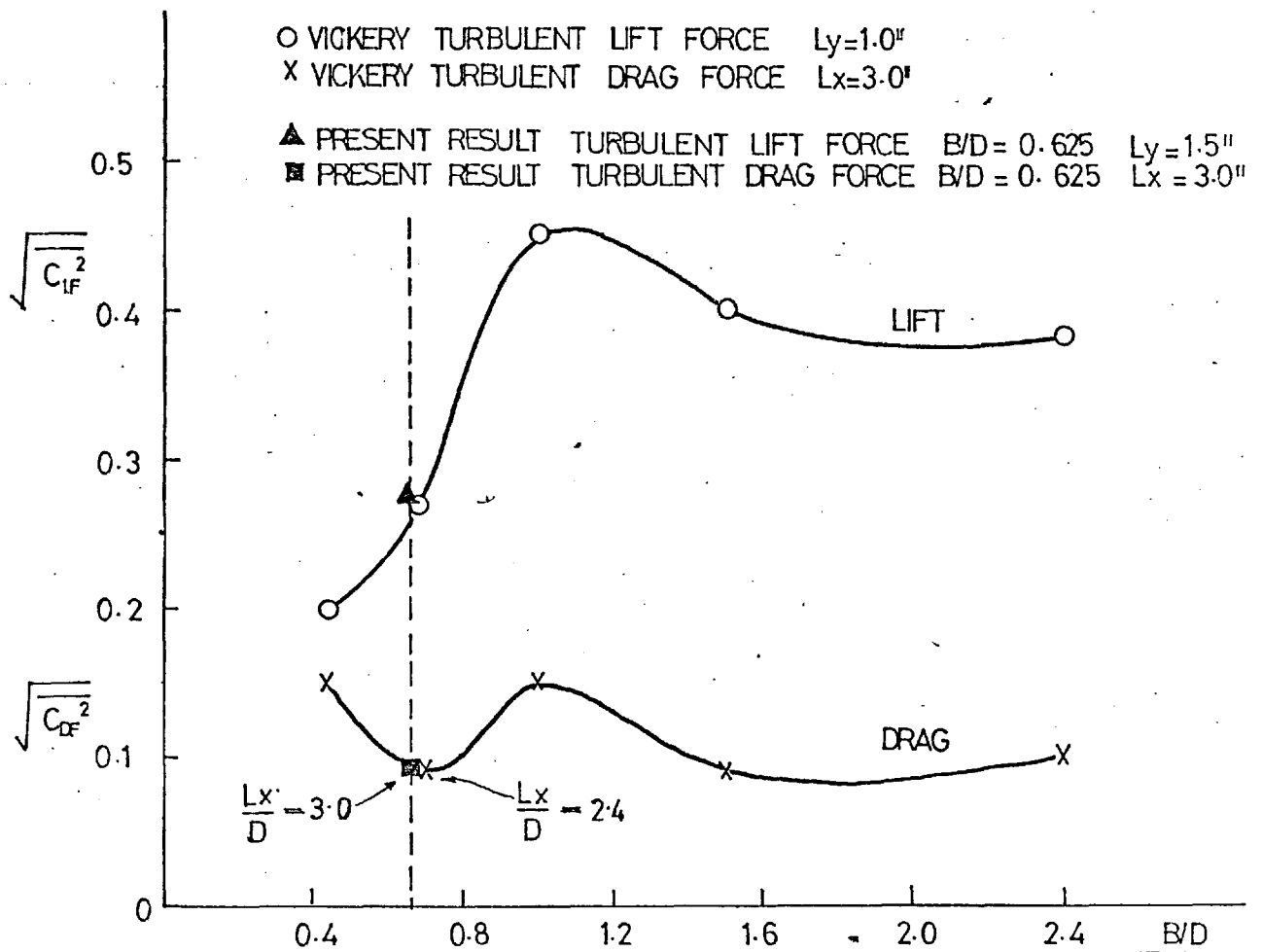


FIG. 4.3 COMPARISON WITH VICKERY'S RESULTS ASPECT RATIO = 15·6

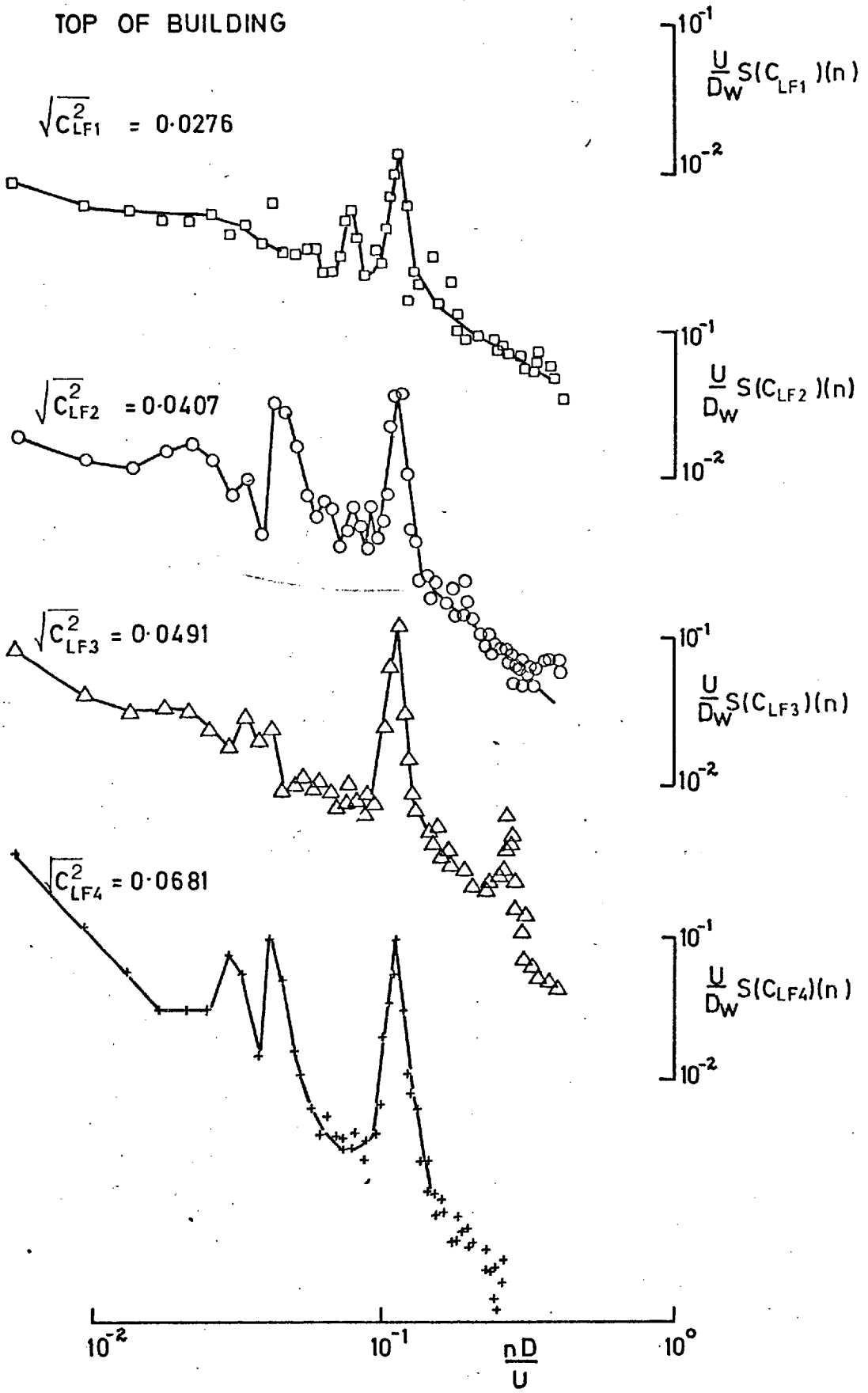
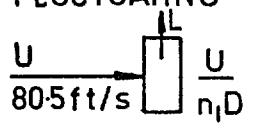


FIG. 44 FLUCTUATING LIFT FORCE SPECTRA



= 22·4 SMOOTH FLOW.

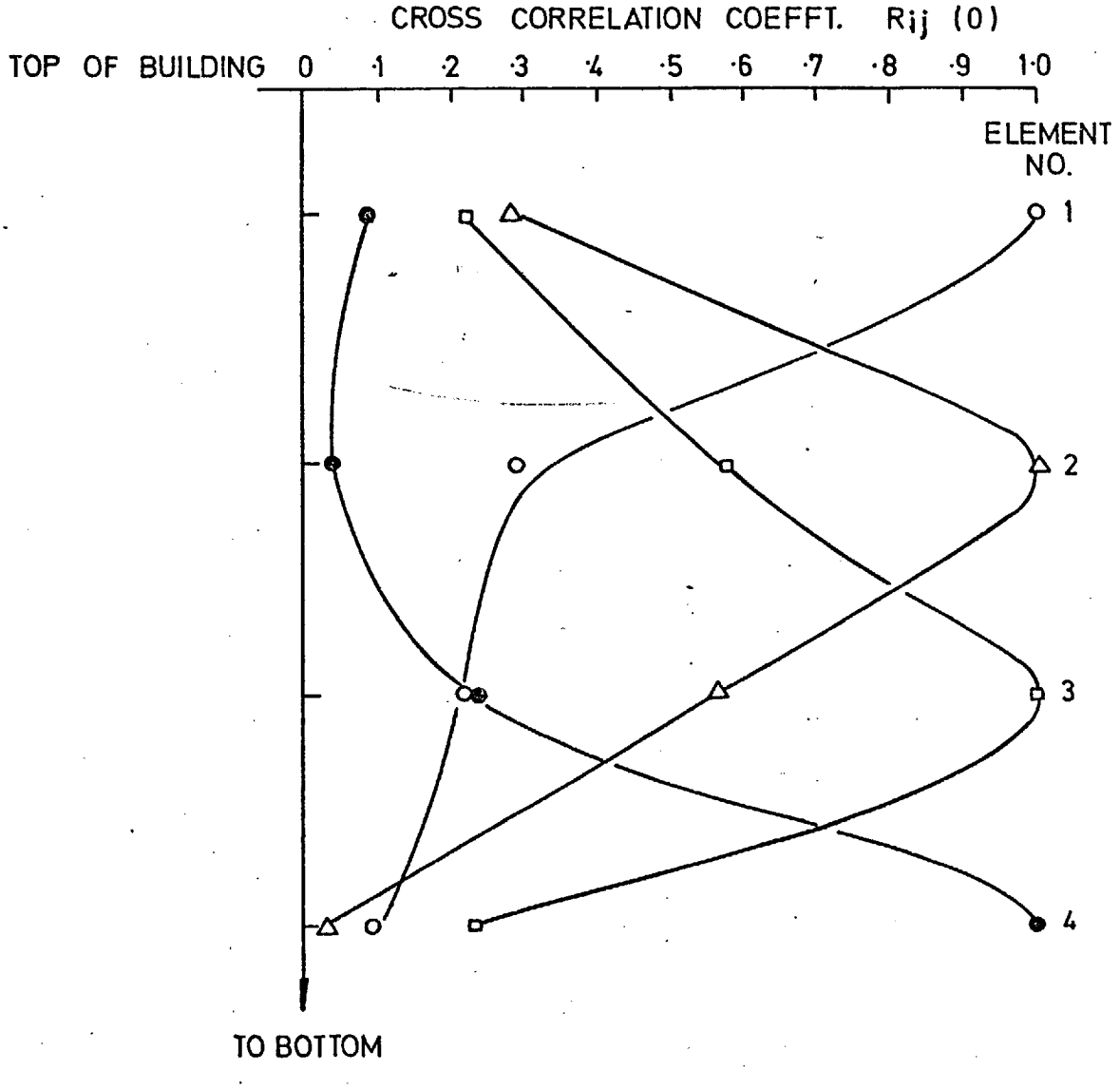


FIG.45 LIFT FORCE CROSS CORRELATIONS $\frac{U}{n_1 D} = 22{\cdot}4$

SMOOTH $\frac{U}{80{\cdot}5\ ft/s}$

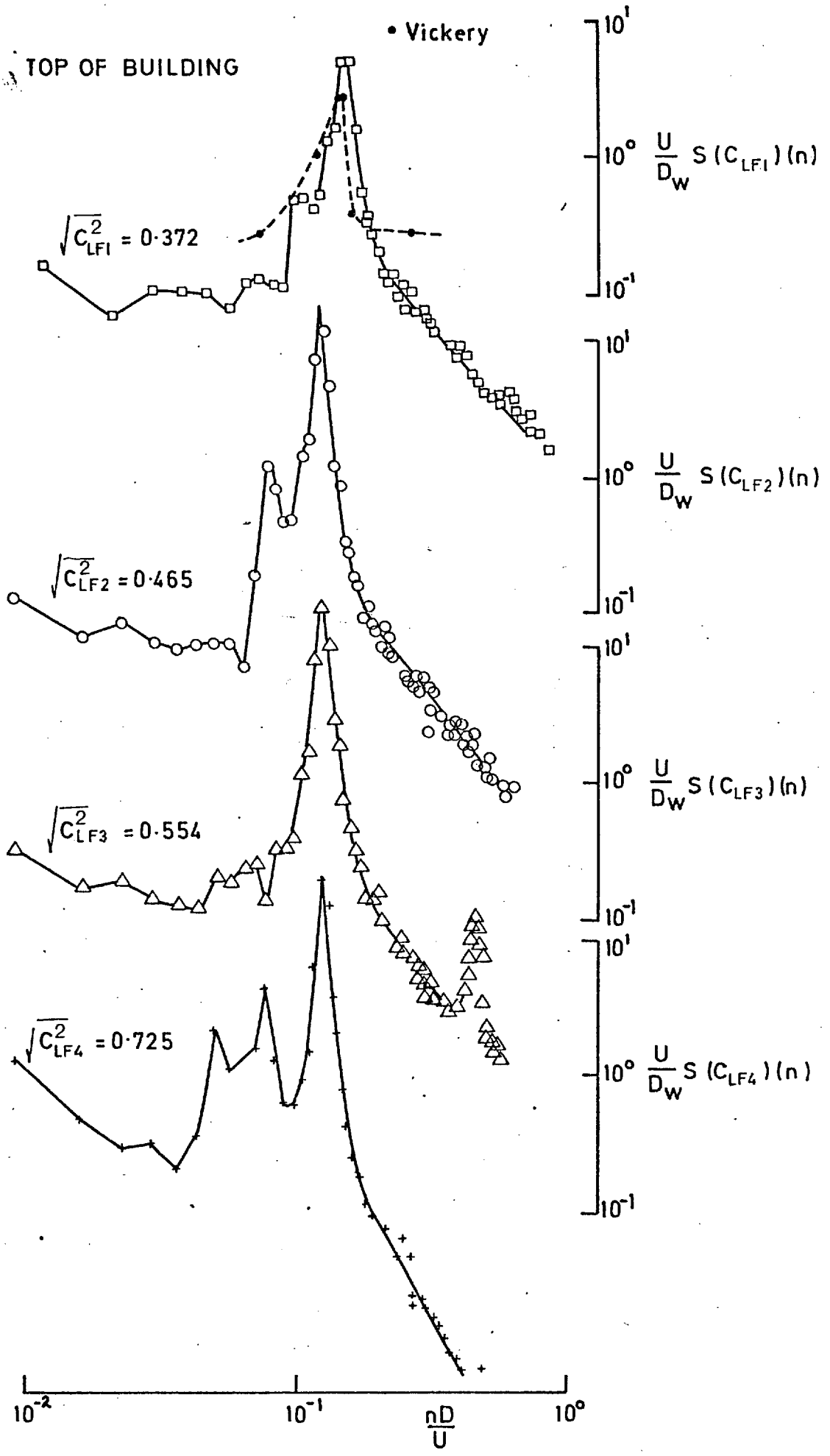
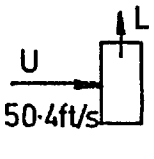


FIG.46 FLUCTUATING LIFT FORCE SPECTRA



$\frac{U}{n_1 D}$=14. TURBULENT FLOW.

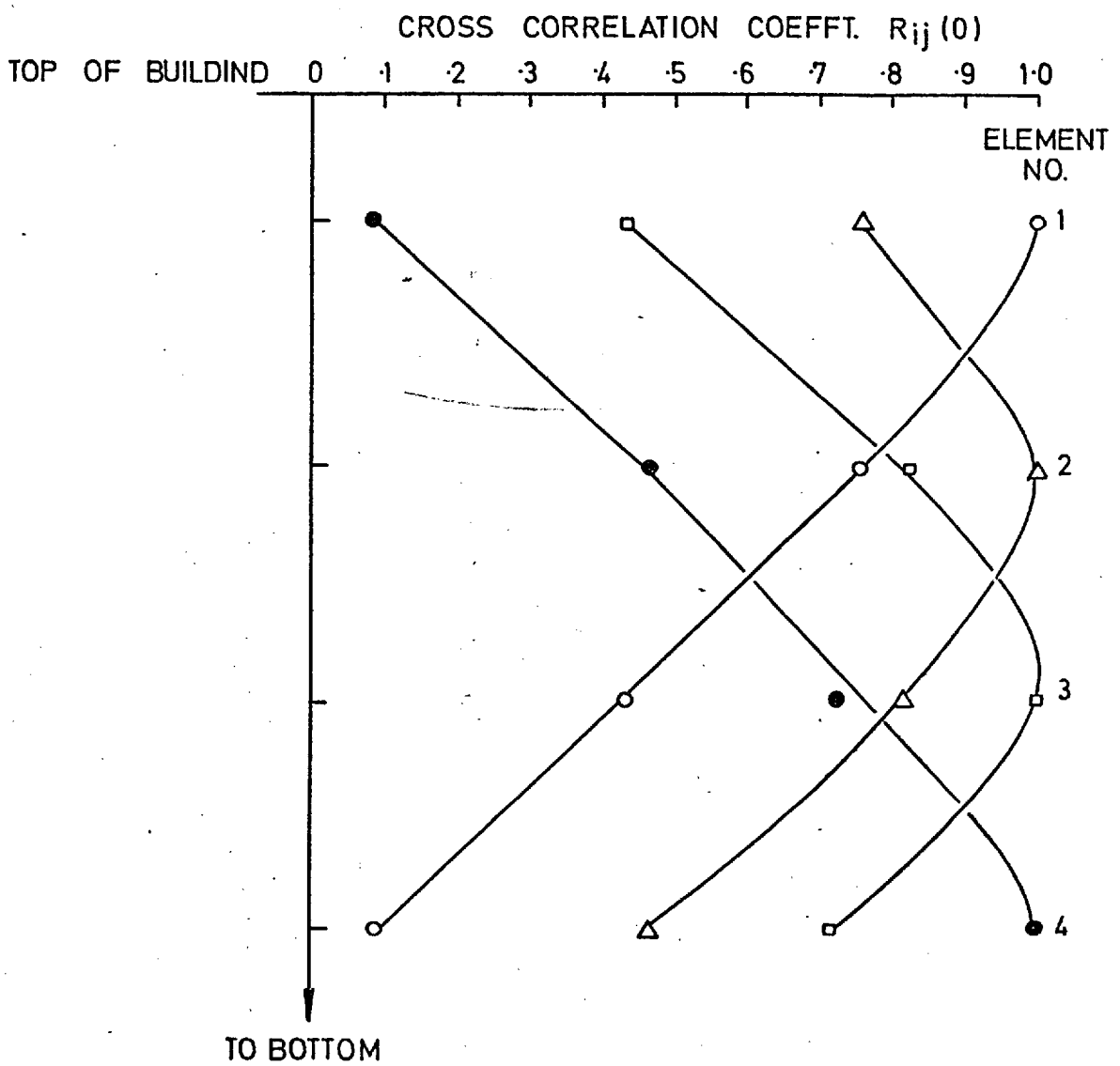


FIG. 47 LIFT FORCE CROSS CORRELATIONS $\frac{U}{n_1 D} = 14$

TURBULENT $\frac{U}{50{\cdot}4 ft/s}$ L

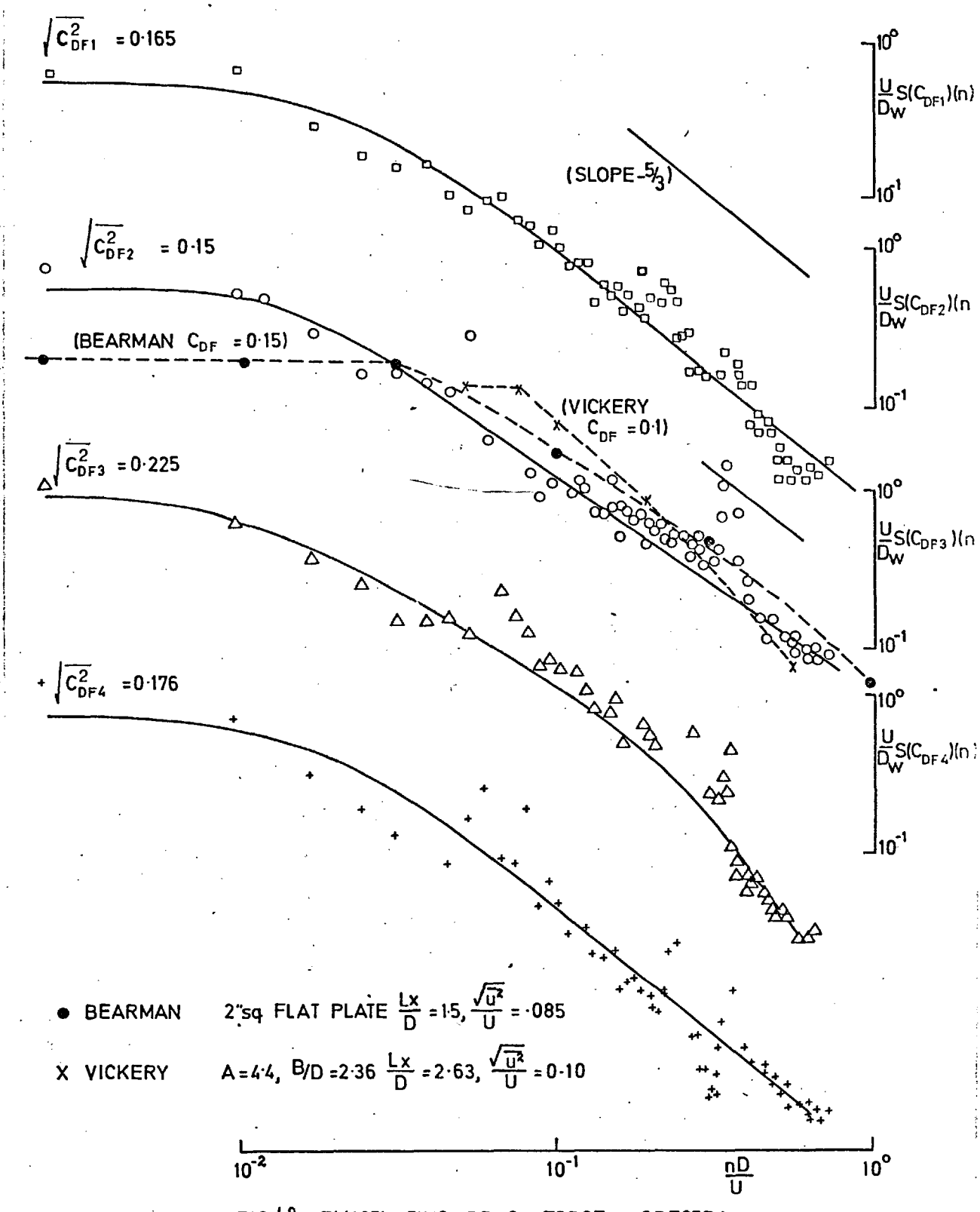


FIG 48 FLUCTUATING DRAG FORCE SPECTRA

$\frac{U}{50{\cdot}0\,ft/s}$ B D D $\frac{U}{n_1 D}$ = 50 TURBULENT FLOW $\frac{Lx}{D}$ = 1·5

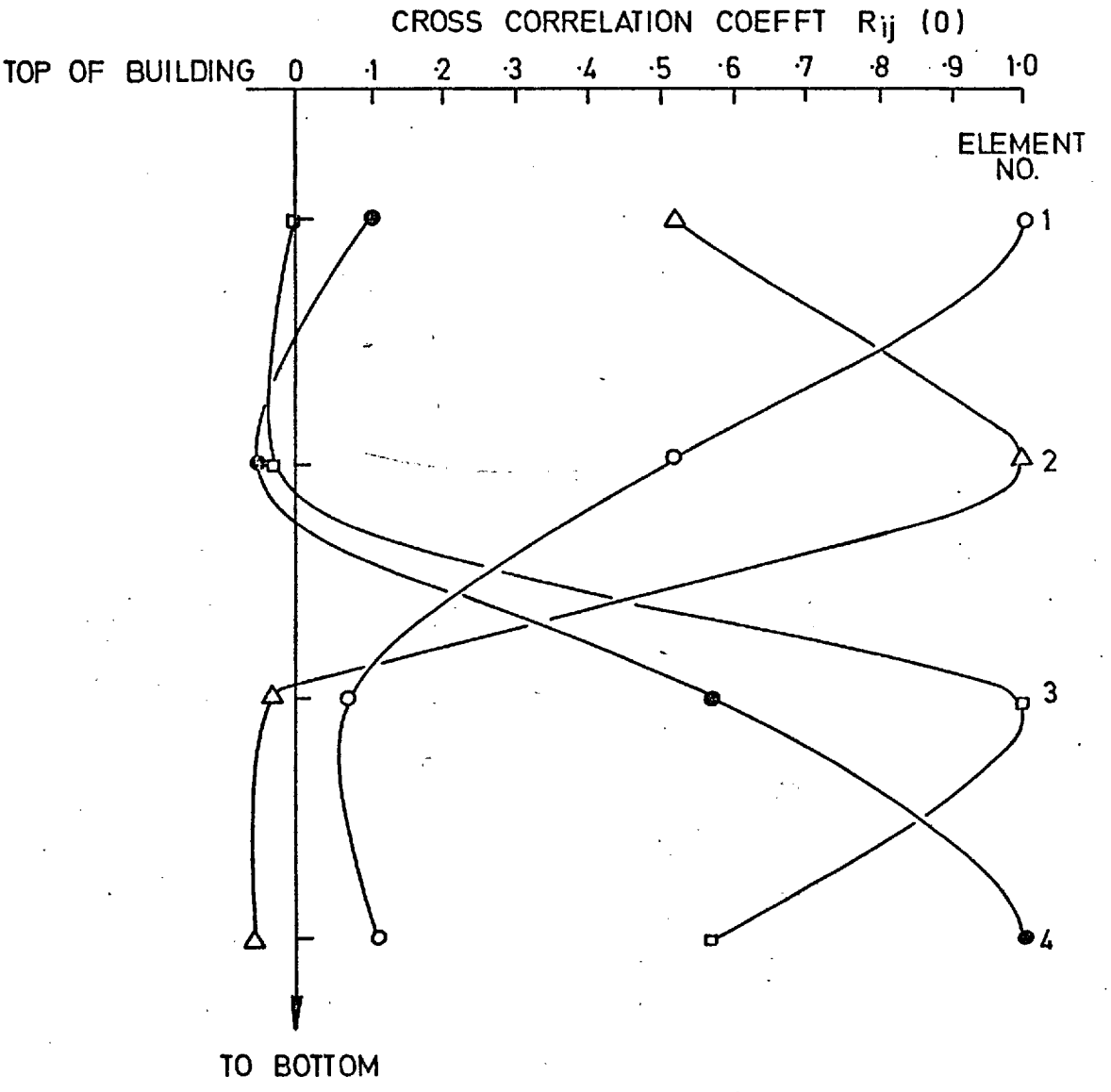


FIG.49 DRAG FORCE CROSS CORRELATIONS $\frac{U}{n_1 D} = 50.$

TURBULENT $\frac{U}{50{\cdot}0\,ft/s}$ D

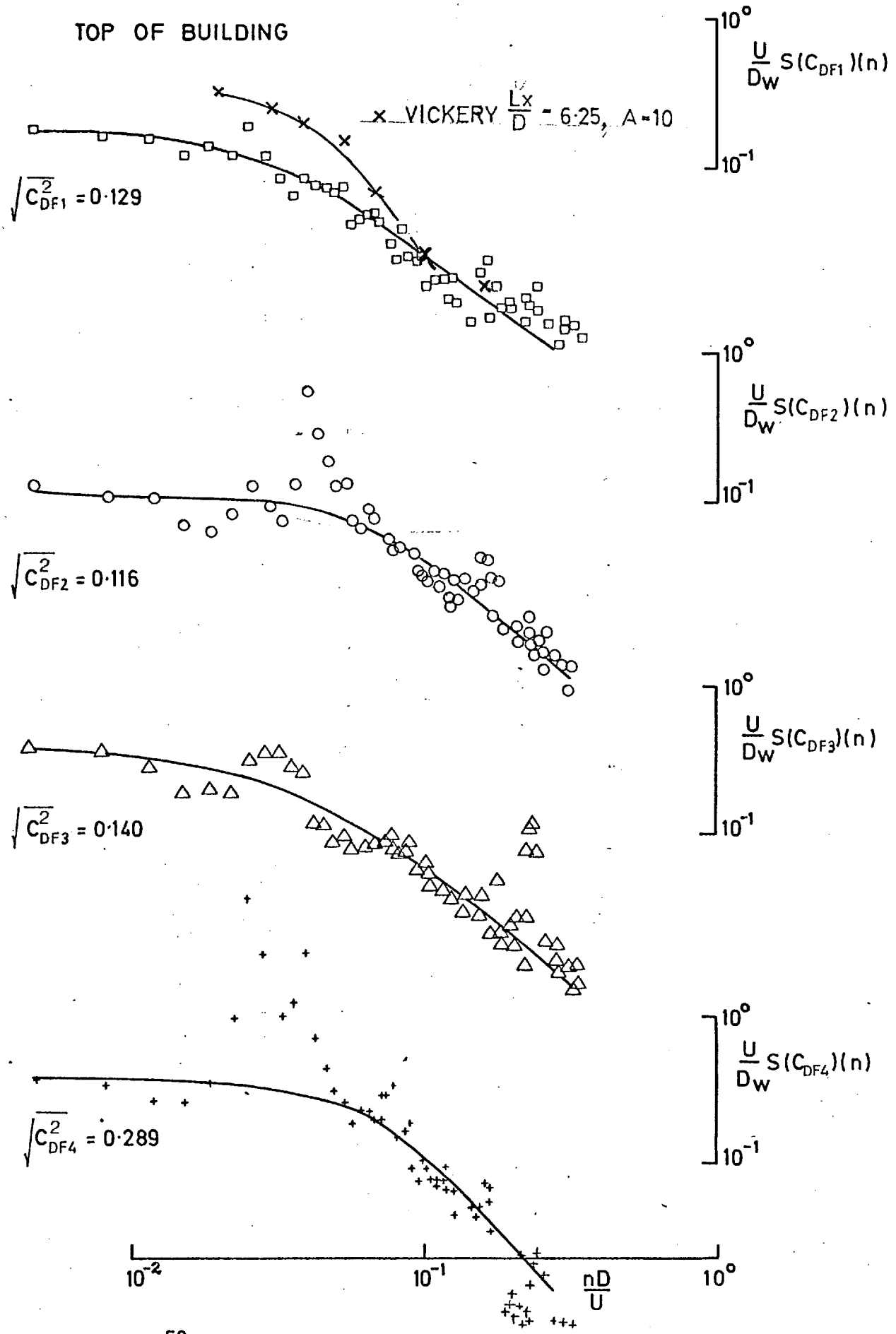


FIG.50 FLUCTUATING DRAG FORCE SPECTRA

$\frac{U}{50{\cdot}07 ft/s}$ → D $\frac{U}{n_1 D}$ = 30·8 TURBULENT FLOW

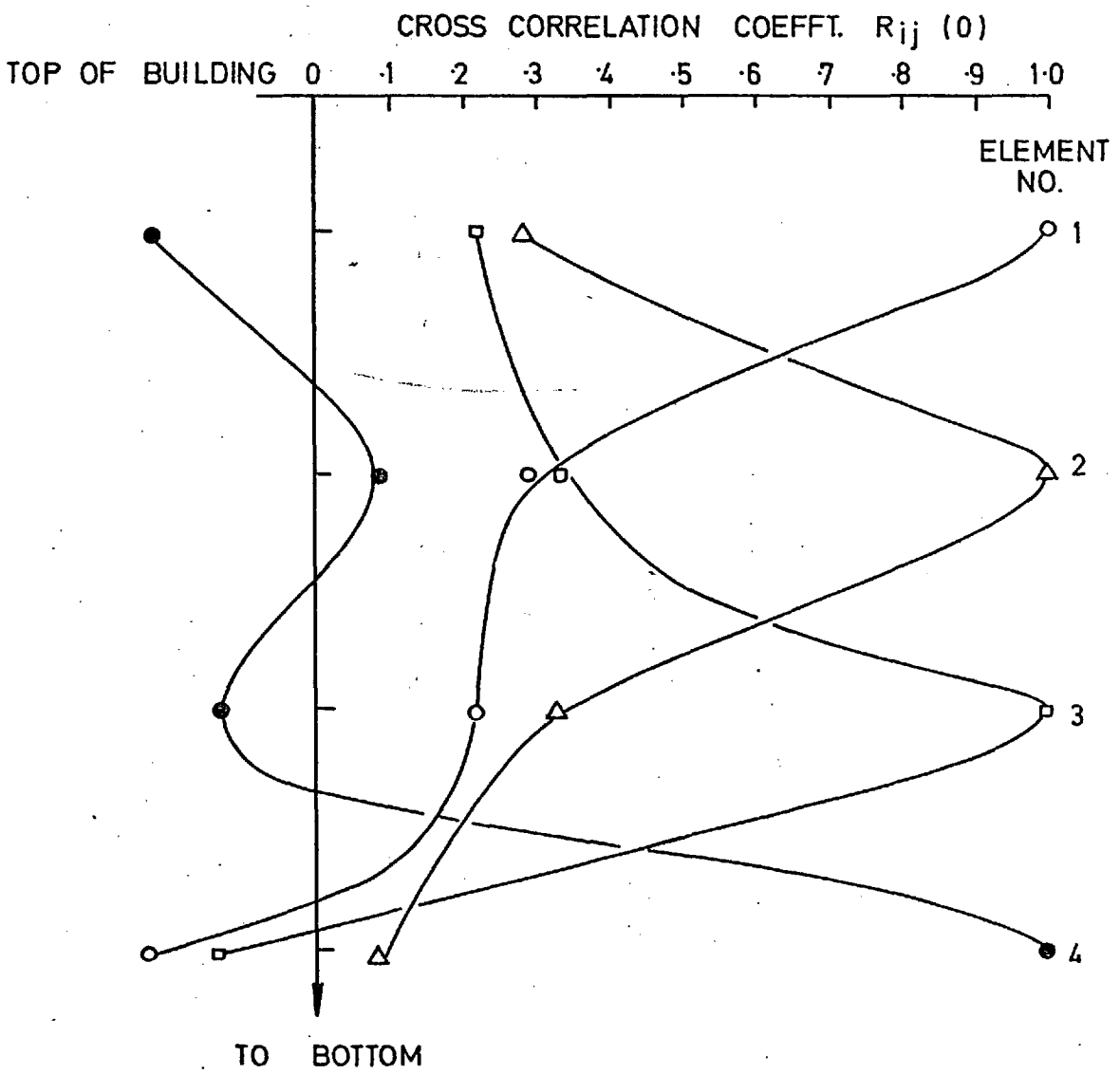


FIG. 51 DRAG FORCE CROSS CORRELATIONS $\frac{U}{n_1 D}$ =30·8

TURBULENT $\frac{U}{50{\cdot}0\,ft/s}$ D

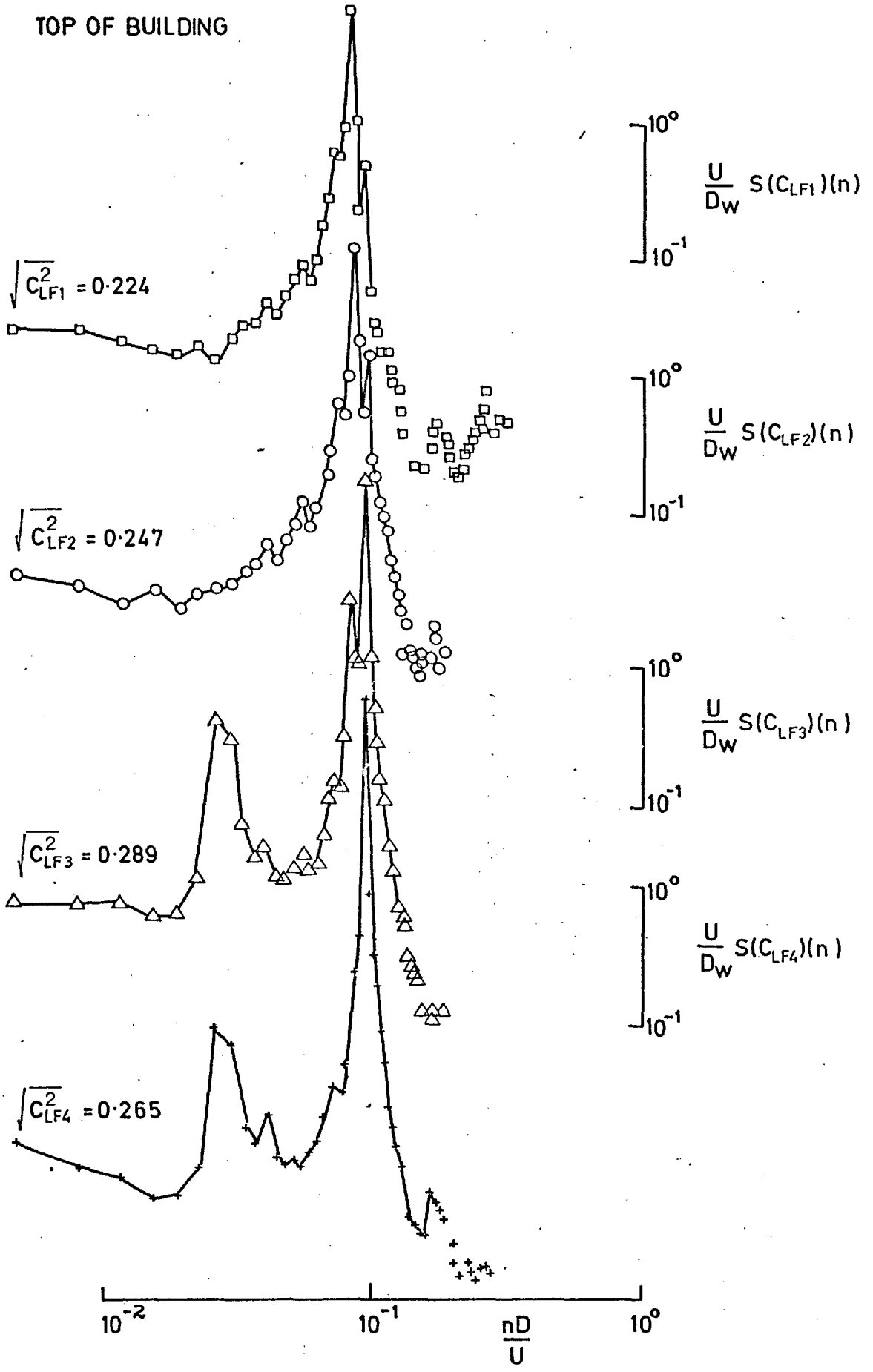
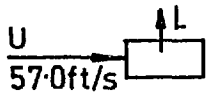


FIG. 52 FLUCTUATING LIFT FORCE SPECTRA



$\frac{U}{57{\cdot}0 ft/s}$ $\frac{U}{n_1 D} = 35$. SMOOTH FLOW.

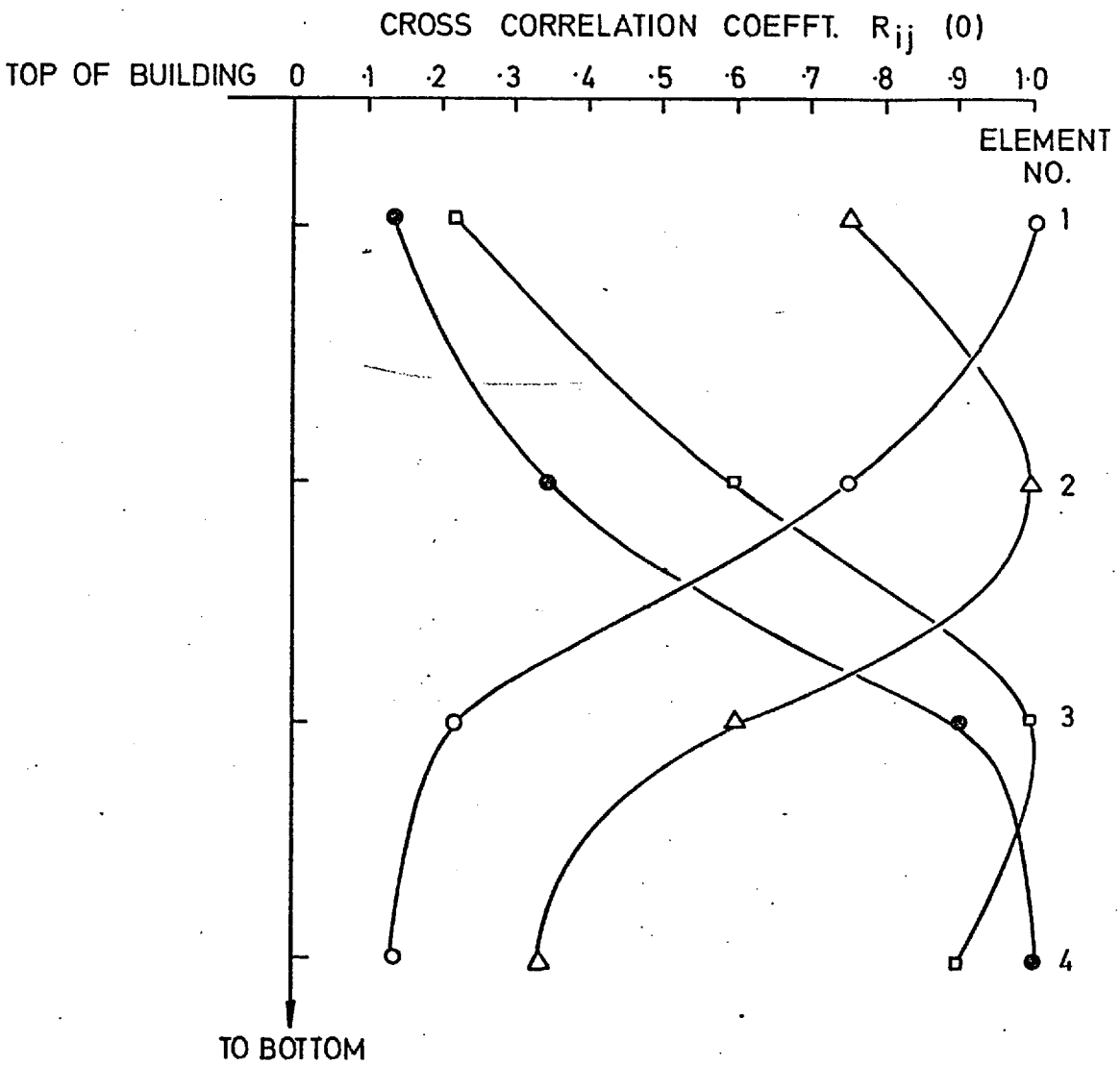


FIG. 53 LIFT FORCE CROSS CORRELATIONS $\frac{U}{n_1 D} = 35$.

SMOOTH $\frac{U}{57 \cdot 0 \text{ ft/s.}}$ L

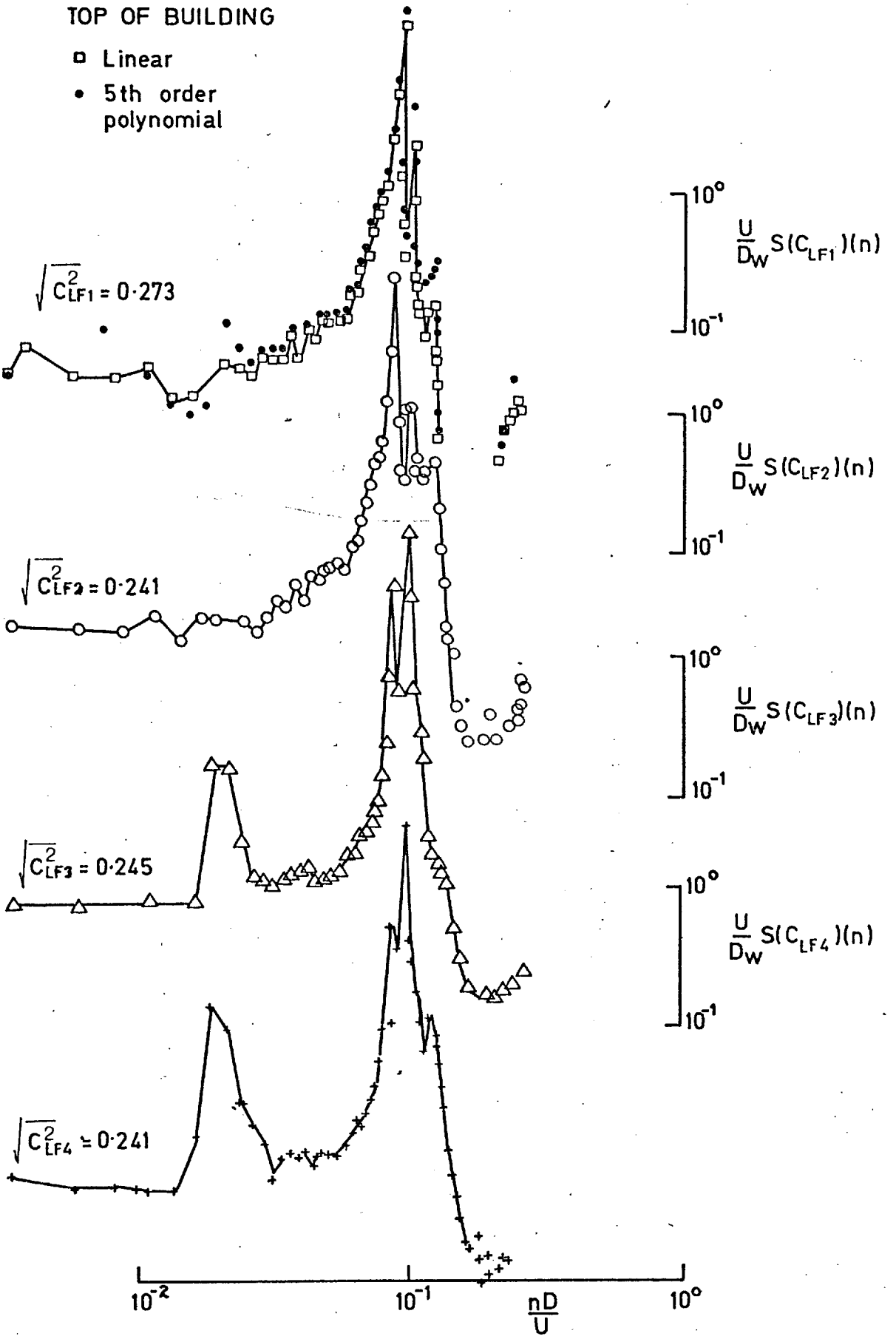
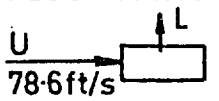


FIG. 54 FLUCTUATING LIFT FORCE SPECTRA



$\frac{U}{n_1 D} = 48{\cdot}4$ SMOOTH FLOW.

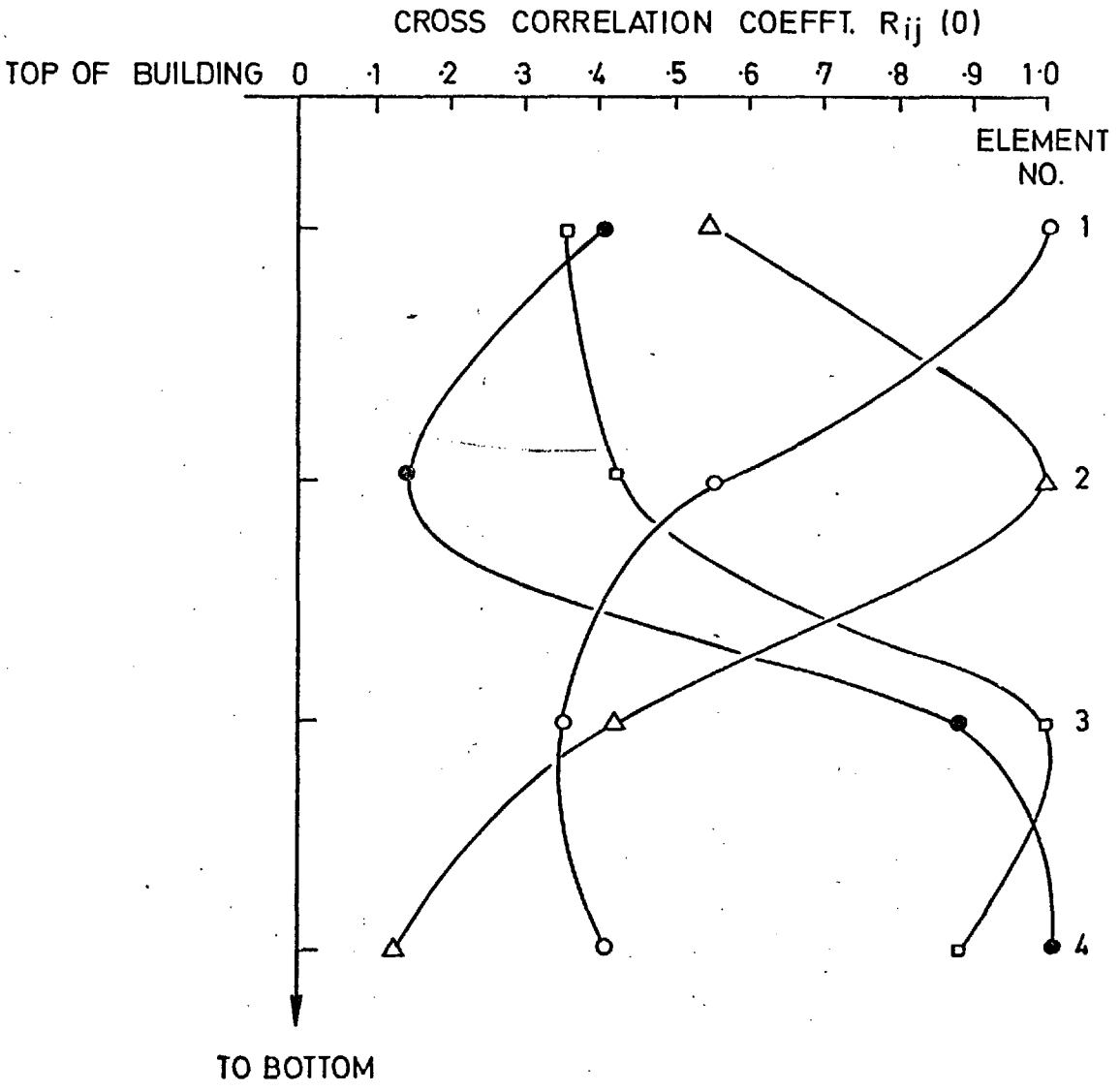


FIG. 55 LIFT FORCE CROSS CORRELATIONS $\frac{U}{n_1 D} = 48{\cdot}4$

SMOOTH FLOW $\frac{U}{78.6\,ft/s.}$ L

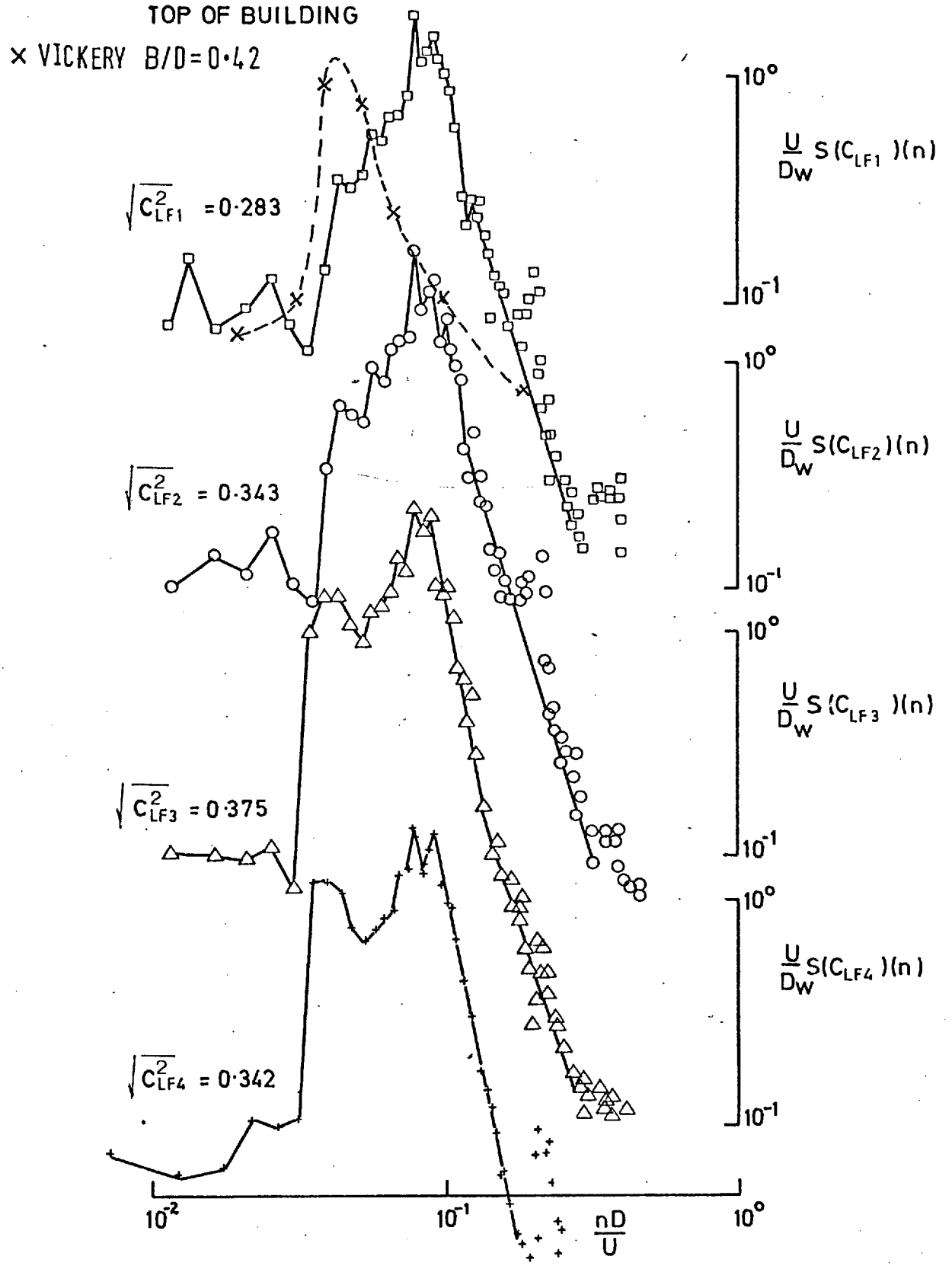


FIG. 56 FLUCTUATING LIFT FORCE SPECTRA

$\frac{U}{50{\cdot}07\,ft/s}$ L $\frac{U}{n_1 D}$ =31·1 TURBULENT FLOW.

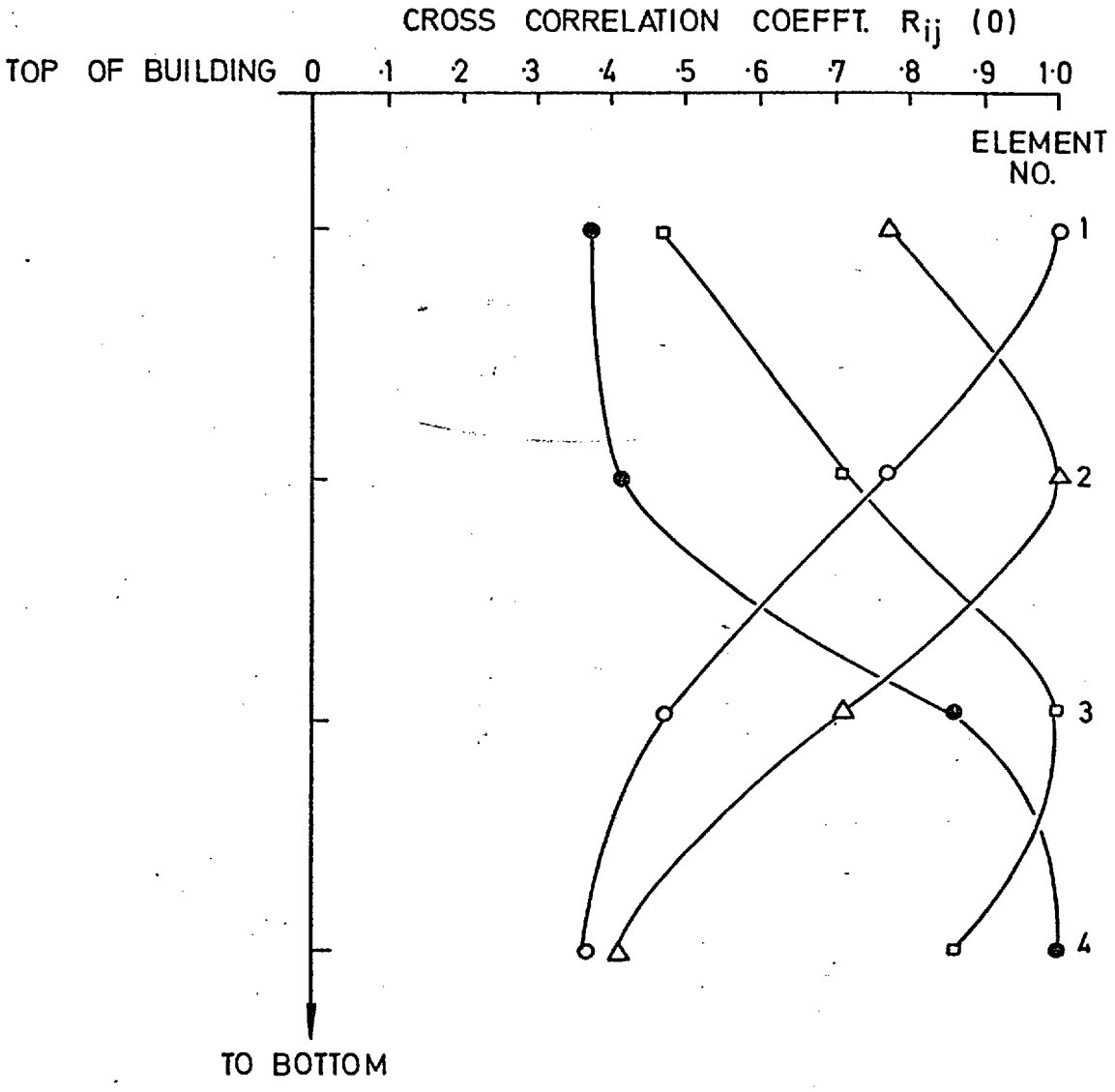


FIG.57 LIFT FORCE CROSS CORRELATIONS $\frac{U}{n_1 D} = 31{\cdot}1$

TURBULENT $\frac{U}{50{\cdot}0 ft/s}$ L

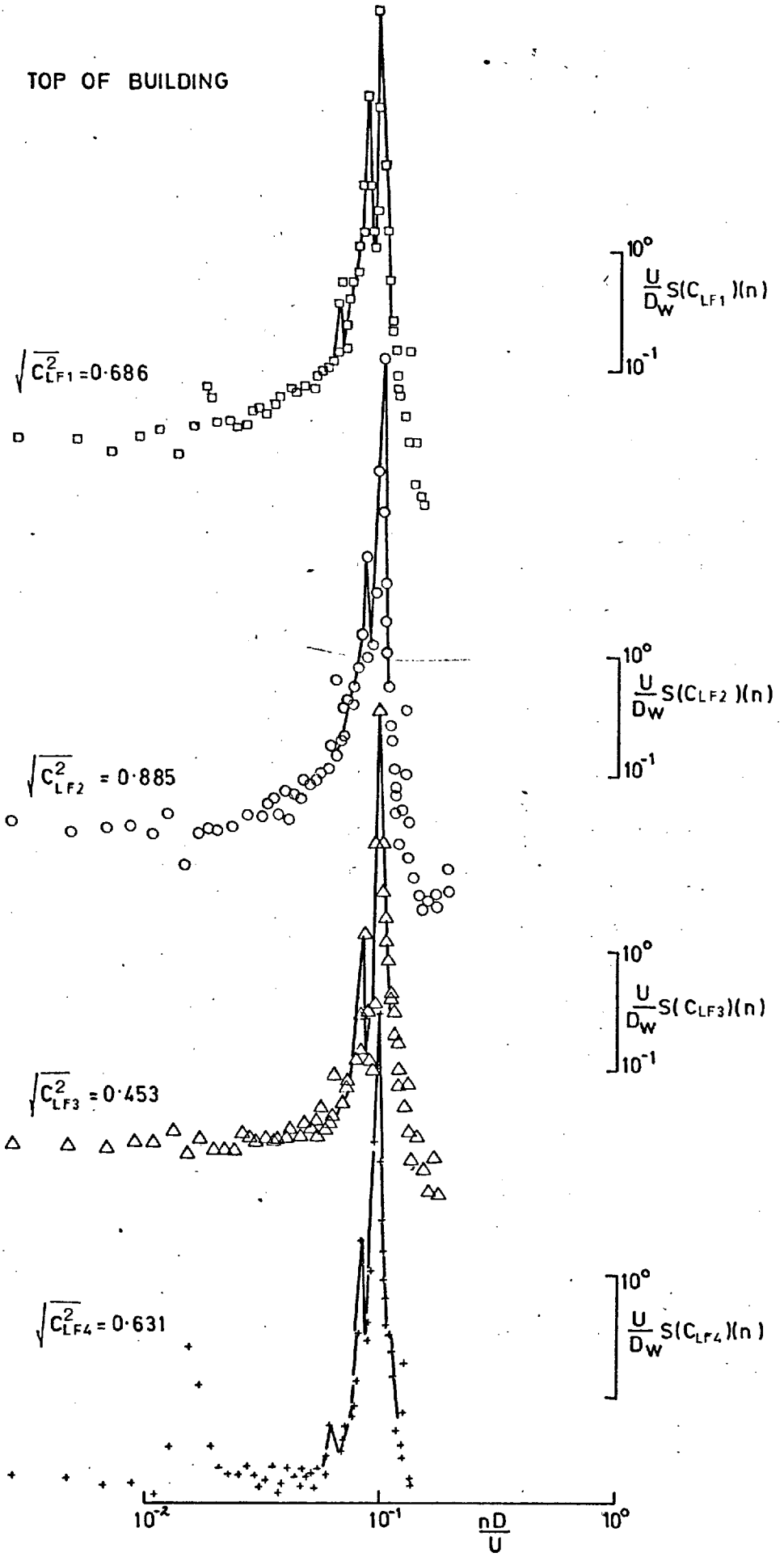
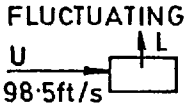


FIG. 58 FLUCTUATING LIFT FORCE SPECTRA



$\frac{U}{n_1 D} = 60{\cdot}6$ SMOOTH FLOW.
(RESONANT 2nd MODE)

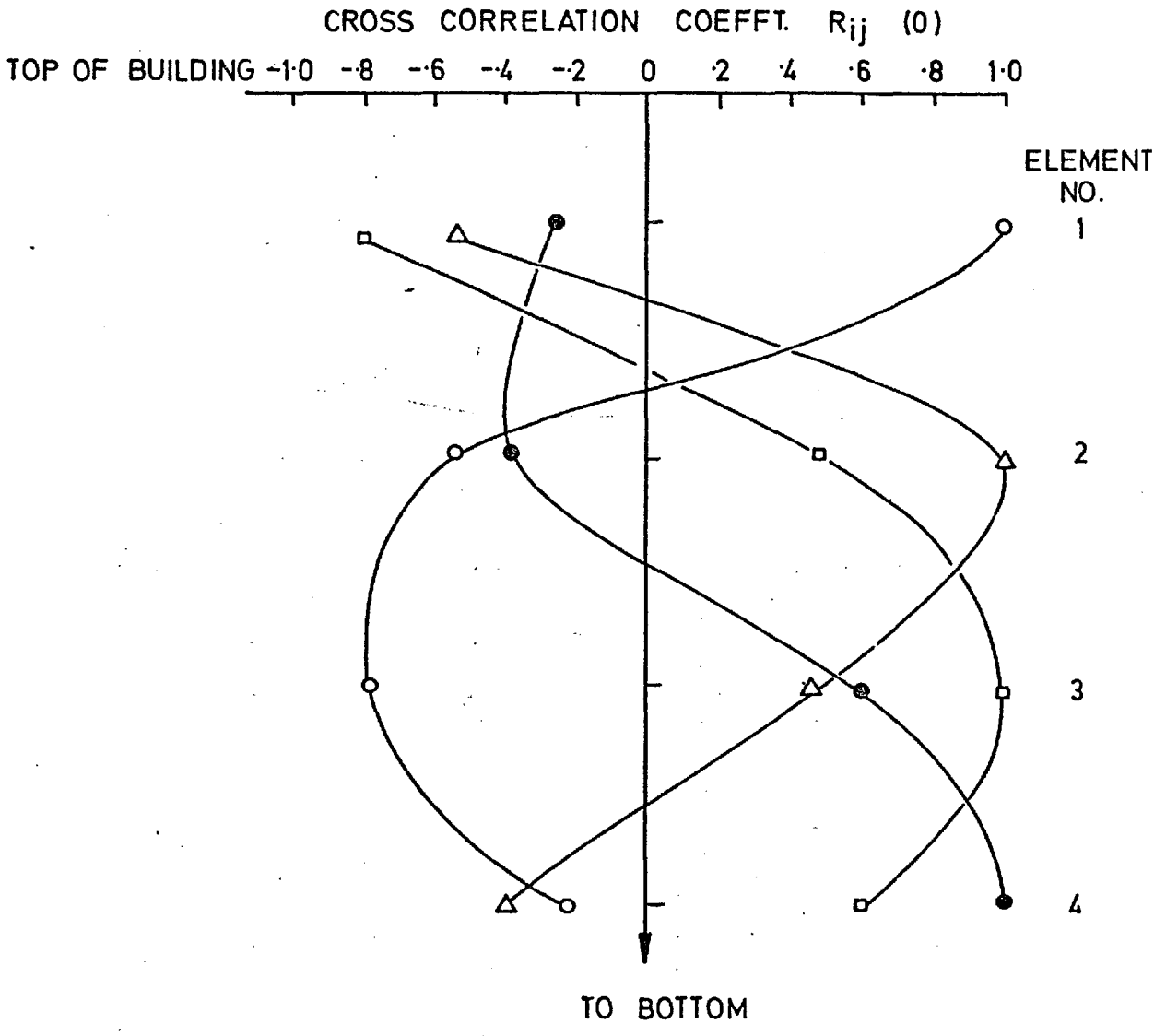


FIG. 59 LIFT FORCE CROSS CORRELATIONS $\frac{U}{n_1 D} = 60{\cdot}6$

SMOOTH $\frac{U}{98{\cdot}5 ft/s}$  (RESONANT 2nd MODE)

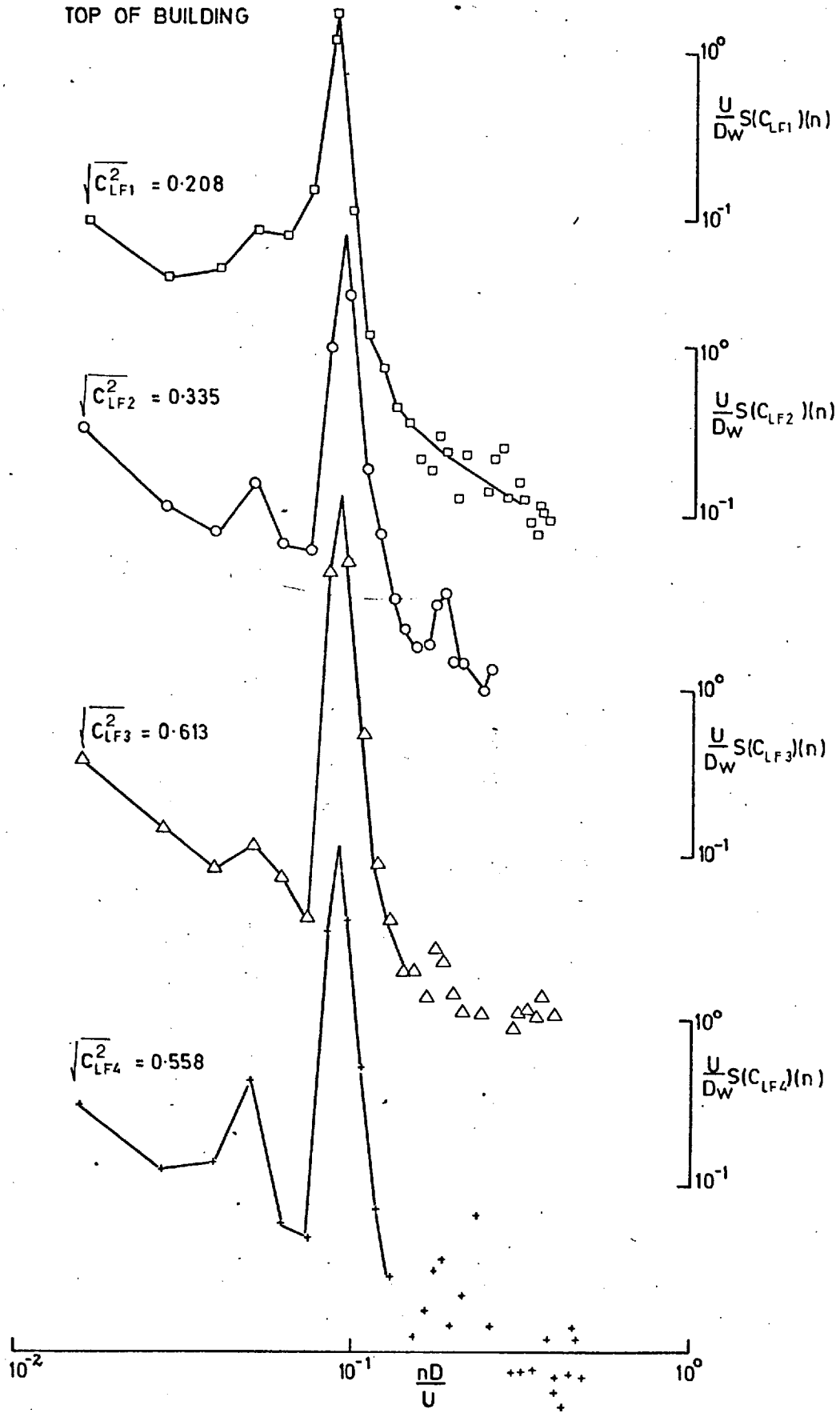


FIG. 60 FLUCTUATING LIFT FORCE SPECTRA -

$\frac{U}{18{\cdot}3\ ft/s}$ L $\frac{U}{n_1 D}$ =11·25 SMOOTH FLOW.
(RESONANT 1st MODE)

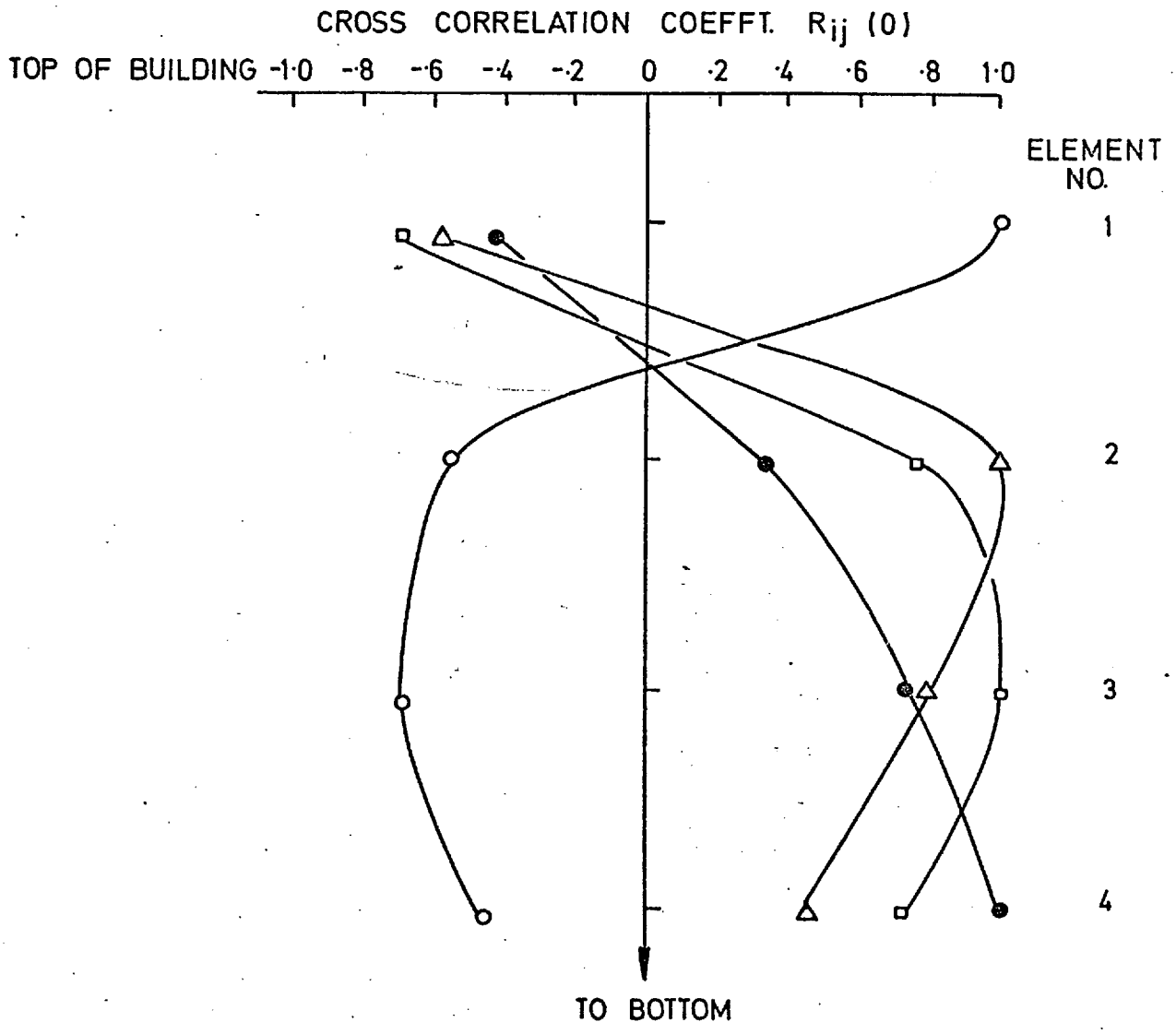


FIG. 61 LIFT FORCE CROSS CORRELATIONS $\frac{U}{n_1 D}$ = 11·25

SMOOTH $\frac{U}{18{\cdot}2\,ft/s}$ → L (RESONANT 1st MODE)

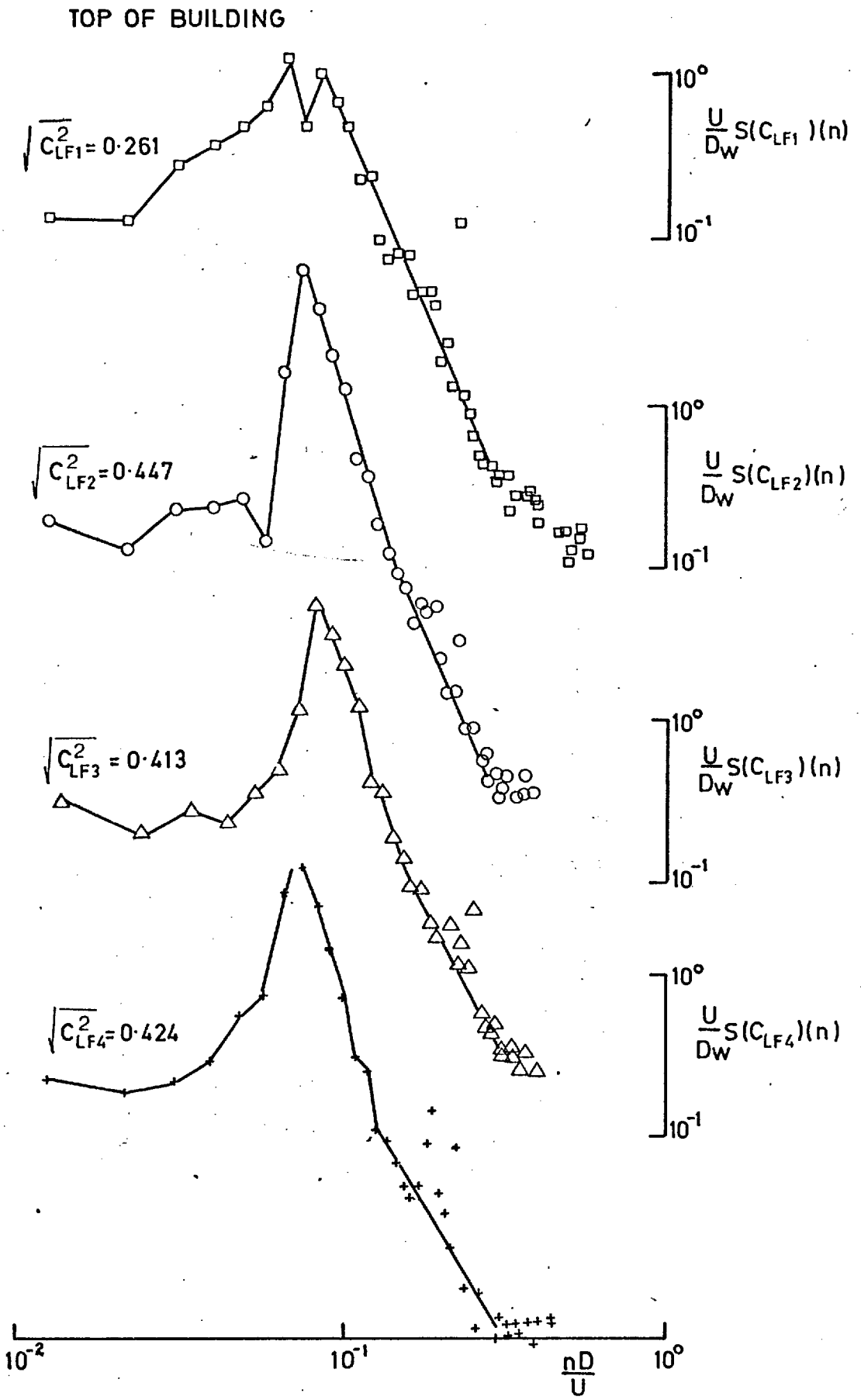


FIG. 62 FLUCTUATING LIFT FORCE SPECTRA $\frac{U}{22{\cdot}7\,ft/s}$  $\frac{U}{n_1 D} = 14$. TURBULENT FLOW.

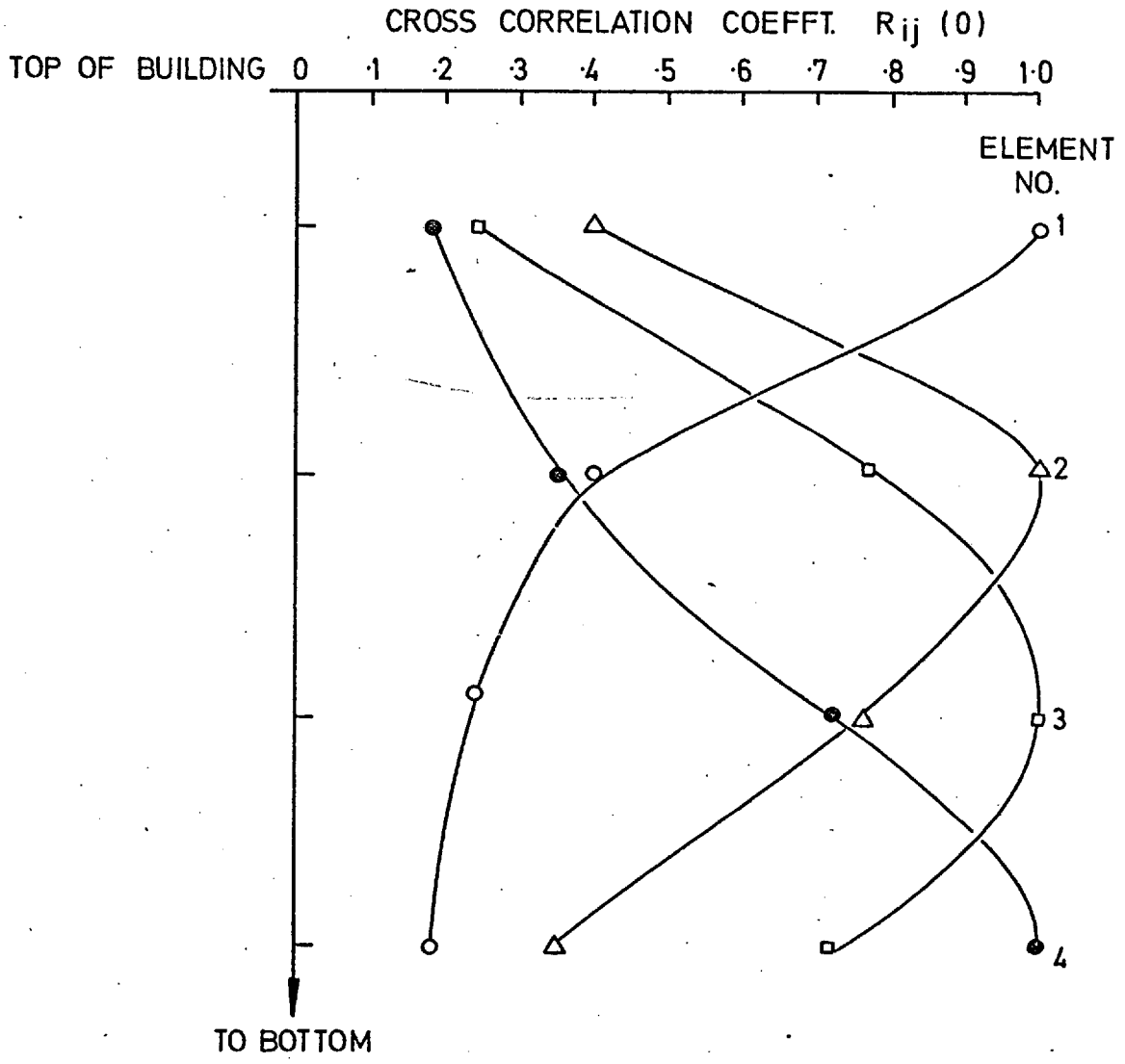


FIG. 63 LIFT FORCE CROSS CORRELATIONS $\frac{U}{n_1 D} = 14.$

TURBULENT $\frac{U}{22{\cdot}7 ft/s}$ L (RESONANT 1st MODE)

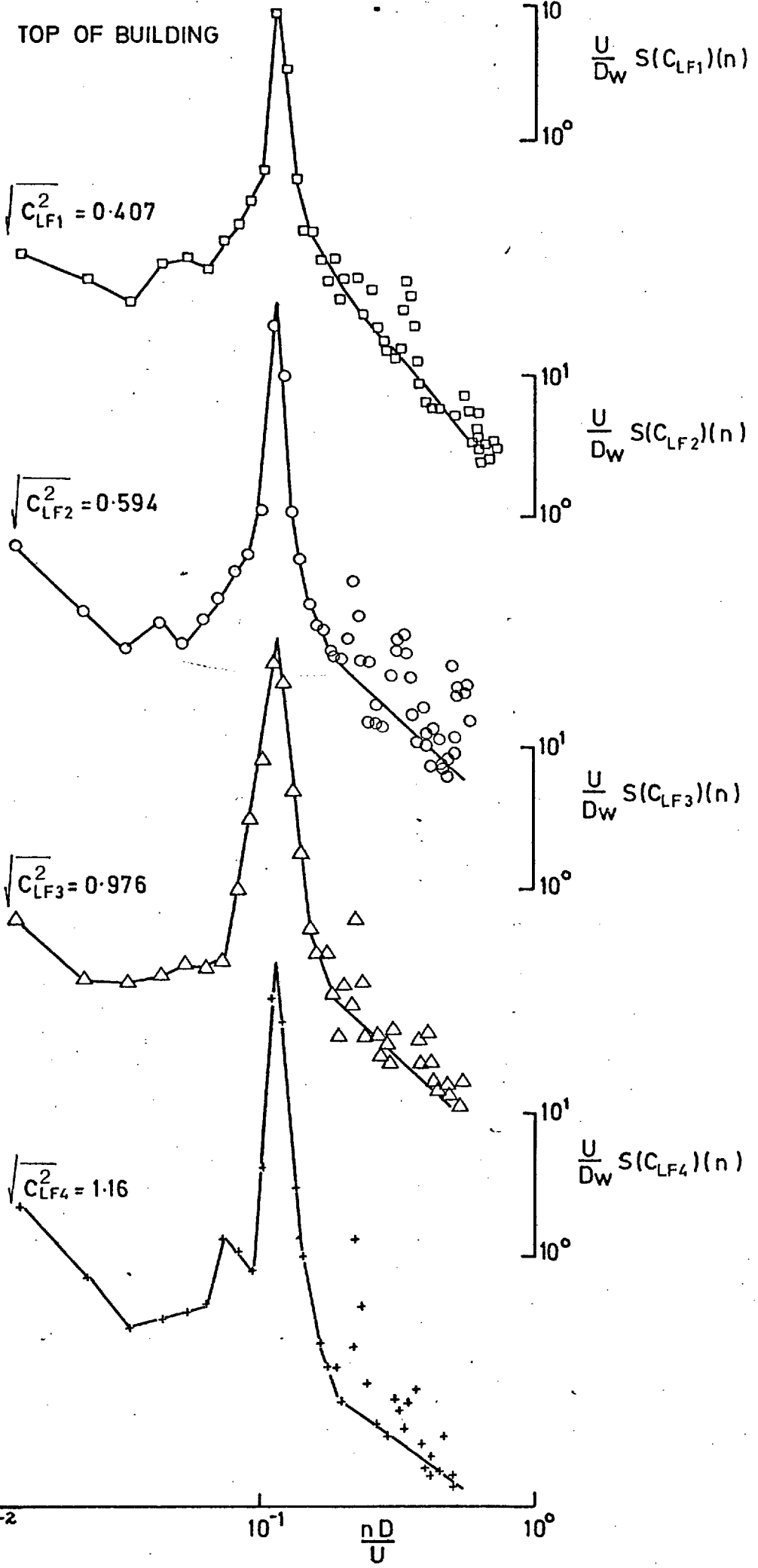
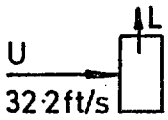


FIG.64 FLUCTUATING LIFT FORCE SPECTRA



TURBULENT FLOW.
(RESONANT 1st MODE)

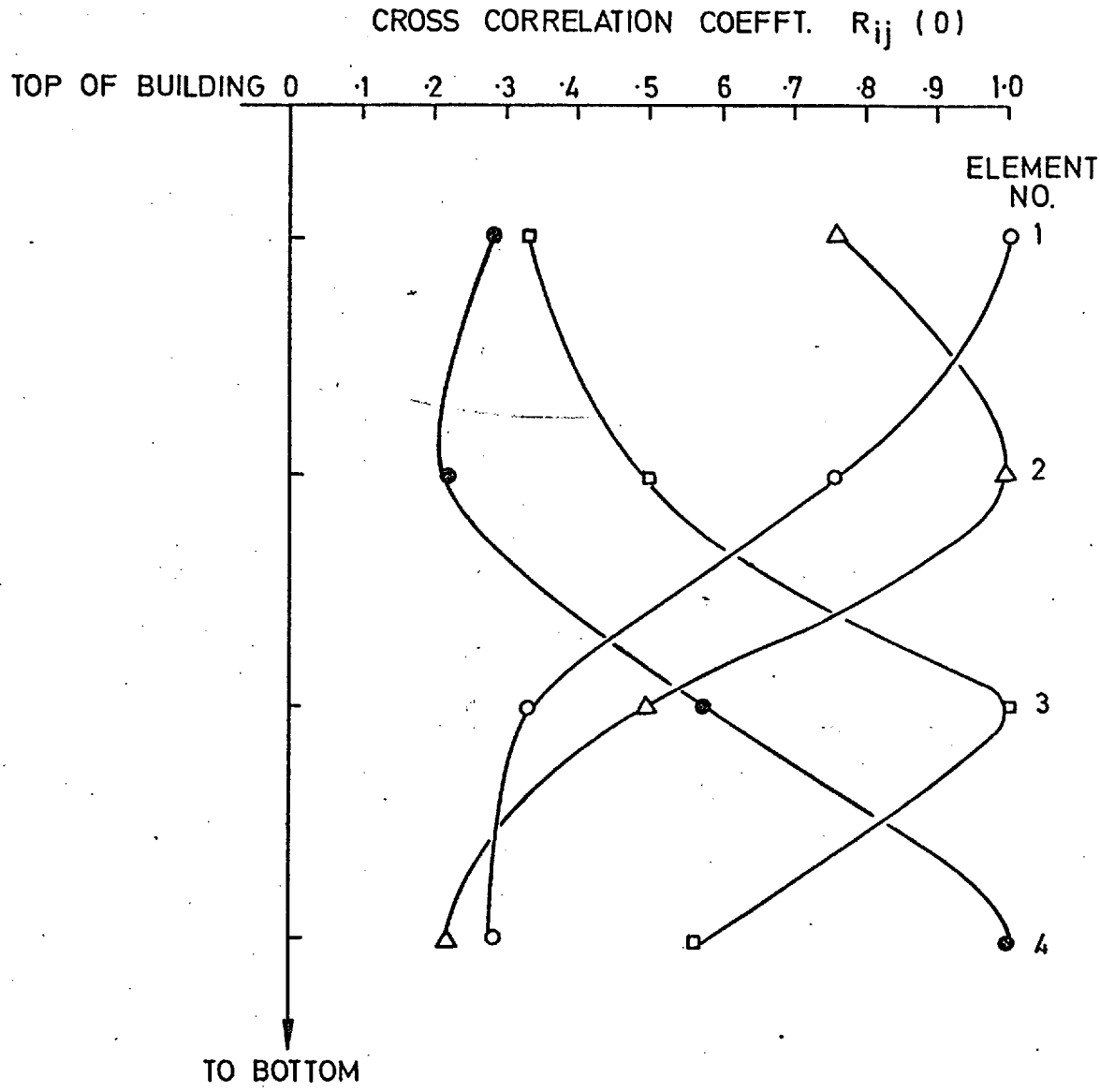
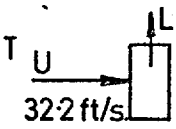


FIG. 65 LIFT FORCE CROSS CORRELATIONS $\frac{U}{n_1 D} = 8{\cdot}8$ TURBULENT 

(1st MODE RESONANT).

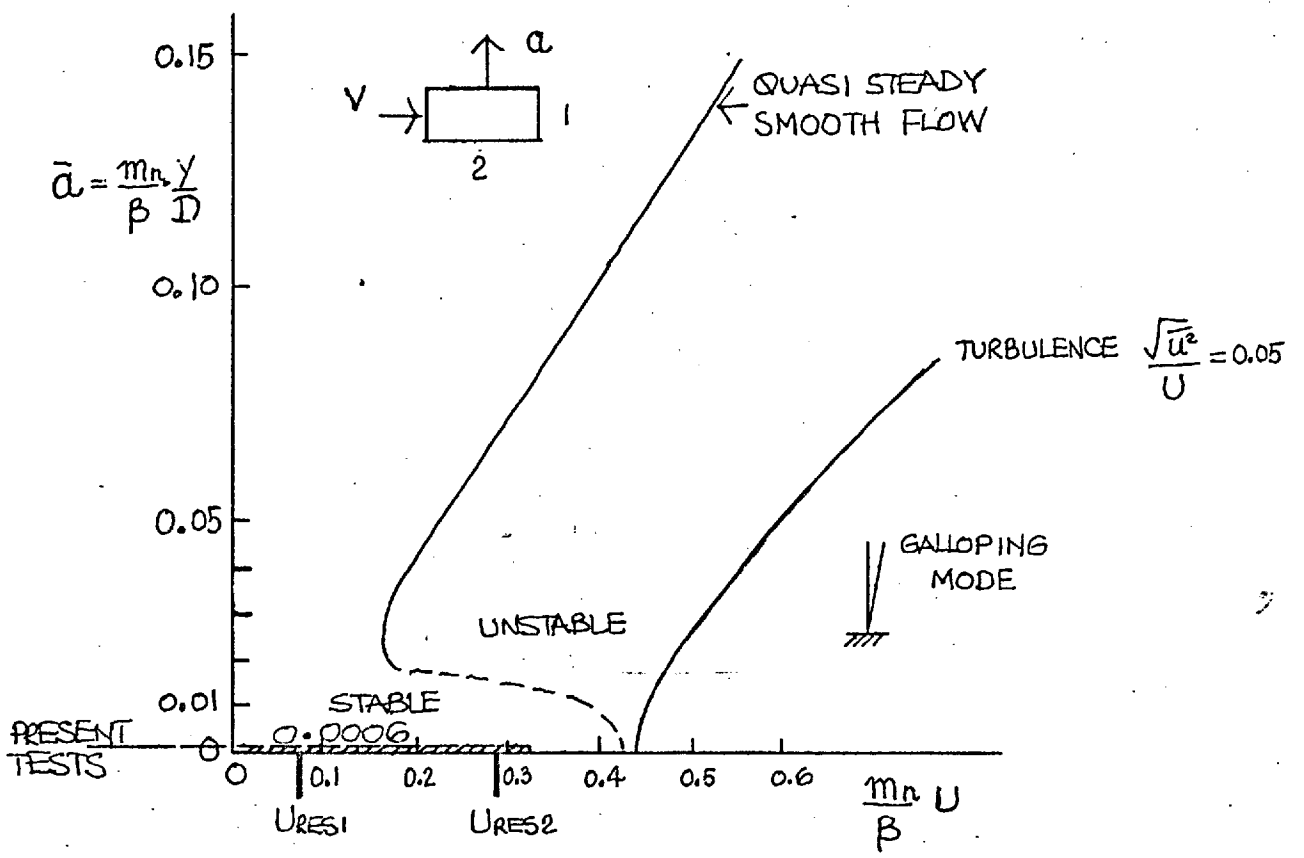


FIGURE 66 : GALLOPING 1:2 SECTION

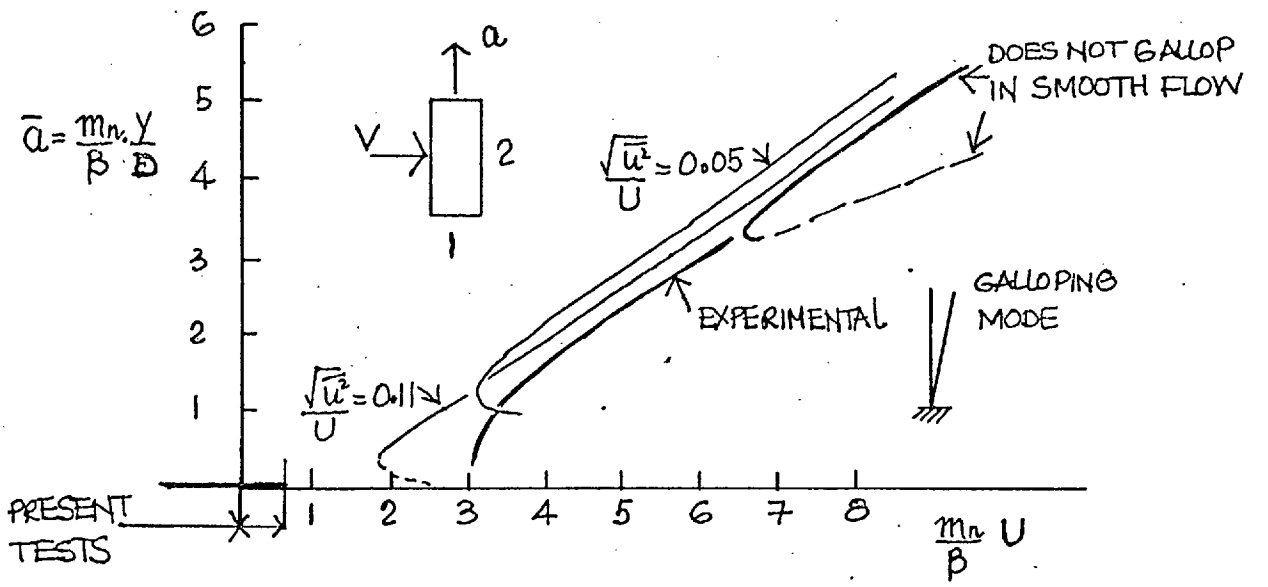


FIGURE 67: GALLOPING 2:1 SECTION.

PAPER No. 312

INTERNATIONAL SYMPOSIUM

VIBRATION PROBLEMS IN INDUSTRY

10-12 APRIL 1973

KESWICK, ENGLAND

A technique for evaluating the fluctuating aerodynamic forces on a flexible building

by

N. ELLIS

organised by

UK ATOMIC ENERGY AUTHORITY
WINDSCALE

and

NATIONAL PHYSICAL LABORATORY
TEDDINGTON

A TECHNIQUE FOR EVALUATING THE FLUCTUATING AERODYNAMIC FORCES ON A FLEXIBLE BUILDING

by

N. ELLIS*

A new computer orientated technique is presented that allows a spatial distribution and coherence of the fluctuating aerodynamic forces on a flexible building model to be determined by measuring the fluctuating random response. This inverse approach places no restrictions on the nature or coherence of these forces, thereby allowing the technique to be applied to models of real buildings in complex environments.

The linearity of the structural model used in wind tunnel tests is verified experimentally by dynamically vibrating the model with known random and harmonic forces. The prediction of these input forces with unity coherence and correct phase verifies the structural and computing techniques used.

Two techniques for predicting the input force spectra are outlined and one of these is shown to be susceptible to small bias errors.

The acceleration response for smooth and turbulent unsheared flow together with lift displacement and force power spectra at the top of the model are discussed.

A paper to be presented at the International Symposium on Vibration Problems in Industry. Keswick, England, April 1973.

* Research Assistant, Aeronautics Department, Imperial College, London SW7 2BY.

1. INTRODUCTION

A major problem associated with tall slender structures with a free end is to try and evaluate how the fluctuating lift and drag forces vary along the length of the structure, and further, the problems associated with the effect of dynamic displacement patterns on these fluctuating forces.

To investigate this problem a flexible model was designed, the basic idea being to invert the standard procedure of predicting dynamic response from "given" dynamic loads and instead use the response at twelve stations (6 lift, 6 drag) to predict the corresponding "actual" input forces, and their coherence. This is dynamically equivalent to solving the coupled equation of motion for a multi degree of freedom system to find the random input forces. A model was designed with assumed structural and aerodynamic parameters so that it would give measurable accelerations at both the tip and near the base of the model, in smooth and turbulent flow.

Fluctuating drag forces have been predicted by various authors[1,2,3] using an aerodynamic admittance function between the fluctuating velocity spectrum and the resulting fluctuating pressure. This assumed admittance function has been shown[2] to give good agreement with experimental results at high frequencies, $\frac{nD}{U} > 0.03$, but is in error at low frequencies.

As will be outlined later an initial technique using the multi degree of freedom frequency response function failed to predict known random input forces because of ill conditioning. From this a new technique evolved that predicted known random input forces with correct coherence and phase, without the knowledge of the frequency response or damping parameters. This new technique was used to analyse the fluctuating lift force power spectra and coherence at the tip of the model in smooth unsheared flow. The dynamic linearity of the model is verified by plotting the structural response loci for the frequency band of interest. It is hoped that the technique when fully developed will be used in predicting the fluctuating loads on buildings situated in highly complicated aerodynamic environments, for example, the case of a building between other buildings.

2. EXPERIMENTAL MODEL

The main object was to design a flexible model that would act as an 'n' degree of freedom transducer allowing the unsteady aerodynamic forces and their coherence to be predicted.

3. FLEXIBLE MODEL DESIGN

A matrix finite element analysis of the model was applied using simple beam elements, and the resulting dynamic eigenvalue problem for the assembled structure solved to obtain the model's resonant frequencies and mode shapes. These were used in conjunction with assumed harmonic aerodynamic forces from Vickery[4] to estimate the nodal accelerations for wind tunnel tests. (see Section 4). Figs. 18 to 21 show the actual acceleration response of the model for varying flow conditions.

The main problem associated with designing such a model was to obtain low structural resonant frequencies with a fixed base model that would be excited by vortex shedding and turbulent flow forces, and still have a model representative of a building structure. A rectangular section of 50 mm x 31 mm was chosen rather than a square, this allowing the effect of both section and aspect ratio to be considered. The height of the model is 500 mm giving two aspect ratios for the model of 10.0 and 15.8. This sectional shape also keeps the lift and drag resonant frequencies distinct, minimising coupled oscillations.
Fig. 1 shows the model isolated from floor vibrations by a seismic mass.
Fig. 2 shows the model in the wind tunnel.
Fig. 3 shows a section of the model during construction.
Fig. 4 shows the accelerometers set into the model.

The dimensions of the model were chosen to keep the length scale of the grid induced turbulence greater than D , the width of the model, and to minimise blockage effects. Perspex was chosen as the shell material, combined with six lead nodal masses, this being the best combination to give low structural resonant frequencies (see Figs. 7 to 9). Perspex has two other advantages:

(i) its bending damping ratio is approximately 2% critical thereby reducing any effect aerodynamic or acoustic damping may have.

(ii) as in (i) the high damping reduces the effect of the galloping instability.

4. MATHEMATICAL MODEL

The equation of motion for an 'n' degree of freedom system subject to harmonic input forces is

$$M\ddot{X} + (1+ig)K_\alpha X = Pe^{i\omega t} \qquad \ldots (1)$$

where M is the assembled mass matrix

K_α is the assembled stiffness matrix

igK_α is the complex stiffness matrix representing structural damping

Consider the model to consist of six simple beam elements each having a stiffness matrix

$$K_\epsilon = \frac{EI}{\ell^3}\begin{bmatrix} 12 & -12 & -6\ell & -6\ell \\ -12 & 12 & 6\ell & 6\ell \\ -6\ell & 6\ell & 4\ell^2 & 2\ell^2 \\ -6\ell & 6\ell & 2\ell^2 & 4\ell^2 \end{bmatrix}$$

Argyris[5] shows how these elements can be assembled giving

$$K_\alpha = \sum_{i=1}^{6} A_i^t \, k \, A_i$$

where A_i is a Boolean selection matrix.

Also

$$\begin{Bmatrix} P \\ M \end{Bmatrix} = \begin{bmatrix} K_{11} & K_{12} \\ K_{21} & K_{22} \end{bmatrix} \begin{Bmatrix} X \\ \theta \end{Bmatrix}$$

Considering the rotary inertias to have negligible effect on the resonant frequencies, the stiffness matrix K_α can be reduced to

$$K_\beta = K_{11} - K_{12}K_{22}^{-1}K_{21}$$

The solution of the homogeneous equation of motion

$$M\ddot{X} + K_\beta X = 0$$

defines the eigenvalue problem

$$(\lambda I - D)X = 0 \qquad \text{where} \qquad D = M^{-1}K_\beta$$

the solution of which yields λ , Φ , the eigenvalues and eigen-

vectors respectively, typical elements of which are

λ_i the i'th resonant frequency[2]

and Φ_i the i'th eigenvector

The eigenvalue problem was solved using a computer iterative technique, and the theoretical and experimental eigenvectors are shown on Figs. 7 to 9 for comparison. The torsional eigenvalues were also evaluated to check that torsional oscillations would not occur in wind tunnel tests. Fig. 5 shows the computer flow chart used in the above analysis.

5. ESTIMATED RESPONSE OF THE MATHEMATICAL MODEL

A major design problem was to try to ensure that the model would respond in the wind tunnel, and that this response is measurable at both the tip and near the base of the model. From Vickery[4] a Strouhal number of 0.1 was chosen and approximate fluctuating lift and drag coefficients used in the equation of motion (1) to estimate the acceleration response. Fig. 5 shows the computer flow chart for this estimation of response.

6. VERIFICATION OF LINEARITY

The definition of linearity is outlined by the application of Kennedy and Pancu's[6] technique for measuring eigenvectors, as applied to 'n' degree of freedom systems, and plotting the real and imaginary parts of the response to a constant amplitude sinusoidal input force applied using vibrators.

The 'n' degree of freedom damped equation of motion can be orthogonalised using the undamped eigenvectors Φ, when damping is assumed proportional to stiffness.

i.e. using the transformation to a generalised system

$$X = \Phi q$$

$$M\ddot{X} + (1+ig)\underset{\beta}{K}X = Pe^{i\omega t}$$

becomes 'n' single degree of freedom systems

$$m_{11}\ddot{q}_1 + (1+ig_1)k_{11}q_1 = Q_1 e^{i\omega t}$$

$$\vdots$$

$$m_{nn}\ddot{q}_n + (1+ig_n)k_{nn}q_n = Q_n e^{i\omega t}$$

At close to the i'th resonance

hence $X = \Phi q$

becomes $= \Phi_i q_i + B$

where B is a column of constants,

and chosing the k'th nodal response

$$x_k = \phi_{ik} q_i + B_i$$

thus the excitation of the model results in a displacement x_k proportional to q_i at the i'th resonance.

For a single degree of freedom system

$$m_{11}\ddot{q}_1 + (1+ig_1)k_{11}q_1 = Q_1 e^{i\omega t}$$

the solution of which is

$$q_1 = \frac{Q_1}{k_{11}}\left(\frac{1-\beta^2}{(1-\beta^2)^2+g_1^2} + i\frac{-g_1}{(1-\beta^2)^2+g_1^2}\right)$$

$$= R + iI$$

where $\beta = \frac{\omega}{\omega_i}$

The point of resonance in the response loci is defined where a line joins the centre of the circle to the point where

$$\frac{d(\frac{q_1}{Q_1})}{d(\beta^2)}$$ is a minimum

The ratios of the diameters of the circles are the experimental eigenvectors. Figs. 7 to 9 show that the assumption of damping proportional to stiffness is correct for the 1st, 2nd, and 3rd modes respectively, as this implies that the resonant point is always parallel to the I axis, furthermore, this damping varies for each individual mode. Small non linearities in a structure can cause distortion in the response loci, while large non linearities cause "jumps", and the frequency at which these "jumps" occur varies depending on whether the frequency is increasing or decreasing. Since Figs. 7 to 9 show no traces of these effects, hence the model has linear dynamic characteristics.

7. INITIAL TECHNIQUE

This technique was first conceived when trying to determine the nodal force spectra from the nodal displacement spectra. The displace-

ment spectra being experimentally found from accelerometers. It will be shown that this approach generates a perturbation which may arise from small experimental errors, and to avoid this a new approach was developed. As outlined in Lin[7]

$$S_x(\omega) = H(\omega)\, S_p(\omega)\, H^{t}_{*}(\omega) \qquad \text{and consequently}$$

$$S_p = H^{-1} S_x H^{-t}_{*} \qquad * \text{ complex conjugate}$$

thus knowing the multi degree of freedom displacement spectra S_x the corresponding nodal force spectra S_p can be found. This technique therefore requires the full experimental freqency response function to be inverted for every frequency considered. The cross correlation function of the generalised displacements can be defined as

$$R_q(\tau) = E[\, q(t)\, q^t(t+\tau)\,]$$

and using the model's eigenvectors Φ , with the transformation

$$X = \Phi q$$

hence

$$R_q = \Phi^{-1} R_x \Phi^{-t}$$

where R_x is the cross correlation function of nodal displacements,

and

$$S_q = \Phi^{-1} S_x \Phi^{-t} \qquad \ldots \text{(i)}$$

in terms of the nodal displacement spectra.

For the generalised force spectra

$$Q = \Phi^t P \quad , \text{ and as above}$$

$$S_Q = \Phi^t S_p \Phi \qquad \ldots \text{(ii)}$$

$$= h_q^{-1} S_q h^{-t}_{*q} \qquad \ldots \text{(iii)}$$

where h_q is the generalised frequency response function and is a diagonal complex matrix.

Substituting (i) and (ii) into (iii)

$$S_p = \Phi^{-t} h_q^{-1} \Phi^{-1} S_x \Phi^{-t} h^{-t}_{*q} \Phi^{-1}$$

hence $$H^{-1} = \Phi^{-t}\, h_q^{-1}\, \Phi^{-1}$$

and since h_q is diagonal no complex inversion of H is necessary.

where $$h_q = k_q - \omega^2 m_q + i g k_q$$

$$k_q = \Phi^t K \Phi$$

$$m_q = \Phi^t M \Phi$$

and h_q can be determined experimentally as outlined in Section 6 on linearity, where k_{qii} is found from $k_{qii} = \omega_i^2 m_{qii}$

Having completed the experimental determination of the frequency response function, wind tunnel tests were carried out to obtain the displacement spectra S_x for various flow conditions. A typical feature of the force spectra obtained using this technique was the high amount of low frequency energy, orders higher than expected. This phenomenon was further clouded by the apparent convergence at higher frequencies. To explain this a perturbation analysis was conducted.

8. PERTURBATION ANALYSIS OF THE INITIAL TECHNIQUE

Using the experimental frequency response function, mathematical white noise force spectra were input at stations 3 and 6, and S_x the nodal response found. A 1% bias error was introduced in S_{x1}, this being synonymous with a small experimental error. The inverse procedure using S_x to find S_p gave results outlined in Fig. 10, these being similar to wind tunnel results in that very small errors in S_x cause orders of change in the predicted input forces at lower frequencies, and convergence at higher frequencies.

9. MATHEMATICAL EXPLANATION OF PERTURBATION

The effect of forming S_p from S_x via H, the frequency response function, is that a random force pattern associated with a given random displacement pattern is formed. Consider the displacement at any one station to have a small bias error due to recording, then the nodal force pattern associated with this small "kink" can be very large indeed, since this kink will appear as a combination of the higher modes.

Mathematically the random displacement pattern can be defined as

$$X = \sum_{i=1}^{6} a_i \Phi_i$$

where Φ_i is the i 'th eigenvector

and a_i is a column of constants

Consider the solution of the undamped equation of motion

$$[K - \omega^2 M]X = P$$

where X has a small error Δ with associated δP

i.e. $X' = X + \Delta$ $P' = P + \delta P$

at low frequencies $\omega \rightarrow o$ gives the "error" eigenvalue problem

$$K\{X+\Delta\} = P+\delta P$$

giving $K\Delta = \delta P$ for the error

and using $\Delta = \Phi a$ and $K\Phi = \Phi \lambda$

substitution gives $\delta P = \Phi \lambda a$

and a typical element

$$\delta P_i = \phi_{i1}\lambda_1 a_1 + \phi_{2i}\lambda_2 a_2 + \cdots \phi_{6i}\lambda_6 a_6$$

Both ϕ_{ij} and a_i are of order unity.

but $\lambda_6 >> \lambda_1$ or $\omega_6^2 >> \omega_1^2$

where ω_i is the i 'th resonant frequency.

Hence any small error associated with X introduces the higher order terms $\phi_{6i}\ \lambda_6\ a_6$ at low frequencies,

with convergence as $\omega \rightarrow \omega_6$ (see Fig. 10).

10. THE NEW TECHNIQUE

The new technique was developed from the field and point transfer matrix approach as outlined in Lin[7]. Consider the beam elements and lumped masses m_i defined at their nodal points (as in Diagram A below)

The model is subjected to the random fluctuating pressure field $P(t)$, this being represented by the discrete nodal forces $P_i(t)$, the nodal masses having random accelerations $\ddot{X}_i(t)$. Fig. 6 shows the data gathering and computing techniques used in forming the input force spectra $S_p(\omega)$. It basically consists of recording the random accelerations and strains simultaneously, digitising, then taking moments instantaneously, working from the tip downwards. For example, to find $P_1(t_i)$

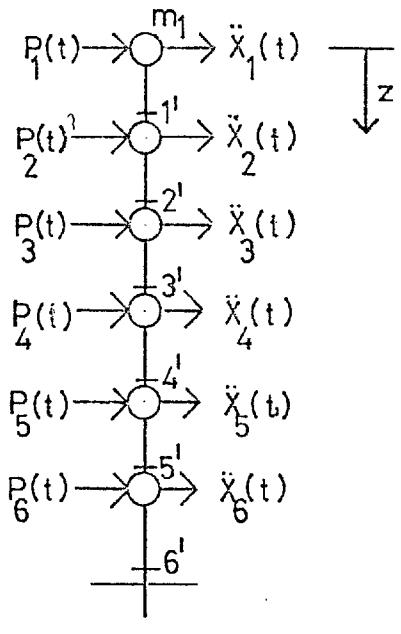


DIAGRAM A

$$M_{1'}(t_i) = \frac{EI}{y}\,\mathcal{E}^{*}_{1'}(t_i) \quad , \text{ where } \mathcal{E}^{*}_{1'}(t_i) \text{ is complex}$$

$$P_1(t_i) = m_1\ddot{X}_1(t_i)\,z_{1'} + M_{1'}(t_i) \quad \text{for} \quad i = 1, n$$

and $$P_2(t_i) = m_1\ddot{X}_1(t_i)\,z_{2'} + m_2\ddot{X}_2(t_i)\,z_{1'} - P_1(t_i)\,z_{2'} + M_{2'}(t_i) \quad \text{for} \quad i = 1, n$$

$$\vdots$$

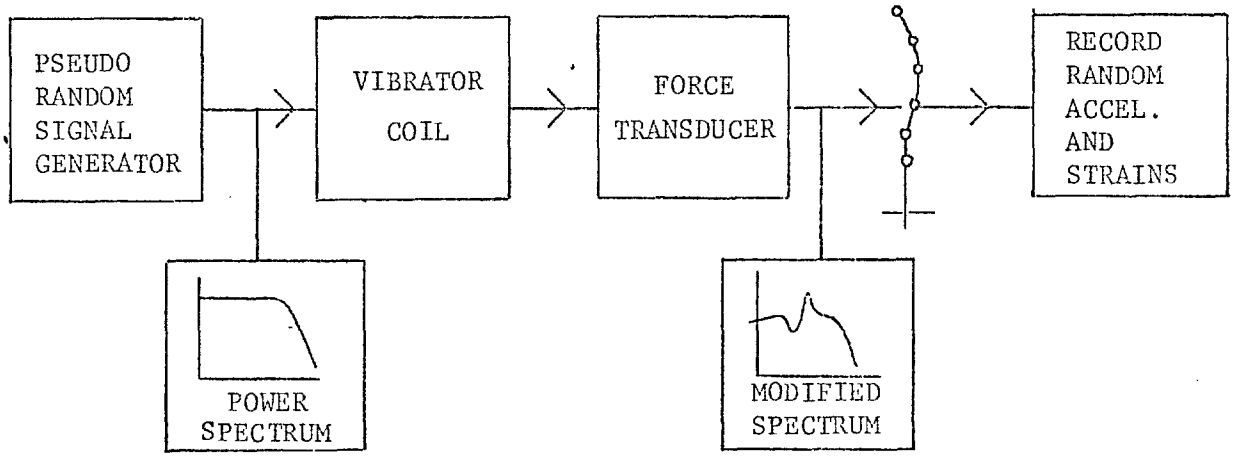
etc

hence by measuring the instantaneous bending strains and accelerations the nodal forces $P(t_i)$ and $S_p(\omega)$ can be found. The dynamic strains $\mathcal{E}^{*}(t_i)$ will have a small complex part that keeps the equation of motion balanced at resonance. This technique does not suffer from the perturbations encountered in the "initial technique", as is verified in Section 11 on the prediction of random forces. It also has the added advantage that the input forces are found without the knowledge of the

frequency response function or damping, as this is inherent in measuring $\mathcal{E}_{i'}(t)$.

11. PREDICTION OF KNOWN RANDOM AND HARMONIC INPUTS

To prove that the technique works practically, the model was dynamically vibrated with known random and harmonic forces applied using vibrators as shown below.



DYNAMIC TEST SET UP

The pseudo random signal generator has a flat power spectrum output. The vibrator coil mass introduces a random inertia force that can considerably modify the flat power spectrum, depending on the displacement of the model at the point where the force transducer is connected. The effect of this added inertia force is shown in the difference between Figs. 11 and 14. Fig. 11 shows close agreement between the actual and predicted force spectra at station 1 (tip). Figs. 14 and 15 show a different modified input force spectrum at station 1, together with the coherence and phase between the actual and predicted. Ideally the coherence should be unity and phase zero in the band width of interest. To verify that the technique predicts input resonant forces, a sinusoidal force was predicted with unity coherence and zero phase as in Figs. 12 and 13. Figs. 16 and 17 show the prediction of a random force at the position between stations 2 and 3.

12. RESULTS - WIND TUNNEL TESTS

Fig. 20 shows the lift acceleration response for the critical section with the 50 mm side normal to the flow. As outlined by Nakaguchi et al[8], the critical section is that section which has a two

dimensional drag coefficient of 2.8 compared with 2.0 for a flat plate. In this case the influence of the tip flow seems to control the vortex formation in that vortices are generated in "bursts" and not in a continuous manner. This gives small r.m.s lift accelerations although during a burst they are instantaneously large. As shown in Fig. 21, the effect of oncoming turbulence is to wash out the tip effect and allow coherent vortex formation. In smooth flow the base pressure C_{pb} is -0.62 at the top and -0.9 at close to the base, compared with -1.0 for both positions in turbulent flow. Thus a more two dimensional wake is formed together with a greater rate of entrainment of air from the base, and stronger vortex shedding, in turbulent flow.

Fig. 18 shows how the 1st and 2nd lift modes can be excited in smooth flow, the 31 mm face being windward. With the 1st mode in resonance with vortex shedding at $R_e = 1.26 \times 10^4$, the lift displacement power spectrum for the top position (Fig. 22) indicates that most of the power is centred at $\frac{nD}{U} = 0.085$. The corresponding force spectra on Fig. 23 agrees with this in that most of the lift force power is centred at $\frac{nD}{U} = 0.085$ with a smaller peak at $\frac{nD}{U} = 0.1$ for both top and 2nd from top positions. This result contrasts with the lift force power spectra for $R_e = 5.4 \times 10^4$ (Fig. 25), where the displacement power is approximately two orders lower (see Fig. 24 for $R_e = 3.7 \times 10^4$), in that the frequency at which the peak power is centred reduces from $\frac{nD}{U} = 0.10$ at the top to $\frac{nD}{U} = 0.085$ at the 2nd position. Further evidence suggests that the shedding frequency returns to the tip value lower down the model, this being in agreement with Maull and Young's[9] results from hot wire measurements of velocity fluctuations in the wake of a bluff body with a free end. The fluctuating lift coefficients are found to be 0.48 and 1.23 for top and 2nd top positions respectively, the difference being due to tip flow effects. The fluctuating lift coefficient for the 1st mode resonant condition appears to be much larger than the above values and this is thought to be due to aeroelastic forces. Further investigations of this phenomenon are being made before final results for this resonant condition are presented.

13. CONCLUSIONS

The new technique presented in this paper predicts the fluctuating aerodynamic forces and their coherence down a flexible building model. The test model used has linear dynamic characteristics.

The validity of the results obtained using the technique is verified by the prediction of known random and harmonic forces.

The fluctuating lift coefficient for the tip of the model in smooth flow for $R_e = 5.4 \times 10^4$ was found to be 0.48 and 1.23 for top and 2nd top positions respectively.

At 1st mode resonance with the vortex shedding frequency in smooth flow an aeroelastic interaction takes place that considerably increases the fluctuating lift coefficients.

In conclusion, emphasis has been placed on the description of the technique rather than detailed interpretation of the fluctuating aerodynamic forces obtained, this being a separate problem which is at present under investigation.

Acknowledgement: The author wishes to acknowledge the Building Research Establishment for financial assistance, and to Dr. P.F. Kilty and Dr. P.W. Bearman, Aeronautics Department, Imperial College, for advice and assistance.

MATHEMATICAL SYMBOLS

- A_w - windward area
- $\mathbf{A}_i$ - Boolean selection matrix
- $\mathbf{B}$ - column of constants
- c_{1j} - coherence between forces referred to top position
- C_{LFi} - fluct. lift coefft. (lift force r.m.s/$(1/2 \cdot \rho U^2 \cdot A_w)$)
- $\mathbf{D}$ - dynamical matrix
- G_L - r.m.s. lift acceleration response
- $\mathbf{I}$ - unit matrix
- $\mathbf{K}_\epsilon$ - element stiffness matrix
- $\mathbf{K}_\alpha$ - assembled stiffness matrix
- $\mathbf{K}_\beta$ - reduced stiffness matrix
- $\mathbf{M}$ - mass matrix
- $M_{i'}$ - instantaneous dynamic moment (complex)
- $\frac{nD}{U}$ - non dimensional frequency
- $\mathbf{P}$ - column of random input forces (complex)
- $\mathbf{Q}$ - generalised random input forces (complex)
- $\mathbf{q}$ - generalised displacements (complex)
- R_e - Reynolds number
- $S_p(\omega)$ - input nodal force spectra (complex)
- $S_Q(\omega)$ - generalised input nodal force spectra (complex)

$S_X(\omega)$ - spectra of nodal displacements (complex)

$S_q(\omega)$ - generalised spectra of nodal displacements (complex)

S_N - Strouhal number

X - column of nodal displacements (complex)

λ - eigenvalues

ω_i - resonant frequencies

Φ - matrix eigenvectors

Φ_i - i'th eigenvector

k_q - generalised stiffness matrix

m_q - generalised mass matrix

Δ - bias error associated with X

$\hat{\epsilon}(t_i)$ - column of instantaneous strains (complex)

REFERENCES

1. Davenport, A.G. The application of statistical concepts to wind loading on structures. Proc. Inst. Civ. Engrs. VOL 19, paper 6480, 1961.

2. Bearman, P.W. Turbulence-induced vibrations of bluff bodies. Paper H1. Symposium on Flow-Induced Structural Vibrations, Karlsruhe, Germany, August 1972.

3. Vickery, B.J. On the flow behind a coarse grid and its use as a model of atmospheric turbulence in studies related to wind loads on buildings. N.P.L. Aero Rep. 1143, 1965.

4. Vickery, B.J. Load fluctuations in turbulent flow. Proc. Amer. Soc. Civ. Engrs. paper Em 1, Feb. 1968.

5. Argyris, J.H. & Kelsey, S. Energy theorems and structural analysis. Butterworths, 3rd Edition, 1971.

6. Kennedy, C.C. & Pancu, C.D.P. Use of vectors in vibration measurement and analysis. Jrnl. Aero Sci., November 1947.

7. Lin, Y.K. Probabilistic theory of structural dynamics. McGraw-Hill

8. Nakaguchi, H. Hashimoto, K. & Muto, S. Proc. of Symposium of Low Speed Wind Tunnels. Tokyo Univ. April 1967.

9. Maull & Young Vortex shedding from a bluff body in shear flow. Paper H2. Symposium on Flow-Induced Vibrations, Karlsruhe, Germany, August 1972.

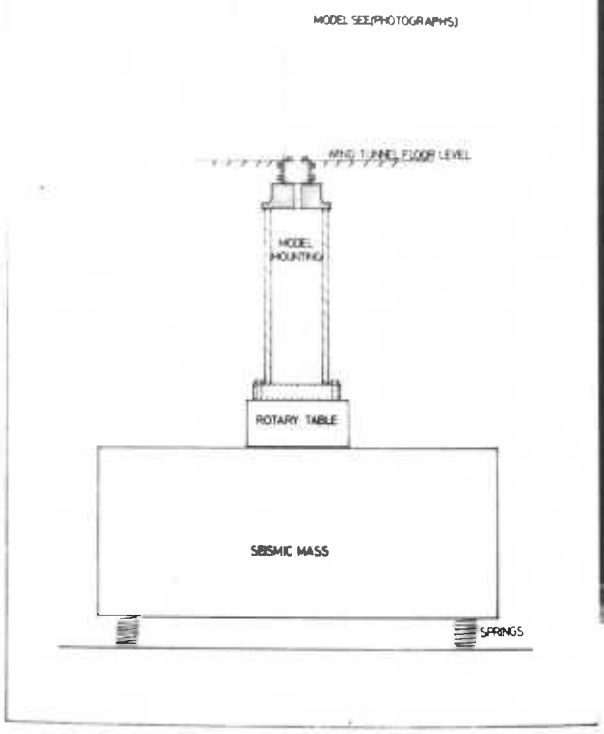


FIG 1 MODEL ON SEISMIC MASS

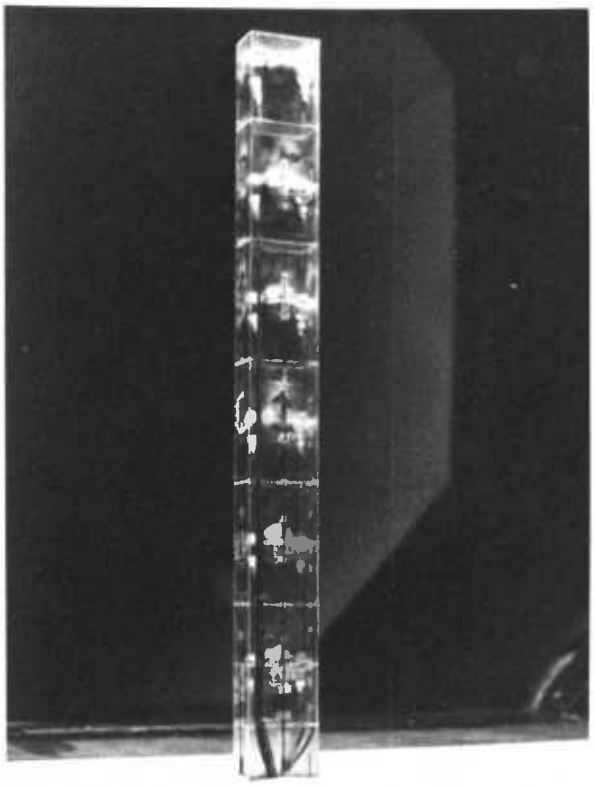


FIG 2 MODEL IN WIND TUNNEL

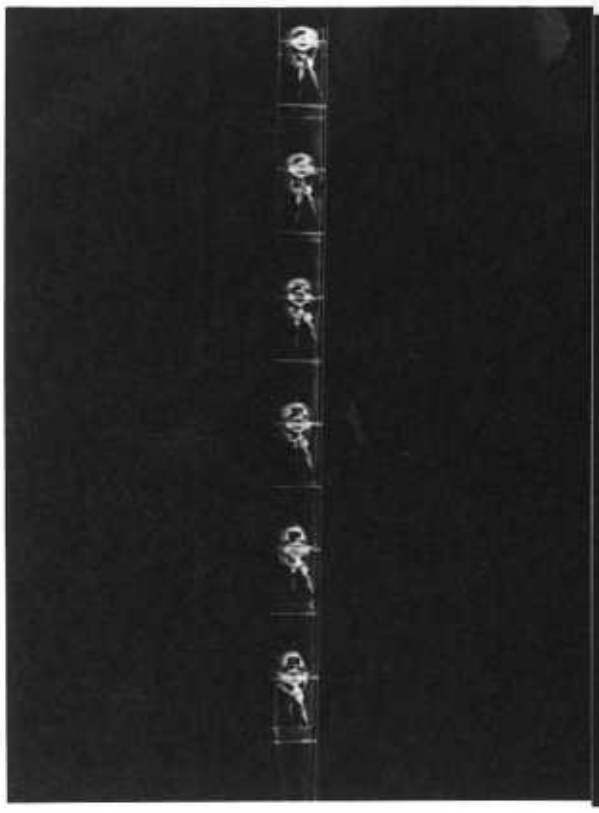


FIG 3 SECTION OF MODEL

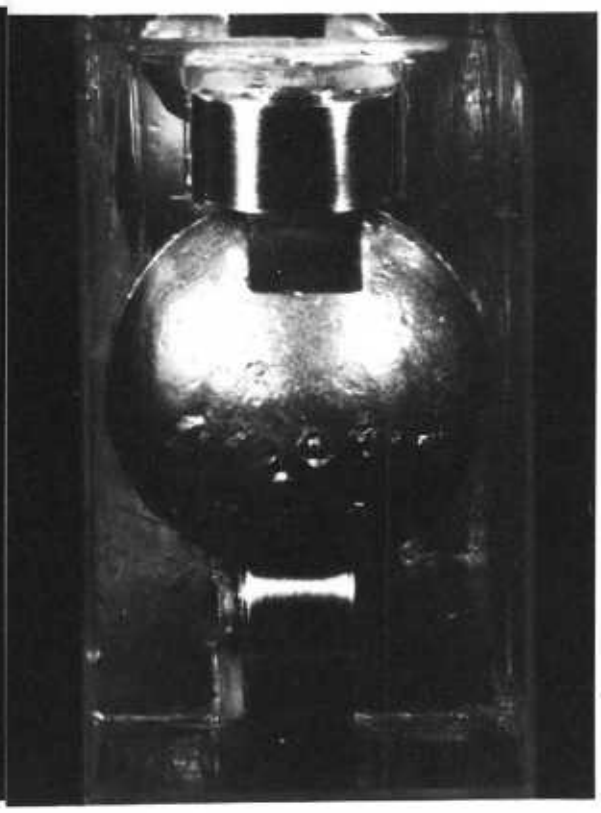


FIG 4 INBUILT ACCELEROMETERS

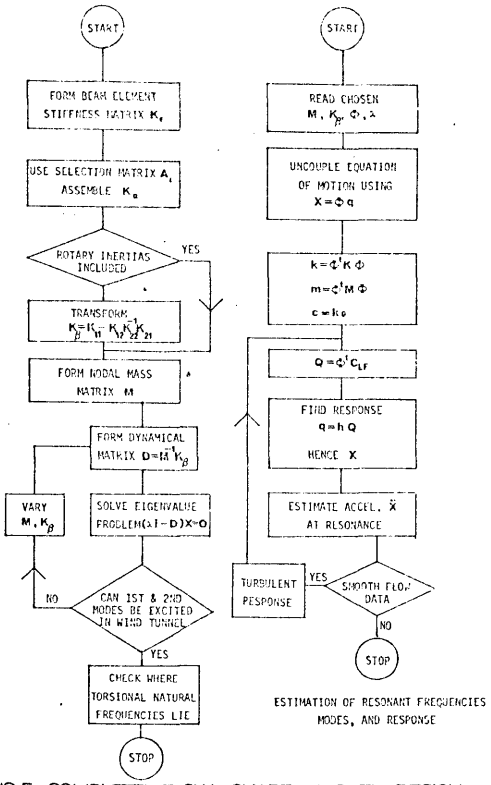


FIG 5 COMPUTER FLOW CHART - MODEL DESIGN

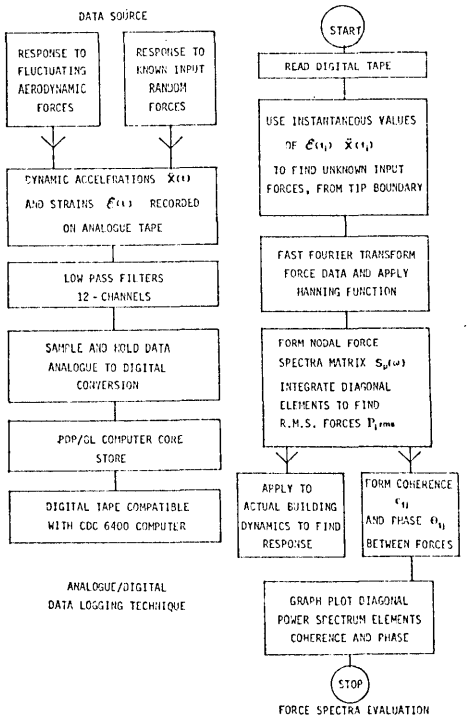
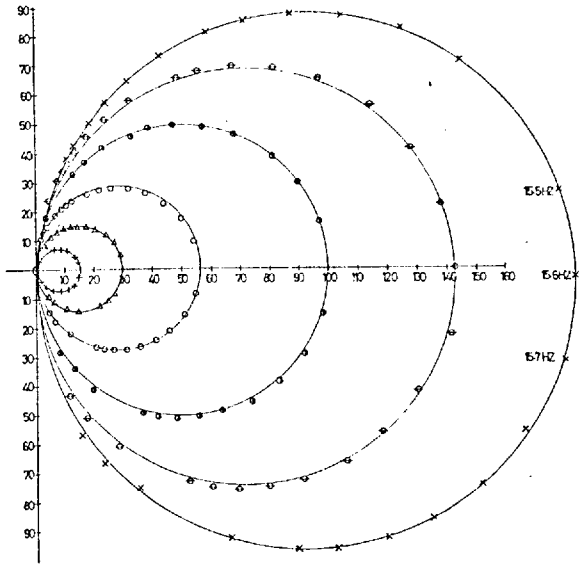
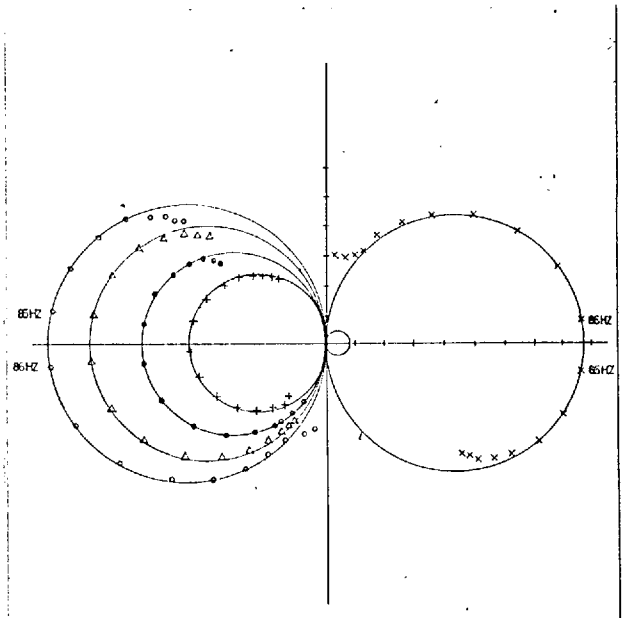


FIG 6 COMPUTER FLOW CHART - FORCE PREDICTION



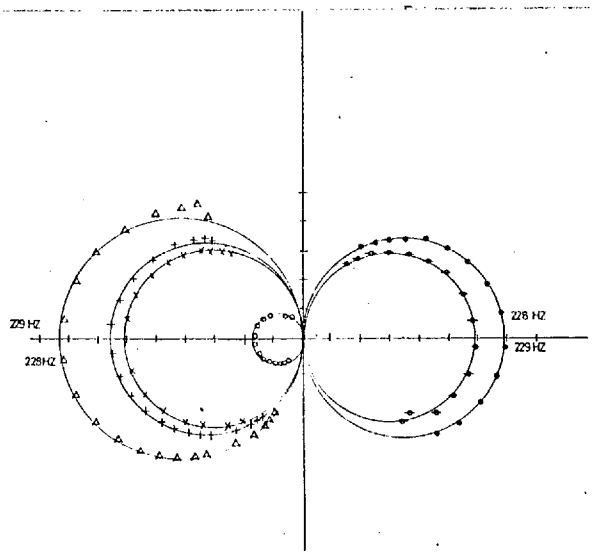
EXPERIMENTAL EIGENVECTOR	THEORETICAL EIGENVECTOR	DAMPING $\frac{\Delta\omega}{\omega}$	RESONANT FREQUENCY
1.000	1.000	0.033	15.6 HZ
0.790	0.765	0.033	15.6
0.527	0.530	0.033	15.6
0.302	0.312	0.033	15.6
0.159	0.120	0.033	15.6
0.070	0.044	0.033	15.6

FIG 7
STRUCTURAL RESPONSE LOCII (FIRST MODE)



EXPERIMENTAL EIGENVECTOR	THEORETICAL EIGENVECTOR	DAMPING $\frac{\Delta\omega}{\omega}$	RESONANT FREQUENCY
0.952	0.912	.045	85.0 HZ
0.032	- 0.051	.046	85.0
- 0.971	- 0.756	.044	85.0
- 1.099	- 1.070	.044	85.0
- 0.962	- 0.759	.045	85.0
- 0.565	- 0.278	.046	85.0

FIG 8
STRUCTURAL RESPONSE LOCII (SECOND MODE)



EXPERIMENTAL EIGENVECTOR	THEORETICAL EIGENVECTOR	DAMPING $\frac{\Delta\omega}{\omega}$	RESONANT FREQUENCY
- 0.727	- 0.633	0.023	229 HZ
0.710	0.652	0.022	229
0.036	0.052	0.022	229
- 0.247	- 0.253	0.022	229
- 1.000	- 1.000	0.022	229
- 0.796	- 0.801	0.022	229

FIG 9
STRUCTURAL RESPONSE LOCII (THIRD MODE)

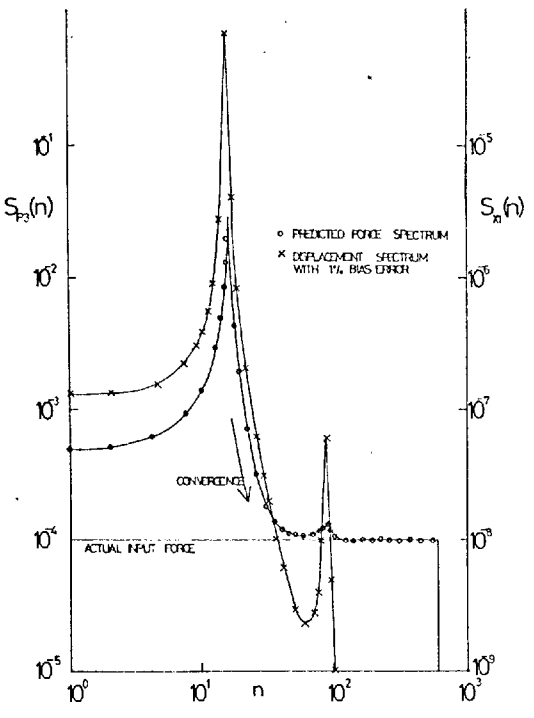


FIG 10 MATHEMATICAL PERTURBATION OF ORIGINAL SYSTEM

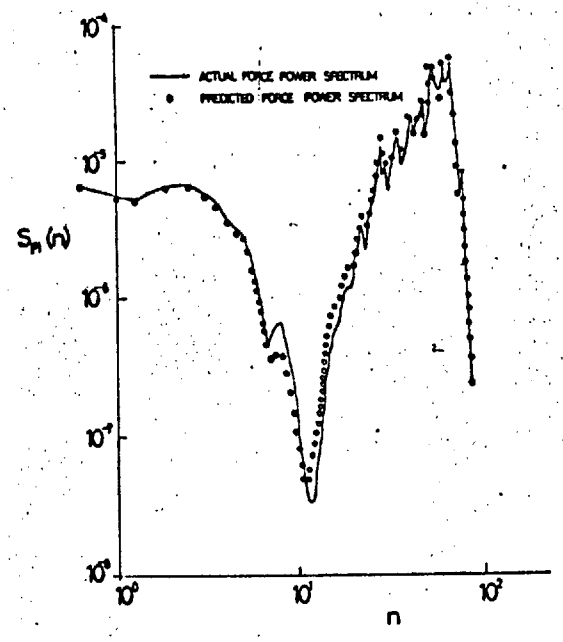


FIG 11 COMPARISON OF ACTUAL AND PREDICTED FORCE POWER SPECTRA

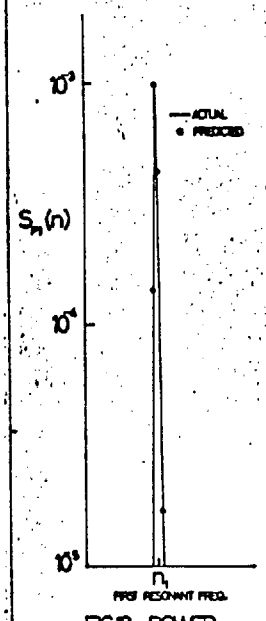


FIG 12 POWER SPECTRUM

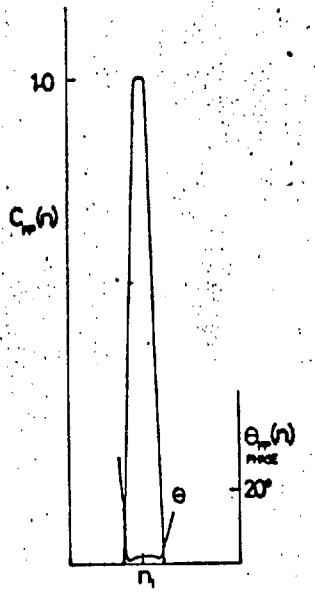


FIG 13 COHERENCE AND PHASE

SINUSOIDAL FORCE AT RESONANCE

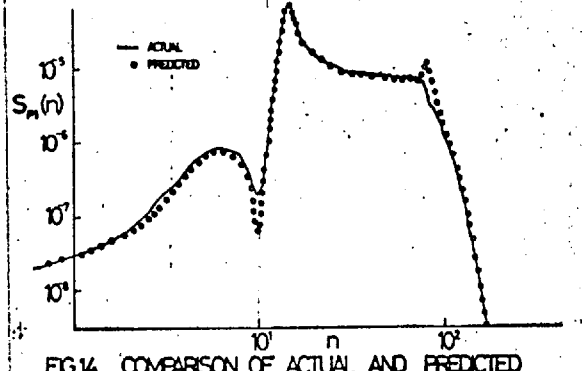


FIG 14 COMPARISON OF ACTUAL AND PREDICTED FORCE POWER SPECTRA

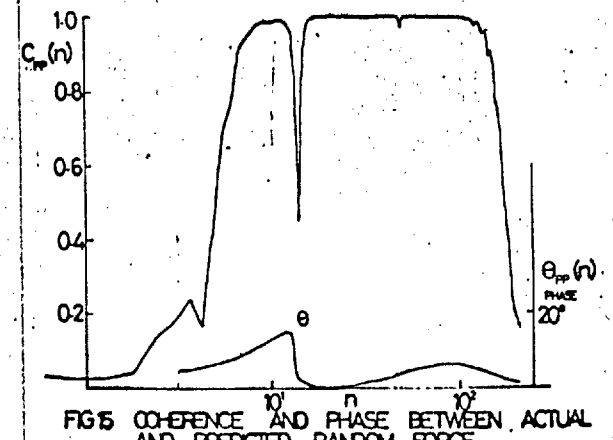


FIG 15 COHERENCE AND PHASE BETWEEN ACTUAL AND PREDICTED RANDOM FORCE

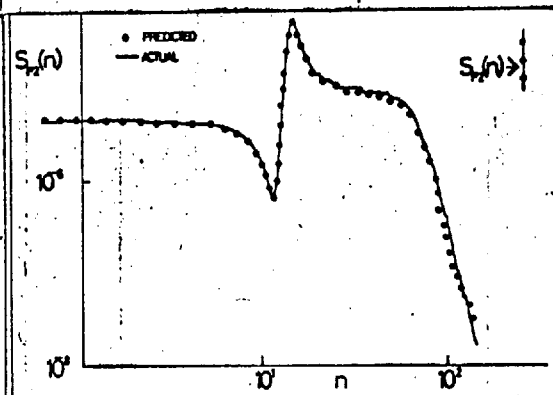


FIG 16 COMPARISON OF ACTUAL AND PREDICTED FORCE POWER SPECTRA

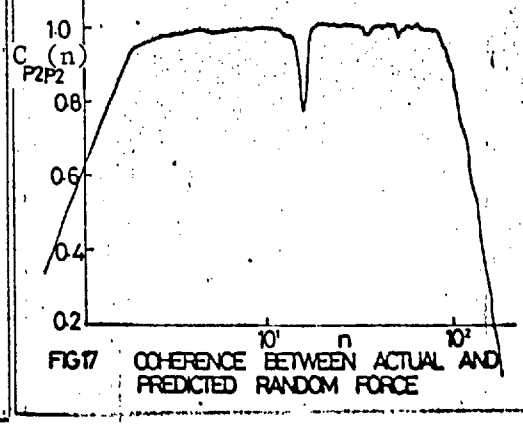


FIG 17 COHERENCE BETWEEN ACTUAL AND PREDICTED RANDOM FORCE

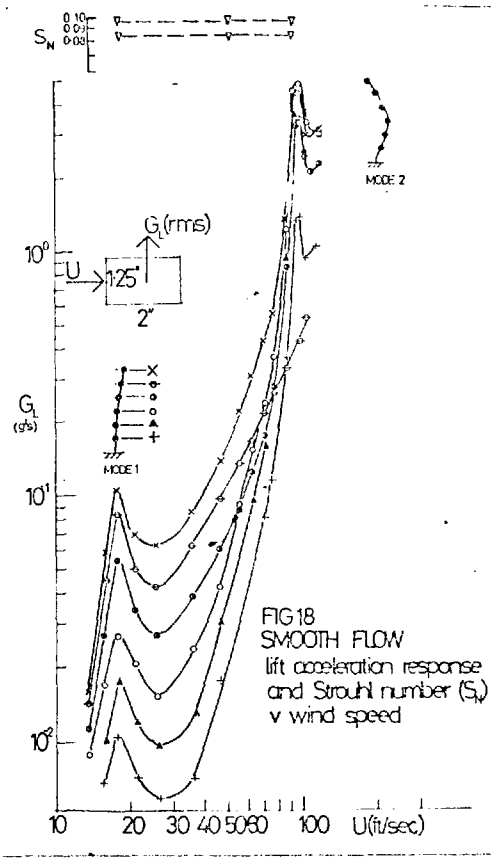


FIG 18
SMOOTH FLOW
lift acceleration response and Strouhl number (S_N) v wind speed

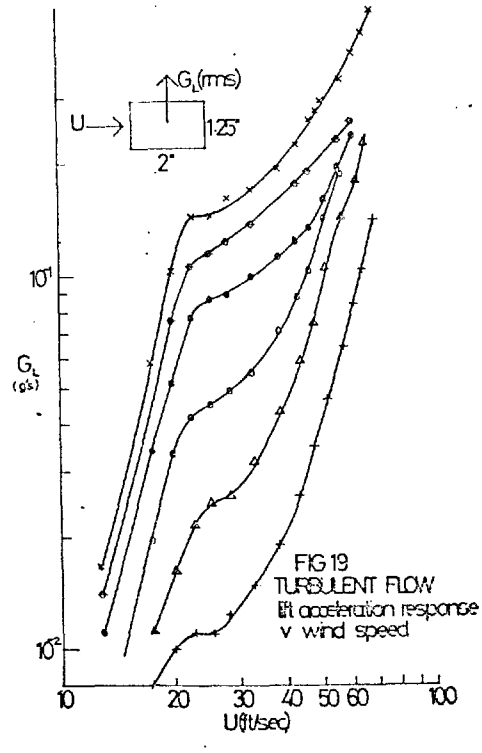


FIG 19
TURBULENT FLOW
lift acceleration response v wind speed

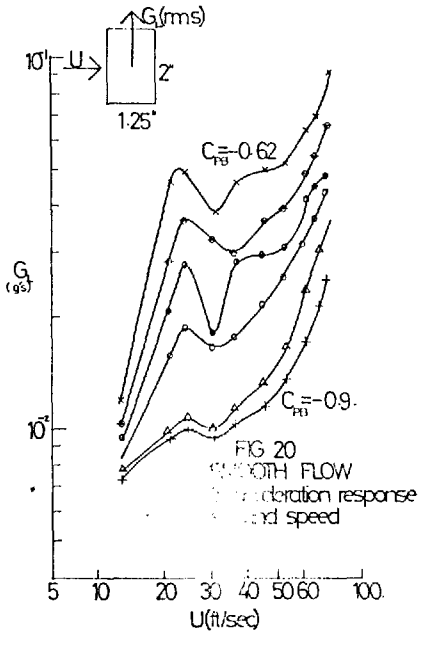


FIG 20
SMOOTH FLOW
lift acceleration response v wind speed

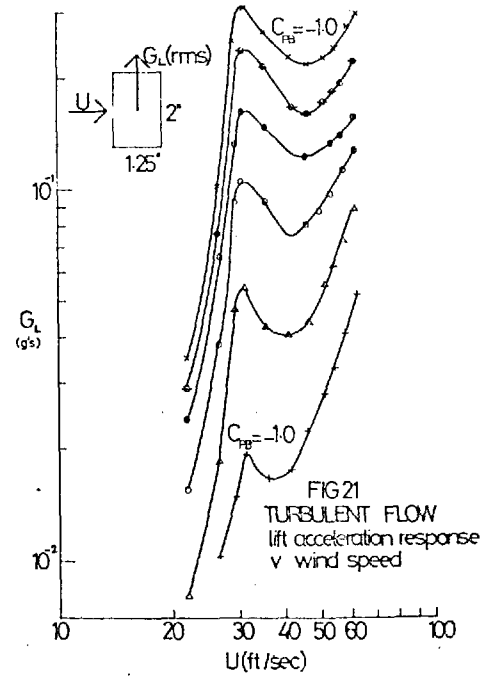


FIG 21
TURBULENT FLOW
lift acceleration response v wind speed

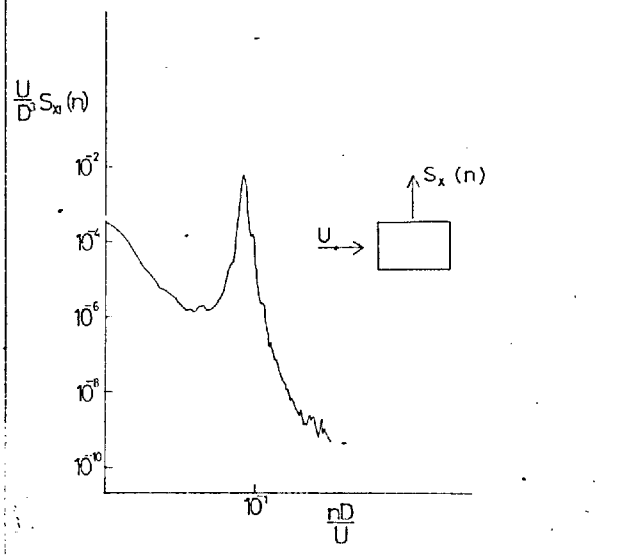


FIG 22 SMOOTH FLOW LIFT DISPLACEMENT POWER SPECTRUM V $\frac{nD}{U}$ Re=1·26x10⁴ (U=19ft/sec)

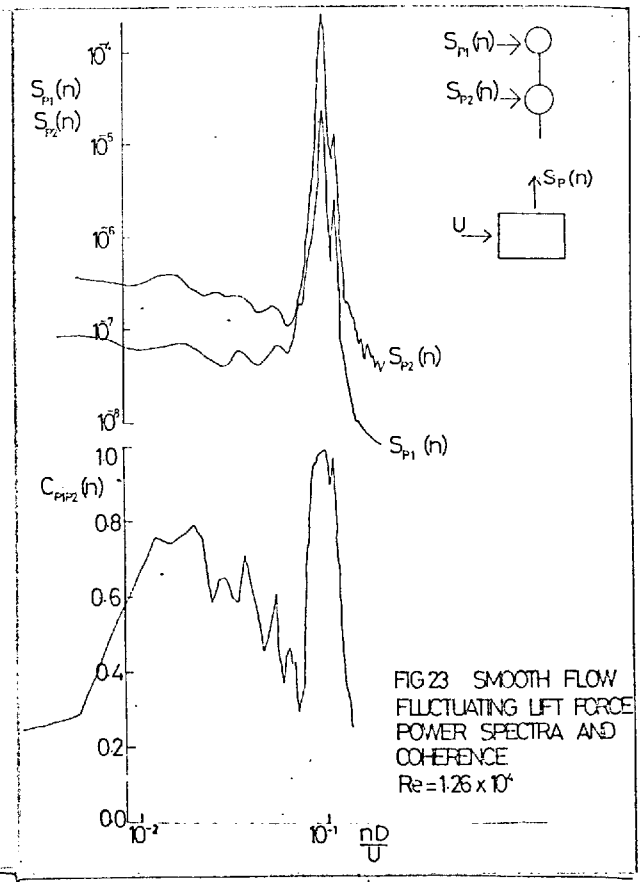


FIG 23 SMOOTH FLOW FLUCTUATING LIFT FORCE POWER SPECTRA AND COHERENCE Re=1·26x10⁴

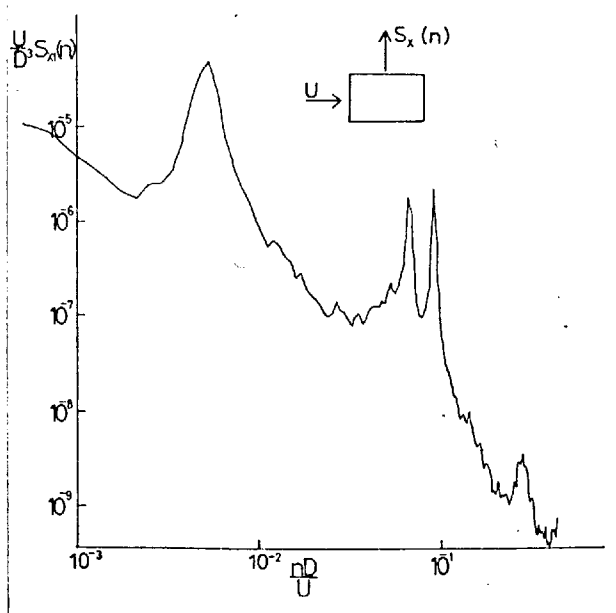


FIG 24 SMOOTH FLOW LIFT DISPLACEMENT POWER SPECTRUM V $\frac{nD}{U}$ Re=3·7x10⁴ (U=56ft/sec)

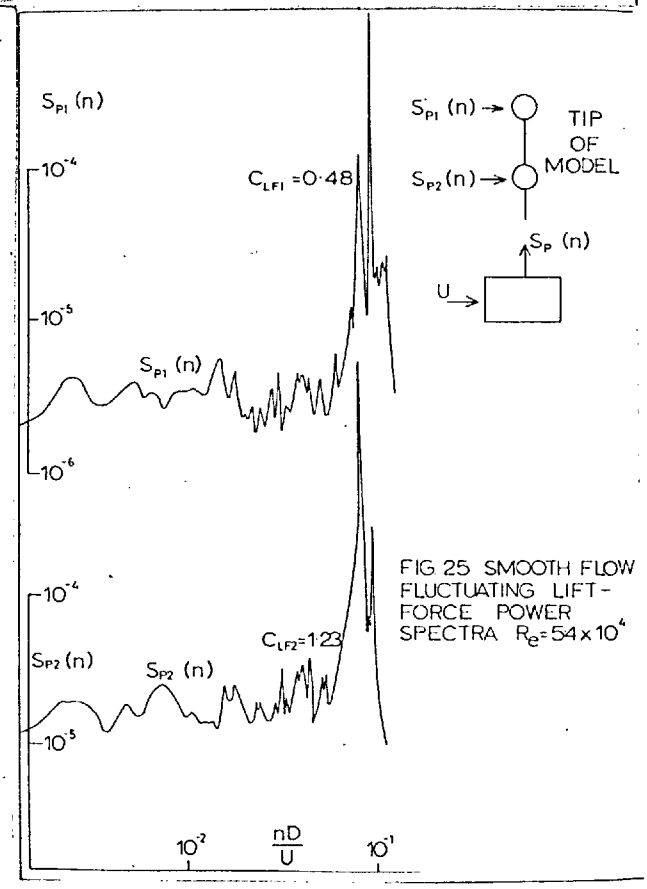


FIG 25 SMOOTH FLOW FLUCTUATING LIFT-FORCE POWER SPECTRA $R_e=5·4\times10^4$

PAPER No.312

INTERNATIONAL SYMPOSIUM

VIBRATION PROBLEMS IN INDUSTRY

10-12 APRIL 1973

KESWICK, ENGLAND

Supplement to
a technique for predicting the fluctuating aerodynamic forces on a flexible building

by

N. ELLIS and P. F. KILTY

organised by

UK ATOMIC ENERGY AUTHORITY
WINDSCALE

and

NATIONAL PHYSICAL LABORATORY
TEDDINGTON

This section has been modified since submission to improve the prediction of the unknown input forces by:

1. treating the aerodynamic force as a distributed force, P per unit length, and allowing the distributed force to vary linearly over each element,
2. including the mass of the shell (using kinematically consistent lumped masses), and
3. incorporating varying damping in the frequency domain

From Diagram B two equations of equilibrium can be formed at time instant t_i . In matrix form

Moments:

$$M = \alpha P + \beta S - [\gamma m + \eta \lambda + \rho]\ddot{X} \qquad \text{(i)}$$

Shear Forces:

$$\delta P + \Omega S = [m + \pi_s \lambda + \pi_\rho]\ddot{X} \qquad \text{(ii)}$$

Substituting for S in (i) from (ii) gives

$$P = [\alpha - \beta \Omega^{-1} \delta]^{-1} \{ M + [\Gamma - \Lambda]\ddot{X} \} \qquad \text{(iii)}$$

where $\Gamma = \gamma m + \eta \lambda + \rho$:

moments due to: masses, shell, cross panels

and $\Lambda = \beta \Omega^{-1} \{ m + \pi_s \lambda + \pi_\rho \}$

shear forces: masses, shell, panels

and using the transformation $\ddot{\xi} = \lambda \ddot{X}$

where λ relates the accelerations of the stations to the measured nodal accelerations, assumed to vary linearly between nodal points.

Eqn. (iii) is the matrix equivalent of the equations on p. 10 if point loads are assumed and damping neglected, this allowing the solutions for P in the time domain.

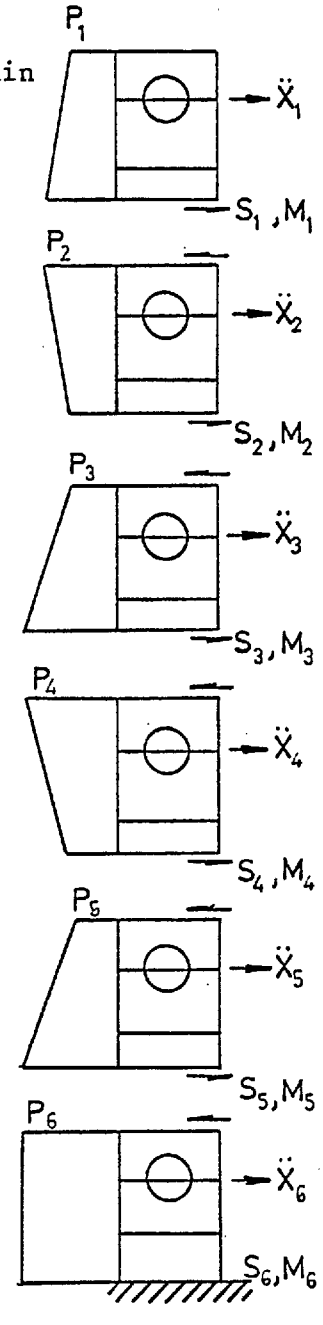


DIAGRAM B

Now $M(\omega) = \frac{EI}{\ell}\left(1 + i g(\omega)\right) \mathcal{E}(\omega)$, where the strain $\mathcal{E}$ is complex due to the effects of the higher modes, not damping as indicated on p. 10, that is, at resonance the input forces are subdivided into the forces exciting the higher modes, and damping forces. The damping plays a less important role where the strains are small, and the effect of the higher modes predominate - see for example the prediction of a sinusoidal force at the top of the model for first mode resonance (Fig. 12). The damping will obviously play a more important role where the strains are larger. When damping $g(\omega)$ is included, Eqn. (iii) must be solved in the frequency domain.

Thus the Fourier transform of Eqn. (iii)

$$P(\omega) = \left[\alpha - \beta\,\Omega^{-1}\delta\right]^{-1}\left\{ M(\omega) + \left\{\Gamma - \Lambda\right\}\ddot{X}(\omega)\right\}$$

where $M(\omega)$ are the Fourier components of the moments shown on Diagram B.

and $P(\omega)$, $\mathcal{E}(\omega)$, $\ddot{X}(\omega)$, are the complex Fourier coefficients.

The variation of the damping $g(\omega)$ with ω is formed as outlined in Section 6, also see graphs Figs. 7, 8, and 9.
And the force spectra matrix

$$S_p(\omega) = P(\omega)\,\overline{P^{t}_{*}(\omega)} \quad \text{for varying } \omega \ .$$

The effect of these modifications on the aerodynamic forces is being investigated, and it is hoped that the results will be available at the Conference.

Mathematical Notation - Supplement

α	6 x 6	matrix	relates	moments	at	cuts	due	to	distributed	P
β	"	"	"	"	"	"	due	to	S	
γ	"	"	"	"	"	"	"	"	m	(nodal masses)
η	"	"	"	"	"	"	"	"	shell mass	
ρ	"	"	"	"	"	"	"	"	cross panels	
δ	6 x 6	matrix	relates	shear	forces	at	cuts	due	to	distributed P
Ω	"	"	"	"	"	"	"	due	to	S
π_s	"	"	"	"	"	"	"	"	"	shell mass
π_ρ	"	"	"	"	"	"	"	"	"	cross panels